On the rotation and clustering of galaxies

Efstathiou, George

Efstathiou, George (1979) *On the rotation and clustering of galaxies*, Durham theses, Durham University. Available at Durham E-Theses Online: http://etheses.dur.ac.uk/10464/

ON THE ROTATION AND CLUSTERING OF GALAXIES

George Efstathiou

July 1979

Being an account of work done at the Department of Physics and submitted to the University of Durham in accordance with the regulations for admission to the degree of Doctor of Philosophy.

On The Rotation and Clustering of Galaxies

George Efstathiou

Abstract

The tidal torque theory for the origin of galactic rotation has been investigated using N-body computer simulations. The results show that this process is considerably less efficient than was previously thought, though consistent with recent observations of the rotation of giant elliptical galaxies. Spectroscopic observations of three elliptical galaxies along both major and minor axes are presented. Two galaxies were found to be slowly rotating, inconsistent with rotationally supported oblate spheroids. No convincing evidence for minor axis rotation was found. An investigation of the clustering of particles in Friedmann models of the Universe has been carried out using N-body simulations. The results of these computations have been analysed in terms of the two- and three-point correlation functions and various velocity statistics. It is found that the shapes of the two- and three-point functions are dependent upon the cosmological density parameter Ω, and that the shape of the two-point function is in rough agreement with simple analytic treatments based on the homogeneous spherical cluster model for the collapse of protoclusters. The effects of particle discreteness and two-body relaxation, which are particularly important in the N-body models are examined. The approach is compared to the detailed kinetic theory calculations of Davis and Peebles. The cosmological implications of the results are discussed. Other statistics, such as the multiplicity function are also considered.

Contents

Preface

The work described in this thesis has not been submitted for any degree, diploma or other qualification at any other university. The work has been carried out in collaboration: Chapter 2 with Bernard Jones, Chapter 3 with Richard Ellis, Chapter 5 with Mike Fall and Craig Hogan, and Chapter 6 with Dave Carter and Richard Ellis.

"Imaginary universes are so much more beautiful than this stupidly constructed "real" one.

G.H. Hardy, A Mathematicians Apology,
(1940)

CHAPTER 1

INTRODUCTION

Galaxy formation is perhaps the most difficult and speculative branch of modern cosmology. It is hard to imagine that the primordial matter composing the Universe was perfectly uniformly distributed. But if we admit to primordial inhomogeneities there is a danger of completing a full circle, of feeding in the correct initial conditions to produce the observed Universe. The usefulness of such an exercise is dubious.

The difficulty occurs because the problem of galaxy formation is tied up with the problem of initial conditions, and perhaps the origin of the Universe itself. It is not surprising, therefore, that even within the framework of hot Big Bang cosmology there exist a plethora of different theories which attempt to explain the origin of galaxies and clusters. The purpose of this introduction is to review briefly some of these theories and to indicate my reasons for working on the gravitational instability theory.

1.1 The Microwave Background and the Origin of Light Elements

The discovery of the microwave background by Penzias and Wilson (1965) has had an enormous impact on modern cosmology. Observations have shown that:

(i) The microwave background has an approximately black-body spectrum with a temperature of $T \approx 2{\cdot}7$ K.

(ii) The background radiation is isotropic. Recent measurements (summarized by Boynton, 1977) yield upper limits of $\Delta T/T \lesssim 10^{-3}$ on angular scales between $2'$ to $30'$.

If it is assumed that the Universe can be described at early epochs by the standard Friedmann models (and observation (ii) above gives some evidence for this assumption) then the hot Big Bang theory can be used in order to compute the primeval light element abundances. The first convincing calculations on the production of helium in the primeval fireball were performed by Peebles (1966). Using the black-body temperature measured by Penzias and Wilson, Peebles found that the helium abundance (by mass) should be 28% in the case of an Einstein de-Sitter ($\Omega = 1$[*]) world model. This agrees remarkably well with the observed "cosmic" helium abundance. Detailed calculations by Wagoner, Fowler and Hoyle (1967) allowed predictions for the abundances of other light elements such as D and Li^7. The interesting point in the case of D and Li^7 is that the predicted abundances (unlike He^4) are extremely sensitive to the present baryon density. If taken literally, the calculations of D abundance suggest

---

[*] Throughout this thesis, $\Omega = \rho/\rho_c$, where ρ_c is the density in an Einstein-de Sitter universe, $\rho_c = 3H_0^2/8\pi G$.

that $\Omega \lesssim 0{\cdot}1$ (Gott, Gunn, Schramm and Tinsley, 1974), i.e. the Universe is open by a wide margin. It is difficult to assess the significance of this result because the observed deuterium abundance is very small and may, therefore, be affected by recent production or astration.

An interesting feature of the hot Big Bang model is that the photon entropy per baryon, σ, remains constant during the expansion with a value

$$\sigma = \frac{4\,a\,T^3}{3nk} \approx 1{\cdot}3 \times 10^8 \,(\Omega\, h^2)^{-1} \qquad (1.1)^*$$

For a hot Universe σ must by definition be $\gg 1$, but at present the standard hot Big Bang theory offers no convincing reason as to why σ should take this particular value.

The hope here is that σ can be calculated on the basis of a theory of elementary particles incorporating baryon non-conservation and CP violation. An attempt along these lines has been made recently be Weinberg (1979). A radically different model has, however, been proposed by Rees (1978). In Rees' picture the background radiation is generated by starlight at redshifts $z \gtrsim 100$ and the radiation is thermalised by a combination of dust, molecules, or perhaps by free-free absorption if

---

* Throughout this thesis, h will denote Hubble's constant H_0 in units of 100 km s^{-1} Mpc^{-1}.

the stars can significantly photo-ionize the pregalactic medium. The stars, having burnt out, may then provide the dark mass required to bind galaxy clusters and account for galaxy halos. The model allows a calculation of the entropy/baryon and Rees finds $\sigma \sim 10^8$ to within an order of magnitude. Rees' model does not offer a satisfactory account of the synthesis of light elements and this would seem to be the model's major difficulty. Nevertheless, Rees' model does serve to illustrate the magnitude of the assumptions involved in using the hot Big Bang model to study the very early Universe.

1.2 Theories of Galaxy Formation.

Within the context of the standard hot Big Bang models, three theories have been studied in some detail in recent years. These are: (i) The cosmic turbulence theory, (ii) Gravitational instability of adiabatic perturbations - the so called "pancake theory", (iii) Gravitational instability of isothermal perturbations- the "entropy perturbation theory".

In addition to these three theories, several other proposals have been made invoking primeval magnetic fields (Wasserman, 1978), black holes (Mezaros, 1974; Carr, 1975), lagging cores (Novikov, 1965), matter-antimatter annihalation in the early Universe (Harrison, 1968; Stecker and Puget, 1972). These proposals remain largely conjectural since in most cases they do no better than theories (i), (ii) and (iii) at the expense of introducing more "free" parameters or "exotic" objects which have no firm empirical foundation at present. I shall not discuss them further and instead I shall concentrate attention on theories (i), (ii) and (iii).

a) Cosmic turbulence

Cosmic turbulence was first introduced in the context of Big Bang cosmology by Ozernoi and Chernin (1968) and has since been studied in great detail by Ozernoi and coworkers (see e.g. the detailed review by Jones, 1976, and references therein). The theory attempts to explain the masses and angular momenta which are characteristic of large galaxies, and the pattern of galaxy clustering in terms of one parameter w_{max}, the maximum turbulence velocity specified at some epoch, say, the time t_{equ} when $\rho_r = \rho_m$. It is assumed that during the radiation era, energy transfer between eddies on different scales established a Kolmogorov spectrum $v \propto l^{\frac{1}{3}}$ over scales $l_{min} < l < l_{max}$. Here l_{min} is the scale at which dissipation of turbulence becomes dominant (ie when the Reynolds number $R \sim 1$) and l_{max} is the maximum scale over which an eddy can turn within a Hubble time and hence participate in the energy cascade $l_{max} \sim v_{max}$ t. The pre-recombination turbulence must be subsonic $v_{max} < c/\sqrt{3}$ (and hence $l_{max} < l_{horizon} = ct$) otherwise the Universe will be chaotic. During recombination the photon mean free path increases rapidly and the Thomson drag force acting on the electrons exerts a damping on the velocity spectrum. Calculations by Kurskov and Ozernoi (1974) and Jones (1977) show that only motions on mass scales greater than

$$M_D \sim 5 \times 10^{11} \quad (\Omega h^2)^{-7/2} \; M_\odot \tag{1.2}$$

will survive recombination. The post-recombination evolution of cosmic turbulence has been considered by Peebles (1971a). Since the sound speed drops sharply the turbulence will become supersonic. If the eddy turn over timescale is less than the Hubble timescale (strong turbulence) then strong compression will occur soon after recombination resulting in overdense lumps. If the eddy turn over time is greater than the Hubble timescale (weak turbulence), the velocity spectrum that survives dissipation acts as a source term, generating density fluctuations. Even in this case, the work of Jones (1977) and Peebles (1971a) taken together show that overdense lumps are formed unless w_{max} is taken to be so small that (i) the theory can no longer account for the angular momenta characteristic of spiral galaxies, (ii) the maximum scale on which the Kolmogorov spectrum could be established

$$M_{max} \gtrsim 3 \times 10^{15} \; (\Omega \; h^2)^{-2} \; w_{max}^3 \; M_\odot \tag{1.3}$$

is less than the damping mass scale (equ. 1.2). On mass scales $> M_{max}$, the velocity spectrum will retain its primordial form and so the theory loses the ability to make predictions using only one parameter w_{max}.

In addition to the above mentioned problems, the cosmic turbulence theory suffers from the following difficulties in the pre-recombination era:

(i) The arguments which suggest the establishment of a Kolmogorov spectrum over the inertial range have not yet been established rigorously.

(ii) Given the velocity w_{max} at t_{equ}, there exists some time t_f at which the metric perturbations $\delta g/g$ become of order unity (Barrow, 1977), hence at sufficiently early times the Universe is non-Friedmannian.

The non-Friedmannian nature of the early universe is sufficient to upset the standard picture of the nucleosynthesis of light elements. The problem has been considered in some detail by Barrow (1977) who finds that helium and deuterium abundances within the range indicated by observations may only be obtained on galactic scales if $\Omega < 1{\cdot}4 \times 10^{-2}$.

In view of all these problems it is perhaps not surprising that the cosmic turbulence theory has lost popularity recently.

b) Pancake theory

The elements of the pancake theory were first given in a paper by Sunyaev and Zeldovich (1972). They consider small amplitude primeval adiabatic perturbations of the standard Friedmann models. During the radiation era adiabatic perturbations execute acoustic oscillations on scales smaller than the Jeans length $\lambda_J \sim ct/\sqrt{3}$. During the acoustic phase, radiative diffusion and viscous dissipation lead to damping on small scales. This process, together with the damping of perturbations during the recombination process, has been studied by several authors, notably Silk (1968) and Peebles and Yu (1970). The detailed calculations by Peebles and Yu indicate a critical damping mass of

$$M_S \sim 3 \times 10^{12} (\Omega h^2)^{-5/4} M_\odot \qquad (1.4)$$

Clearly, unless $\Omega h^2 \gtrsim 1$ the "Silk mass" M_S exceeds that of a typical bright galaxy ($\sim 10^{11} M$). However, as noted by Zeldovich (1974) in a low density cosmological model with $\Omega = 0{\cdot}1$, $h = 0{\cdot}5$ (which are the values favoured by Gott et al, 1974) , the Silk mass takes the value $M_S \sim 3 \times 10^{14} M_\odot$ which is close to the mass of a rich cluster of galaxies. If these parameters are adopted, the first objects to condense will be of cluster (or supercluster) size and so galaxies must form by the subsequent fragmentation of these gas clouds. These gas clouds will collapse anisotropically (Zeldovich, 1970) and form a pancake consisting of a hot shocked layer of gas in which is embedded a cool dense layer. Fragmentation of the cool gas occurs in the cool layer with characteristic masses in the range $10^6 M_\odot \lesssim M \lesssim 10^9 M_\odot$ (Doroshkevich et al, 1978). It is well known (Binney, 1974).that vorticity is generated as gas flows across a curved shock front and that in collapsing pancakes this mechanism can adequately explain the vorticity of spiral galaxies. Hence, off the central plane of the pancake, turbulence will be of great importance. The characteristic masses of the first fragments to condense in the cool layer are smaller than those of typical bright galaxies, but according to Doroshkevich et al, the gas clouds agglomerate by gravitational instability into protogalaxies with masses in the range $10^9\ M_\odot - 10^{12}\ M_\odot$.

This theory is quite attractive. The work done to date shows no contradiction with observations. Indeed, several observations have a natural explanation on the basis of this picture. These are as follows:

(i) The recently published map of the Shane-Wirtanen galaxy catalogue (Soneira and Peebles, 1976) shows marked filamentary structure. The reality of these structures is a matter of current debate but such large scale structure would be expected from the uni-dimensional collapse of pancakes.

(ii) Redshift surveys of particular areas of sky indicate that large regions of space are apparently devoid of galaxies (e.g. Gregory and Thompson, 1978). On the pancake picture these holes would represent the large inter-pancake regions where galaxies could not form. It is difficult to assess the statistical significance of these observations until a very large "fair" volume of space has been surveyed so that we can estimate the frequency distribution of such holes.

(iii) The Local Supercluster appears to be highly flattened (see e.g. the pictures of Tulley, 1977). Again this finds an explanation in the pancake theory in terms of anisotropic collapse.

Perhaps the weakest point of this theory lies in the notion of large scale shocks, i.e. it requires a belief that the gas cloud will not fragment before the shocks are generated as would occur if, say, isothermal perturbations were present on small scales. The explanations of the observations listed above do not rely on the generation of large scale shocks whilst the calculations of galaxy masses, radii and angular momenta do. There is also another possible problem. There has been a great deal of work in recent years on the statistical analysis of galaxy catalogues (see chapter 4), but until the dissipative processes are well understood, it will be difficult to provide a quantitative model for the clustering of galaxies.

c) Entropy perturbations

During the radiation era, entropy perturbations do not grow since the matter is strongly coupled to the radiation field by Thomson drag (Peebles, 1965). However, they are not damped during recombination and hence the spectrum of perturbations at recombination reflects the primordial spectrum. The Jeans mass just after recombination takes the value

$$M_J \sim 102\ M_\odot\ \sigma^{-\frac{1}{2}} = 1 \cdot 1 \times 10^6 \ (\Omega h^2)^{-\frac{1}{2}} \qquad (1.5)$$

which is much smaller than a typical galactic mass. The important feature of this theory compared with the pancake theory is that structure on small scales collapses first, i.e. galaxies form before clusters. One might then hope to explain the large scale structure of the universe using gravitational instability rather than large scale dissipative processes. Hence an attractive feature of this theory is that quantitative calculations should be relatively simple. The approach taken in this thesis is to make a quantitative study of the non-linear problem of dissipationless clustering using N-body simulations and to compare the results with observation.

Before the theory can make quantitative predictions it is necessary to make some assumption regarding the spectrum of density perturbations at recombination. We shall assume that the density perturbations can be approximated as a random Gaussian (random phase) process with power spectrum at recombination

$$\langle |\delta_{\underline{k}}|^2 \rangle = \left(\frac{k}{k_m} \right)^n \qquad (1.6)$$

Hence the initial conditions are fixed by two parameters, k_m which defines the amplitude of the perturbations at recombination, and the spectrum index n. It must be emphasised that the equation (1.6) is to be regarded merely as a working hypothesis. The test will be to see how wide a range of phenomena can be correctly predicted on this assumption.

The theory should be able to explain at least the following:

(i) The masses, radii and angular momenta of galaxies.

(ii) The origin of the Hubble sequence.

(iii) The pattern of galaxy clustering.

Important clues as to the characteristic masses and radii of galaxies have emerged from the cooling arguments of Binney (1976), Silk (1977), Rees and Ostriker (1977). In this thesis, I have paid particular attention to the problem of the angular momenta of galaxies and to the problem of galaxy clustering.

Both of these problems have been previously studied but these treatments could hardly be described as satisfactory.

On the observational side, advances in absorption line spectroscopy have led to the measurement of rotational velocities and velocity dispersions of a large number of elliptical galaxies with which to compare theoretical predictions. The statistical analyses of galaxy catalogues by Peebles and coworkers has resulted in important data on the pattern of galaxy clustering allowing a comparison with theoretical predictions.

It is apparent, from this brief review, that the gravitational instability theories are currently the most succesful theories of galaxy formation. The entropy perturbation theory in the form outlined above is the simpler, but that, of course, does not mean it is a better theory. It does mean, however, that it will be the easier to bring into direct confrontation with observational data.

CHAPTER 2

THE TIDAL TORQUE THEORY

2.1 Introduction.

If the entropy perturbation theory is to prove a viable theory for the formation of galaxies and galaxy clusters, it is important that we understand the origin of cosmic angular momentum in this context. In the absence of primordial vortical motions and large scale shocks, a natural way to produce rotating systems is through the tidal interactions between neighbouring protostructures. The tidal torque theory has had a controversial history. Originally proposed by Hoyle (1949), it was subsequently introduced within the framework of Big Bang cosmology by Peebles (1969) where he concluded that tidal torques are sufficient to explain to within an order of magnitude the angular momentum of our galaxy. Since then, analytic calculations have been performed by Oort (1970) and Harrison (1971) and both concluded that Peebles had overestimated the efficiency of the tidal torque mechanism. The reasons for these discrepancies can be attributed to the authors' assumptions concerning the matter distribution around the developing protogalaxies. For example, unless the galaxy formation process is very efficient there is likely to be a substantial fraction of matter distributed between protogalaxies and this matter may compensate the field irregularities due to neighbouring protogalaxies. Another point, made by Oort, is that protogalaxies may align themselves so as to minimise their quadrupole interactions. It is difficult to make quantitative analytic estimates of the importance of these effects, since they require a treatment of tidal interactions during the non-linear stage of protocluster growth.

In this chapter I shall address the problem using N-body simulations for the development of structure in an expanding universe. This approach should include the above mentioned effects and provide a description of the non-linear stages of cluster evolution. Peebles (1971b) has performed a series of small (N=100) numerical experiments, the results of which agreed (roughly) with his earlier analytic calculations. The small particle number meant, however, that even this numerical treatment was over-simplified.

Recently new theoretical estimates of the efficiency of the tidal torque mechanism have been computed, using Monte-Carlo models, by Gott and Thuan (1976) and Thuan and Gott (1977). These estimates fit nicely with Gott and Thuan's proposal that the flattening of elliptical galaxies is related to their rotation through the Maclaurin spheroid models. In section 2.5 I compare the results from the numerical simulations with observational data and the Maclaurin spheroid hypothesis.

2.2 Linear Perturbation Theory.

If the numerical simulations are to be believed, they should at least reproduce the results of linear perturbation theory. Here I briefly review Peebles (1969) calculation.

Define a coordinate system $\underline{x}$ by $\underline{r} = a(t)\,\underline{x}$, where a(t) satisfies the Friedmann equations

$$3\ddot{a} = -4\pi G\bar{\rho}\,a \tag{2.1}$$

$$\bar{\rho} \propto a^{-3} \tag{2.2}$$

In this coordinate system, the equation of continuity becomes

$$\frac{D\rho}{Dt} + (3H + u_{i,j})\rho = 0 \tag{2.3}$$

The Euler equation becomes

$$\frac{Du_i}{Dt} + 2Hu_i = -a^{-2}\phi_{,i} \tag{2.4}$$

and the potential ϕ satisfies

$$-a^{-2}\nabla^2\phi = 4\pi G(\rho - \bar{\rho}) \tag{2.5}$$

here $\underline{u} = \dot{\underline{x}}$ and $\frac{D}{Dt}$ is the convective derivative

$$\frac{D}{Dt} \equiv \frac{\partial}{\partial t} + u_j\partial_j$$

If we write $\delta = (\rho - \bar{\rho})/\bar{\rho}$, the solutions to equs. (2.3)-(2.5) in the linear case ($\delta \ll 1$) and $\Omega = 1$, are

$$\delta = \delta(\underline{x})\ t^{2/3} \qquad (2.7a)$$

$$u^{\alpha} = \sum_{\underline{k}}{}' u_{\underline{k}}^{\alpha}\ e^{i\underline{k}\cdot\underline{x}} \qquad (2.7b)$$

$$u_{\underline{k}}^{\alpha} = \frac{2i}{3}\ \frac{a}{t^{1/3}}\ \frac{k_{\alpha}}{k^{2}}\ \delta_{\underline{k}} \qquad (2.7c)$$

where $\delta_{\underline{k}}$ is the Fourier transform of the function $\delta(\underline{x})$

$$\delta(\underline{x}) = \frac{3}{5}\left[\delta_1(\underline{x}) - t_1 \frac{\underset{\sim}{\nabla}\cdot\underline{u}_1}{a_1}\right]\frac{1}{t_1^{2/3}}$$

(Peebles and Dickie, 1969). Under the assumption of a power law spectrum of fluctuations at recombination (equation 1.6) with random phases for the amplitudes of $\delta_{\underline{k}}$, Peebles (1969) derives the following expression for the r.m.s. value of the angular momentum of matter within a sphere of radius x_o about its centre of mass

$$\langle \mathcal{L}^2 \rangle^{\frac{1}{2}} = \frac{8\pi}{45}\ \frac{\bar{\mathcal{L}}}{t}\ (ax_o)^5 \langle \delta_s^2 \rangle I^{\frac{1}{2}}\ J^{-1} \qquad (2.8)$$

where $\langle \delta_s^2 \rangle$ is the mean square deviation of the excess fraction of mass within a sphere of radius x_o

$$\langle \delta_s^2 \rangle = t^{4/3} \sum_{\underline{k}} |\delta_{\underline{k}}|^2\ W(kx_o)^2 \qquad (2.9)$$

and

$$W(y) = 3\left(\frac{\sin y}{y} - \frac{\cos y}{y^3}\right)$$

The dimensionless coefficient $I^{\frac{1}{2}}J^{-1}$ is tabulated by Peebles for various values of the power spectrum index n and is of order unity in the range $-1 < n < 0$.

Hence from equ.(2.8) we can see that according to linear theory, the angular momentum grows as $t^{5/3}$ and is of second order in the amplitude $\delta(\underline{x})$.

It is also instructive to examine the nature of the tidally induced velocity field. From equ. (2.4) we derive the following equation

$$\left[\frac{D}{Dt} + 2H\right]\sigma_{jk} + \sigma_{jk}\,\sigma_{ji} + \frac{2}{3}\theta\,\sigma_{ik} - \frac{1}{3}\,\sigma^{2}\,\delta_{ik} - \omega_{jk}\,\omega_{ij} + \frac{1}{3}\,\omega^{2}\,\delta_{ik} = -a^{-2}E_{ik} \qquad (2.10)$$

where

$\theta = u_{i,i}$ is the expansion

$\sigma_{i,j} = \frac{1}{2}\left(u_{i,j} + u_{j,i}\right) - \frac{1}{3}\theta\,\delta_{ij}$ is the shear

$\omega_{i,j} = \frac{1}{2}\left(u_{i,j} - u_{j,i}\right)$ is the vorticity

and $E_{ik} = \phi_{,i,k} - \frac{1}{3}\nabla^{2}\phi\,\delta_{ik}$ is the tidal field,

(see e.g. Ellis, 1971). Now, if the vorticity ω_{ij} is assumed to be zero at recombination, it will remain so at any later time by virtue of the Kelvin circulation theorem (see below). Hence, we see from equ. (2.10) that the effect of a tidal field is to induce a shear flow. Equ. (2.10) may be readily solved in the linear case to give

$$\sigma_{ij} = \frac{2i}{3t}\, a \sum_{\underline{k}} \delta_{\underline{k}} \left(\frac{k_i k_j}{k^2} - \tfrac{1}{3}\,\delta_{ij} \right) e^{i\underline{k}\cdot\underline{x}} \qquad (2.11)$$

and hence,

$$\left\langle |\sigma^2| \right\rangle^{1/2}_{x_0} = \frac{1}{t}\sqrt{\frac{8}{27}} \left\langle \left|\frac{\delta\rho}{\rho}\right|^2 \right\rangle^{\frac{1}{2}}_{x_0} \qquad (2.12)$$

The effect of shear is to elongate the perturbation. The ellipticity ϵ will be of order σt. Hence (2.12) shows that the distortion will grow as $t^{2/3}$ and is of first order in the amplitude $\delta(\underline{x})$. At the onset of non-linearity, quite significant elongations will be produced with $\epsilon \sim 0{\cdot}5$. This agrees with the detailed analysis of Binney and Silk (1979) who also considered a simple model for the non-linear generation of anisotropy.

2.3 The Origin of Vorticity.

Here I mention an old problem which has been studied by several authors (Tomita, 1973; Peebles, 1973a; Binney, 1974). As has been shown above, tidal forces will generate a shear field. The problem with the tidal theory is in how to account for the origin of vorticity. The difficulty arises from the application of Kelvin's circulation theorem, which when applied to equ. (2.4) states that

$$\frac{d}{dt} \oint a^2\, \underline{u}\cdot d\underline{s} = 0 \qquad (2.13)$$

Hence (2.13) tells us that a fluid flow which is initially irrotational will remain irrotational if the fluid is homentropic. The origin of cosmic vorticity is concerned, therefore, with the violation of equ. (2.13).

The problem has been discussed by Peebles (1973a) who points out that during the collapse of a protogalactic cloud to a spiral disk a substantial amount of dissipation must have taken place, hence equ. (2.13) will be violated and vorticity generated.

In the case of a stellar system, or a system which has fragmented into a large number of discrete gas clouds, the fluid approximation will break down and a better description of the system will be afforded by the collisionless Boltzmann equation. In this case Peebles argues that the mixing of stellar orbits will result in general to non-zero circulation along stream lines of flow.

In fact a circulation theorem may be derived from the equations of stellar hydrodynamics, representing the time dependence of circulation along stream lines of flow, which reads

$$\frac{d}{dt}\oint\langle \underline{u}\rangle.d\underline{s} \;=\; -\oint\frac{1}{\rho}\,\partial_i\left\{\rho\, v_i' v_j'\right\}ds_j \qquad (2{\cdot}14)$$

where $\langle Q\rangle = \int Q(\underline{x},\underline{v})f\; d^3\underline{v}$ and $v_i' = v_i - \langle v_i\rangle$.

On this problem, I take the same view as Peebles, i.e. objections to the tidal torque theory based on the circulation theorem grossly oversimplify the physics of the problem, which in many cases will be more complicated than would allow a simple application of the theorem.

2.4 Numerical Simulations.

As mentioned in section 2.1, the direct numerical integration of the equations of motion of self-gravitating particles in an expanding universe allows a study of the non-linear development of gravitational clustering.

A preliminary investigation of the tidal torque picture was carried out using an N-body program written by the author. This program used a fourth-order polynomial method with individual time-step per particle so as to accurately treat short range encounters, following the method of Aarseth (1972). The program allowed treatment of small ($N \lesssim 200$) systems and experiments were carried out in much the same way as those of Peebles (1971b). However, the small particle number meant that only a few particles could be assigned to an individual protogalaxy interacting with either a halo of particles or a superimposed tidal field. Such a treatment is manifestly over-simplified and although it served to illustrate that tidal torques can generate a significant amount of angular momentum the results are quite sensitive to the initial conditions (cf. Peebles, 1971b). A more satisfactory treatment may be attempted by increasing the number of particles. Such calculations are described below.

a) Initial conditions

Three models have been analysed. Each contain 1000 particles distributed pseudo-randomly within a sphere of unit radius. Each particle was assigned a velocity $\underline{v} = H\underline{r}$ with the constant H being determined by the total mass of the system so that the expansion would correspond to that of an Einstein-de Sitter universe ($\Omega = 1$). On the gravitational instability picture we would expect galaxies to have formed before the rate of expansion of the universe deviated significantly from the $\Omega = 1$ case, since the growth of small fluctuations effectively ceases at a redshift $z \simeq (1/\Omega_0) - 1$ for $\Omega_0 < 1$.

One of the models, Model A, contained 990 particles of unit mass together with 10 seed mass particles of 10 mass units each. This was an experiment to see the effect of enhancing the clustering process, but the results differed little from those from the other two models which contained 1000 particles each of unit mass (Models B and C).

b) The integrations

The numerical integration of Newton's equations of motion were performed using an N-body program developed by S.J. Aarseth and kindly loaned to the author. This program employs a fourth-order polynomial method with the Ahmad-Cohen scheme for the seperate treatment of particles internal and external to a neighbour sphere (Ahmad and Cohen, 1973; Aarseth, in preparation).

The potential used was of the form

$$\phi_{ij} = \frac{-\,Gm_i m_j}{(r_{ij}^2 + \varepsilon_o^2)^{\frac{1}{2}}} \qquad (2.15)$$

and ε_o was chosen so that its value was a few percent of the final cluster radii ($\varepsilon_o = 0{\cdot}05$) in order to ensure numerical stability. The conventional units for N-body calculations, in which G=1, were employed.

Each model was allowed to expand by a factor of $\simeq 17{\cdot}5$. Total energy was conserved to within 0•15 per cent for each model.

2.5 Results.

Fig. 2.1 shows model A at various times during the integration. Each diagram is scaled so that the coordinates are effectively comoving with the Hubble expansion.

a) Linear analysis

Fig. 2.2(a,b) shows the results of a comparison of Model A with linear theory. $\langle \delta_s^2 \rangle^{\frac{1}{2}}$ and $\langle \mathcal{L}^2 \rangle^{\frac{1}{2}}$ have been estimated by dropping ten randomly centred spheres of radius $x_o = 0{\cdot}3$ such that they did not overlap the boundary. According to linear theory

$$\langle \delta_s^2 \rangle^{\frac{1}{2}} = Aa(t) + Ba(t)^{-3/2} \qquad (2.16)$$

where the second term on the right hand side of equ. (2.16) represents the decaying mode (e.g. Weinberg, 1972). The

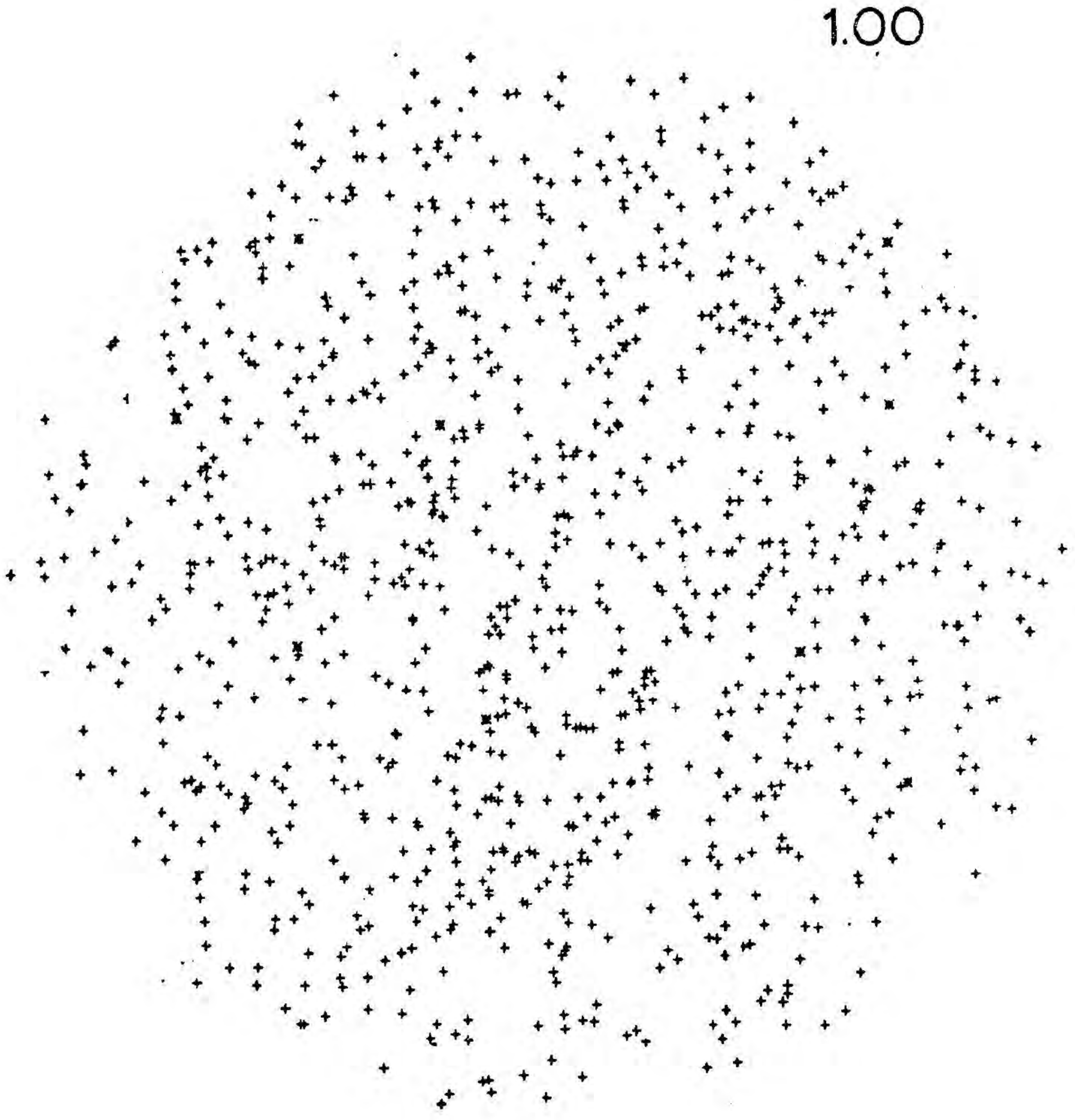

Figure 2.1 a

Figure 2.1 b

Figure 2.1 c

Figure 2.1 d

N-body models begin with zero peculiar velocities, hence the appropriate boundary conditions are $\langle\delta_s^2\rangle^{\frac{1}{2}} = \delta_i$, $\frac{d\langle\delta_s^2\rangle^{\frac{1}{2}}}{da} = 0$, when $a=a_i$. Hence the growth rate is given by

$$\langle\delta_s^2\rangle^{\frac{1}{2}} = \delta_i \frac{2}{5}\left[\frac{3}{2}\left(\frac{a}{a_i}\right) + \left(\frac{a}{a_i}\right)^{-3/2}\right] \qquad (2.17)$$

Hence, the decaying mode will rapidly become negligible compared to the growing mode. The dashed line in Fig. 2.2a represents $\langle\delta_s^2\rangle^{\frac{1}{2}} \propto a(t)$ and the agreement is fairly satisfactory until the later stages when non-linear effects reduce the growth rate.

In Fig. 2.2b the dots show $\langle\chi^2\rangle^{\frac{1}{2}}$ as measured from the particles within the spheres. The crosses show the evaluation of equ. (2. 8) using $\langle\delta_s^2\rangle^{\frac{1}{2}}$ from Fig. 2.2a and I have taken $I^{\frac{1}{2}}J^{-1} = 1{\cdot}0$*.

---

* Peebles finds that the integral I converges only in the range $-1 < n < 0$. However, in calculating the integrals, proper allowance must be made of the change in the slope of the power spectrum due to non-linear effects for $k > k_m$. In this case, for $n < 0$ the dominant contribution to I comes from wavenumbers $k < 1/x_o$. If $n > 0$ we should include the contribution for $1/x_o \lesssim k \lesssim k_m$. The numerical calculations begin with Poisson initial conditions and so $n=0$, but I would expect the contribution to I between $1/x_o \lesssim k \lesssim k_m$ to be small, therefore, I have set $I^{\frac{1}{2}}J^{-1}=1{\cdot}0$. For subrandom distributions with $n > 1$, $\langle\delta_s^2\rangle$ no longer measures the density perturbations on scales x_o. This is because of leakage of high wavenumbers through the sidelobes of the Fourier transform of the square window function used to define $\langle\delta_s^2\rangle$. In this case we can still use linear theory provided we define a window function that suppresses high wavenumbers (e.g. Peebles, 1974a).

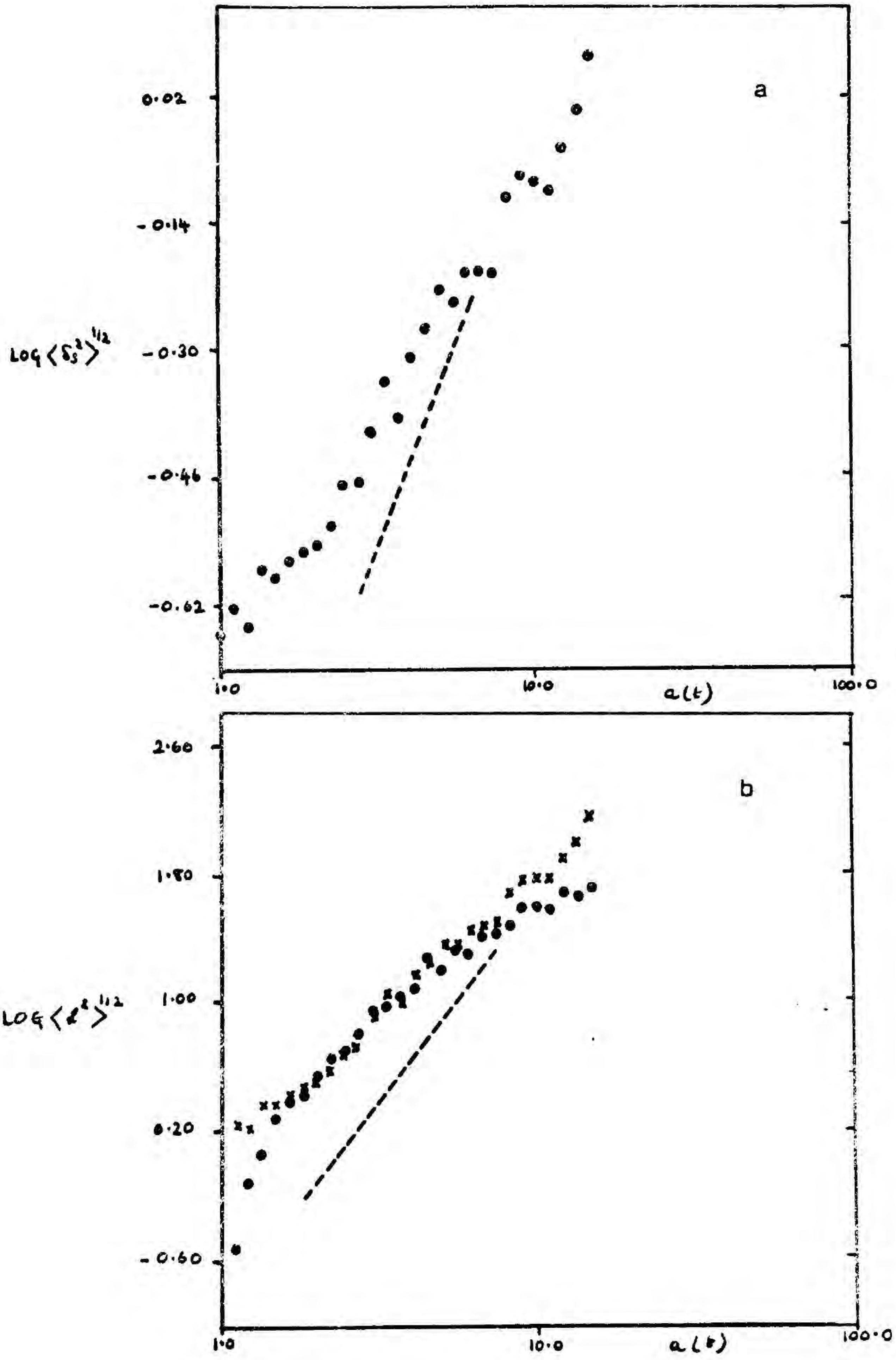

Figures 2.2 Comparison of Model A with the results of linear theory.

The dashed line shows the expected slope from linear theory $\langle \mathcal{L}^2 \rangle^{\frac{1}{2}} \propto t^{5/3} \propto a^{5/2}$. Deviations from the $t^{5/3}$ growth at later stages is due to non-linear effects, and deviation at early stages is due to having begun the model with random density fluctuations but no velocity perturbations so that the angular momentum about the centre of mass of each sphere is zero.

b) Cluster analysis

In an Einstein-de Sitter universe, a uniform spherical protogalaxy will detach itself from the rest of the universe when it reaches a density of $9\pi^2/16$ times the background density (Field, 1974). Individual proto-clusters were detected by using this overdensity criterion and the further restriction that they contained at least 10 particles. The detection algorithm works as follows.

Initially a small search sphere is centred on each particle of the simulation. The particles that lie within each search sphere are found and the density within each search sphere is determined. If $\rho < \alpha\bar{\rho}$ (where α is the density criterion being used, and $\bar{\rho}$ is the background density), the particle on which the sphere is centred is designated as a field member. If $\rho > \alpha\bar{\rho}$ the particle is designated as a cluster member. The cluster members are then sorted according to the membership of each one's search sphere and smaller overlapping clusters are deleted. This provides a list of candidate clusters. The search sphere is then centred on the centroid of each candidate cluster and the centroid is determined iteratively by by recentering the sphere on the newly determined centroid until convergence within a given tolerance is reached. This process is repeated until $\rho = \kappa\bar{\rho}$ for each search sphere. At this stage each search sphere represents a cluster and the members in each search sphere are taken as the cluster members.

In a few cases (for large clusters) the same cluster was listed twice but in subsequent analysis only distinct clusters were used. In no case was a particle assigned membership to more than one distinct cluster and all detected clusters were gravitationally bound.

The efficiency of the algorithm was checked by visual comparison with pictures like those of Fig. 2.1. The algorithm would not correctly detect very elongated systems: however, since such systems were not apparent in the pictures, this was not considered to be a problem.

c) Angular momentum

Fig. 2.3 shows the build up of angular momentum $\mathcal{L}$ with time for several clusters. The arrow indicates the the time at which they were detected. The dashed line in this figure shows the linear growth rate $\mathcal{L} \propto t^{5/3}$.

It is apparent that most of the angular momentum is acquired during the early stages of the cluster's growth, as was predicted by Peebles (1969).

Fig. 2.4 shows the angular momentum to mass relationship for the models together with the expected relationship $\mathcal{L} \propto M^{5/3}$. This is, at present consistent with observation (Freeman, 1973), although Jones (1976)

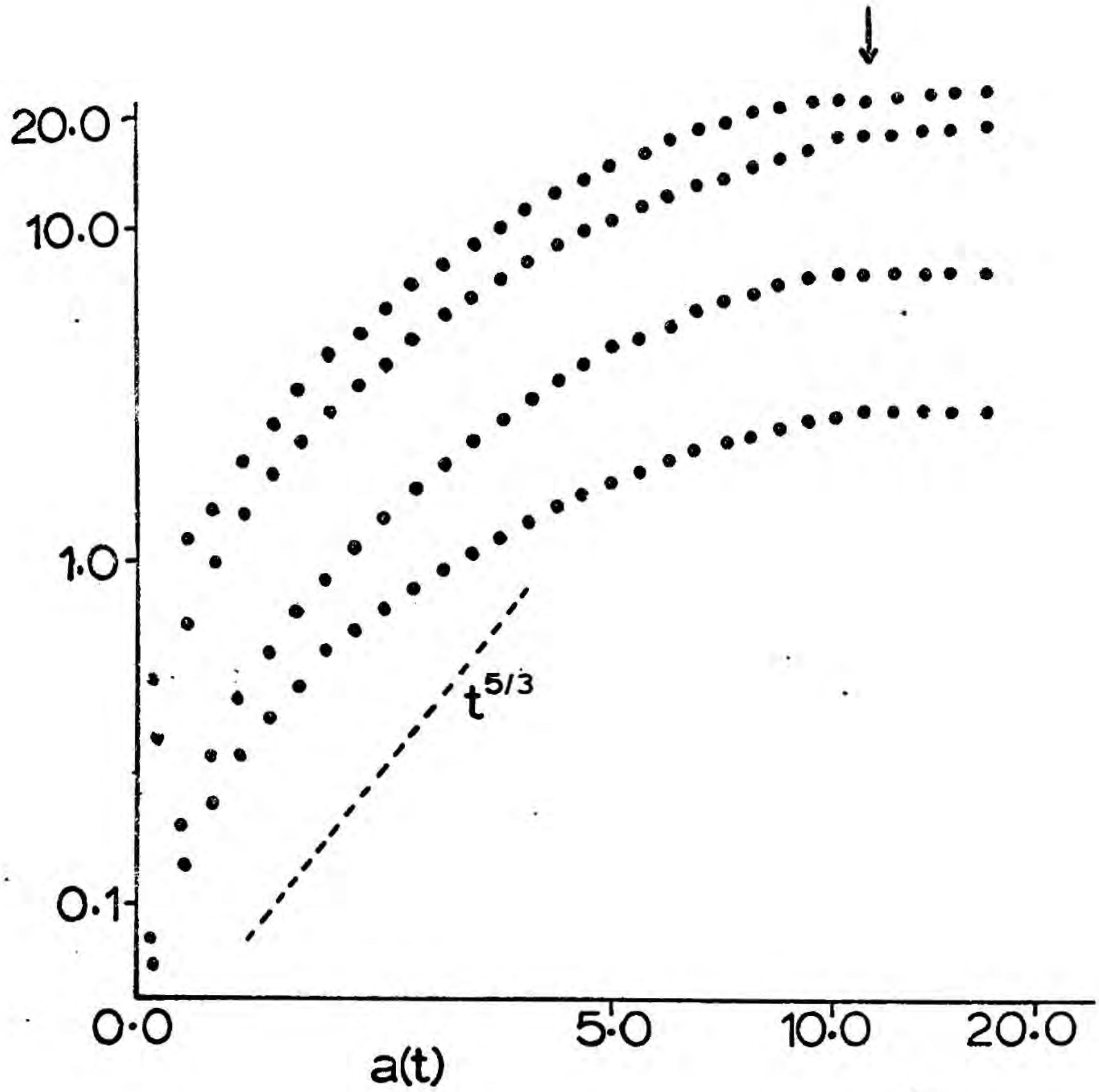

Figure 2.3. The growth of angular momentum for four clusters. The arrow indicates the times at which the relative overdensity reaches the value $9\pi^2/16$.

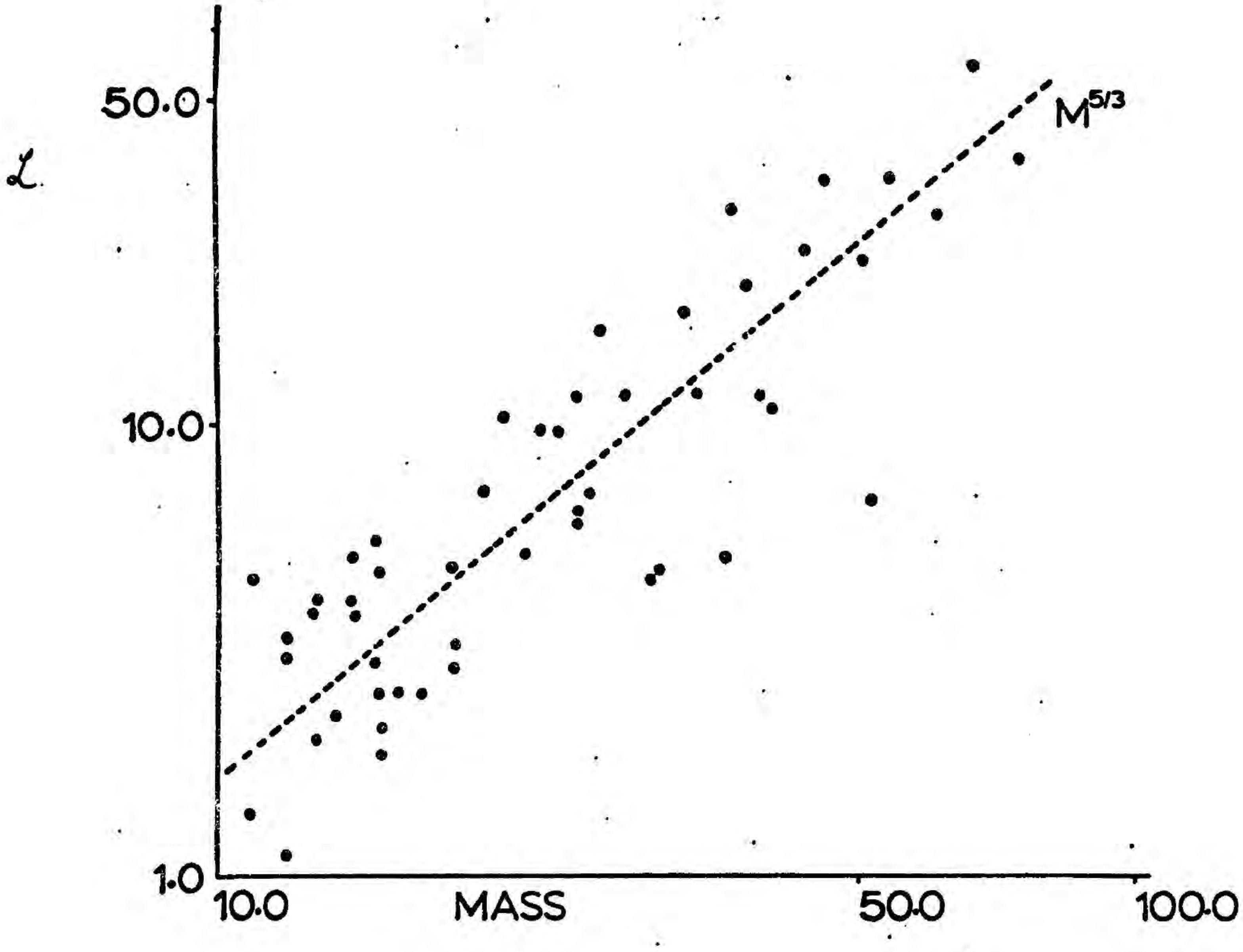

Figure 2.4. Mass versus angular momentum for the condensations. The dashed line shows the expected $\mathcal{L} \propto M^{5/3}$ relationship.

has emphasised that such relationships are to be viewed with caution as they may be an artifact of the selection criteria and the data analysis. It does, in principle, offer an observational test of the tidal torque theory.

The angular momentum of the model clusters can be compared with observed galaxies in terms of the dimensionless parameter

$$\lambda = \mathcal{L} E^{\frac{1}{2}} G^{-1} M^{-5/2} \tag{2.18}$$

introduced by Peebles (1971). Here E is the total energy of the system. Figs. 2.5(a,b) show λ versus M for clusters identified at a(t) = 11·9 and 17·5 respectively. Intuitively,one might expect a systematically lower value of λ for high mass systems than for low mass systems. However, this effect is not statistically significant in Fig 2·5(a,b). We also find that λ is relatively insensitive to the epoch of cluster detection and to the overdensity criterion used.

An alternative measure is the ratio of the kinetic energy of rotation to the potential energy evaluated at the epoch of turnaround

$$t_i = \frac{T_{rot}}{|W|} \tag{2.19}$$

This quantity has been used by Gott and Thuan (1976) and Thuan and Gott (1975,1977) in relation to their Maclaurin

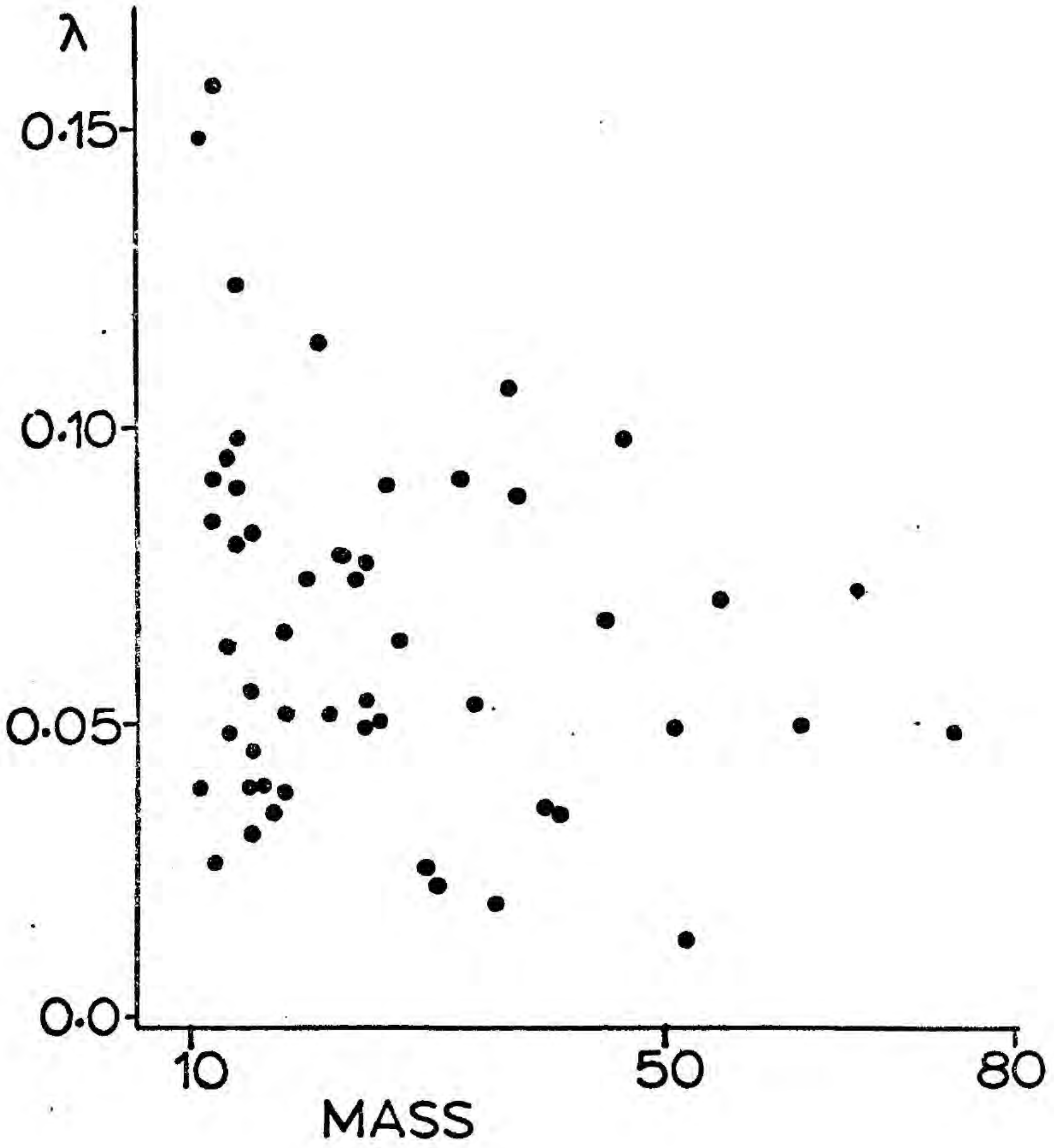

Figure 2.5 a. λ versus M for clusters at a(t)=11·9.

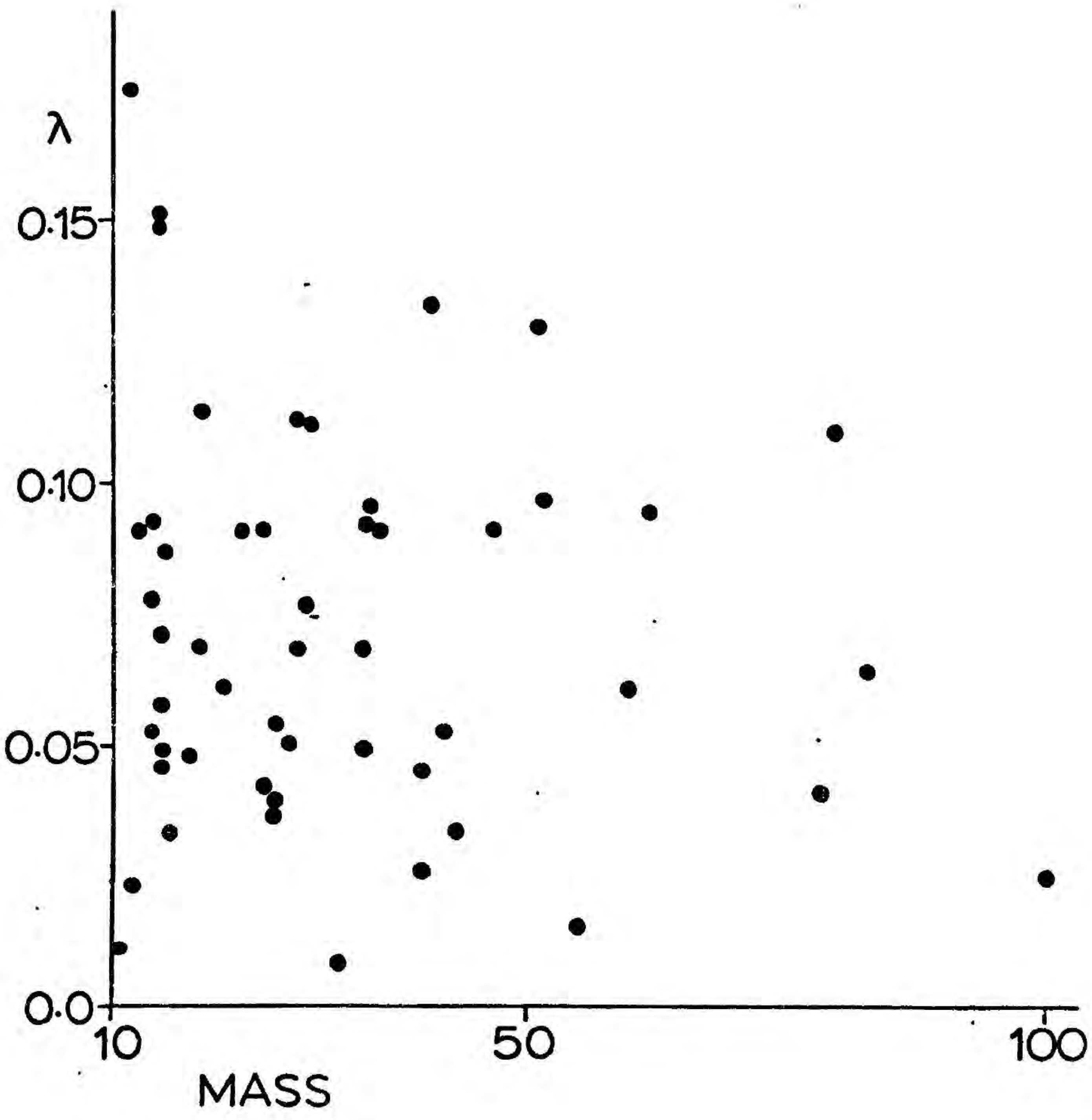

Figure 2.5 b. λ versus M for clusters at a(t)=17•5.

spheroid models of spiral and elliptical galaxies. For a homogeneous spherical cloud, λ is related to t_i by

$$t_i(1-t_i) = \frac{125}{36}\lambda^2 \tag{2.20}$$

Thus λ may be converted to t_i. The quantity $t = T_{rot}/|W|$ may be measured for each cluster at the epoch of detection, but since the systems are centrally condensed t will not, in general be equal to t_i, although it is interesting to make the comparison.

The quantity $t_k = T_{rot}/T_{tot}$ is also measured, T_{tot} being the total kinetic energy of the cluster when it is virialised. The clusters are subject to a density criterion of $\rho/\bar{\rho} = 100$ and this results in a smaller sample.

Figs. 2.6(a,b) show histograms of λ and t_i for 51 clusters, and Fig. 2.6(c) shows t_k for 31 clusters. Marked on the histograms are the median values for the distributions together with the median values calculated by Thuan and Gott (1977). Note that in each case, Thuan and Gott's estimates are excessive. The model results are summarised in Table 2.1.

d) Boundary effects

An obvious source of error in the above calculations is due to considering a small sample of clusters. The clusters close to the boundary lack neighbours with which they can interact and this may lead to an underestimate of λ. In principle this could be checked by running larger simulations but in practice this requires

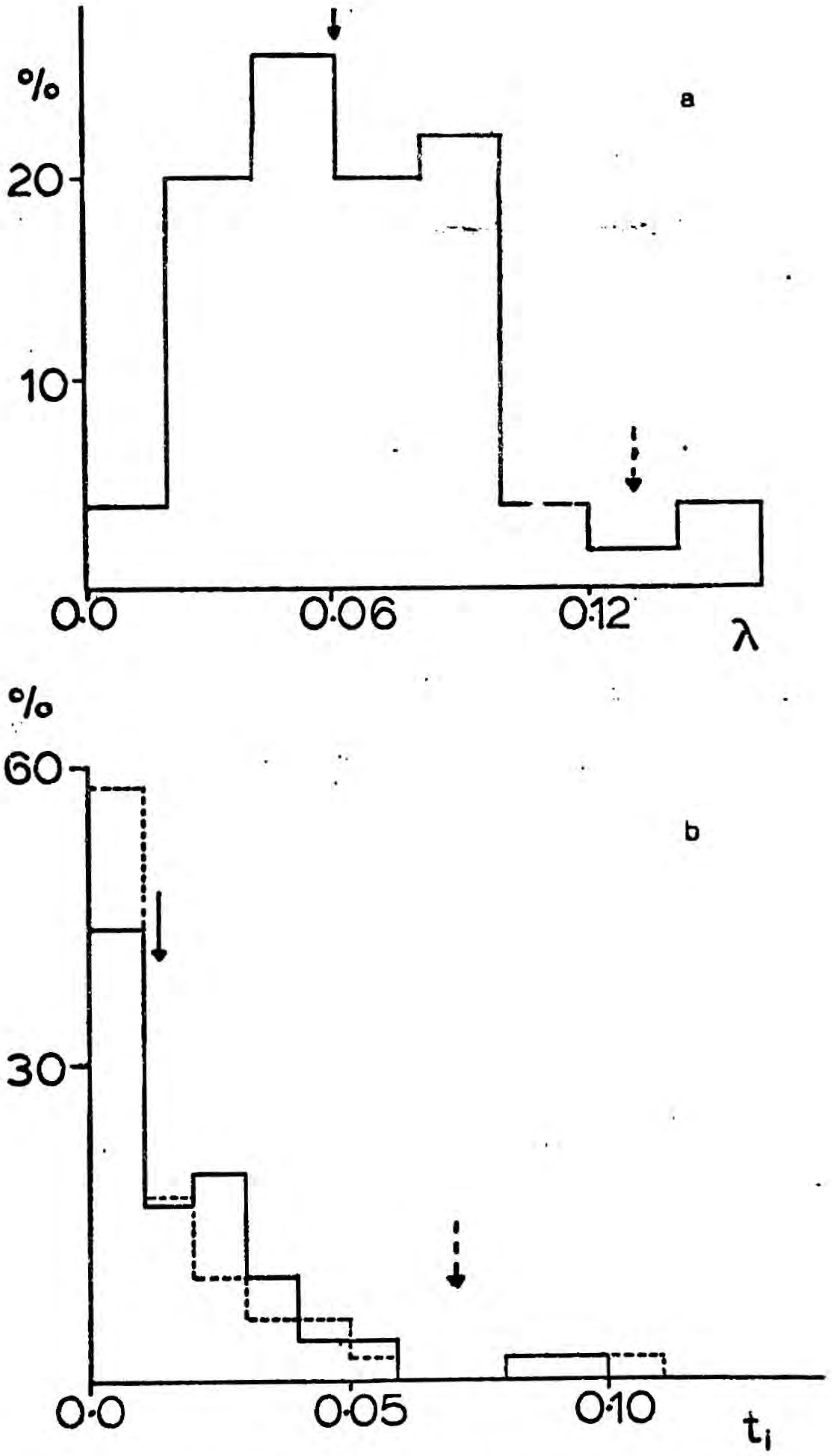

Figure 2.6. (a) Histogram of λ values constructed from Fig. 2.5a. (b) Histogram of t_i values, the heavy lines show the distribution obtained by converting λ to t_i according to equ. (2.20). The dashed lines

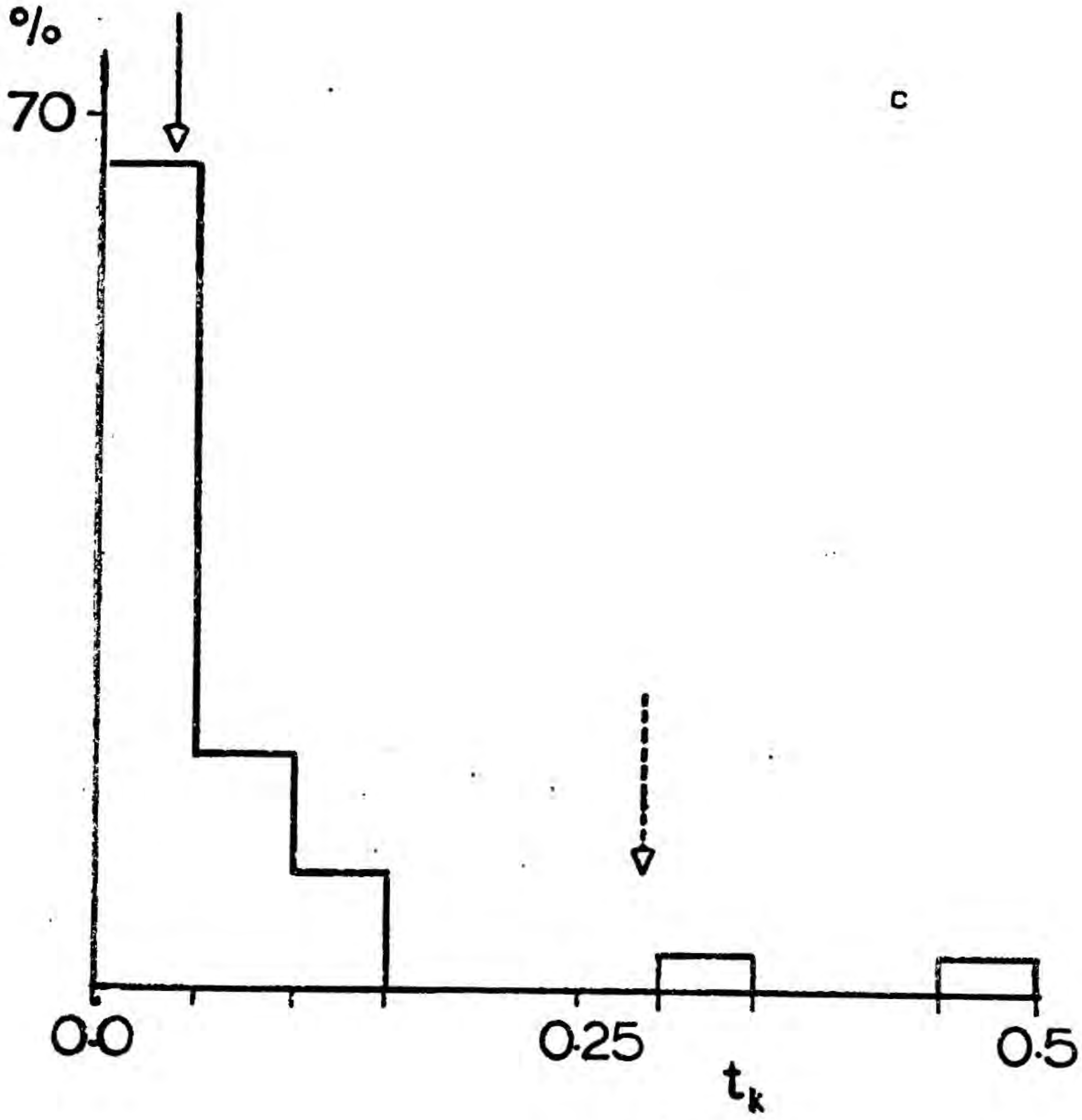

Figure 2.5 continued. (c) Histogram of t_k values at a(t)=17·75. In each case the heavy arrows point to the medians of the distributions, the dashed arrows are the medians of Thuan and Gott (1977).

Table 2.1. Results from the numerical simulations.

	Median	Mean
λ	0·06	0·07 ± 0·03
t_i	0·01	
t_k	0·04	

a large amount of computing time since direct summation N-body programs have an operation count of N^2. I have thus applied two checks.

i. Clearly, if there exists a correlation between λ and the distance of a cluster from the centre of the sphere, the calculations would be suspect. The clusters were divided into two roughly equal samples. Sample (1) contained clusters within a radius of 0·85R from the centre of the sphere, and Sample (2) contained the remainder. The mean values of λ were calculated for each sample, with the results that for Sample (1) $\bar{\lambda} = 0{\cdot}064$ and for sample (2) $\bar{\lambda} = 0{\cdot}069$.

I therefore conclude that there does not appear to be a significant correlation between λ and the distance of a cluster to the boundary.

ii. Monte Carlo calculations, of the type described by Thuan and Gott were performed. Fifteen particles of equal mass were distributed in a sphere of radius $4{\cdot}4R_o$ according to the distribution

$$P(r) = 0 \qquad r < R_o$$

$$P(r) = \frac{1}{\frac{4}{3}\pi R_o^3}\left(\frac{16}{9\pi^2}\right) \qquad r > R_o \tag{2.21}$$

where $P(r)d^3\underline{r}$ is the probability of finding a neighbouring galaxy in the volume element $d^3\underline{r}$. A further 523 particles were distributed with respect to the inner 15 particles, in a shell defined by $4{\cdot}4R_0 < r < 14{\cdot}4R_0$, so that each particle in the inner sphere experiences tidal effects from at least $10R_0$. The particles in the inner shell were treated as randomly orientated oblate spheroids of semi-major axis R_0, and semi-minor axis $\frac{1}{2}R_0$, and the torque on each particle was calculated by summing over the whole sample and also by summing over just the galaxies within $4{\cdot}4R_0$. This was repeated 50 times, resulting in the histograms displayed in Fig. 2.7.

The differences between the two distributions are easy to understand, since the greatest error in the estimate of a torque will occur for an intrinsically low angular momentum system lacking a close neighbour.

Scaling the histograms of Fig. 2.7 with that of Fig. 2.6(a) is somewhat arbitrary owing to the difference between the shapes of the distributions. However, taking the mean value of λ for the inner distribution to be $\bar{\lambda} = 0{\cdot}07$, the 'true' mean value would be $\bar{\lambda} \simeq 0{\cdot}08$. Similarly, taking the median value of the inner distribution as $\lambda_m = 0{\cdot}06$ yields a 'true' median value of $\lambda_m \simeq 0{\cdot}08$.

If these calculations are realistic, then it would appear that boundary effects are not serious.

2.6 Comparison with Observation and Discussion.

a) Spiral systems

In the absence of dissipation and as long as the Universe follows an $\Omega = 1$ expansion, equ. (2.18) together with the results of Table 2.1, may be directly applied to cosmological systems.

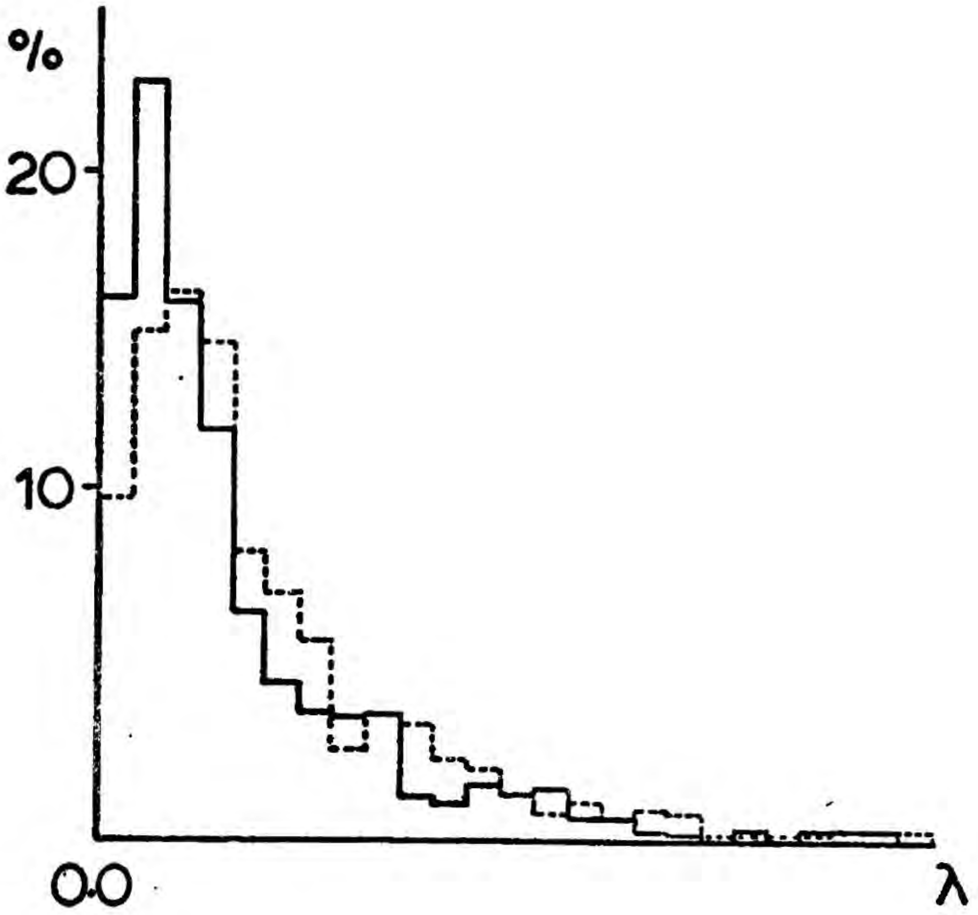

Figure 2.7. Monte Carlo simulations. The heavy lines show the distributions of torques obtained from considering galaxies within $4 \cdot 4R_o$. The dashed line shows the distribution of torques obtained from considering galaxies within $14 \cdot 4R_o$. For scaling of the abscissa, see text.

It is quite clear that dissipation has played a major role in the formation of the discs of spiral galaxies. In applying equ. (2.18), an estimate of the collapse factor of a typical spiral galaxy is required.

Innanen (1966) has deduced a value for the angular momentum of our Galaxy. He finds that

$$\mathcal{L}_I \approx 1 \cdot 5 \times 10^{67} \text{ kg m}^2 \text{ s}^{-1} \tag{2.22}$$

The mass of the disc is taken to be 1.2×10^{11} M_o and it is assumed that at the epoch of maximum expansion the Galaxy was a uniform sphere of radius $R_{max} = \beta \times 10$ kpc. Using these values, an estimate of the λ parameter for the Galaxy is

$$\lambda_I = 0 \cdot 7 \beta^{-\frac{1}{2}} \tag{2.23}$$

If the Galaxy has collapsed from a maximum radius of 100 kpc as seems reasonable on observational grounds (Eggen, Lynden-Bell and Sandage, 1962), then

$$\lambda_I = 0 \cdot 22 \tag{2.24}$$

and this is approximately a factor of 4 greater than the median value listed in Table 2.1. In view of the crudeness of the comparison, this discrepancy may not be too serious.

However, the collapse factor may be estimated by using the Gott and Thuan (1976) Maclaurin spheroid model for the formation of spiral discs, in which case

$$\frac{R_{disc}}{R_{max}} = \frac{4}{\pi} t_i \tag{2.25}$$

(such a relationship, up to factors of order unity, must be true for any model by virtue of conservation of angular momentum). For the median value of t_i deduced from the simulations, equ(2.25) inmplies that

$$\frac{R_{max}}{R_{disc}} \gtrsim 65 \tag{2.26}$$

or for a typical disc system with R_{disc} = 10 kpc, the disc material collapsed from a distance $R \gtrsim 650$ kpc ! For a disc of mass $\sim 10^{11}$ M , equ. (2.26) implies a free-fall time of

$$t_{ff} = \pi \sqrt{\frac{R^3}{8GM}} \sim 2 \times 10^{10} \text{ yrs} \tag{2.27}$$

clearly this is impossible since the collapse time is longer than the age of the Universe.

These arguments would not apply if the discs of spiral galaxies did not collapse under their own gravity. Just such a hypothesis has been proposed recently by White and Rees (1978), in which disc systems form by gas falling into the potential wells of the unseen halo matter. This modifies the cooling arguments of Rees and Ostriker (1977) thereby leading to disc systems of $\approx 10^{11}$ M . In this theory, the value of λ for the halos (λ_H) would agree with the tidal torque estimate presented above, as long as the halo material clustered dissipationlessly. However, the gas that settles into the halo's potential well and eventually forms the disc of a spiral galaxy is not initially self-gravitating. In this case, a back of the envelope calculation suggests

$$\frac{R_{max}}{R_{disc}} \simeq \frac{9\pi}{125\lambda_H^2} F \tag{2.28}$$

if the equilibrium disc is self-gravitating, here F represents the ratio of the mass in the gaseous component to that of the halo component at the time of galaxy formation. To obtain $R_{max}/R_{disc} \sim 10$ with $\lambda_H \sim 0{\cdot}07$ requires $F \sim 1/7$, a result which fits nicely within the general framework of White and Rees' theory. A more detailed version of this argument may be made using Mestels' (1963) hypothesis (Efstathiou and Fall, in preparation).

A strong prediction of the tidal torque theory is that there should exist a correlation between the spin vectors of sufficiently isolated binary pairs of galaxies. A recent study by Sharp, Lin and White (1979) shows little evidence for such a correlation. This may not be surprising if 80% of the matter in the Universe were in an invisible clustered component, e.g. there is no reason to suppose that the spiral discs in a binary pair formed synchronously, an effect which would help destroy any correlation.

It is well known that the observed flat rotation curves in the outer regions of spiral galaxies indicate the presence of massive dark halos (e.g. Krumm and Salpeter, 1977). A strong conclusion from the work presented here is that the discs of spiral galaxies must have formed by the collapse of gas onto pre-formed heavy haloes.

b) Elliptical systems

Thuan and Gott (1975) have proposed that elliptical galaxies formed in a dissipationless fashion as purely stellar systems, the flattening of the relaxed objects being related to their angular momentum by the Maclaurin spheroid model.

Recent observations of the rotation of giant elliptical galaxies (Bertola and Capaccioli, 1975; Illingworth, 1977; Davies, 1978; Schechter and Gunn, 1979; see also chapter 6), have shown that ellipticals rotate much more slowly than would be expected if they were rotationally supported oblate spheroids. One possible interpretation of the data, that ellipticals are rapidly rotating prolata (Miller, 1978; see also Dzyuba and Yakubov, 1970), appears to be ruled out by the data of Schechter and Gunn (1979). The most likely explanation (Binney, 1978) is that ellipticals are slowly rotating and that their flattening is due to velocity anisotropy rather than due to rotation.

If ellipticals collapsed without dissipation, the results from the numerical simulations are inconsistent with the picture of ellipticals being rotationally supported.

To show this, consider elliptical galaxies in virial equilibrium as oblate spheroids with eccentricity e. In this case, using equs. (5) and (10) of Binney (1978), the ratio of rotational kinetic energy to the kinetic energy of random motions is

$$\frac{T_{rot}}{T_{ran}} = \frac{(3-2e^2)\sin^{-1}e - 3e\sqrt{1-e^2}}{\frac{3Q_3}{2}e^2\sin^{-1}e + 3(e\sqrt{(1-e^2)} - (1-e^2)\sin^{-1}e)} \tag{2.29}$$

where Q_3 is the anisotropy parameter defined as $Q_3 = -\dfrac{\breve{\pi}_{33}}{T_{11}+T_{22}}$ in Binney's notation and the system rotates about the 3-axis. Binney shows that equ. (2.29) is independent of the radial profile of the galaxy. For illustrative purposes I take the equilibrium galaxy to be a uniform spheroid, in which case T_{rot}/T_{ran} may be related to t_i for a uniform sphere at maximum expansion ,

$$4t_i(1-t_i) = \frac{125}{9}\lambda^2 = \frac{\sin^{-1}e}{e^4}\left[\frac{(3-2e^2)\sin^{-1}e - 3e(1-e^2)^{\frac{1}{2}}}{1+\frac{3Q_3}{2}}\right] \tag{2.30}$$

which is equivalent to **equ. (27) of Gott and Thuan** (1976) if $Q_3=0$. From (2.30) with $Q_3=0$, to produce an E3 galaxy requires $\begin{matrix}\lambda = 0\cdot166\\ t_i = 0\cdot061\end{matrix}$ well in excess of the values of Table 2.1. Binney (1978) shows that **Illingworth's** data may be adequately accounted for in terms of oblate spheroids with $Q_3 \sim 2$.

For an E3 galaxy with $Q_3 = 2$, equ. (2.30) yields $\lambda = 0{\cdot}064$, $t_i = 0{\cdot}014$

in good agreement with the values of Table 2.1.

The results from the N-body simulations show that rotation will be dynamically unimportant for most systems which suffered a dissipationless collapse. The main conclusions of this section may also be extended to clusters of galaxies where it also seems that rotation can be of little dynamical importance. White (1976) has previously concluded that the flattening of clusters of galaxies is probably due to their mode of formation rather than due to rotation.

c) Origin of the Hubble sequence

The following discussion deviates slightly from the main theme of this chapter; hence it has been kept brief. A fuller discussion of the rôle of angular momentum in the problem of the origin of the Hubble sequence has been given by Efstathiou and Jones (1979), of which this section is a précis.

The conclusions from the last two sections imply that the key process in determining whether a protogalactic cloud becomes an elliptical or spiral is dissipation.

On the White and Rees (1978) theory, however, it is difficult to see how elliptical galaxies could have formed dissipationlessly. As the halo material clusters, the luminous material would be disrupted. Dissipation, however, ensures that the luminous matter will have a much higher density contrast than the dark matter, thereby avoiding disruption, i.e. if the luminous parts of galaxies are to survive as distinct subunits within bound virialized clusters, they must have dissipated a substantial amount of their binding energy.

One possible solution to this problem, originally due to Toomre (1977), is that elliptical galaxies formed by the merging of spiral discs. In this case it is also important to assess the contribution to the angular momentum of the merged products due to orbital motion. Numerical simulations have been performed which include galaxy merging (Aarseth and Fall, 1979). These show that most mergers occur from bound nearly linear orbits and hence the angular momentum of the merged products is low ($\lambda \approx 0{\cdot}07$). The numerical simulations clearly show that merged galaxies occur preferentially in clusters and in about the right numbers to be interpreted as elliptical galaxies. Further, neglecting the orbital contribution to the angular momentum and assuming that the merging of N identical galaxies with randomly orientated spin vectors occurs at zero energy ($E_m = NE_i$), as is indicated by the numerical simulations of Aarseth and Fall, λ_i for a galaxy prior to merging is related to λ_m for the merger product by $\lambda_m = N^{-3/2} \lambda_i$. In this case, relatively few mergers ($\lesssim 3$) are required to give $\lambda_m = 0{\cdot}07$ taking $\lambda_i = 0{\cdot}43$, the value appropriate to self-gravitating Freeman discs (Fall, 1979 in preparation). This result agrees with the results of numerical simulations by Aarseth and Fall which include internal randomly orientated spin vectors for each galaxy.

It should be emphasized, however, that the failure of dissipationless galaxy formation on the White and Rees theory, due to the disruption problem, arises if clustering proceeds hierarchically, as would occur with a power law spectrum of fluctuations at the epoch of recombination (see chapters 4 and 5). There may be no problem if the fluctuation spectrum were not a power law, so that galaxies formed by a process more akin to accretion onto a pre-formed galactic nucleus, as in the "onion-skin" model of Binney and Silk (1978).

2.7 Conclusions.

The results of this chapter are consistent with the results of Peebles' previous work, the major change being in the interpretation. The main conclusions are,

A. Tidal torques can account for a substantial amount of cosmic angular momentum.

B. Disc systems must have dissipated a large fraction of their binding energy, and the gas destined to form a disc collapsed onto a pre-formed halo several times ($\gtrsim 7$) more massive than the disc material.

C. Rotation will be dynamically unimportant for most systems which suffered a dissipationless collapse.

D. Tidal torques are not efficient enough to interpret the flattening of ellipticals as due to rotation, if they collapsed dissipationlessly.

CHAPTER 3

THE APPARENT FLATTENING OF ELLIPTICAL GALAXIES: DEPENDENCE UPON ABSOLUTE MAGNITUDE

3.1 Introduction.

The possibility of a correlation between the degree of flattening of elliptical galaxies and their absolute magnitudes was studied by Fish (1964) who found little evidence for any effect.

Thuan and Gott (1977) have constructed theoretical models for the flattening of elliptical galaxies based on the rotation acquired from the tidal torque process. They predict a decrease in the flattening of elliptical galaxies for absolute magnitudes $M < M^*$ (where M^* is the characteristic magnitude of the galaxy luminosity function), because massive galaxies are harder to torque than less massive galaxies. This effect, they claim, is consistent with the observational data. As has been described in the previous chapter, their model relies on the following main hypotheses:

a. The tidal torque process is very efficient, with $\lambda_m \simeq 0{\cdot}13$.

b. Elliptical galaxies have suffered no dissipation.

c. The flattening of ellipticals is due to their rotation as described by the Maclaurin spheroid model.

d. Elliptical galaxies are oblate.

The weight of observational evidence is now very much against the hypothesis (c) and the results of Chapter 2 strongly suggest that the tidal torque mechanism is considerably less efficient than assumed by Thuan and Gott.

Nevertheless the problem is still of interest to cosmology. For example, if the flattening of elliptical galaxies were due to tidally induced shear motions generated during their early development as discussed by Binney and Silk (1979), there should be a bias towards prolate structures. The model also predicts a correlation between flattening and mass similar to that predicted by Thuan and Gott.

Here we re-examine the problem using a wider body of data than was available to either Fish or Thuan and Gott.

3.2 Data.

Thuan and Gott took ellipticities and redshifts for 82 elliptical galaxies from Nilson's (1973) catalogue, supplementing it with a further 55 from the Turner and Gott (1976) group catalogue. In the latter case where a redshift was not available, the galaxy was assigned the mean velocity of the group.

Dr. R.S. Ellis and myself have compiled a list of 335 elliptical galaxies taking data from the Second Reference Catalogue (de Vaucouleurs, de Vaucouleurs and Corwin, 1976), the Nilson catalogue and a list of redshifts and magnitudes kindly made available to us by Dr J. Huchra. The Second RC gives the ellipticity corrected to a standard isophote of B=25 mag sec^{-2}. In some cases, where a galaxy had a redshift and apparent magnitude but was not included in the Second RC we used the ellipticity given by Nilson. This was the case for 10 of the galaxies in our sample.

For this analysis, the data sample need not be complete to a limiting magnitude provided that there are no selection effects that effectively correlate ellipticity with absolute magnitude. To test for such effects we studied the sample and found no bias, for example, in the fraction of round galaxies or the error in measured ellipticity with apparent magnitude.

We have to analyze the shapes in projection, but this would affect bright and faint galaxies in the same way provided that the samples are sufficiently large in number.

Many of the ellipticities, apparent magnitudes and velocities are uncertain. We have, therefore, concentrated on the higher quality measurements excluding those designated as uncertain,peculiar, or distorted. Errors in the apparent magnitudes and velocities will not seriously affect the analysis because the galaxies are binned in intervals $\Delta M \gtrsim 1$ mag. From the observational dispersions provided in the Second RC we calculate that our absolute magnitudes will be photometrically accurate to $\Delta B_T \simeq 0{\cdot}25$ mag (somewhat larger in the cases where transfers between different magnitude systems are necessary).

In calculating M we corrected for galactic extinction using a cosecant law, excluding those galaxies with latitudes $|b| \leqslant 10^{\circ}$. We also corrected for the K term which is marginally important for the larger velocity galaxies. The main error for the low velocity galaxies arises from the assumption that each velocity is a quiescent Hubble velocity. Random velocity dispersions elongate clusters in redshift space and this will appear as a smearing in M that decreases with increasing distance.

243 galaxies survived the selection criteria. The distribution of ellipticities in this sample is typical of the distribution of ellipticities of all the ellipticals in Nilson's catalogue (Fig. 3.1) indicating that our selection criteria do not intreduce a bias in the sample.

The distribution of ellipticities with absolute magnitude of our sample is shown in Fig. 3.2. The value of $B_T^* = -21{\cdot}45$ mag was taken from Tinsley (1977) using $H_o = 50$ km $\sec^{-1}$ Mpc^{-1} .

3.3 Results.

Fig. 3.3 gives the observed histograms for the ellipticities normalised to 100 percent for three cuts in M, at $M < M^* - 0{\cdot}5$ mag, $M > M^* + 0{\cdot}5$ mag referred to as B (bright side) and F (faint side) respectively and also for $M^* - 0{\cdot}5$ mag $\lesssim M \lesssim M^* + 0{\cdot}5$ mag. Also shown are the theoretical predictions taken from Thuan and Gott (1977) which allow for projection and for 10% measurement errors. Using the ellipticity dispersions supplied in the Second RC we find that the 10% errors are entirely justifiable for our sample.

On the basis of these histograms we have performed chi-squared tests between theory and data. We also looked

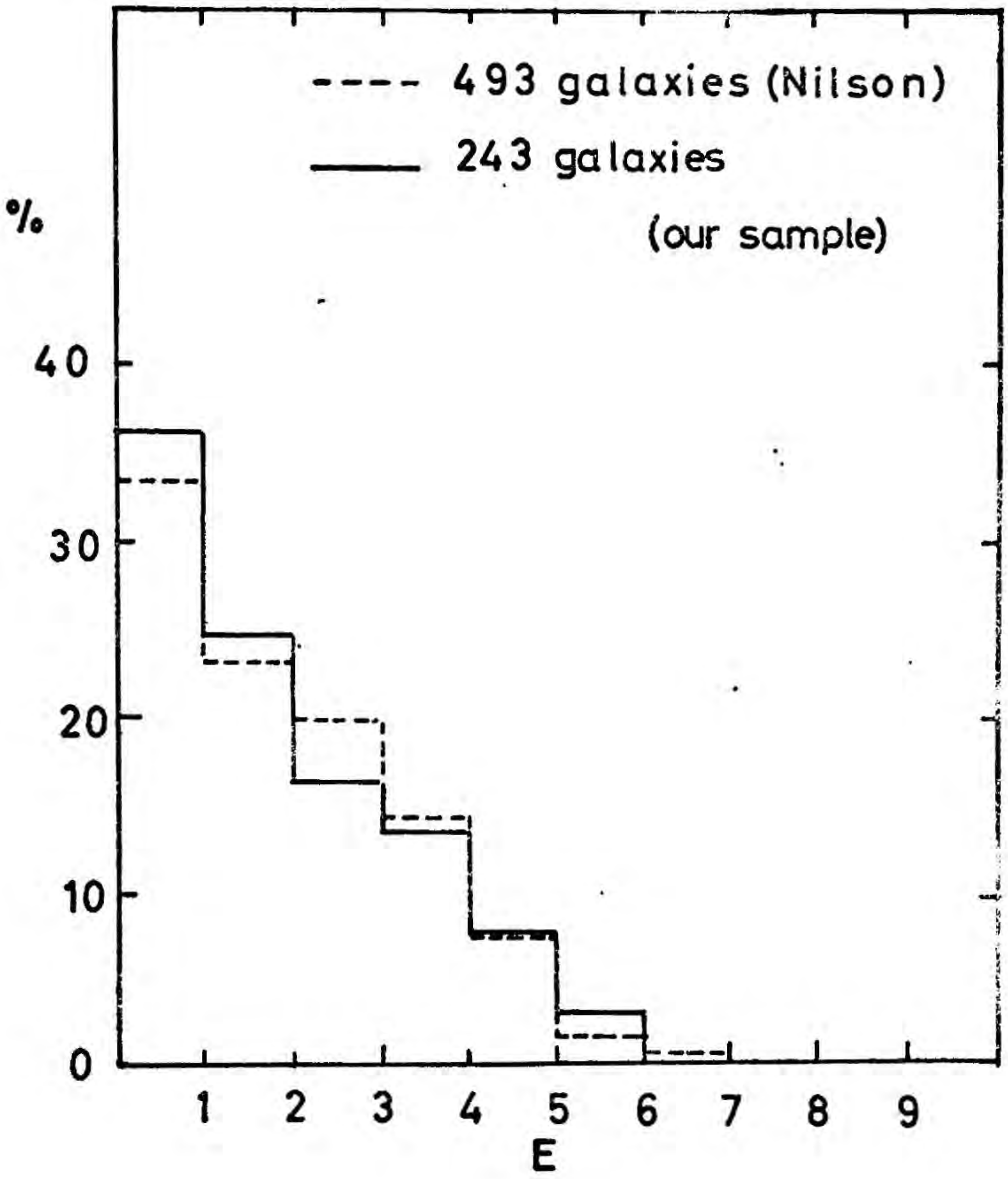

Figure 3.1. Comparison of the ellipticities of the galaxies in our sample with those in Nilson's catalogue.

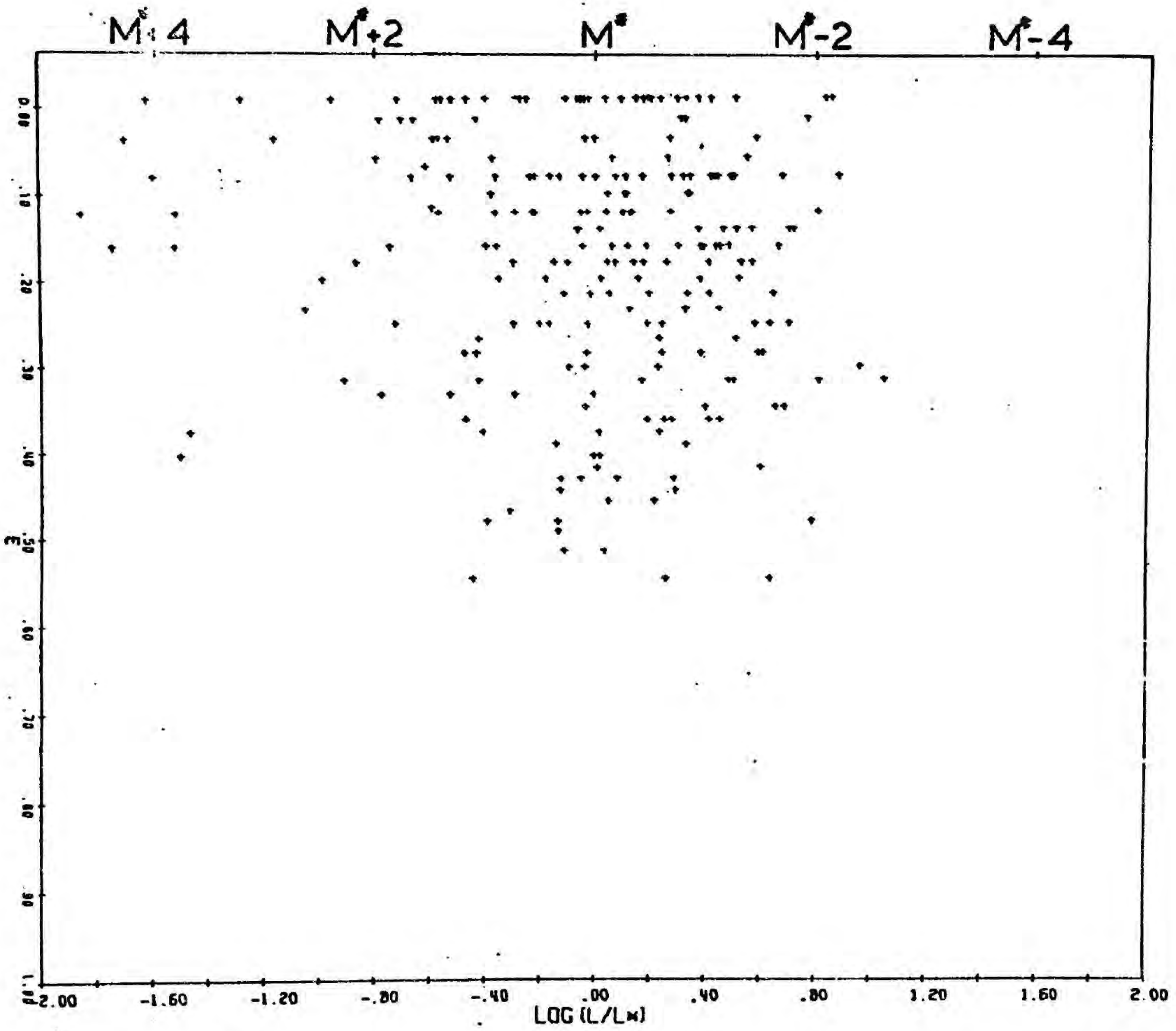

Figure 3.2. Ellipticities and absolute magnitudes for 243 E galaxies.

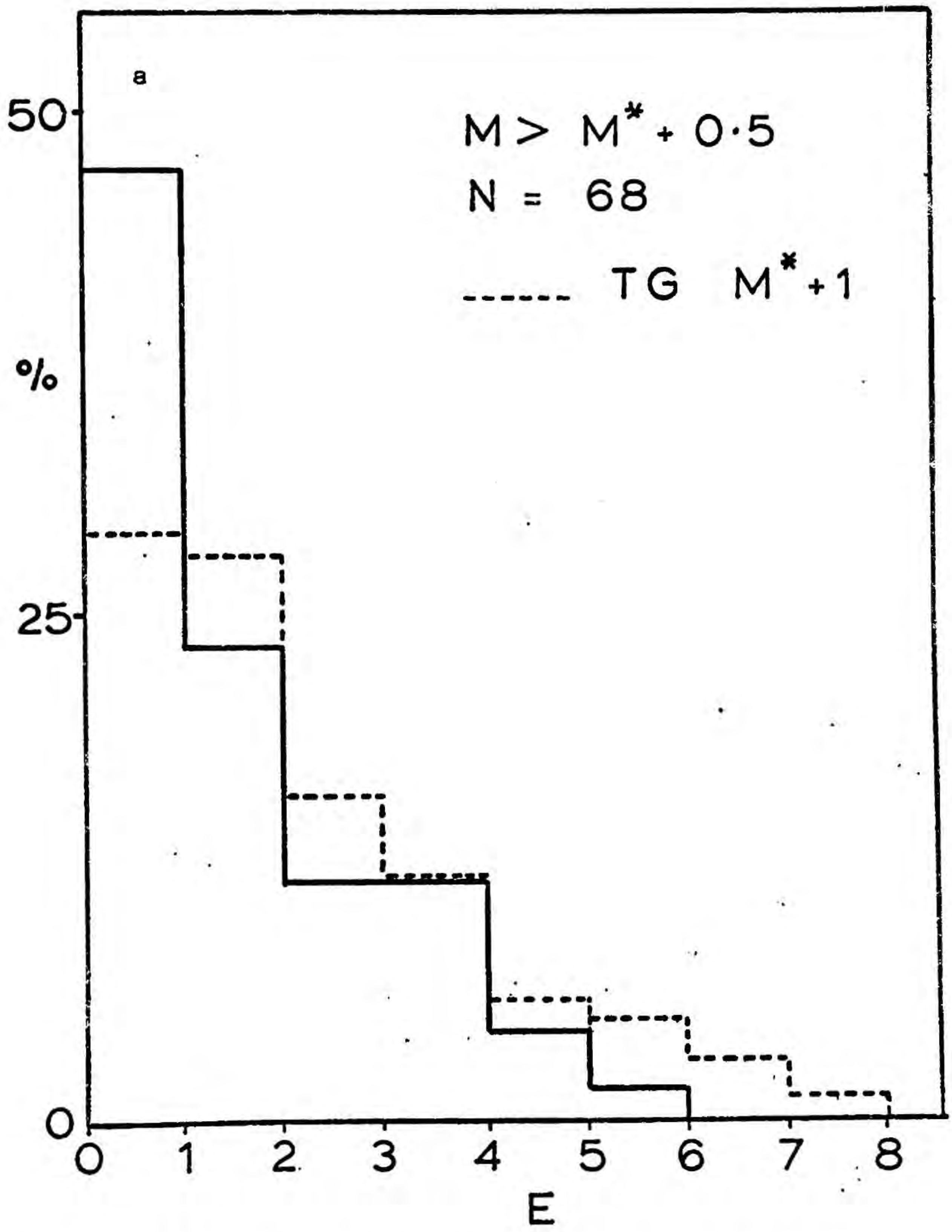

Figure 3.3. Frequency distributions of ellipticities for three intervals in absolute magnitude as marked. The numerical predictions of Thuan and Gott are also shown. N is the number of galaxies for the interval.

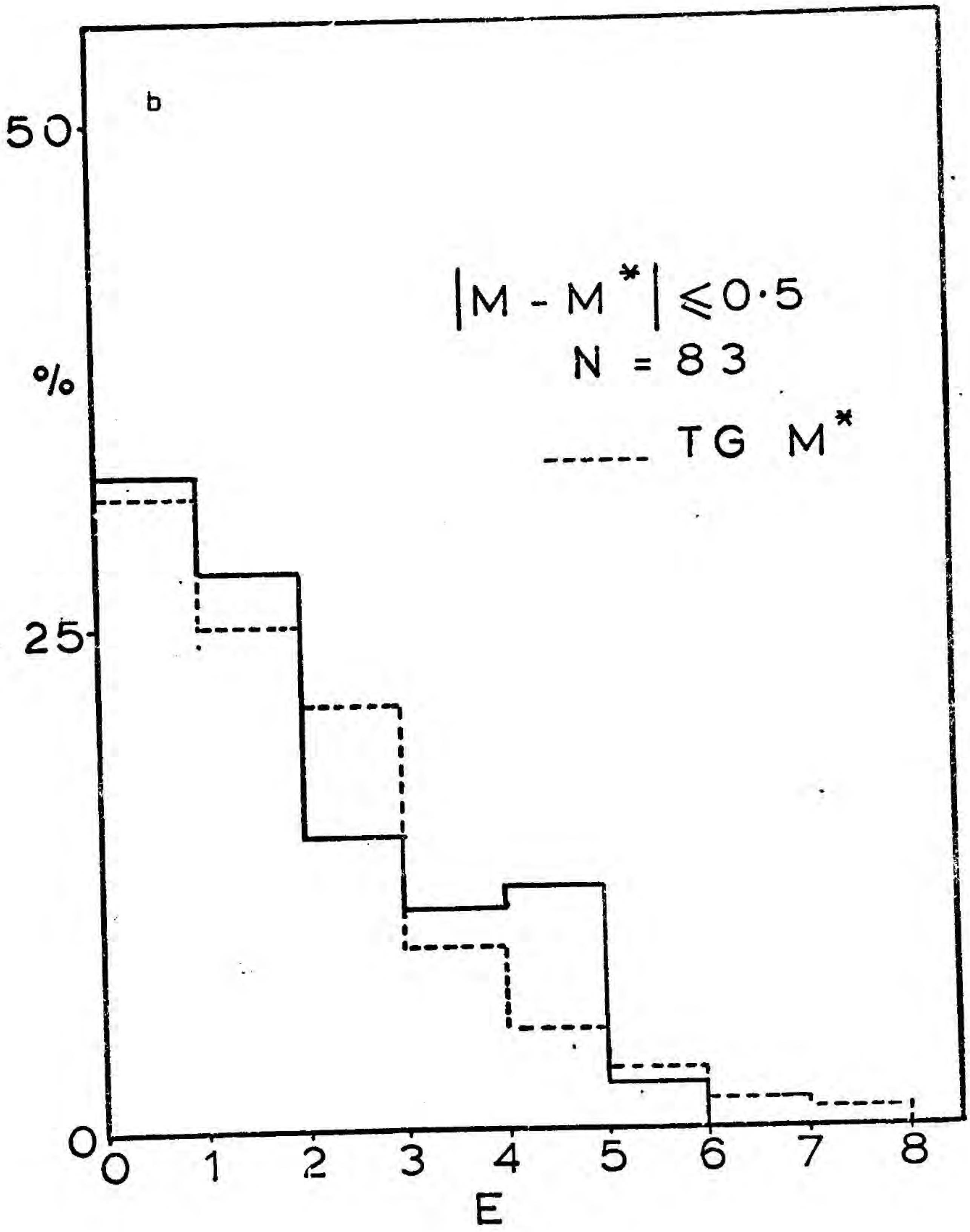

Figure 3.3 continued.

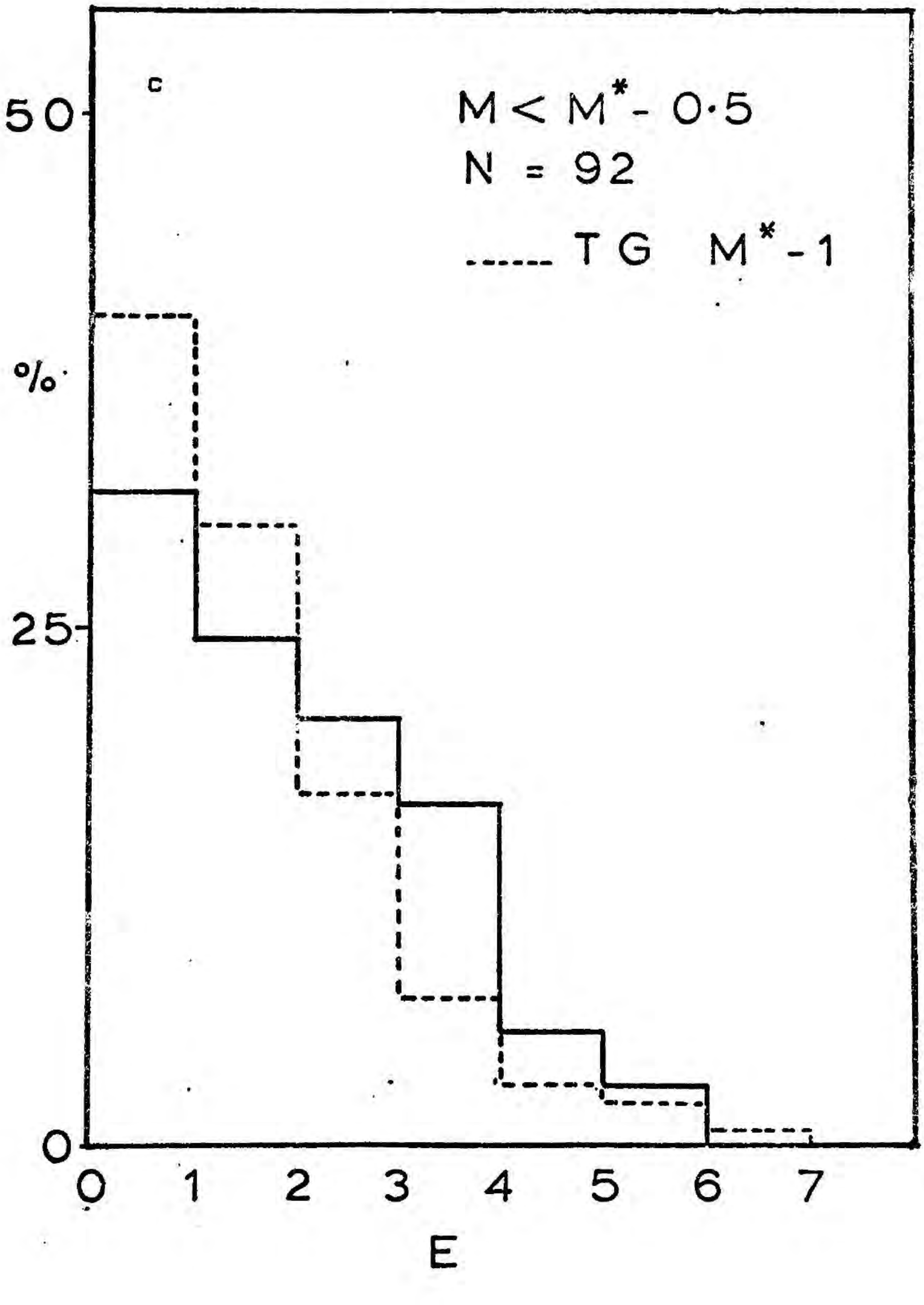

Figure 3.3 continued.

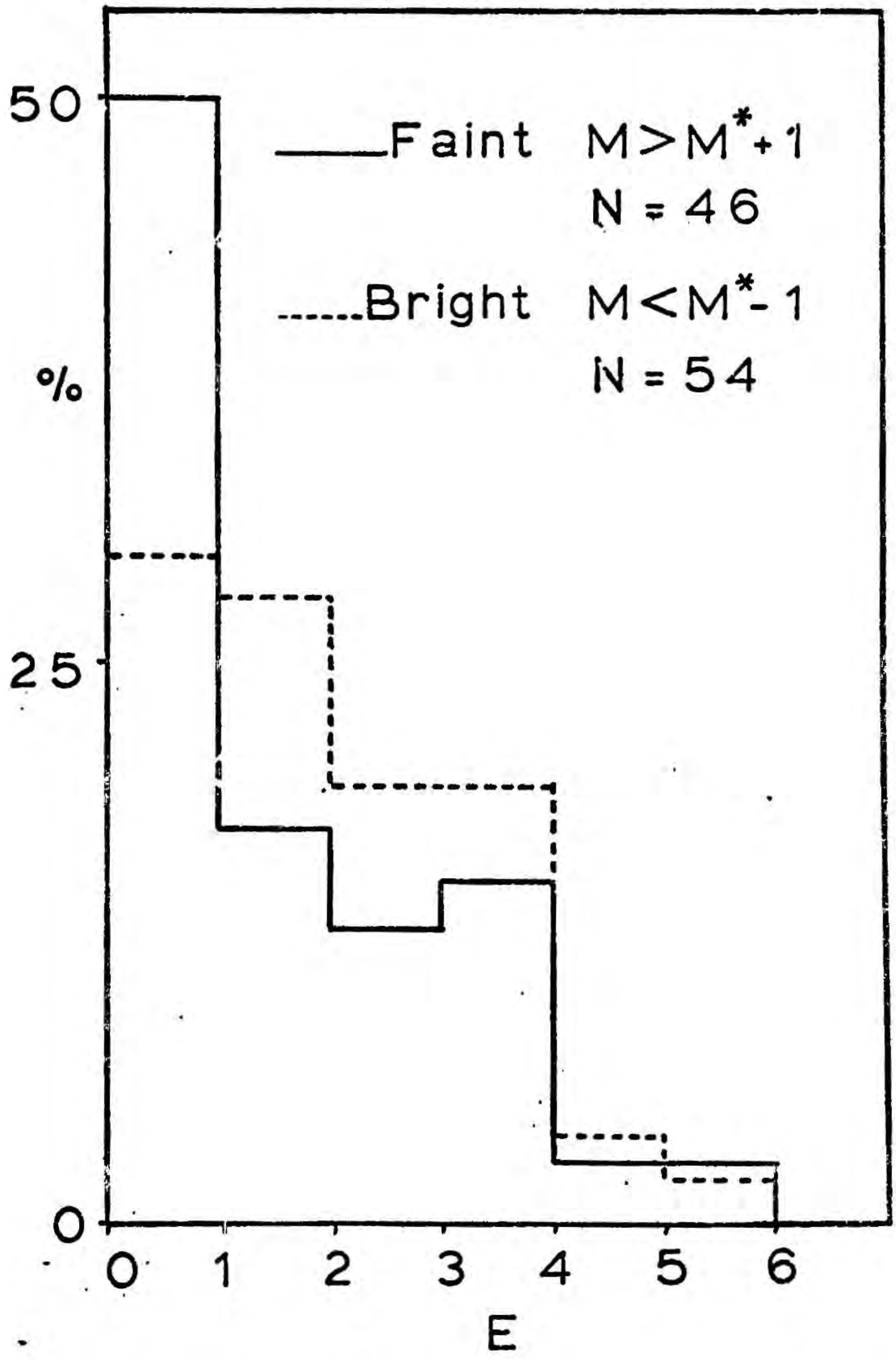

Figure 3.4. Frequency distributions of ellipticities for two intervals in absolute magnitude more widely separated than in Fig. 3.3.

Table 3.1. Statistical Results.

Test	$P(\chi^2)$	Number of Galaxies
B versus $TG(M^*-1)$ Fig. 3.3c	0·01	92
F versus $TG(M^*+1)$ Fig. 3.3a	0·02	68
$\lvert M-M^*\rvert > 0\cdot5$ mag versus $TG(M^*)$. Fig. 3.3b	0·43	83
F versus B Fig. 3.3a&c	0·12	68+92
F versus B Fig. 3.4	0·07	46+54

for correlation with absolute magnitude. Our results, summarized in Table 3.1 show that the agreement between the Thuan and Gott theory and the observations is poor.

Close examination of Fig. 3.3 reveals that if any trend between E and M is to be seen it is in the opposite sense to that claimed by Thuan and Gott, namely more round faint galaxies. A similar remark has been made by van den Bergh (1977). In fact the effect is qualitatively present in the data used by Thuan and Gott.

In an attempt to accentuate this effect we have also binned the data in intervals $|M - M^{*}| \leqslant 1{\cdot}0$ mag. The histograms are shown in Fig. 3.4. The effect appears to have increased and a chi-squared test between the two extreme bins reveals the difference to be significant at about the 7 percent level. We have checked the round galaxies responsible for this effect and find them to be typical of the whole sample.

3.4 Discussion.

The analysis clearly rules out the models of Thuan and Gott but as explained in section 3.1 there are other reasons that strongly suggest that the models are wrong.

We also find weak evidence for a correlation of absolute magnitude with ellipticity in the sense of ellipticity increasing with increasing M.

A possible explanation may be in terms of galactic cannibalism (Ostriker and Tremaine, 1975). Dynamical friction in aspherical clusters causes the more massive galaxies to have a more elongated distribution than the cluster as a whole (Binney, 1977). Cannibalism between these massive galaxies will lead to elongated bright galaxies which may be responsible for part of the effect in our sample.

A larger sample will be necessary to confirm this effect, but if true it may present problems for tidal explanations of the flattening of elliptical galaxies.

CHAPTER 4

THE LOW ORDER CORRELATION FUNCTIONS

4.1 Introduction.

Statistical analyses of galaxy clustering have been considered by various authors (Neyman, Scott and Shane, 1953; Limber, 1954; Rubin, 1954; Kiang, 1967; Totsuji and Kihara, 1969). However, the recent upsurge of interest in the study of galaxy clustering, has been mainly due to the empirical results obtained by P.J.E. Peebles and coworkers from their statistical analyses of catalogues of extragalctic objects. (Peebles, 1973b; Hauser and Peebles, 1973; Peebles and Hauser, 1974; Peebles, 1974b; Peebles and Groth, 1975; Groth and Peebles, 1977; Seldner and Peebles, 1977). Peebles et al have used the low-order spatial correlation functions as measures of galaxy clustering.

Recently, several other statistics have been applied to the clustering of galaxies (Gott and Turner, 1977; Bhavsar, 1978; Shanks, 1979). Discussion of these statistics is postponed until the next chapter.

The aim of this chapter is to investigate whether gravitational instability can explain the observed forms of the low-order galaxy correlation functions under simple initial conditions.

The problem has received considerable attention in recent years (see e.g. the comprehensive review by Fall, 1979, and references therein), but the extreme complexity of the problem has led to a variety of results by different authors.

In this chapter I study the problem using N-body simulations and compare the results with the numerical integration of the BBGKY hierarchy of kinetic equations performed by Davis and Peebles (1977) for the case $\Omega = 1$.

The highly clustered nature of the presently observed pattern of galaxy clustering prevents a simple truncation of the BBGKY hierarchy and so one must necessarily resort to simplifying approximations before even a numerical treatment is feasible. The N-body approach, on the other hand, is relatively assumption free. Given a set of initial conditions and an accurate computer code, the subsequent evolution of the system includes two-body and collective relaxation effects which are usually omitted in simple analytic treatments. However, for the problem of galaxy clustering, the N-body approach does have a serious flaw due to the discreteness of the fundamental point particles. This problem has been emphasised by Peebles (1977) and Fall (1978) and is also discussed in Section 4.3 below. For this reason I prefer not to identify the particles in the numerical simulations with galaxies, although I do discuss the cosmological implications of my results.

The BBGKY approach of Davis and Peebles assumes more reasonable initial conditions than do the numerical simulations. It is, however, difficult to judge the extent to which their results depend on the approximations that are made. It is important, therefore, to compare their results with other methods of attack, and also to study the problem in the cases $\Omega < 1$.

In the next section I describe the empirical results obtained by Peebles and coworkers. The remaining sections discuss my assumptions, method of attacking the problem and results.

4.2 Empirical Results.

a) Definitions

The two-point correlation function $\xi(r)$ is defined such that

$$\delta P = n^2 \left(1 + \xi(r) \right) \delta V_1 \, \delta V_2 \qquad (4.1)$$

is the joint probability of finding galaxies in the volume elements δV_1, δV_2 separated by distance r and n is the mean space density of galaxies. Hence $\xi(r)$ measures deviations of the pattern of galaxy clustering from a Poisson distribution. The data available to Peebles and coworkers has consisted of the galaxy coordinates in projection. Hence, in order to estimate the form of $\xi(r)$, they have measured the angular two-point function $w(\theta)$. $w(\theta)$ is defined in an exactly analogous way to $\xi(r)$ and is related to ξ via an integral equation first derived by Limber (1953). Higher order correlation functions may also be defined, e.g. the three-point function ζ :

$$\delta P = n^3 \left[1 + \xi(r_{12}) + \xi(r_{23}) + \xi(r_{13}) + \zeta(r_{12}, r_{23}, r_{31}) \right] \delta V_1 \, \delta V_2 \, \delta V_3 \qquad (4.2)$$

where δP is the joint probability of finding galaxies in each of the three elemental volumes δV_1, δV_2, δV_3 with separations r_{12}, r_{23}, r_{13}. Similarly, the four-point and higher order correlation functions may be defined.

In practice it proves difficult to estimate correlation functions of higher order than the four-point function because of the computational effort involved.

Recently, attempts have been made to estimate the spatial two-point correlation function $\xi(r)$ using redshift as a distance indicator (Davis, Geller and Huchra, 1978; Kirshner, Oemler and Schechter, 1979). However, the samples considered are so small that they cannot properly be regarded as fair samples. In addition, peculiar velocities alter the shape of the correlation function (as measured in redshift space) at small separations. At large separations peculiar velocities will have a negligible effect and ξ measured in redshift space should prove to be a valuable method of studying the large scale distribution of galaxies.

b) Main observational results

The basic result of Peebles and coworkers (e.g. Peebles, 1974b) is that the spatial two-point correlation function has an approximately power law form over a wide range of scales

$$\xi(r) = \left(\frac{r_o}{r}\right)^{\gamma} \quad (0 \cdot 1 h^{-1} \text{ Mpc} \lesssim r \lesssim 9 h^{-1} \text{ Mpc}) \tag{4.3}$$

$$\gamma = 1 \cdot 77 \pm 0 \cdot 06 \qquad r_o = 5 \cdot 3 \times (1 \cdot 5)^{\pm 1} h^{-1} \text{ Mpc}$$

In a revised analysis of the Lick catalogue, Groth and Peebles (1977) report the existence of a sharp break in the two-point correlation function at a value of approximately

$$\xi_{break} \sim 0\cdot3 \qquad r_{break} \sim 9h^{-1}\ \mathrm{Mpc}$$

This result is rather tentative as the feature does not appear as pronounced in the unsmoothed counts. Groth and Peebles present several arguments to support the idea that the feature is an intrinsic property of the galaxy distribution. There are three obvious ways to check this observation:

A. Measure the two-point angular correlation function of a large sample of galaxies, over large angular scales in the southern sky ($m < 18$).

B. Measure the two-point angular correlation function for a very deep ($m > 19$) sample of galaxies.

C. Measure the two-point spatial correlation function using a large sample of galaxy redshifts (either magnitude but preferably volume limited).

Method A attempts to sample large distances by measuring correlations on a large angular scale and is, therefore, likely to be affected by galactic obscuration and plate to plate variations.

Method B attempts to sample large distances by using a very deep sample. In this case, projection effects will be severe and $w(\theta)$ will be small. This method has been applied by the Durham group (Shanks et al, 1979 in preparation). Shanks et al find evidence for a feature, in rough agreement with the results of Groth and Peebles, although even in this case galactic obscuration proves to be a problem in that on some plates, the feature appears only after large scale trends in the density gradient are removed. A detailed account of this work may be found in Tom Shanks' Ph.D. thesis (1979, in preparation).

Method C appears to be the most promising. It has been applied to a small (166) magnitude limited sample by Kirshner, Oemler and Schechter (1979). Their results appear to be inconsistent with those of Groth and Peebles. The main criticism of this work is the smallness of the sample and also the severity of the edge corrections necessary in estimating ξ . However, Marc Davis and his collaborators at Harvard are currently undertaking an ambitious redshift survey (all galaxies in the Zwicky catalogue with $m < 14{\cdot}5$, $b^{II} > 40$, $\delta > 0$) and so there is a good chance that a solution to this problem is within sight.

In addition to these results concerning the two-point correlation function, Peebles and Groth (1975), and Groth and Peebles (1977) have discovered that the three-point galaxy correlation function has the following simple analytic form

$$\zeta(r_{12},r_{23},r_{31}) = Q\Big[\xi(r_{12})\,\xi(r_{23}) + \xi(r_{23})\,\xi(r_{31}) + \xi(r_{31})\,\xi(r_{12})\Big] \qquad (4.4)$$

$$Q = 1{\cdot}3 \pm 0{\cdot}2$$

Equ. (4.4) is found to be in good agreement with the data over the range of scales $0{\cdot}1h^{-1}$ Mpc $\lesssim r \lesssim$ $2h^{-1}$ Mpc, i.e. over length scales such that $\xi > 1$.

Fry and Peebles (1978) have recently estimated the four-point correlation function for the 10' x 10' Lick counts and find that it is consistent with the form

$$\eta_{1234} = R_A\Big[\xi_{12}\,\xi_{23}\,\xi_{34} + \text{SYM.(12 terms)}\Big] + R_B\Big[\xi_{12}\,\xi_{13}\,\xi_{14} + \text{SYM.(4 terms)}\Big] \qquad (4.5)$$

with $R_A = 2{\cdot}5 \pm 0{\cdot}6$ and $R_B = 4{\cdot}3 \pm 1{\cdot}2$

These simple relationships between the higher order functions and the two-point function have been interpreted by Peebles (1974b, 1974c, 1979) as implying a hierarchical pattern of galaxy clustering. Indeed, Soneira and Peebles (1978) have succeeded in producing a plausible map of the galaxy distribution, using a simple hierarchical model based on equs. (4.3)-(4.5).

In addition to these main results, several other results have been obtained by Peebles and coworkers, such as cross-correlations between galaxies and other extragalactic objects. These are not of direct relevance here.

4.3 Assumptions and the Aim of the Computations.

a) Assumptions

The main assumptions are listed below:

A. The Universe is described by standard Friedmann world models ($\Lambda = 0$, pressure = 0).

B. Particles interact only by gravity according to Newton's laws.

C. All particles have equal mass.

D. At the start of a calculation all particles have zero peculiar velocities.

E. At the start of a calculation particles are weakly clustered. In terms of the two- and three- point correlation functions we have $\zeta \ll \xi$.

As a starting point for a discussion of galaxy clustering, assumptions A-D are quite reasonable. Some of the consequences of relaxing the condition C will be discussed in section (4.5). Assumption E is less reasonable. Under the standard assumption of a power law spectrum of isothermal fluctuations at the epoch of recombination (equ. 1.6) there will be a scale length $x_m \sim k_m^{-1}$ at which $\langle|\delta\rho/\rho|^2\rangle_{k_m} \sim 1$, that is, the fluctuations on scales scales $\lesssim x_m$ will be non-linear. As noted by Davis and Peebles (1977, henceforth to be referred to as DP), it is not guaranteed that a weak-coupling epoch (as in assumption E) ever existed in the real Universe. It is more likely that at epochs prior to galaxy formation the clustering was always highly non-linear on small enough scales (i.e. $\rho \gg \xi \gg 1$).

In the power-law fluctuation picture, the amplitude of the fluctuations and the value of the spectrum index n are determined by pre-recombination physics, or perhaps they are initial conditions at the big bang. In the hierarchical clustering picture we must have $-3 \lesssim n \lesssim 4$. The lower limit is fixed by the requirement that galaxies form before clusters and the upper limit is fixed by the minimum growth rate of fluctuations in an expanding universe (Peebles, 1974a). The value n=-1 has been proposed by various authors (Zeldovich, 1970; Gott and Rees, 1975) but there is as yet no compelling reason to favour any particular value within this range. One of the aims of studying the correlation function is to see whether equ. (1.6) together with a value of n within this range can explain the observations.

In the case $\Omega = 1$, Peebles (1974b) has derived the scaling relation

$$\xi(r) \propto r^{-\gamma} \qquad \xi \gg 1 \qquad (4.6)$$

$$\gamma = \frac{3(n + 3)}{(n + 5)}$$

The observed slope of $\gamma = 1{\cdot}8$ thus implies n=0 if $\Omega = 1$.

b) Aim of the computations

In the approach of DP, the BBGKY hierarchy is truncted by using the empirical result that ζ is related to ξ by equ. (4.4). The velocity moment hierarchy is truncted by assuming that the relative velocity of particle pairs has zero skewness about the mean and together with some subsidiary approximations the equations are simplified to the extent that numerical solution becomes feasible.

DP find the asymptotic behaviour,

$$\xi \propto x^{-\gamma} \frac{1}{(1+z)^{3-\gamma}} \qquad \gamma = \frac{3(n+3)}{(n+5)} \qquad \xi \gg 1 \qquad (4.7a)$$

$$\xi \propto x^{-(3+n)} \; \Delta_g^2(z) \qquad \xi \ll 1 \qquad (4.7b)$$

where, $\Delta_g(z)$ is the growing mode solution of the linear density perturbation equation (see section 4.5c). These results are independent of the assumptions made in closing the hierarchy. Equ. (4.7b) can be derived from linear theory and equ. (4.7a) follows if (i) the equations admit a similarity transformation (i.e. $\Omega = 1$, discreteness effects negligible) and (ii) the stability condition is satisfied (i.e. the index γ does not change appreciably within a Hubble time). Using numerical simulations, Peebles (1978) has verified the stability assumption for the case $\gamma = 1{\cdot}8$ (and also for the case $\gamma = 1{\cdot}5$, Peebles, private communication).

The BBGKY computations yield values for the parameter Q in equ. (4.4) and the shape of ξ in the transition region $\xi \sim 1$, between the asymptotes defined by equs. (4.7). The results of these calculations yield a startling result, in that they suggest that the velocity dispersion within a protocluster grows while it is still a small density perturbation so that when the cluster fragments out of the general expansion it has enough internal kinetic energy to satisfy the virial theorem. Henceforth, this phenomenon will be referred to as "pre-virialization". If the shape of the correlation function is approximated by a two power law model, with slope given by equ. (4.7a) for $\xi > \xi_{\text{break}}$ and by equ. (4.7b) for $\xi < \xi_{\text{break}}$, DP find that $\xi_{\text{break}} \sim 0{\cdot}2$. Simple analytic treatments (e.g. Gott and Rees, 1975) based on the homogeneous spherical cluster model predict $\xi_{\text{break}} \gg 1$. The reason for this discrepancy is that in the spherical cluster model, a cluster reaches maximum expansion at a density contrast $\delta\rho/\rho = 9\pi^2/16 - 1$. It must then collapse by a factor of ~ 2 in order to generate enough kinetic energy to satisfy the virial theorem. The stability condition and equ. (4.7a) are then applicable only for $\xi \gtrsim 400$, hence $\xi_{\text{break}} \gg 1$.

As DP point out, it is difficult to know whether their computations correctly describe pre-virialization effects, or whether their approximations have artificially eliminated virialization effects. The aim of this chapter is to provide an independent method of attacking the problem and to decide which of the two pictures is more correct. It is also important to examine galaxy clustering in low density cosmological models.

N-body simulations have been used, in order to study galaxy clustering, by several authors (Press and Schechter, 1974; Miyoshi and Kihara, 1975; Groth and Peebles, 1976; Fall, 1978; Aarseth, Gott and Turner, 1978 and papers in preparation). Where possible I shall compare my results to those of the above mentioned authors.

c) The effects of discreteness

For a distribution of point particles with mean interparticle separation λ , the power spectrum may be related to the correlation function by the approximate relation

$$|\delta_k|^2 \propto 1 + \frac{4\pi}{\lambda^3} \int_0^{\pi/k} \xi(r)\, r^2\, dr \qquad (4.8)$$

In a weakly clustered system, such as the starting point of an N-body calculation, the power spectrum will be of Poisson form (n=0) on scales $\lesssim \lambda$. With small N-body simulations, with N $\sim$1000, $\lambda \sim (1/10)R$ where R is the radius of the bounding sphere, so for a large range of scales ($\lesssim R/10$) the correlations will be built up by discrete particle interactions. This problem has been studied analytically in the weak coupling limit by several authors, (Fall and Saslaw, 1976; Fall and Severne, 1976; Inagaki, 1976; Norman and Silk, 1978).

From equ. (4.8), the collective terms dominate over the discreteness terms in the BBGKY hierarchy on scales r if

$$C(r) = \frac{4\pi}{\lambda^3} \int_0^r \xi(y)\, y^2\, dy \;>\; 1 \tag{4.9}$$

Physically, C(r) measures the average number of clustered particles within a sphere of radius r centred upon a randomly chosen particle. As clustering develops, the term C(r) grows with time (see section 4.5 below and Appendix A), and hence the discreteness terms decrease in importance as time increases. Even in the highly non-linear case ($\xi \gg 1$), discreteness terms will be dominant on scales less than r_d defined by $C(r_d) = 1$. Intuitively one imagines that on scales less than r_d the particles are distributed as binary pairs rather than in clusters. This idea is borne out by studying the BBGKY equations in the limits $\xi \gg 1$, $r \ll r_d$. In this case, the discreteness terms are dominant. Under the assumption of stability on small scales, equs. (A.2)-(A.4) become

$$\frac{\partial \mathcal{S}'}{\partial t} - 3\,\frac{\dot{a}}{a}\left[x\,\frac{\partial \mathcal{S}'}{\partial x} + 2\mathcal{S}' \right] = \frac{-4Gm^2}{a}\,\frac{\partial (xA)}{\partial x} \tag{4.10a}$$

$$\frac{\partial \mathcal{S}'}{\partial x} = -\,2Gm^3 a\,\frac{\partial \xi}{\partial x} \tag{4.10b}$$

$$\frac{\partial \rho}{\partial t} = - \frac{1}{x^2 a^2} \frac{\partial}{\partial x} \left(\frac{x^3 A}{m} \right) \qquad (4.10c)$$

where $\mathcal{S}' = \frac{\partial}{\partial x} (x^2 \Pi) - 2x\Sigma$ and the notations and definitions follow those of DP.*

For power law dependence of $\rho \propto x^{-\gamma}$, equs. (4.10) have power law solutions

$$A = -ma\dot{a}\,\rho \qquad (4.11a)$$

$$\Pi \propto \Sigma \propto m^3 a \frac{\rho}{x} \qquad (4.11b)$$

from which we deduce that the radial and tangential velocity dispersions obey the equation,

$$(\gamma - 1) \langle v_r^2 \rangle + 2 \langle V_t^2 \rangle = \frac{2Gm}{ax} = \frac{2Gm}{r} \qquad (4.12)$$

This is to be compared with the situation where discreteness effects are negligible and the collective interactions dominate. One then has

$$(\gamma - 2) \langle v_r^2 \rangle + \langle v_t^2 \rangle = \frac{4\pi Gmn}{a} QM_\gamma x^2 \qquad (4.13)$$

---

* To present the notation and definitions here would require several pages! Hence, in the interest of brevity I refer the reader to DP.

where,

$$M_\gamma = \frac{1}{2(2-\gamma)(4-\gamma)} \int \frac{dy}{y^2}\left(1 + \frac{1}{y^\gamma}\right)$$

$$\left[(1+y)^{4-\gamma} - |1-y|^{4-\gamma} - (4-\gamma)y\left\{(1+y)^{2-\gamma} - |1-y|^{2-\gamma}\right\}\right]$$

$$M_{1\cdot 8} = 4\cdot 2$$

(Davis and Peebles equ. 100).*

Equs. (4.12), (4.13) and (A.1)-(A.5) serve to illustrate the formal difference between the set of equations solved by DP and those considered here.

On scales less than r_d, I would expect the correlation function slope γ to be dependent on the dynamics of the binaries rather than taking the value given by the scaling relation equ. (4.6).

For the purposes of the work described here, however, discreteness effects may not be a serious problem because I concentrate on an intermediate range of scale between r_d and R. The issue here is simple: do clusters virialize at high overdensities (as measured by ξ) as in the homogeneous spherical cluster model, or

---

* Equ. (4.12) has been derived in another way by Peebles, 1976b. It is interesting to note that observational determination of $\langle v^2 \rangle$ may indicate whether giant galaxies act as fundamental point particles, for if this were the case, Peebles' (1976a) application of equ. (4.13) to Turner's binaries, with separations ~ 50kpc, would be in error.

at low overdensities as suggested by Davis and Peebles? The models are analysed when clustering has developed sufficiently that $C(r) \gg 1$ on scales corresponding to the transition region $\xi \sim 1$. Hence over the scales of interest here, collective interactions should dominate.

In the next section I describe the numerical methods that have been used.

4.4 Numerical Methods.

The Aarseth direct summation program and its use in the cosmological context has been adequately described in the paper by Aarseth, Gott and Turner (1979). I have also applied this computer program, which is identical to that used in chapter 2 except that it was modified by the author to specularly reflect particles from a boundary which remains fixed at unit radius in the comoving frame. This was done in order to conserve particle numbers. Since such reflections result in a net loss of kinetic energy, this was integrated seperately in order to use energy conservation as a check for numerical consistency. Typically, energy was conserved to within 10^{-3} per cent of the total kinetic energy. The softened potential, equ. (2.15), was used.

In addition to those runs performed using the program mentioned above, further models were supplied to me by Aarseth and Fall. These were run using a program which employed a comoving system of coordinates.

The scheme does have some disadvantages because it can only handle $\sim$ 1000 particles. The small number of particles leads to quite large experiment by experiment variation in the results even for models with statistically similar initial particle distributions and cosmological parameters. A further worry is that with small simulations there may be "coherence-length" problems when the characteristic clump size approaches that of the whole system. Also, it is difficult to estimate the importance of edge effects.

These problems may be resolved by using large simulations and in the following subsections I shall briefly describe the main features of a scheme that can treat large numbers of particles. This will be refered to as the P^3M (Particle Particle / Particle Mesh) scheme. The P^3M scheme was developed by J.W. Eastwood and the modifications for its application to the cosmological problem were carried out by the author.

a) Equations of motion and energy conservation

The equations of motion in comoving coordinates may be derived from the Lagrangian

$$\mathcal{L} = \sum_i \tfrac{1}{2} m_i \, a^2 \, \dot{\underset{\sim}{x}}_i^2 \quad - \quad \frac{m}{a} \, \phi_i(\underset{\sim}{x}_i) \qquad (4.14)$$

where a satisfies the Friedman relations

$$\dot{a}^2 + k = \frac{8\pi}{3} G \bar{\rho} a^2 \qquad (4.15a)$$

$$\rho_o = \bar{\rho} a^3 \qquad (4.15b)$$

and

$$\nabla^2\phi = 4\pi G(\rho(x,t) - \rho_o) \qquad (4.16)$$

The equations of motion read,

$$\ddot{\underset{\sim}{x}}_i + 2\frac{\dot{a}}{a}\dot{\underset{\sim}{x}}_i = -\frac{1}{a^3}\underset{\sim}{\nabla}\phi_i \qquad (4.17)$$

The Layzer-Irvine equation (Irvine, 1961; Layzer, 1963) in comoving coordinates may be derived from the Lagrangian (4.14)

$$\frac{d}{dt}(a^4T) + a\frac{dW}{dt} = 0 \qquad (4.18)$$

where

$$T = \sum_i \tfrac{1}{2}\, m\, a\, \dot{\underset{\sim}{x}}_i^2$$

$$W = \sum_i m_i\, \phi_i(x_i)$$

T and W are related to the corresponding quantities in proper coordinates by the relations, $\hat{T} = a^2T$, $\hat{W} = W/a$. Equ. (4.18) together with momentum conservation was used to monitor the accuracy of the program (section c below). It is interesting to note that in the case of an isolated sphere of particles (as in the Aarseth simulations) the Layzer-Irvine equation reads,

$$\frac{d}{dt}(a^4T) + a\frac{dW}{dt} = \frac{4}{3}\pi G\rho_o a\sum_i{}' m_i\, \underset{\sim}{x}_i\cdot\dot{\underset{\sim}{x}}_i \qquad (4.19)$$

The term on the right hand side of equ. (4.19) averages to zero as the radius of the sphere tends to infinity if the Universe is homogeneous and isotropic on the large scale. For a finite system, however, the term will increase in importance as clustering develops on the scale of the system. This explains the peculiar behaviour of the correlation energies in some of the Aarseth experiments. In some cases it was found that the energies stabilised to a constant ratio $\hat{T}/\hat{W} \sim 0{\cdot}4$ whilst the energies themselves continued to grow, a physically impossible situation if equ. (4.18) applied.

In solving equ. (4.17) I use the time centred leapfrog scheme. If the timestep is Δt, and the force on a particle at time t is F(t), then the particles are moved according to

$$\underset{\sim}{v}(t+\tfrac{1}{2}\Delta t) = \underset{\sim}{v}(t-\tfrac{1}{2}\Delta t)\left[\frac{1 - H(t)\Delta t}{1 + H(t)\Delta t}\right] + \frac{\underset{\sim}{F}(t)\Delta t}{a^3(t)\left[1 + H(t)\Delta t\right]}$$

$$\underset{\sim}{x}(t+\Delta t) = \underset{\sim}{x}(t) + \underset{\sim}{v}(t+\tfrac{1}{2}\Delta t)\Delta t$$

where $H(t) = \dfrac{\dot{a}(t)}{a(t)}$

b) Calculation of the forces

In the P^3M scheme, the total force $\underset{\sim}{F}_i$ acting on particle i is calculated in two parts

$$\underset{\sim}{F}_i = \underset{\sim}{F}_m + \underset{\sim}{F}_{sr}$$

The mesh part of the force, $\underset{\sim}{F}_m$, is long range and smoothly varying. Its harmonic content is restricted so that it can be accurately approximated by a particle-mesh force calculation. The short range part, $\underset{\sim}{F}_{sr}$, is rapidly varying, having non-zero contributions only from those particles within a sphere of radius r_e of particle i. It is calculated by directly summing the contributions from particles within the sphere.

The potential mesh is a regular lattice of M^3 mesh points covering the whole of the volume of the cubical computational box (we take M=32 for the calculations discussed in section 4.5). Masses are assigned to the mesh according to the triangular shaped cloud (TSC) charge assignment/force interpolation scheme (Eastwood and Hockney, 1974). The mesh defined potential is then found by convolving the density distribution and the mesh defined Greens function using discrete Fourier transforms. The potential values are differenced to obtain the mesh part of the force $\underset{\sim}{F}_m$. The numerical error in the computation of the mesh forces is minimised by introducing errors into the definition of the Greens function which largely offset the inaccuracies introduced by charge assignment, potential differencing and force interpolation.

The short range part of the force is calculated by direct summation. This part of the calculation uses the linked-list technique (e.g. Hockney, Goel and Eastwood, 1974), which provides a means of rapidly locating the coordinates of all particles in a subregion of the computational box. The linked list addressing is then used to sweep through all pairs of particles and add their respective interparticle forces to the momenta. The particle positions are then updated, thus completing one timestep cycle.

In order to obtain a reasonably large timestep whilst maintaining numerical stability, the force between two particles is cut off at a separation d_m in a manner which corresponds to a galaxy with a linearly decreasing density profile. This is done purely for computational economy and not for any physical reason, especially since the force maintains constant shape in comoving coordinates. A full account of the analysis and optimisation of the P^3M algorithm is given by Eastwood (1976) and a published version of the program (Eastwood et al, 1979) will shortly be available.

c) Accuracy

The accuracy of the P^3M code has been gauged by using equ. (4.18) in the forms

$$(a^4T)^m + (aW)^m - \sum_{n=1}^{m} \Delta t \, W^n \dot{a}^n = C = \text{constant}$$

$$\frac{(a^{n+1})^4 T^{n+1} - (a^n)^4 T^n}{\Delta t} + \frac{a^{n+1}W^{n+1} - a^n W^n}{\Delta t} - W^{n+1}\dot{a}^{n+1} = 0$$

A small timestep has been used, with $H_i \Delta t = 0\cdot022$, where H_i is the initial value of the Hubble constant. During the course of a typical 20000 body run, the error in C was found to be $\Delta C/\Delta(aW) \lesssim 0\cdot02$ using this timestep. The most severe test of the P^3M code was a 1000 body test run. The 528 particles within a sphere inscribing the cubical mesh were used as the initial conditions for a simulation using Aarseth's direct summation program. Despite the different treatment of particles at the boundaries and the different form of the potential, the final particle distributions from these two calculations were remarkably similar. The correlation functions from these experiments agreed on scales larger than the softening parameter used in the P^3M code. In addition to this test, many two-body problems were run as checks during the early stages of the application of the P^3M program. The value of the timestep used in the 20000 body experiments was arrived at on the basis of reproducibility. Several 1000 body experiments were run, the timestep being halved for each run until there was no detectable difference in the final particle positions. When convergence was reached, the lower value of the timestep was chosen and scaled to the value appropriate for a 20000 body run.

The Aarseth program is, of course, more accurate and allows the use of a harder potential due to the individual timestep/particle scheme. In principle the P^3M scheme could be modified so that each particle has an individual time-step. The long range force calculated using Fast Fourier transforms could be calculated at fixed timesteps and treated in much the same way as the long range force in the Ahmad-Cohen (1973) scheme. This would allow more accurate integrations but would require a fairly major overhaul of the present program.

4.5 Results.

A full list of the models that have been run for this investigation and that of chapter 5, together with model parameters is given in Table 4.1. The Freeze models will be discussed in chapter 5.

Figure 4.1(a) shows the starting positions of the particles, in X-Y projection, for model 14F. Fig. 4.1(b) shows the particle positions after the system has expanded by a factor of 9·9. It is interesting that in Fig. 4.1(b) the particle distributions appear quite "filamentary". The same effect, only more enhanced, is apparent from the map of the Lick galaxy counts (Soneira and Peebles, 1978). Such impressions are, of course, highly subjective, but there has been considerable speculation as to whether the hierarchical clustering model could possibly give rise to particle distributions which look "filamentary".

a) Estimation of the correlation functions

The two-point correlation function has been estimated using two different estimators. In the case of particles distributed within a spherical volume, the edge effects

Table 4.1. The N-body experiments.

Model	Distn.	Ω_s	N	ε_o/d_m	Mass Distn.	Type
1A	P	1·0	1000	0·31	E	S
2B	P	1·0	1000	0·06	E	S
3C	P	1·0	1000	0·13	E	S
4	P	1·0	1000	0·31	E	S
* 5D	P	1·0	1000	0·06	E	S
6	P	1·0	1000	0·13	E	S
7A	P	0·775	1000	0·31	E	S
8B	P	0·775	1000	0·06	E	S
9C	P	0·775	1000	0·13	E	S
10	C	1·0	973	0·13	E	S
11	C	1·0	965	0·13	E	S
12	C	1·0	964	0·13	E	S
* 13E	C	1·0	910	0·06	E	S
14F	P	1·0	20000	0·20	E	S
15G	P	1·0	20000	0·20	E	S
16F	P	0·775	20000	0·20	E	S
17G	P	0·775	20000	0·20	E	S
18	P	1·0	1007	0·13	MS	S
19	P	1·0	1007	0·13	MS	S
20	P	1·0	1000	0·13	MV/ML	S
21	P	1·0	1000	0·13	MV/ML	S
* 22D	P	1·0	1000	0·06	E	F
* 23E	C	1·0	910	0·06	E	F

Notes: Models with a letter in common started with identical initial particle positions. The softening parameters ε_o and d_m are given in units of the initial interparticle separation. The initial distributions were either Poisson (P) or Cells (C) and the claculations were either Standard (S) or Freeze (F); See chapter 5. The

Table 4.1. continued-

particle masses were: (E) all particles equal mass; (MS) mass spectrum (see text); (MV/ML) 500 particles of unit mass + 500 massless particles. Asterisked models were kindly loaned to me by Aarseth and Fall.

The models have been arranged to form ensembles as follows:

Ensemble	Models	Distn.	Ω_s
1	1-6	P	1·0
2	10-13	C	1·0
3	7-9	P	0·775
4	14-15	P	1·0
5	16-17	P	0·775
6	18-19	P	1·0
7	20-21	P	1·0

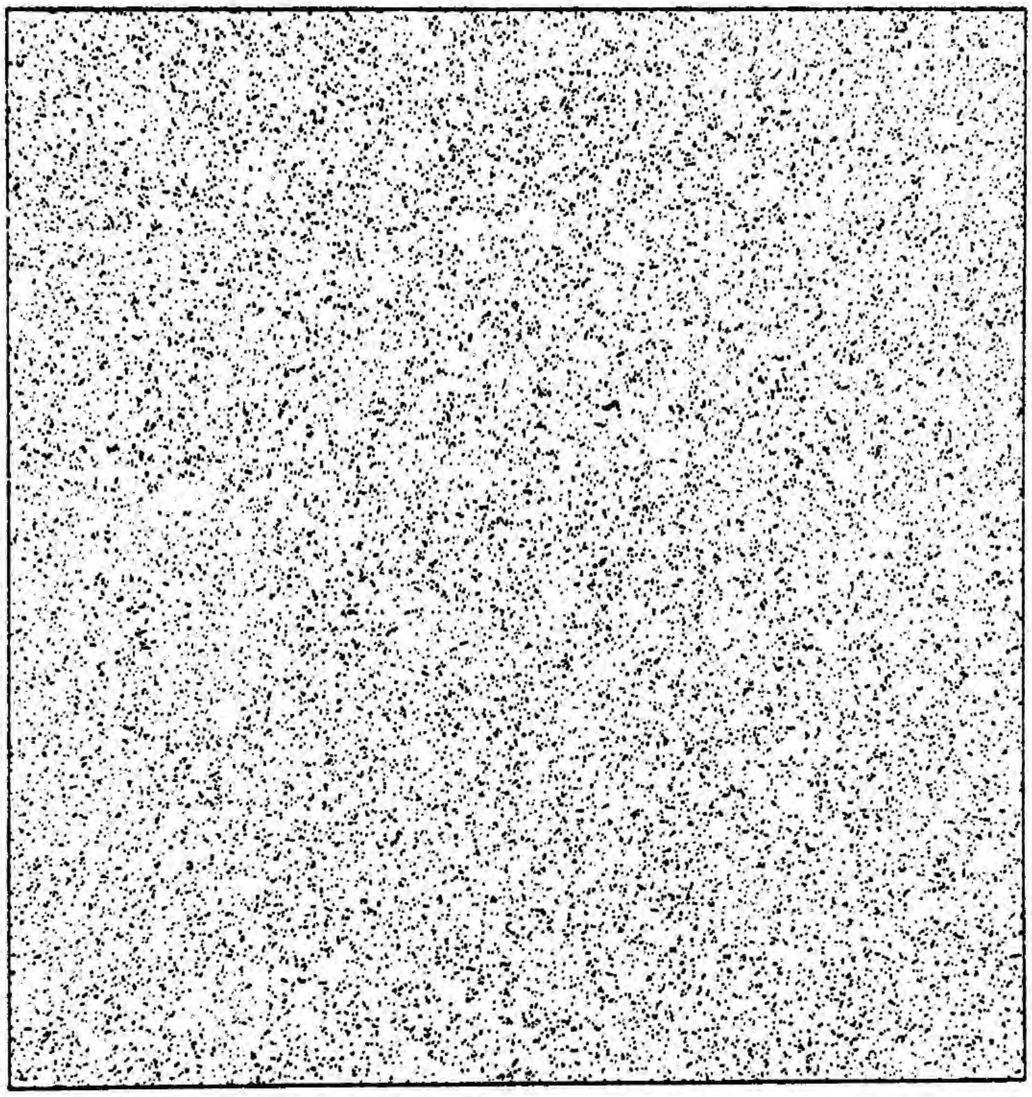

Figure 4.1(a). Initial conditions for a 20000 body numerical experiment. Particles have been distributed at random within a unit cube seen here in X-Y projection.

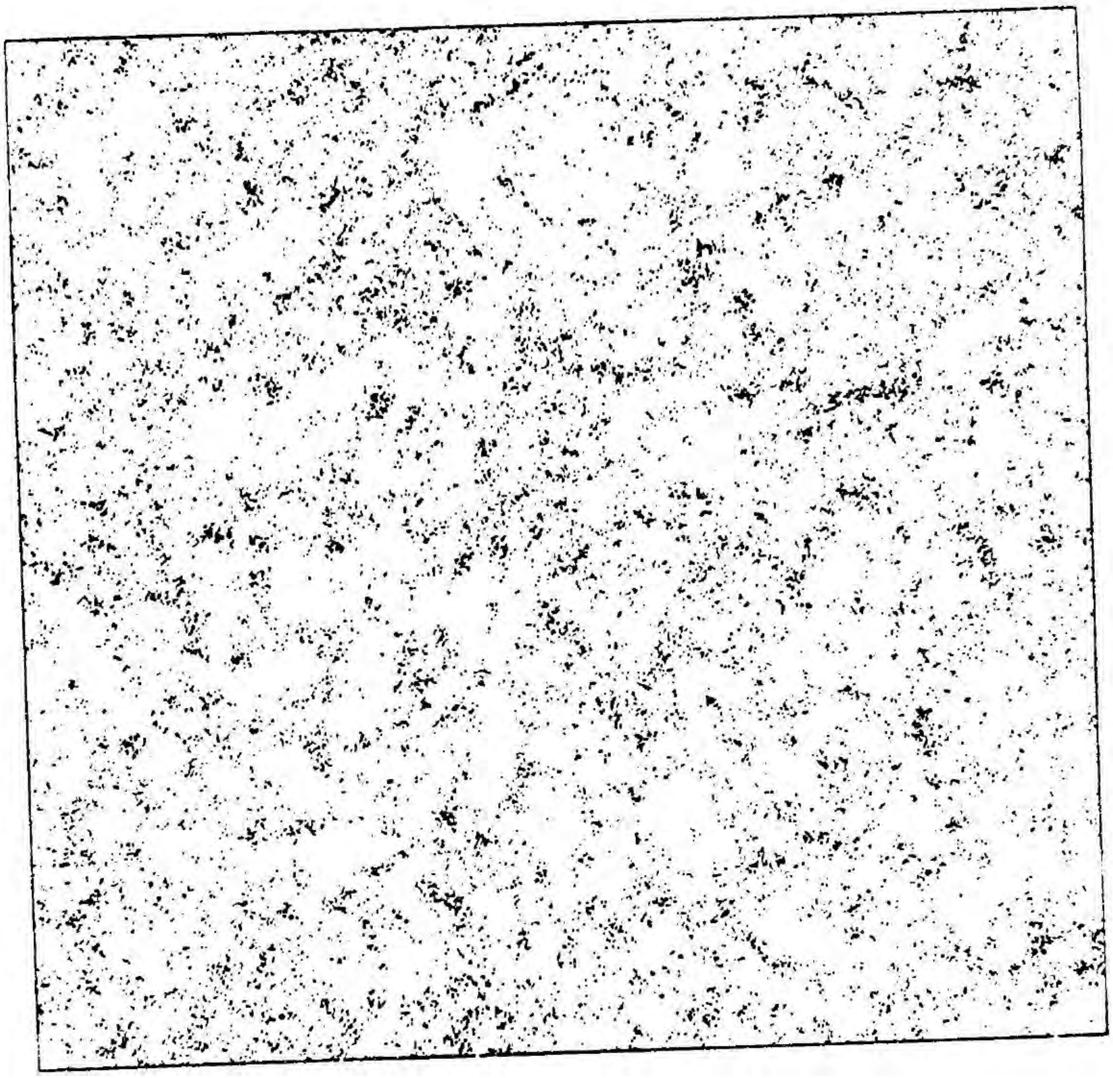

Figure 4.1(b). X-Y projection of the particle positions after the system has expanded by a factor of 9·9. In this case the expansion follows that of an Einstein-de Sitter model, $\Omega_0 = 1 \cdot 0$.

can easily be calculated analytically. In this case one may use the estimator

$$\xi(r_{ij}) = \frac{N_p}{\bar{n}\, N_c\, V(r_{ij})} - 1 \qquad (4.20)$$

where N_p is the number of pairs in a shell with radii r_i and r_j (weighted for edge corrections), $V(r_{ij})$ is the volume of the shell $4/3\,\pi(r_j^3 - r_i^3)$, N_c is the total number of centres, $\bar{n}$ is the mean particle density. Edge corrections are taken into account by using a 'look up' table and so each galaxy is binned in a small interval x-x+dx (x is the distance of the particle from the centre of the reflecting sphere of radius R). The number of pairs is weighted by the factor

$$\frac{V(r_{ij})}{V(r_{ij}) + \gamma(r_j,x) - \gamma(r_i,x)} \qquad (4.21)$$

where

$$\gamma(r_i,x) = 2\pi\Big\{\tfrac{1}{3}\left[r_i^3 - (R-x)^3\right] - \frac{R^2}{4x}\left[r_i^2 - (R-x)^2\right] + \frac{1}{8x}\left[r_i^4 - (R-x)^4\right] + \frac{x}{4}\left[r_i^2 - (R-x)^2\right]\Big\}$$

An alternative method involves the estimator

$$\xi(r_{ij}) = \frac{\langle DD \rangle}{\langle RR \rangle} - 1 \qquad (4.22)$$

Here $\langle DD \rangle$ represents the number of pairs within the spherical shell $4/3\,\pi(x_j^3 - x_i^3)$ determined from the data and $\langle RR \rangle$ represents the pair count within the same spherical shell determined from a random distribution of points within the computational volume. To estimate $\langle RR \rangle$ I have used 20000 particles within the computational volume and interpolated at small separations, since $\langle RR \rangle \propto x^{-3}$ when edge corrections can be neglected. This method may be applied to either the spherical simulations or the the cubical simulations.

The two estimators would yield different answers if the particles were correlated with the boundary of the computational volume, hence ξ has been estimated for most of the 1000 body models using both estimators. The two methods agree point by point at separations $x < R/10$ but differ somewhat for $x > R/10$. The difference is usually less than the variation of ξ between different models within each ensemble. Hence, one may be confident that the results are not strongly estimator dependent. In most of the analysis below, the estimator of equ. (4.22) has been used.

The three-point correlation function is estimated using a straightforward generalisation to three dimensions of the method used by Peebles and Groth (1975)-

$$\zeta = \frac{\langle DDD\rangle - \langle DDR\rangle}{\langle RRR\rangle} + 2 \tag{4.23}$$

and the three-point function $\zeta(x_1, x_2, x_3)$ is parameterised by the "size" parameter x and the "shape" parameters u and v

$$x = x_1 \ , \quad u = \frac{x_2}{x_1} \ , \quad v = \frac{x_3 - x_2}{x_1} \tag{4.24}$$

$$x_1 < x_2 < x_3$$

ζ has been estimated on scales $x < R/10$ using the same logarithmic spacing in x as in the estimate of ξ. Since the comparison between ζ and ξ will be only approximate and since over most of the scale $\zeta \gg 1$, the direct count $\langle DDR\rangle$ has been used in equ. (4.23).

c) Integral constraint and the dependence of ξ on Ω

Groth and Peebles (1976) showed that the quantity $\Delta(r)$ defined by

$$\Delta(r) = a^3 \int_0^r d^3\underline{x} \, (\rho - \bar{\rho}) \tag{4.25}$$

obeys the equation for linear density perturbations

$$\frac{d^2\Delta}{dt^2} + 2\,\frac{\dot{a}}{a}\,\frac{d\Delta}{dt} = 4\pi G\bar{\rho}\,\Delta \tag{4.26}$$

This equation is expected to be obeyed for as long as

$|\Delta(r)| \lesssim \bar{\rho}\, 4\pi r^3/3$. When this condition is not satisfied non-linear effects result in a slower growth rate than predicted by equ. (4.26). The quantity $\langle \Delta^2(r) \rangle$ is related to the two-point correlation function by

$$\frac{\langle \Delta^2(r_o) \rangle}{nV} = 1 + \frac{n}{V} \iint \xi(r_{ij})\, d^3\underline{r}_i\, d^3\underline{r}_j$$

$$\approx 1 + n \int_0^{r_o} \xi(r)\, r^2\, dr \qquad \text{if } \xi(r_o) \ll 1 \qquad (4.27)$$

An alternative derivation of equ. (4.27), from the BBGKY hierarchy is given in Appendix A. Following Groth and Peebles, the solutions to the density perturbation equation may be written

$$\Delta = A\, \Delta_g(z) + B\, \Delta_d(z) \qquad (4.28)$$

Δ_g refers to the growing mode and Δ_d to the decaying mode:

$$\Delta_g = \frac{y}{y_i} \qquad \Omega = 1 \qquad (4.29a)$$

$$\Delta_g = 1 + \frac{3}{x} + \frac{3(1+x)^{\frac{1}{2}}}{x^{3/2}} \ln\left[(1+x)^{\frac{1}{2}} - x^{\frac{1}{2}}\right]$$

$$\Omega < 1 \qquad (4.29b)$$

and

$$\Delta_d = \left(\frac{y}{y_i}\right)^{-3/2} \qquad \Omega = 1 \qquad (4.30a)$$

$$\Delta d = \frac{(1 + x)^{\frac{1}{2}}}{x^{3/2}} \qquad \Omega < 1 \qquad (4.30b)$$

where $y = 1/(1+z)$

$x = (1/\Omega_o -1)/(1 + z)$

Applying the boundary conditions $\Delta = \Delta_i$, $d\Delta/dt = 0$ at $z=z_i$, the growth rates are given by

$$\frac{\Delta}{\Delta_i} = \frac{2}{5}\left[\frac{3}{2}\left(\frac{y}{y_i}\right) + \left(\frac{y}{y_i}\right)^{-3/2} \right] \qquad \Omega = 1 \qquad (4.31a)$$

$$\frac{\Delta}{\Delta_i} = \left(1 + \frac{3}{2x_i}\right)\Delta_g(x) + \left[- \frac{9}{2}(1 + 1/x_i)^{\frac{1}{2}} - 3(1 + 3/2x_i) \ln\left[(1 + x_i)^{\frac{1}{2}} - x_i^{\frac{1}{2}}\right]\right]\Delta_d(x) \qquad (4.31b)$$

$$\Omega < 1$$

Fig. 4.2 shows the time development of $\langle\Delta^2\rangle$ as determined by equ. (4.31). Also shown are the data points from models 1A and 7A with $r_o = 0{\cdot}25$. Deviation from the theoretical curves is expected for

$$1 + 4\pi n \int_0^{r_o} \xi(y)\, y^2\, dy \gtrsim 1 + nV \gtrsim 16{\cdot}6 \qquad (4.32)$$

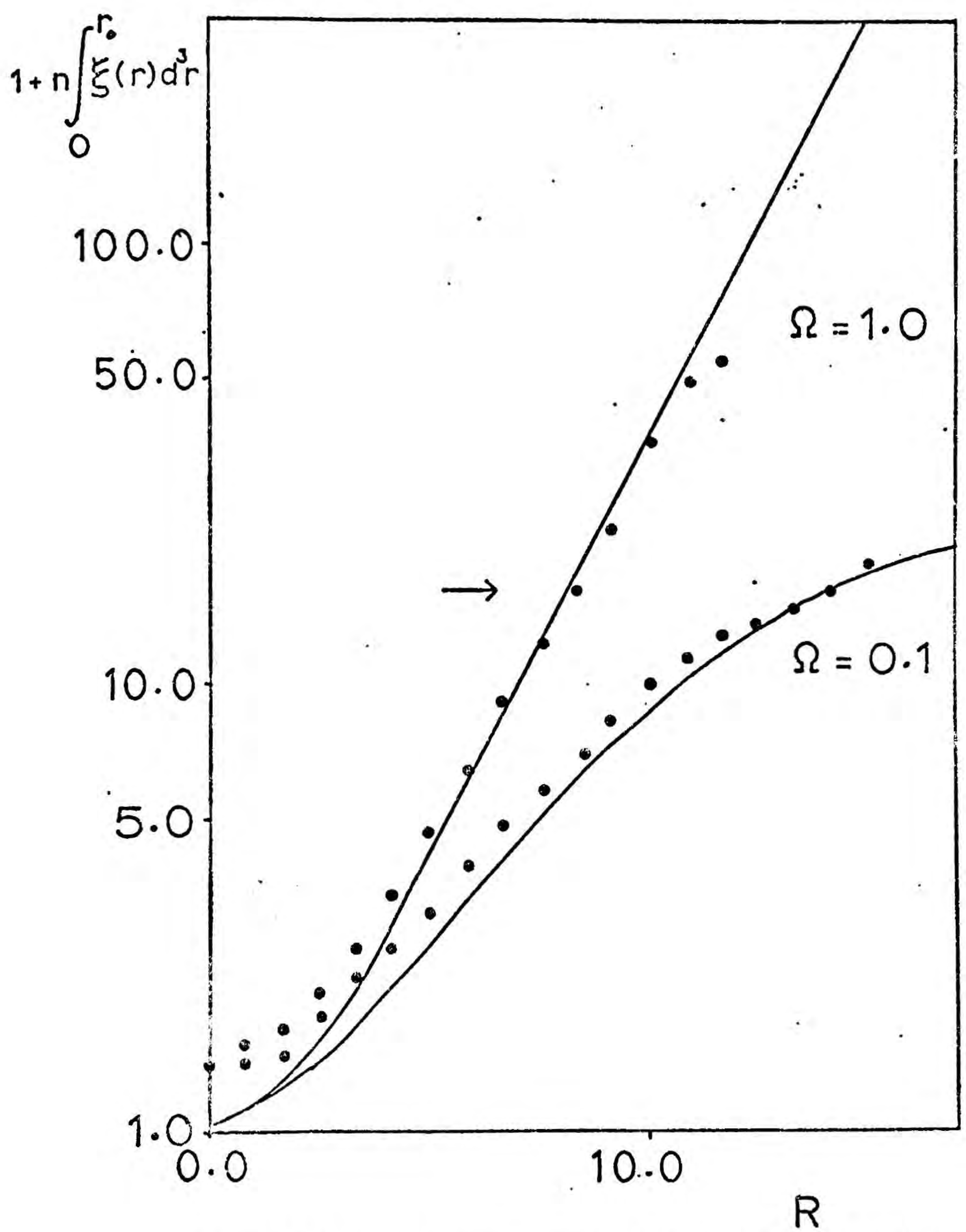

Figure 4.2. Integral constraint applied to models 1A and 7A. The solid lines are the linear theory solutions of the density perturbation equation. In this case $r_0 = 0{\cdot}25\ R$ and the arrow indicates the point at which deviation from the theoretical curves is expected.

It is apparent from Fig. 4.2 that the evolution of (4.27) for the two models is quite different and in good agreement with equs. (4.31).

The decrease in the linear growth rate in a low density universe is expected to influence the shape of the two-point correlation function. In the case $\Omega = 1$, the similarity solution (equs. (4.7a) and (4.7b)) applies. However, in an open cosmological model a characteristic timescale $z_f \simeq 1/\Omega_0 - 1$ immediately presents itself. For $z \gg z_f$ the behaviour is almost identical to that of an $\Omega = 1$ universe, hence $\xi(r)$ would be expected to have an almost identical form to that of an $\Omega = 1$ model. However, for $z \ll z_f$ linear growth is suppressed and the similarity solution is no longer valid. As a simple model for an open universe (Davis, Groth and Peebles, 1977), the linear part of $\xi(r)$ is modelled by equ. (4.7b) with Δ_g given by equ. (4.29b). The non-linear region is assumed to evolve as in the $\Omega = 1$ case by equ. (4.7a) since clusters at small scales are assumed to be in virial equilibrium. Extrapolation between the asymptotic limits yields a feature at large ξ for $\Omega \ll 1$. This is illustrated in Fig. 4.3 for various values of ξ_{break}. If $\xi_{break} \gtrsim 1$ we may expect to see this effect in the N-body models. For very low density models, $\Omega \sim 0 \cdot 1$, the extrapolation becomes rather large, Hence, the argument is necessarily of a qualitative nature.

In Figs. 4.4(a,b) estimates of ξ at various values of

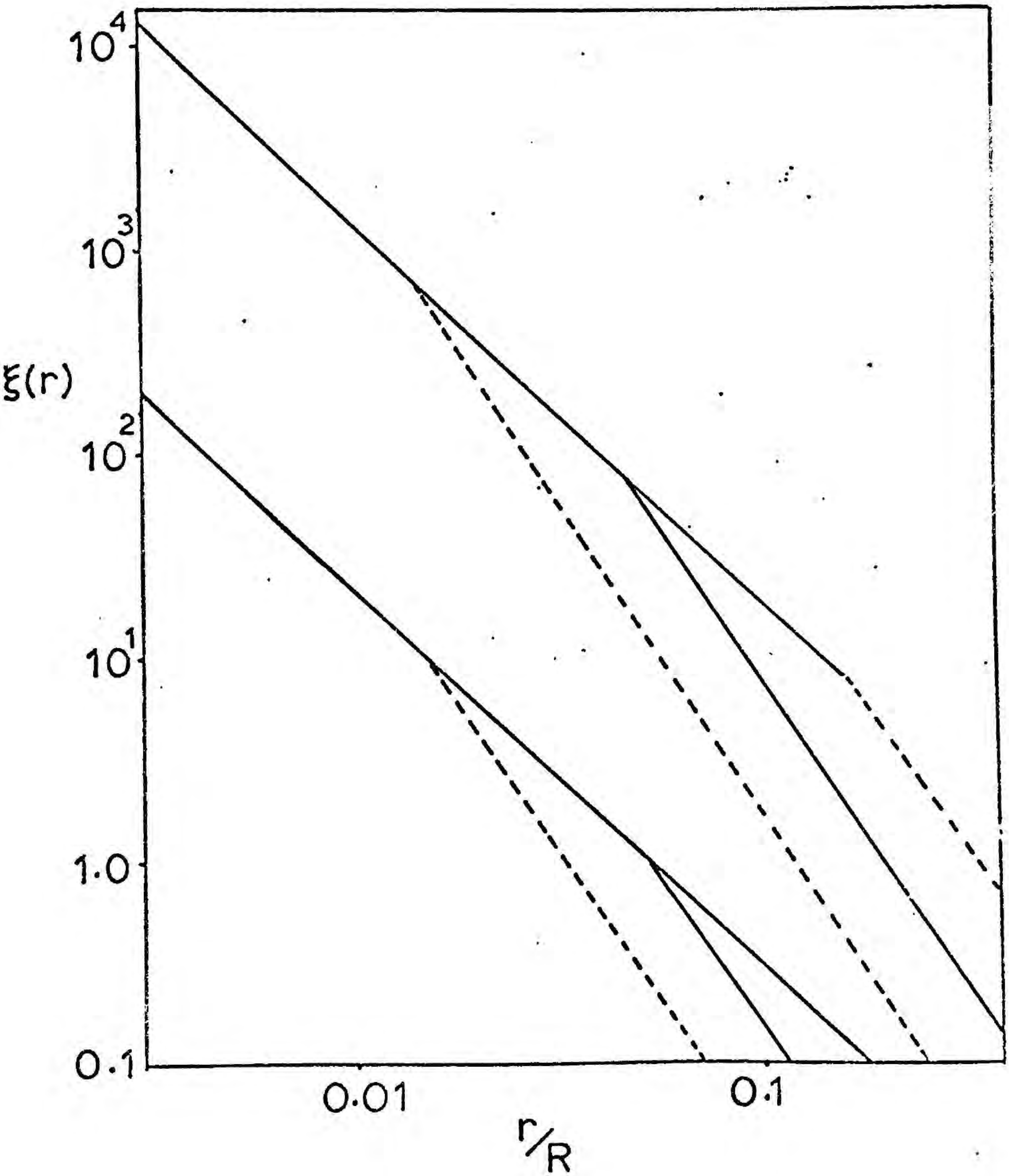

Figure 4.3. Two power law models for $\Omega = 0{\cdot}1$ evolved from $\Omega = 0{\cdot}775$ using values for ξ_{break} of 10, 1, 0·1.

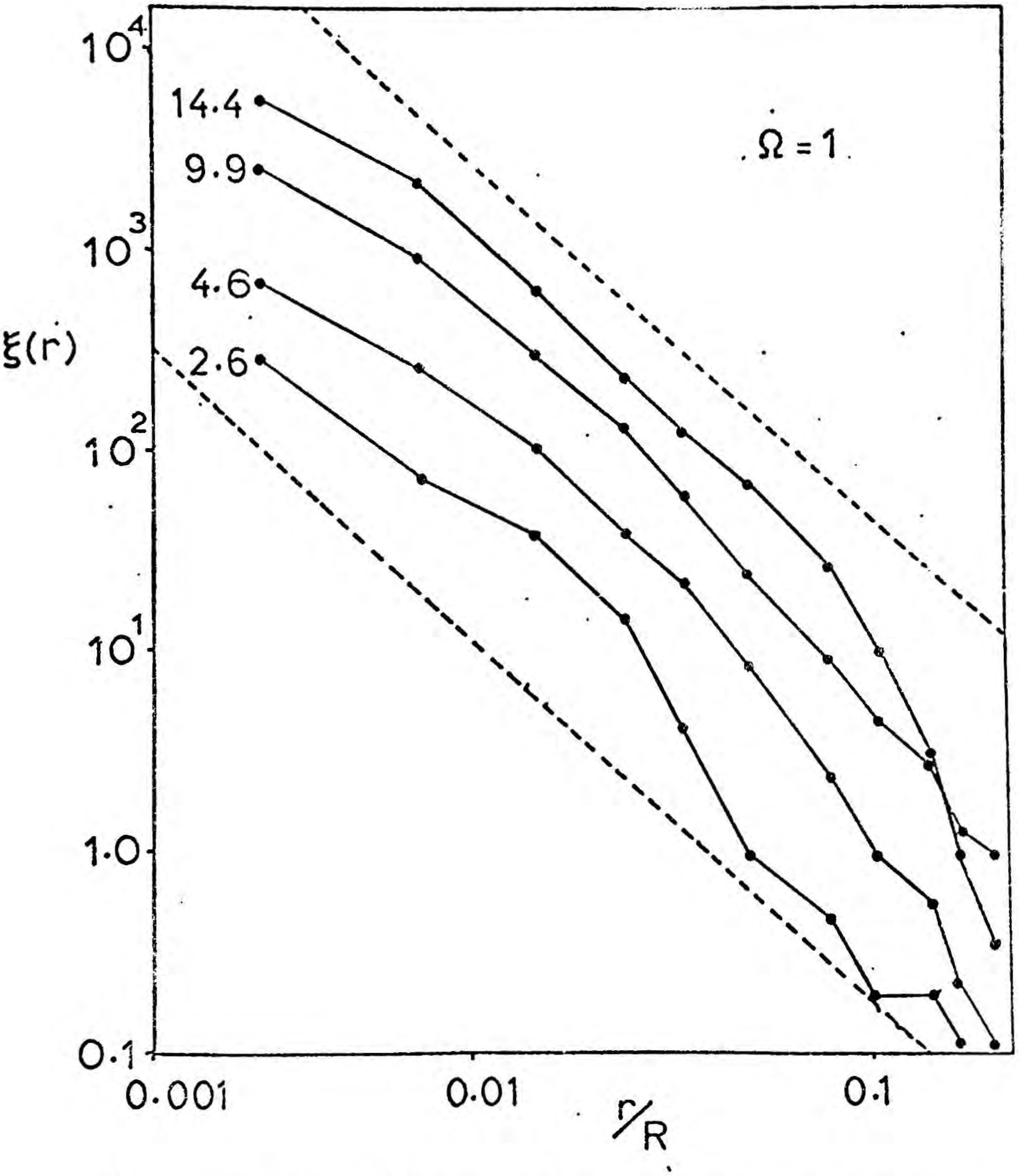

Figure 4.4(a). Estimates of the two-point correlation function for model 1A at several values of the expansion factor. The dashed lines are of slope $\gamma = 1{\cdot}8$.

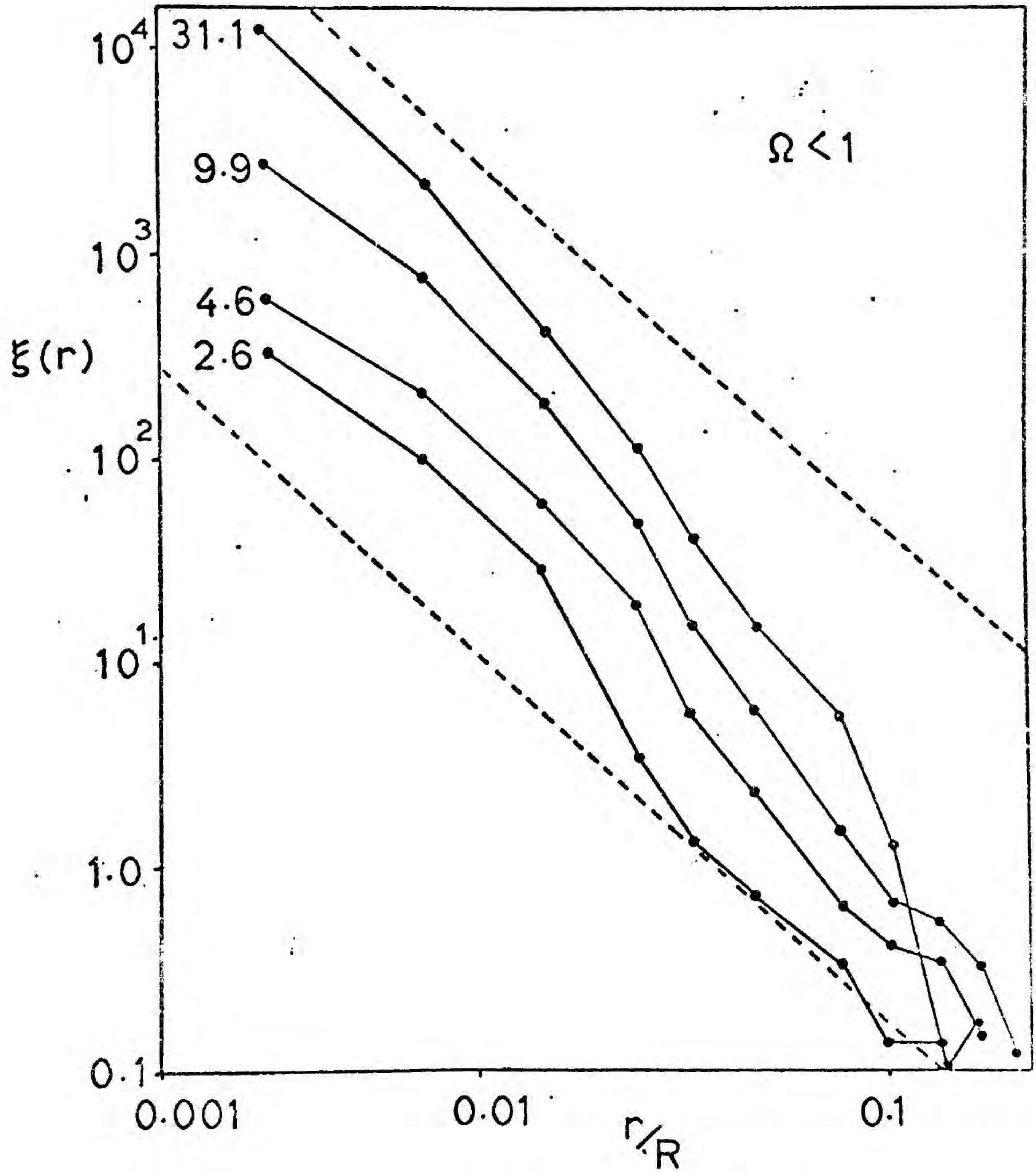

Figure 4.4(b). As for Fig. 4.4(a) except for model 7A.

the expansion parameter are shown for models 1A and 7A.

ξ for the case $\Omega < 1$ is quite obviously steeper than ξ in the case $\Omega = 1$, in qualitative agreement with the argument presented above. There is, however, a large run by run variation in the slope of ξ when using 1000 particles. Therefore, in order to compare the N-body simulations with the observed data in more detail, ensemble averages and larger calculations are required. These will be discussed below. Nevertheless, the two models described here qualitatively confirm the conclusions of Peebles (1974b) concerning the shape of the two-point function and its dependence on the cosmological density parameter.

c) The two-point function in greater detail

Figs. 4.5(a,b,c)* and 4.6(a,b,c) show estimates of of the two-point function for each of ensembles 1-5. The models of ensembles 4 and 5 were evolved to expansion factors of 9·9 and 19·3 respectively whilst some models within ensembles 1-3 were evolved for longer periods. The main results to be presented below do not depend sensitively on the epoch at which the models are analysed, although at late times the 1000 body experiments show signs of coherence length problems (cf. Figs. 4.4)

In general there is good agreement between the 20000 body models over the range $\xi \lesssim 100$. The correlation functions

---

* Models 6 and 12 were run at a late stage during this investigation and are not included in Figs. 5.

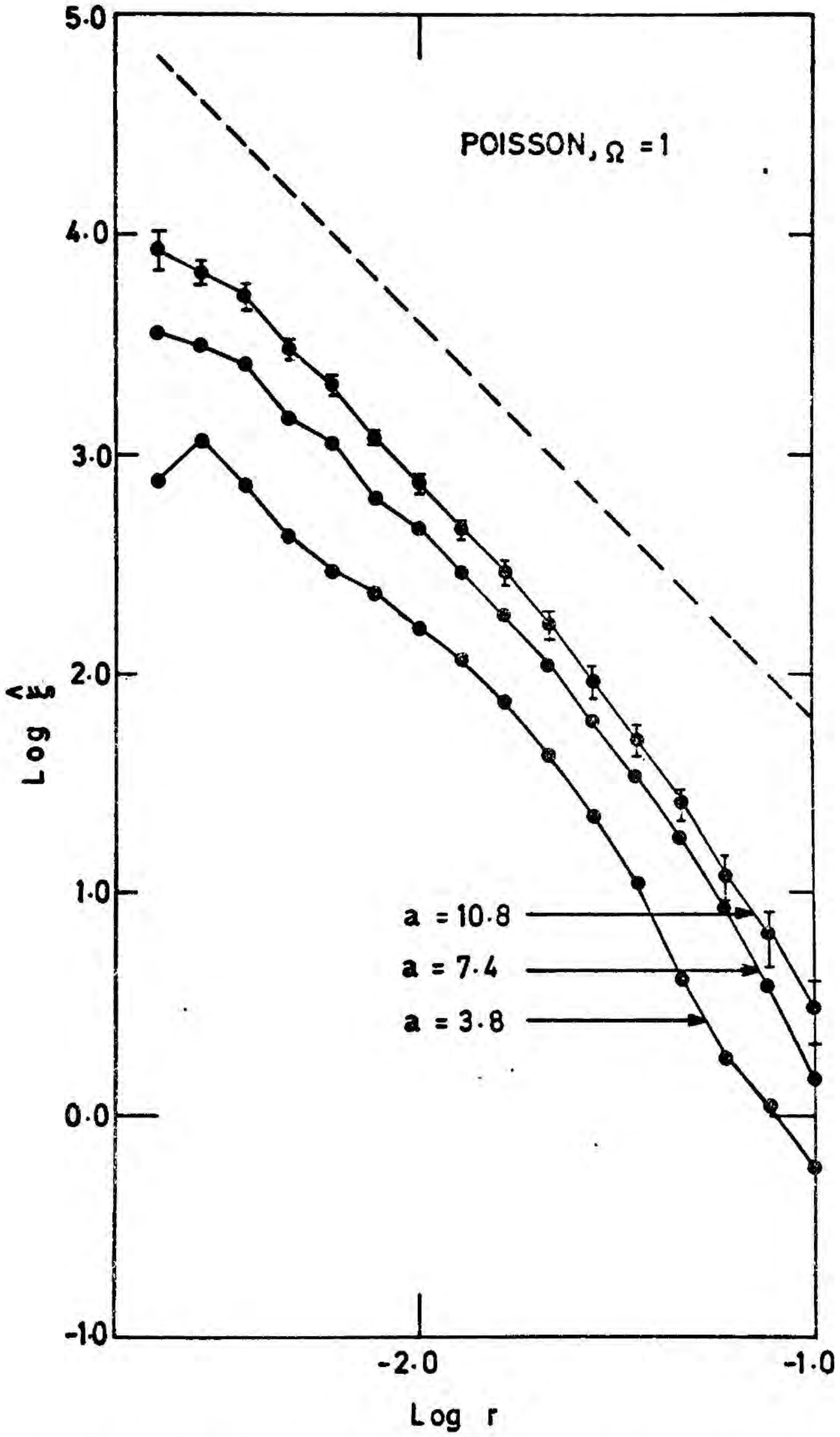

Figure 4.5(a). Estimates of the two-point correlation function for models of ensemble 1 at various values of the expansion parameter a.

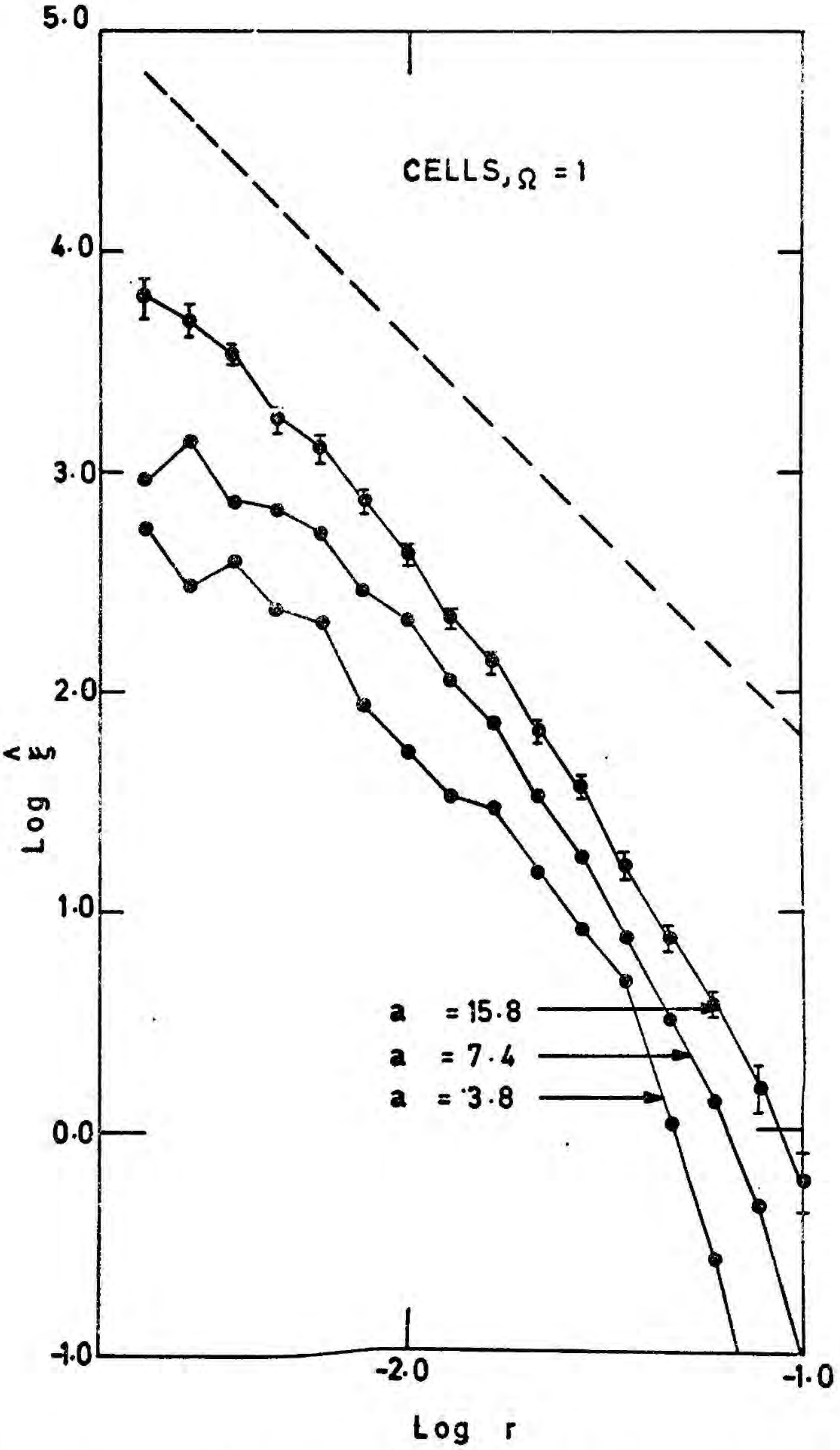

Figure 4.5(b). As Fig. 4.5(a) except for models of ensemble 2.

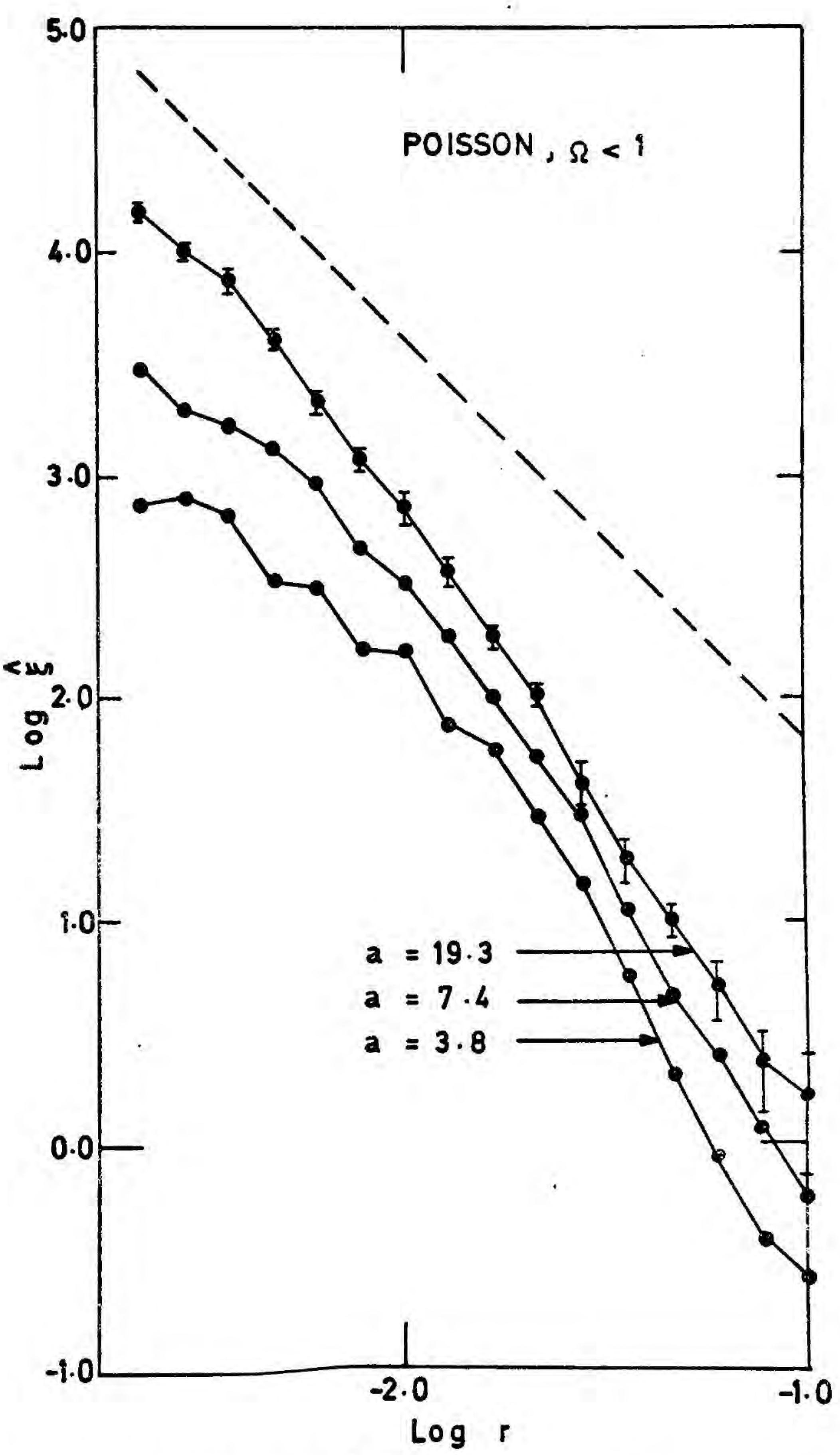

Figure 4.5(c). As Fig. 4.5(a) except for ensemble 3.

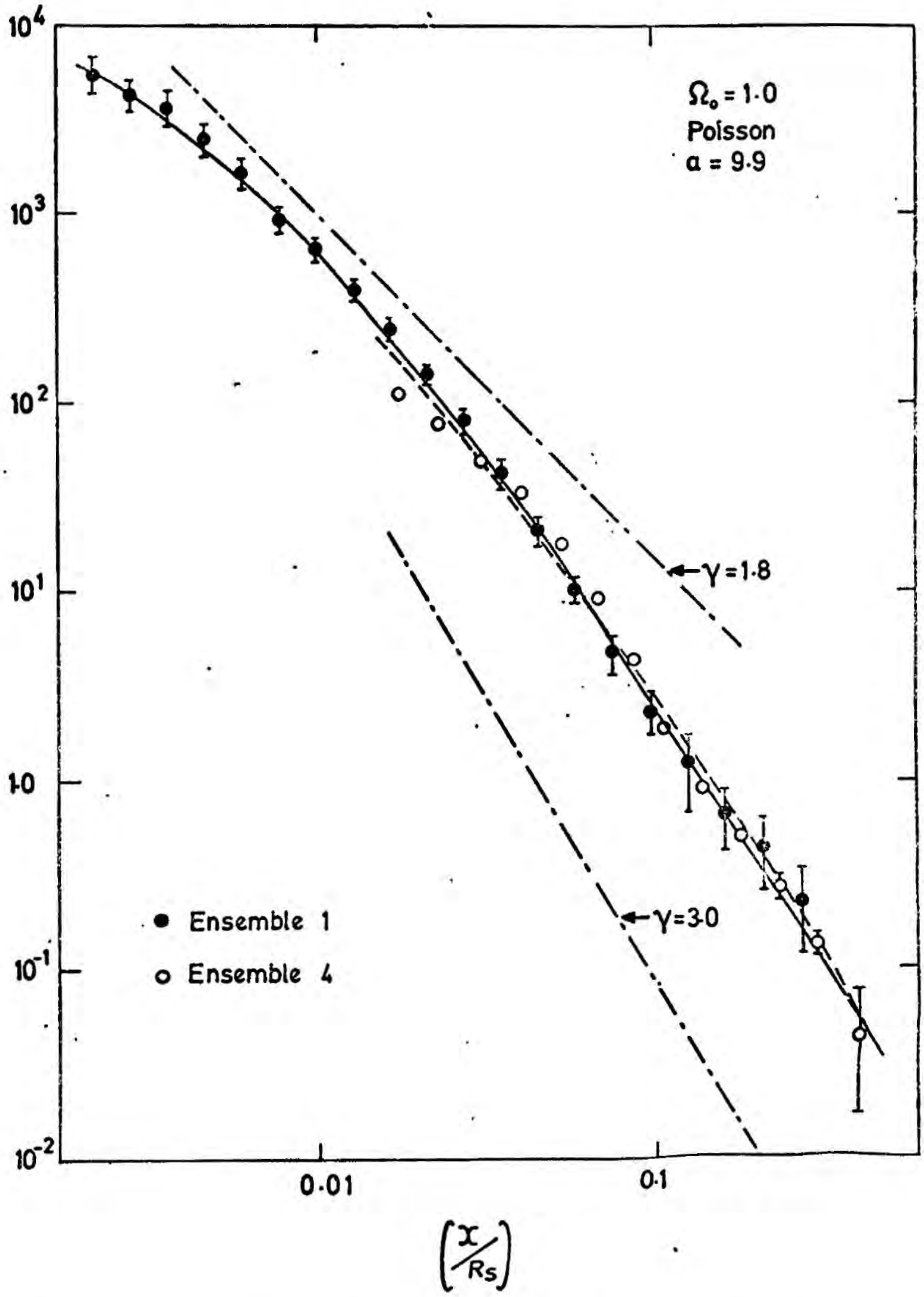

Figure 4.6(a). Two-point correlation function for ensembles 1 and 4 after expansion by a factor a=9.9. The error bars represent one standard deviation in the mean. The solid line shows the least squares fit of Table 4.2. The dashed line shows the result of solving the pair conservation equation using v_{21} of Fig. 4.7(a). The dot-dashed lines show the

Caption for Fig. 4.6(a) continued -

asymptotic slopes of the similarity solution (equs. 4·7(a) and 4·7(b)). In this and the other figures below, the 20000 body models have been scaled in terms of the units used in the 1000 body experiments, hence R_s represents the radius of the bounding sphere.

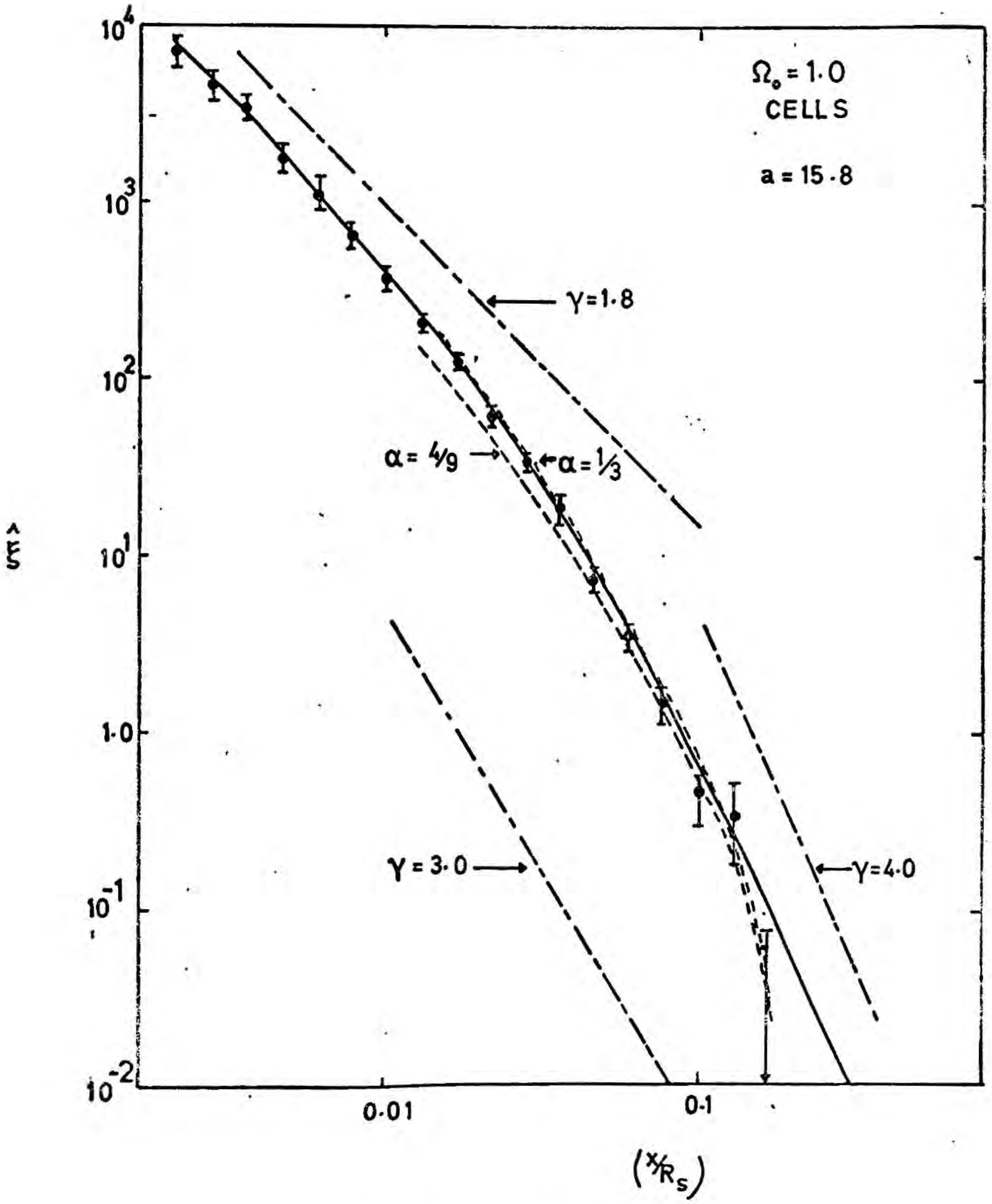

Figure 4.6(b). As for Fig. 4.6(a) except for ensemble 2 after expansion by a factor a = 15•8. Here, the results are shown of integrating equ. (4.34) using two values of the "similarity" parameter α (equ. 4.36).

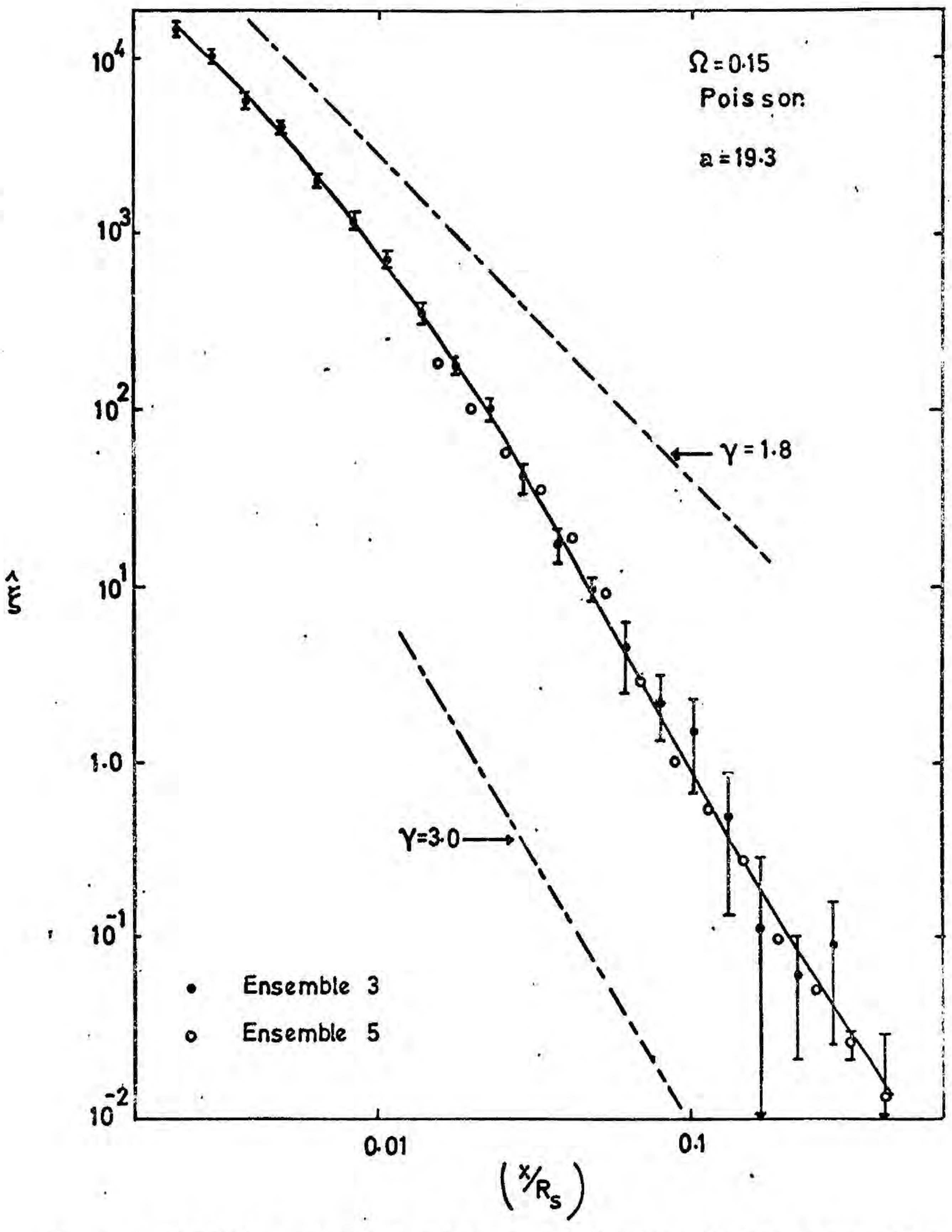

Figure 4.6(c). As for Fig. 4.6(a) except for ensembles 3 and 5 after expansion by a factor $a = 19 \cdot 3$ at which time $\Omega_0 = 0 \cdot 15$.

for the 20000 body experiments flatten off on small scales due to the large softening parameter, but the loss of a few pairs at small scales does not affect the correlation function at large scales very much. I discuss the results for each set of initial conditions below:

A. $\Omega = 1$, Poisson distribution

It can be seen from Figs. 4.5(a) and 4.6(a) that the correlation function deviates from the observed slope $\gamma = 1{\cdot}8$ for $\xi \lesssim 50$, steepening to a slope which is close to the asymptotic slope given by linear theory, $\xi \propto x^{-3}$ (equ. (4.7b)). The fact that the $\approx x^{-3}$ behaviour is reproduced consistently in the 20000 body models suggests that it is not due to a sampling (or coherence length) problem.

An important consistency check is to examine the behaviour of the mean relative peculiar velocity between particle pairs $\langle v_{21} \rangle$ in the transition region $\xi \sim 1$, since ξ and $\langle v_{21} \rangle$ are related by the equation of conservation of particle pairs

$$\frac{\partial \xi}{dt} + \frac{1}{x^2} \frac{\partial}{\partial x} \left(x^2 (1 + \xi) \langle v_{21} \rangle \right) = 0 \qquad (4.33)$$

(DP equ. 41, equ. (A.2) here).

$\langle v_{21} \rangle$ for ensembles 1 and 4 is shown in Fig. 4.7(a) and the arrow marks the separation at which $\xi \approx 1$. The $\langle v_{21} \rangle$ curve rises by a factor of ~ 2 above the Hubble line $v = Hr$ at separations corresponding to $\xi \sim 1$, in

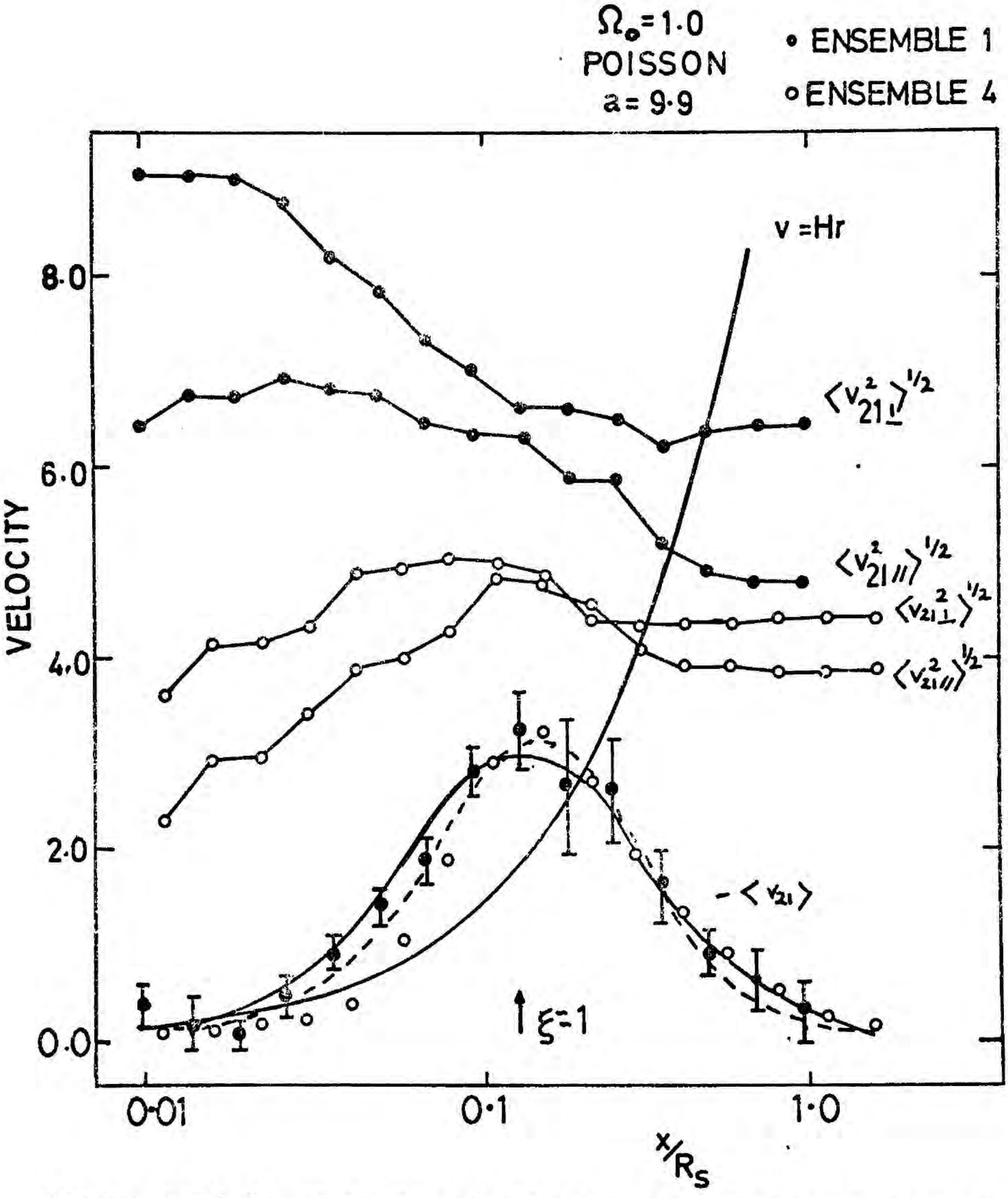

Figure 4.7(a). Velocity statistics for ensembles 1 and 4 at a=9·9. The dashed line shows the result of integrating equation 4.35(a) using ξ of Fig. 4.6(a). To avoid overcrowding the error flags on $\langle v_{21\parallel}^2\rangle$ and $\langle v_{21\perp}^2\rangle$ have not been shown but some idea of their size may be judged by the variation between adjacent points. The solid line shows the fit to $\langle v_{21}\rangle$ used in equ. (4.36b).

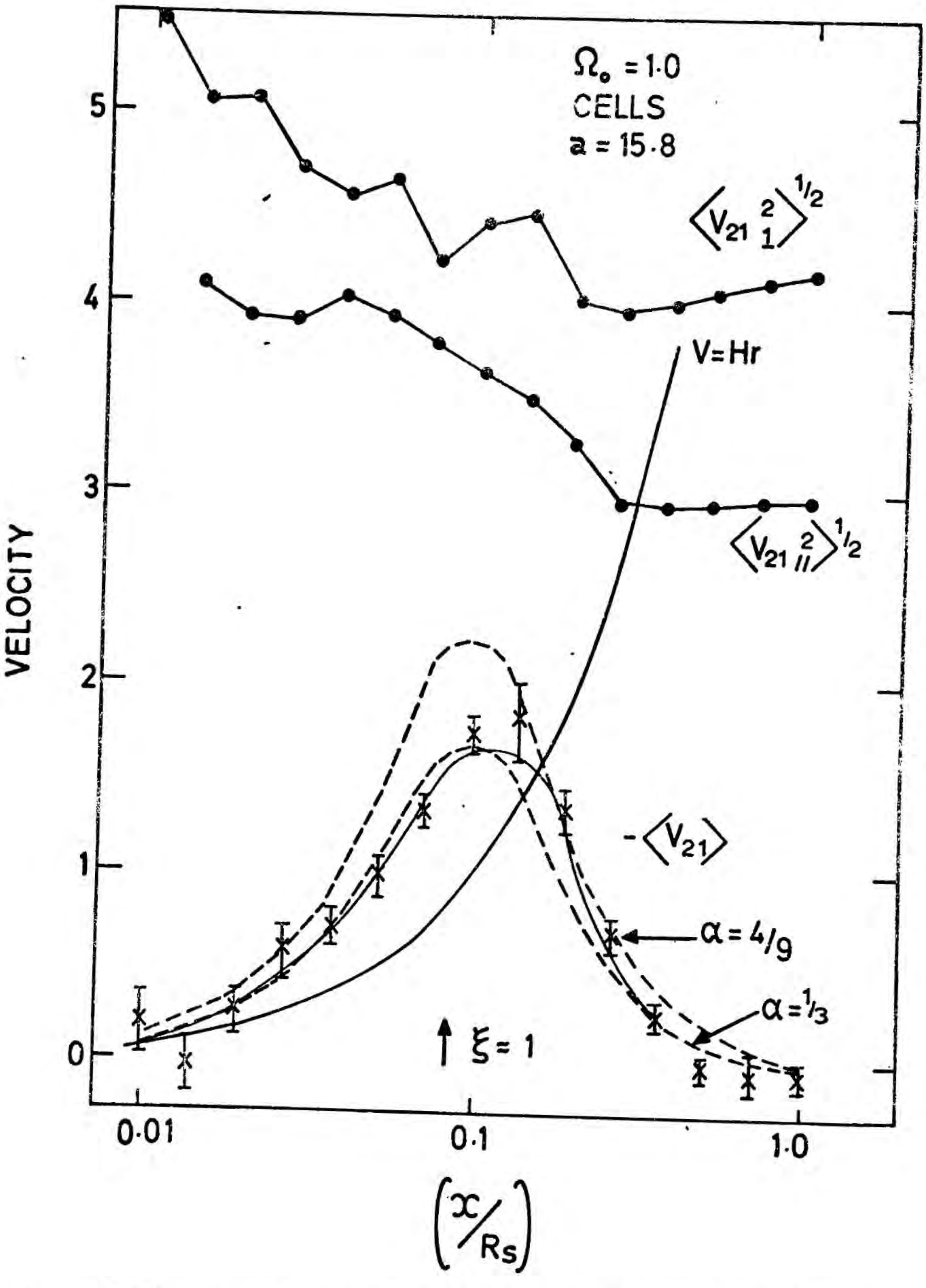

Figure 4.7(b). As for Fig. 4.7(a) except for ensemble 2 at a=15·8. Here are shown the results of integrating equ. (4.35a) using ξ of Fig. 4.7(b) for two values of the "similarity" parameter α.

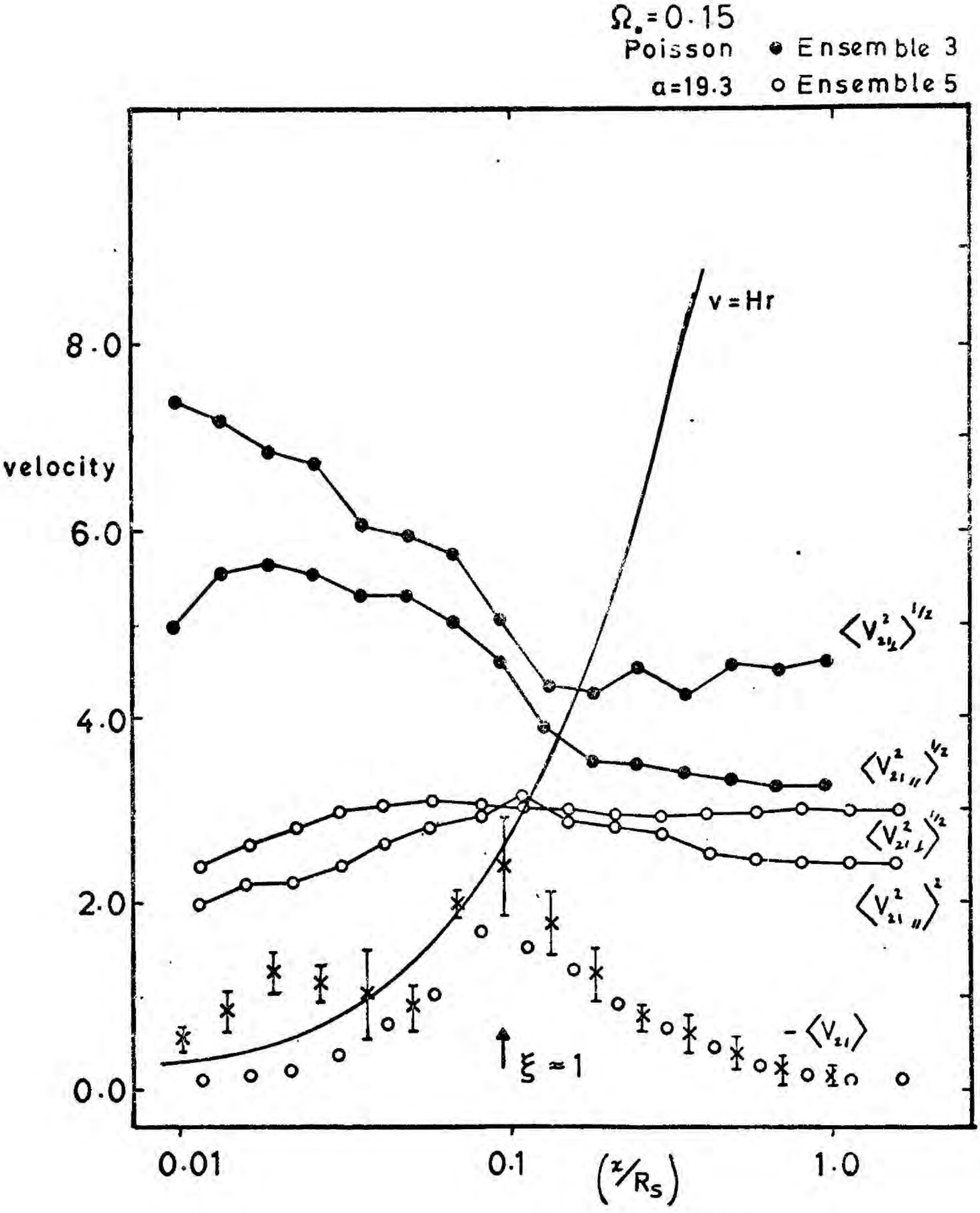

Figure 4.7(c). As for Fig. 4.7(a) except for ensembles 3 and 5 at a=19·3.

contrast to the solutions of DP who find $\langle v_{21}\rangle \sim -\frac{1}{2}H\langle r_{21}\rangle$ when $\xi \sim 1$. This rise in the $\langle v_{21}\rangle$ curve is expected on the basis of equ. (4.33) due to the steepening of ξ for $\xi \lesssim 50$. To show this, I have numerically integrated equ. (4.33) under the assumption of self-similarity.

In section 4.3, it has been argued that the similarity solution may apply over scales corresponding to the transition region $\xi \sim 1$, i.e. $\xi(x,t) \rightarrow \xi(s)$ where $s = x/t^{\alpha}$. In this case equ. (4.33) becomes,

$$-\alpha s \frac{d\xi}{ds} + \frac{1}{s^2}\frac{d}{ds}\left[s^2(1+\xi)\,\hat{v}\right] = 0 \qquad (4.34)$$

where $v(x,t) = t^{\alpha-1}\,\hat{v}(s)$

which may be solved for $\hat{v}$ in terms of ξ or vice versa

$$\hat{v}(s) = \frac{1}{s^2(1+\xi)}\int_0^s \alpha z^3\left(\frac{d\xi}{dz}\right) dz \qquad (4.35a)$$

$$1 + \xi(s) = \frac{K}{s^2(\alpha s - \hat{v}(s))}\exp\left[\int_0^s \frac{3\alpha\, dz}{(\alpha z - \hat{v}(z))}\right] \qquad (4.35b)$$

where K is a constant determined by the condition $\xi \rightarrow 0$ in the limit $s \rightarrow \infty$. The stability assumption $(v = -\frac{2}{3}s)$ in the limit $\xi \gg 1$ gives equ. (4.7a) if the parameter α takes the "similarity" value

$$\alpha = \frac{4}{3(n+3)} \qquad (4.36)$$

A cubic has been fitted by the method of least squares to the points of Fig. 4.6 (a) (minus the first two points from ensemble 4 which are quite obviously affected by the softening parameter), i.e. I have fitted to the form $\log \xi = a_0 + a_1 \log x + a_2 (\log x)^2 + a_3 (\log x)^3$. The parameters a_0, a_1, a_2, a_3 are listed in Table 4.2. The points from ensemble 1 of $\langle v_{21} \rangle$ (Fig. 4.7(a)) have been fitted to a cubic in log x. (The stability condition $v = -Hr$ was imposed at very small scales in order to avoid instability in the fit.) The resulting fit is shown in Fig. 4.7(a). These fits have been used in numerically integrating equs. (4.35) the results of which are shown in Figs. 4.6(a) and 4.7(a). Note that there are no free parameters in the fits and that the agreement is excellent. This exercise serves to illustrate the consistency of the models and in the methods of estimating ξ and $\langle v_{21} \rangle$.

From this analysis it appears that previrialization does not occur in the N-body models and that virialization effects lead to high values of $\xi_{\text{break}} \sim 50$.

One clue as to the effects of discreteness on $\langle v_{21} \rangle$ comes by integrating equ. (4.33) over $d^3\underline{x}$ and using the integral constraint relation equ. (4.27)

$$\langle v_{21} \rangle = -2 \frac{\dot{a}}{a} \frac{\left[1 + 4 \pi n \int_0^{x_0} \xi x^2 \, dx \right]}{n x_0^2 (1 + \xi(x_0))} \qquad \xi(x_0) \ll 1 \qquad (4.37)$$

Table 4.2. Least square cubic fits to ξ

	$\Omega_o = 1$	$\Omega_o = 0{\cdot}15$	$\Omega_o = 1{\cdot}0$
	Poisson, a = 9·9	Poisson, a = 19·8	Cells, a = 15·8
a_o	-2·537	-3·000	-4·415
a_1	-2·957	-2·550	-4·885
a_2	0·092	-0·577	-0·769
a_3	0·119	0·200	-0·0348

Hence as with equ. (4.9), discreteness terms are negligible if $C(x_0) \gg 1$. Equ. (4.37), however, applies only for $\xi(x_0) \ll 1$.

B. Ω =1, Cells distribution

The Cells distribution is set up by having one particle at a random location in each of N contiguous cubical volumes. This distribution corresponds to n = +1 on scales larger than the initial interparticle separation and to n = 0 on smaller scales (Fall, 1978). The two point correlation function for ensemble 2 is shown in Figs. 4.5(b) and 4.6(b) and is seen to be considerably steeper than ξ for the models of ensembles 1 and 4. $\langle v_{21} \rangle$ for ensemble 2 is shown in Fig. 4.7(b) and as in the case of Poisson initial conditions $\langle v_{21} \rangle \sim 2Hr$ on scales corresponding to $\xi \sim 1$. Equ. (4.35) has been integrated using least squares fits to ξ and $\langle v_{21} \rangle$ as in the Poisson case, except that two values of the parameter α have been used: $\alpha = \frac{1}{3}$ corresponding to the similarity solution for n = +1, and α = 4/9 corresponding to n = 0. The results are shown in Figs. 4.6(b) and 4.7(b). The agreement is satisfactory in the case $\alpha = \frac{1}{3}$ but less so using α = 4/9. From these results also, it appears that pre-virialization effects do not occur in the N-body models.

C. Ω = 0·15, Poisson distribution

Figs. 4.5(c) and 4.6(c) show estimates of the two-point correlation function for ensembles 3 and 5.

In the case $\Omega<1$, the similarity solution no longer applies since the clustering hierarchy stops growing at redshifts $z_f = 1/\Omega_0 - 1$, as explained in section 4.5(b). This results in a progressive steepening of ξ for $z < z_f$. Hence ξ for $\Omega_0 = 0\cdot15$ is significantly steeper than in the case $\Omega = 1\cdot0$.

Table 4.2 lists the parameters of the least squares cubic fits to ξ shown as the solid line in Fig. 4.6(c). Fig. 4.7(c) shows $\langle v_{21} \rangle$ for ensembles 3 and 5. Note that on scales corresponding to $\xi \sim 1$ the ratio $\langle v_{21} \rangle / H \langle r_{21} \rangle$ is smaller than in the $\Omega = 1$ case, as would be expected from the argument that led to equ. (4.37), since Δ_g^2 for $\Omega < 1$ grows more slowly than in the case $\Omega = 1$.

D. Comparison with other work

The dependence of the shape of $\xi(r)$ on the cosmological density parameter Ω, discussed above has been confirmed using N-body calculations by Aarseth and Fall (1978, private communication, see Fall, 1979, for graphs of $\xi(r)$) and also by Gott, Turner and Aarseth (1979). Gott et al also find that the shape of $\xi(r)$ is dependent on the initial particle distribution, consistent with the results found here. The main point of disagreement between my results and those of Gott et al is in the detailed shape of the correlation function in the case of Poisson initial conditions and $\Omega = 1$. Gott et al claim that over the observed range $10^4 \gtrsim \xi \gtrsim 1$, their model results can be fitted by $\xi \sim r^{-1\cdot 9}$ with a variation of ± 0·15 in the power law index between different runs.

Since I have analysed results from three independent N-body programs it seems unlikely that the discrepancy is due to numerical errors. The analysis of the $\langle v_{21} \rangle$ curves presented here is consistent with my methods of estimating ξ. It would be of great interest for these authors to construct and analyse ensembles of models and to examine the shape of both $\xi(r)$ and $\langle v_{21} \rangle$ as has been done here. Until this is done it will be difficult to assess the significance of this discrepancy.

My results are, however, consistent with the N-body models of Miyoshi and Kihara (1975) who examined the correlation function over the range $50 \gtrsim \xi \gtrsim 0\cdot 1$ and find $\xi \simeq Ar^{-2\cdot 5}$ in the case of Poisson initial conditions, $\Omega = 1$.

d) Three-point correlation function

The three-point correlation function has been estimated for each of ensembles 1,2 and 3 and are shown in Figs. 4.8(a,b,c). Here the aim is to test whether ζ takes the simple form of equ. (4.4). As a first order approximation I shall take the power-law model for the two-point correlation function $\xi(x) = Ax^{-\gamma}$. In terms of the "shape" parameters u and v and the "size" parameter x equ. (4.4) becomes

$$\zeta(x,u,v) = Q\ A^2 x^{-2\epsilon} \left(u^{-\epsilon} + (u+v)^{-\epsilon} + u^{-} (u+v)^{-\epsilon}\right) \qquad (4.38)$$

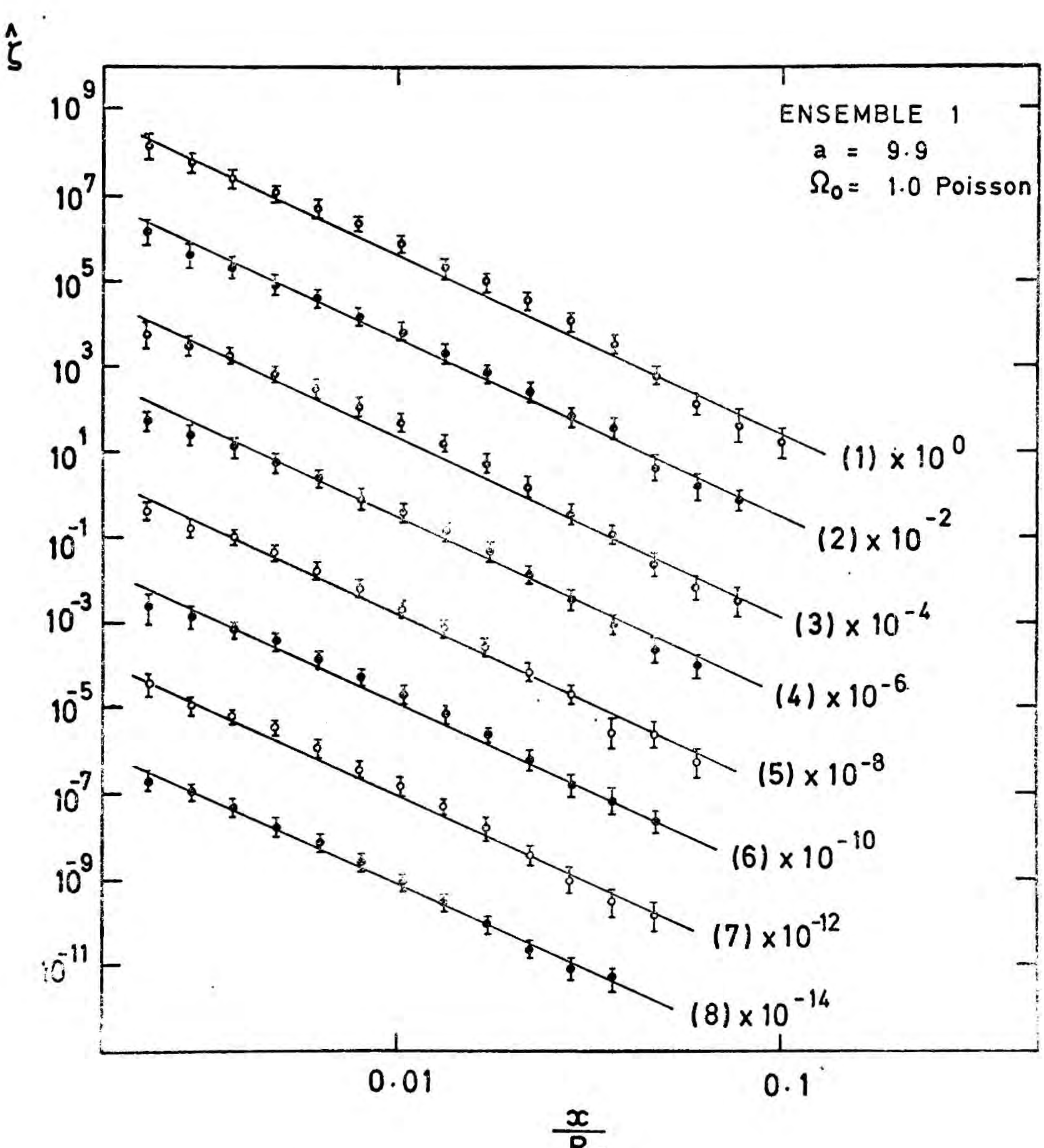

Figure 6.8(a). Estimates of the three-point correlation function for ensemble 1 at a=9·9. The numbers in brackets refer to the u and v bins of table 4.3. For clarity the estimates for each bin in u and v have been multiplied by a factor which is also indicated. The solid lines show the slope 2 from Table 4.4.

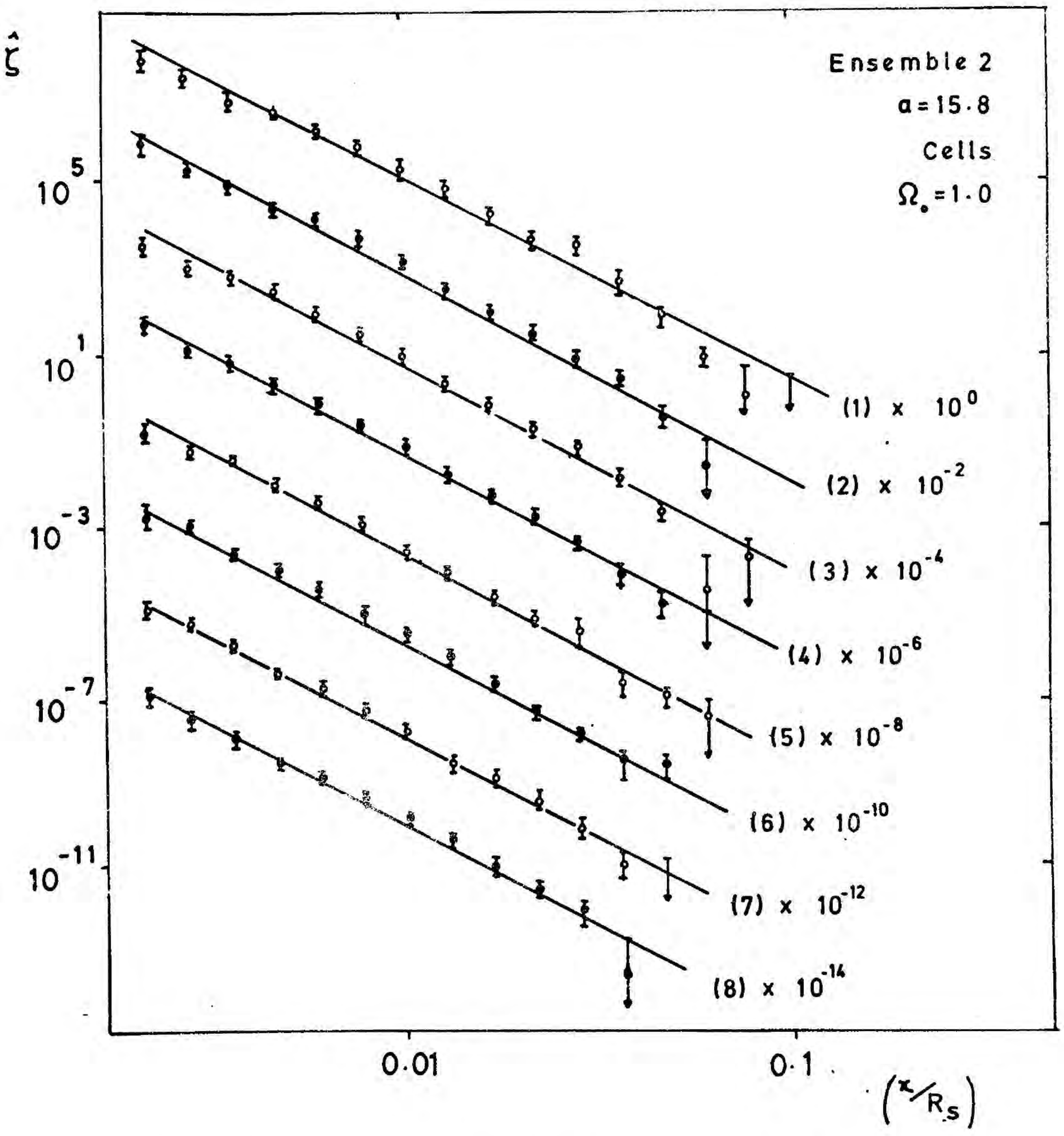

Figure 4.8(b). As for Fig. 4.8(a) except for ensemble 2 at a=15·8.

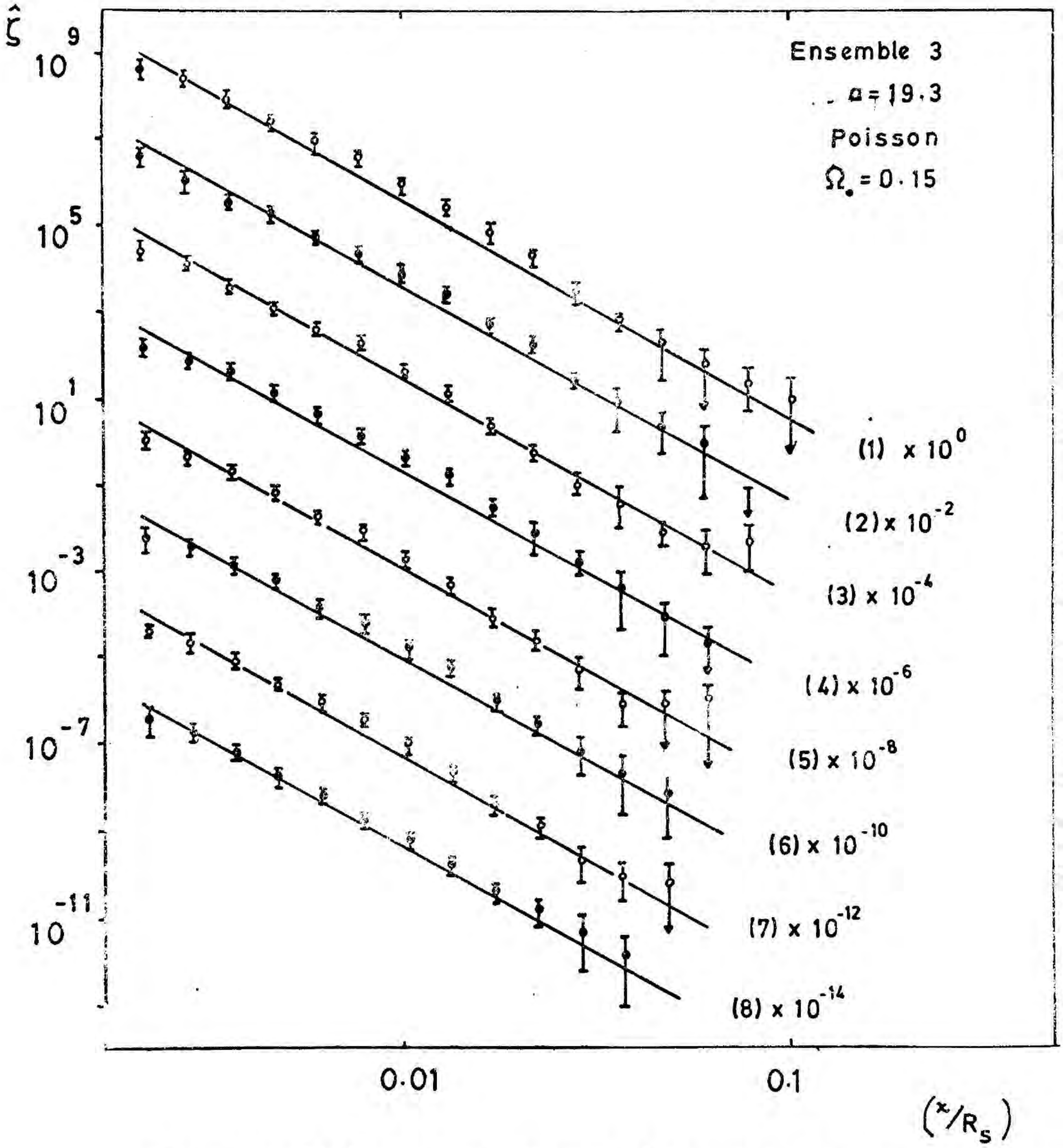

Figure 4.8(c). As for Fig. 4.8(a) except for ensemble 3 at a=19•3.

Least squares power-law fits have been performed to the estimates of ζ shown in Figs 4.8 in order to obtain the slope and amplitude. The amplitude A and slope of the two-point function are also determined by power law least squares fits over the range $0{\cdot}002 \lesssim x/R \lesssim 0{\cdot}1$. The sizes of the u and v bins used in estimating ζ are listed in Table 4.3 and the results of the comparison between ζ and ξ are summarised in Table 4.4. The error on 2γ has been determined from the variation of γ from the models in each ensemble, and the errors on 2ϵ and Q were calculated on the assumption that each u and v bin is statistically independent and are, therefore, likely to be underestimates of the true errors. The results show that the form of ζ is consistent with the simple relation of equ. (4.4) to first order and that this result is not strongly dependent on the initial particle distribution and the cosmological density parameter Ω. This result is in agreement with the results of Gott et al (1979 , in preparation).

The value of Q is found to be unity in good agreement with observations. From the 15th magnitude Zwicky sample and the 10' x 10' Lick counts it is found that $Q = 1{\cdot}3 \pm 0{\cdot}2$. The exact value depends upon the form of the galaxy luminosity function and cosmological model, but probably lies within the range $0{\cdot}8 \lesssim Q \lesssim 1{\cdot}6$ consistent with the N-body models.

In order to ensure a positive dispersion in the

Table 4.3. Range of Shape Parameters

Range of v	Range of u	
$0 < v < 0{\cdot}5$	(1) 1·0 - 1·32	(2) 1·32 - 1·73
	(3) 1·73 - 2·28	(4) 2·28 - 3·0
$0{\cdot}5 < v < 1{\cdot}0$	(5) 1·0 - 1·32	(6) 1·32 - 1·73
	(7) 1·73 - 2·28	(8) 2·28 - 3·0

Table 4.4. Least squares fits to $\hat{\xi}$ and $\hat{\zeta}$.

Ensemble	a	2ϵ	2γ	Q
1	9·9	4·11 ± 0·05	4·1 ± 0·14	1·2 ± 0·1
2	15·8	4·96 ± 0·08	4·8 ± 0·16	0·8 ± 0·1
3	19·3	4·9 ± 0·1	5·0 ± 0·16	1·2 ± 0·1

number of neighbours found within a sphere of given radius r, Q must be greater than $\sim 0{\cdot}3$ (see DP) and the N-body models must certainly obey this physical constraint. On the hierarchical clustering picture Q cannot be too large since particles must satisfy the virial theorem (equ. 4.13) on small scales. Hence it is perhaps not surprising that the N-body models yield values of Q of order unity.

e) Velocity dispersions

Figs. 4.7 (a,b,c) also show the pair velocity dispersions $\langle v_{21\parallel}^2 \rangle = \langle v_r^2 \rangle$ and $\langle v_{21\perp}^2 \rangle = 2 \langle v_t^2 \rangle$ for each of ensembles 1-5. Having established that the models agree roughly with the relation $\zeta \sim Q \xi^2$ the velocity dispersions may be compared with equs. (4.12) and (4.13) from which

$$\langle v^2 \rangle \sim \frac{2Gm}{ax} + \frac{4\pi GmnQM_\gamma x^2 \xi}{a}$$

For ensemble 1, the term $2Gm/r$ is smaller than $\langle v_{21}^2 \rangle$ over most of the length scale shown in Fig. 4.7(a) and that $\langle v^2 \rangle$ is in rough agreement with equ. (4.13), although using $M_{1\cdot 8} = 4{\cdot}2$ results in an overestimate. A detailed comparison is complicated since in these models ξ does not have a simple power law form and the models have a non-negligible softening which would reduce the estimate of $\langle v^2 \rangle$ from that calculated using $M_\gamma = M_{1\cdot 8}$.

I conclude that over most of the range of scales shown in Fig 4.7(a) the velocity dispersions are supported by many particle pairs. The velocity dispersions for ensemble 4 are much lower than those for ensemble 1. This is not surprising, however, since the two-point correlation function for these models is steeper than x^{-2} for $\xi \gtrsim \xi_{break} \approx 50$, hence the dominant contribution to $\langle v^2 \rangle$ arises from clustering on scales where $\xi > \xi_{break}$ and consistent with this, the velocity dispersions remain roughly constant on scales where $\xi < \xi_{break}$. Since a large softening parameter is used in the 20000 body models (of comparable size to the scale at which $\xi = \xi_{break}$) $\langle v^2 \rangle$ will be much lower than in the 1000 body models and this affects all scales larger than the softening parameter. This is to be contrasted with the mean relative peculiar velocity $\langle v_{21} \rangle$ where the contribution from scales $< \langle r_{21} \rangle$ cancels out. It is interesting to note that the velocity dispersions are nearly isotropic on very small and very large scales, but deviate from isotropy (with $\langle v_r^2 \rangle \sim 2 \langle v_t^2 \rangle$) in the transition region $\xi \sim 1$. According to linear theory, on the large scales $\langle v_{21 /\!/}^2 \rangle = \frac{1}{2} \langle v_{21 \perp}^2 \rangle = 2/3 \langle v_1^2 \rangle$ where $\langle v_1^2 \rangle$ is the single particle velocity dispersion, if the correlation function is steeper than x^{-2} on the large scales. This relation holds quite well for the 1000 body models but less well for the 20000 body models.

The results from the other ensembles are shown in Figs. 4.7(b,c) and show the same general behaviour as those from ensembles 1 and 4.

f) Relaxation effects

If discreteness effects are negligible, the correlation functions should be independent of particle masses. In order to test for these effects models have been run (ensembles 6 and 7),in which particles have different masses. The mass distribution used in ensemble 6 was in fact obtained using the final positions of the particles of one 20000 body model of ensemble 4 by replacing all particles within a single cell of a 12 x 12 x 12 mesh by one single particle with mass equal to the number of particles within the cell. This procedure was performed as part of a series of experiments which have not been completed due to a lack of computer time. The mass spectrum resembles quite closely the shape of the multiplicity functions for the case $\Omega = 1$, n=0, (see chapter 5). As in ensemble 1, the particles are distributed pseudo-randomly within a sphere and have zero peculiar velocities.

Fig. 4.9 shows the mass weighted (ξ_m) and number weighted (ξ_n) estimates of the two-point correlation functions. On scales $\xi \lesssim 10$, the two functions are nearly identical but for $\xi \gtrsim 10$ the number weighted function has a noticeably lower amplitude than the mass weighted function. This is just what is expected, since discreteness effects are important on small scales and two-body effects tend to develop core-halo type structures with the more massive particles sitting deeper within the cluster potential well than the less massive particles. The effect is

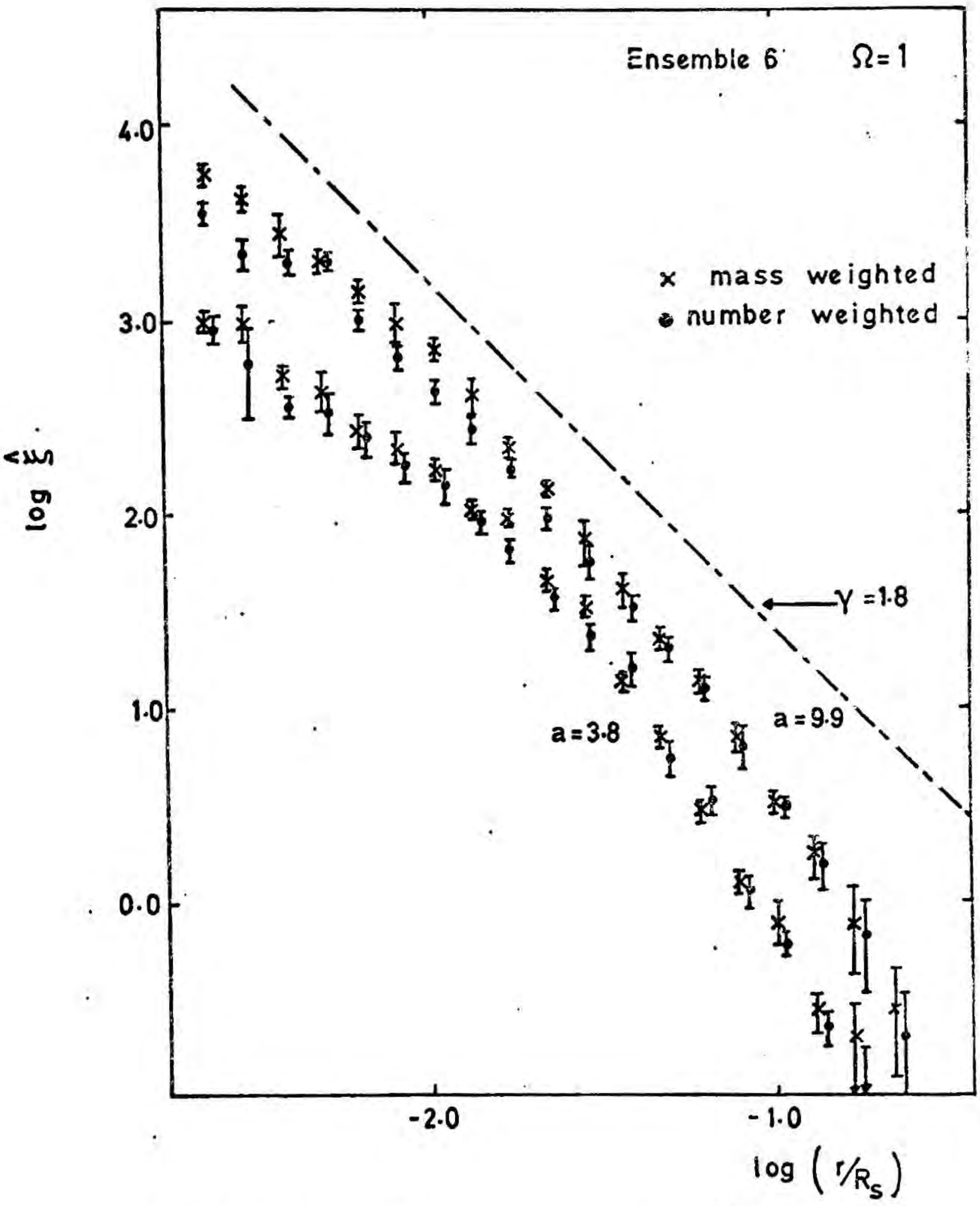

Figure 4.9. Estimates of the number weighted and mass weighted correlation functions for ensemble 6 at two values of the expansion parameter a(t).

quite apparent in pictures of the models (Figs. 4.10a,b).

Recently, Geller and Davis (1978) have used a nearly complete redshift sample (essentially the Shapley-Ames catalogue) to estimate a luminosity weighted correlation function. This is found to be slightly steeper than the number weighted function. The statistical significance of this result is not clear because of the smallness of their sample but the effect is in the right direction to allow an interpretation in terms of mass segregation. It is important to check this result because an implicit assumption in the comparison of most theoretical work with the observational data is that the number weighted functions are true measures of the mass distribution. One important piece of evidence in favour of this is that the three-point function scales as expected in the hierarchical clustering picture (equ. 4.4, see Peebles, 1974c).

The mass segregation effect is more apparent in the calculations of ensemble 7. Here there are 500 particles of unit mass together with 500 particles of zero mass, Poisson initial conditions and zero initial peculiar velocities. Fig. 4.11 shows the autocorrelation function for the massless particles ξ_{mlml}, the autocorrelation function for the massive particles ξ_{mvmv} and the cross-correlation function between massive and massless particles ξ_{mvml}. In this case the two-point functions easily pick out the mass segregation effects, but notice that all three functions converge at large separations.

Figure 4.10(a). X-Y projection of the particle positions for 343 particles with $M > 1$ for one of the models of ensemble 6 after expansion by a factor a=9·9.

Figure 4.10(b). As for Fig. 4.10(a) except for the remaining 654 particles with $M < 1$.

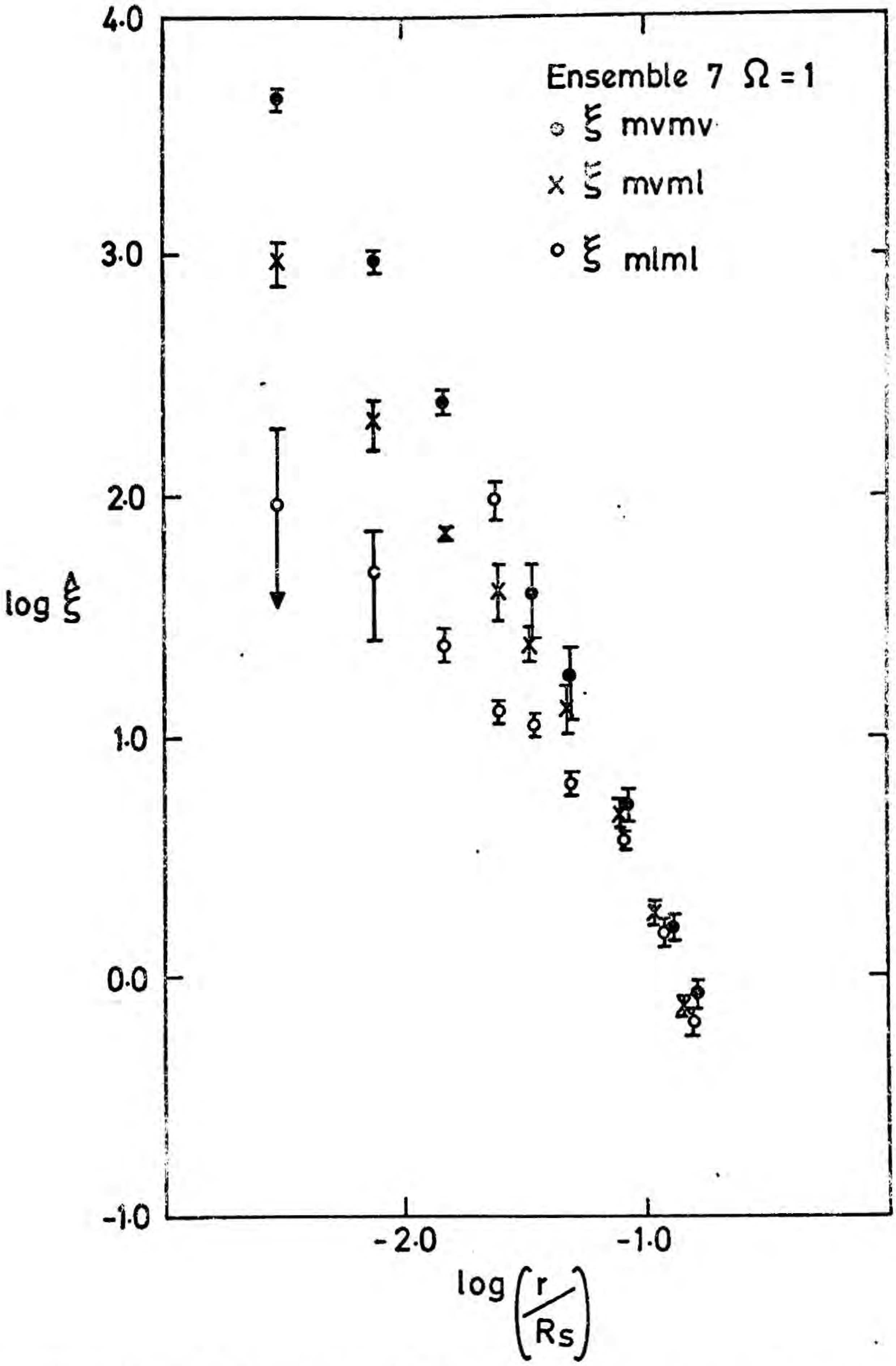

Figure 4.11. Estimates of the autocorrelation function for massive particles ξ_{mvmv}, massless particles ξ_{mlml} and the cross-correlation ξ_{mvml} for ensemble 7 after expansion by a factor a=8·1.

Peebles (1978) has performed N-body calculations to test for the effects of two-body and collective relaxation. As a test for two-body relaxation Peebles included zero mass test particles at the smallest level of a clustering hierarchy and after evolving the system over a Hubble time found no evidence of mass segregation. Peebles' result must not be confused with the result presented here for the experiments differ in an important way. Peebles begins with a highly clustered system in virial equilibrium so that collective interactions dominate on all but the very smallest level of the hierarchy, whereas ensembles 6 and 7 begin with weakly clustered initial conditions.

The effects of relaxation on the shape of the two-point correlation function have been examined in greater detail by Gott, Turner and Aarseth (1979), but whether their results or the results of this chapter have any relevance to the clustering of galaxies in the real Universe is a complicated issue to which I now turn.

4.6 Discussion and Comparison with Observations.

The aim has been to calculate the shape of the two-point correlation function in the transition region $\xi \sim 1$, under the assumptions A-E of section 4.3. Of these, assumption E is particularly worrisome.

The number of clustered galaxies within a radius $r_o \approx 5\ h^{-1}\mathrm{Mpc}$ (corresponding to $\xi(x_o) \approx 1$) is $\langle N \rangle \sim 30$ (taking the mean space density of bright galaxies as

$0{\cdot}02\ h^{-3}\ \mathrm{Mpc}^{-3}$). This number is comparable to the mean number of clustered particles within radius x_0 ($\xi(x_0) \approx 1$) of the particle distributions analysed in section 4.5. Hence, if I am justified in assuming the existence of some epoch z_* when galaxies were weakly clustered and act thereafter as the fundamental point particles, the N-body approach may be applicable. I now explore the consequences of this hypothesis.

Fig. 4.12 shows a comparison of the results from the Poisson models with the observed shape of the angular covariance function $w(\theta)$. Here, Limber's equation has been numerically integrated using the least squares cubic fits to $\xi(x)$ listed in Table 4.2 assuming the galaxy luminosity function of Peebles and Hauser (1974). The data points are taken from Fig. 2 of Davis, Groth and Peebles (1978) where they performed a similar exercise using the BBGKY solutions of Davis and Peebles which are in good agreement with the analysis of the Lick counts (Groth and Peebles, 1977) shown as the open circles in Fig. 4.12.

As can be seen the $\Omega = 1$, $n = 0$ curve deviates significantly from the data points on scales $\theta D^* \gtrsim 1\ h^{-1}\mathrm{Mpc}$ and is clearly incompatible with the observations.

The cause of this discrepancy has a simple physical explanation. The $\langle v_{21} \rangle$ curve is found to rise above the Hubble line Hr on scales corresponding to the transition region $\xi \sim 1$. This type of effect has been discussed by Gott and Rees (1975) on the basis of the homogeneous

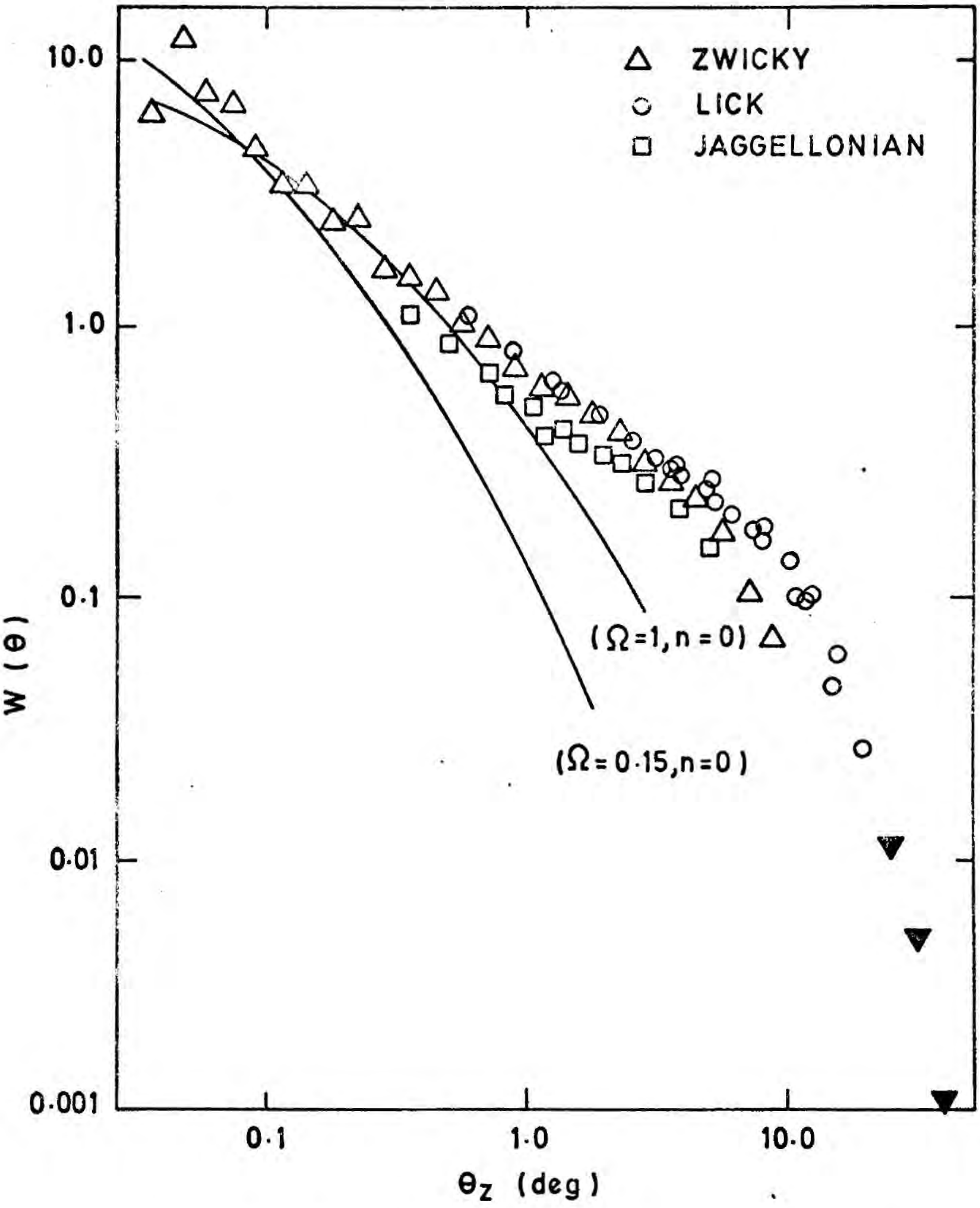

Figure 4.12. Results of projecting the least squares fits of Table 4.2 in the cases $\Omega_0=1\cdot0$, $\Omega_0=0\cdot15$ with Poisson initial conditions. The data points are taken from Fig. 2 of Davis, Groth and Peebles (1977) and the reader is referred to their paper for observational details.

spherical cluster model, and is due to radial infall as the clusters collapse in order to generate enough kinetic energy to satisfy the virial theorem. Whilst the spherical cluster picture is undoubtedly over-simplified, apparently these virialisation effects are present in the N-body models, which cause ξ_{break} to occur at large values of ξ (roughly $\xi_{\text{break}} \simeq 50$).

From Fig. 4.12 it can be seen that the $\Omega = 0{\cdot}15$, $n=0$ curve is an even worse fit to the data, since $\xi(r)$ for these models has a significantly steeper slope than for the $\Omega = 1$, $n=0$ models. One might ask whether an open model with $n < 0$ could be consistent with the data. Gott and Rees (1975) have suggested that $\Omega = 0{\cdot}1$, $n = -1$ may be compatible with the observations and Fall (1979) has argued the case for $\Omega = 0{\cdot}1$, $n \gtrsim -1{\cdot}7$. The problem is very complicated and even a direct N-body approach is not easy because of practical difficulties in setting up an initial particle distribution with the desired power spectrum. Nevertheless, the N-body models of Gott, Turner and Aarseth (1979) serve to illustrate that the low-density cosmological models require $n \lesssim -1$. However, if the observation of the sharp change in slope at $\theta D^* \sim 9\ h^{-1}$ Mpc is correct, it would be difficult to reconcile with gravitational instability in a low density cosmological model with a power law spectrum of fluctuations, since according to linear theory (equ. 4.7b) $\xi \propto x^{-(n+3)}$ for $\xi \ll 1$. In any case, the assumption of a power law spectrum of perturbations (equ. 1.6) with $n \lesssim -1$ must fail because the correlation potential energy $\hat{W}$ and the mean square relative velocities $\langle v_t^2 \rangle$ and $\langle v_r^2 \rangle$ diverge at large separations, i.e. there must exist a break in the power spectrum on large scales if $n \lesssim -1$ (c.f. Fall, 1975).

Now consider the alternative case in which the clustering has always been non-linear on small enough scales, so that the fundamental point particles may be taken to have a very much smaller mass than is typical of a bright galaxy. I have argued in section 4.2 that these are, perhaps, more realstic initial conditions. This represents the case studied by Davis and Peebles who find quite different results to those found here.

Their solutions yield $\xi_{\text{break}} \sim 0{\cdot}3$ for $\Omega = 1$ due to pre-virialization effects and the predictions agree remarkably well with the observations including the change in slope at 9 h^{-1}Mpc. If Davis and Peebles have correctly modelled the clustering process then this is evidence for gravitational instability in a dense universe.

The problem is of such fundamental importance that it is natural to ask whether the results from the N-body models discussed here may be applied in this case. The ability to make predictions in this context is severely limited due to the discreteness problem discussed in sections 4.3 and 4.5. I have suggested that particle discreteness may not be important in the transition region $\xi \sim 1$ but the argument is hardly convincing. Put another way, the N-body models develop clusters which contain typically $\sim$ 30 particles (c.f. Fig. 4.1b). I would be much happier if this number were in the hundreds but unfortunately this would require an excessive amount of computer time.

The fact that the discrepancy between the BBGKY approach and that presented here is so great does indicate that an alternative approach (e.g. Fry and Peebles, in preparation) would be worthwhile and of considerable interest.

CHAPTER 5

OTHER MEASURES OF GALAXY CLUSTERING

5.1 Introduction.

The empirical results reviewed in chapter 4 indicate that the two-point correlation function has a power law form with no preferred scale in the range $0{\cdot}1h^{-1}$ - $9h^{-1}$ Mpc. The estimates for the three- and four-point correlation functions obey the simple relations of equs. (4.4, 4.5) and this has been suggested as evidence that the galaxy distribution is hierarchical (e.g. Soneira and Peebles, 1978). The power law form of $\xi(r)$ suggests that the hierarchy is self-similar and that it represents a fractal of dimension $D = 3 - \gamma \simeq 1{\cdot}2$ in Mandelbrot's (1977) terminology.

The suggestion is often made that a self-similar distribution of matter arises most naturally in the gravitational instability picture for the development of structure in the Universe because the gravitational force-law itself has no preferred scales. But there are still several possiblities:

A. The present distribution reflects initial conditions, but the initial conditions were scale free: as for example, with a power law spectrum of isothermal fluctuations at recombination (equ. 1.6).

B. The present distribution reflects the tendency for the matter to evolve, by relaxation and disruption processes to a self-similar form which is independent of initial conditions (Press and Lightman, 1978;

Silk and White, 1978).

C. Galaxy clustering may be neither self-similar nor hierarchical and the low order angular correlation functions do not shed much light on the issue because they are not sensitive discriminators between different models of galaxy clustering (Shanks, 1979).

The discussion of the previous chapter at least serves to illustrate the complexity of the problem, even within the framework of the gravitational instability picture.

In an attempt to answer some of these problems several new statistics have been applied to galaxy clustering. These are:

i The "multiplicity function" or (differential) mass distribution for the groups of galaxies (Press and Schechter, 1974; Gott and Turner, 1977).

ii The statistic of Bhavsar (1978) which relates the fraction of single galaxies in a group catalogue as a function of density contrast.

iii Mead's analysis, as applied by Shanks (1979).

The main topic of this chapter is the multiplicity function. In section 5.2 we rederive Press and Schechter's expression for the multiplicity function and we make precise the notion of self-similarity. In section 5.3 we present the results from the analysis of some N-body models of chapter 4, and in section 5.4 we briefly describe the connection between the multiplicity function and related functions, such as those of Bhavsar, for the projected distribution of galaxies on the sky. The main conclusions are summarised in section 5.5.

5.2 Theory.

Our starting point is the idea that the distribution of matter in space can be described by a family of 'group catalogues' at different density contrasts. By analogy with Turner and Gott's (1976) prescription, we define a group catalogue $\mathcal{C}(\delta)$ to be all regions of space ("groups") which are specified by some rule and within which the mean mass density is $\rho\delta$ (where ρ is the mean cosmological density). The rule for finding groups is arbitrary, so long as each catalogue contains all matter, but it must be the same for all catalogues of the family in order that the nesting property

$$\delta_1 > \delta_2 \iff \mathcal{C}(\delta_1) \subset \mathcal{C}(\delta_2) \qquad (5.1)$$

be satisfied. The boundaries of the catalogue $\mathcal{C}(\delta)$ at different δ make a contour map of the matter distribution and the topology of the boundaries gives an indication of how hierarchical the distribution is (Fig. 5.1).

It will now prove useful to define a 'nesting kernal' p such that $p(m_1, \delta_1, | m_2, \delta_2)\, dm_1$ is the probability that a group of mass m_2 in the catalogue

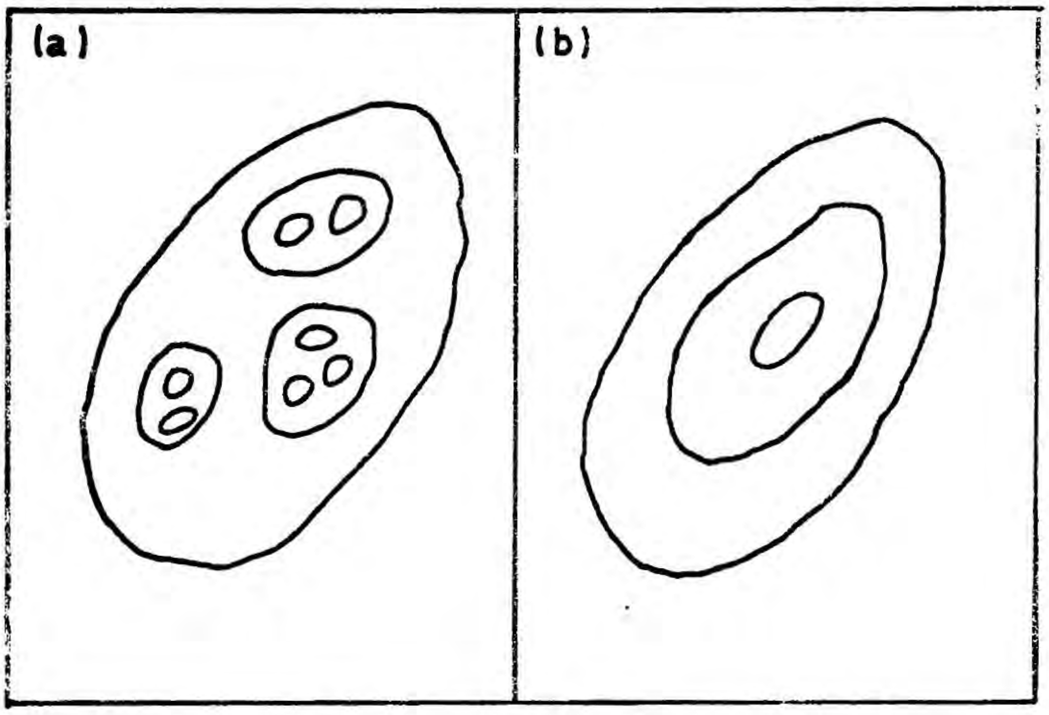

Figure 5.1. Group catalogues at different density contrasts: (a) hierarchical distribution, (b) non-hierarchical distribution. If the distributions are stable in the sense of equ. (5.9) they will remain self-similar during the evolution of clustering. If, on the other hand, relaxation, disruption and merging effects are important, a distribution like (a) might evolve to one like (b).

$\mathcal{C}(\delta_2)$ contains a group in the mass interval (m_1, m_1+dm_1) in the catalogue $\mathcal{C}(\delta_1)$. Of course p must vanish for $m_1 > m_2$ and $\delta_1 < \delta_2$. For consistency it must satisfy the relation

$$p(m_1, \delta_1 \mid m_2, \delta_2) = \int dm\, p(m_1, \delta_1 \mid m, \delta)\, p(m, \delta \mid m_2, \delta_2) \tag{5.2}$$

for all δ such that $\delta_1 > \delta > \delta_2$. A necessary condition for the matter distribution to be self-similar under change of scale is that p satisfy the relation

$$p(m_1, \delta_1 \mid m_2, \delta_2) = kp(km_1, k^{\epsilon}\delta_1 \mid km_2, k^{\epsilon}\delta_2) \tag{5.3}$$

for some ϵ and all positive k. (A sufficient condition would require that the relative locations of groups also be invariant under change of scale.) The exponent ϵ in equ. (5.3) is related to the fractal dimension D of the matter distribution by the following dimensional expressions (with fixed mean density)

$$\begin{aligned} [\text{mass}] &= k^{-1}, \quad [\text{density}] = k^{-\epsilon} \\ [\text{mass}] &= [\text{length}]^{3/(1-\epsilon)} = [\text{length}]^{D} \end{aligned} \tag{5.4}$$

The multiplicity function η is defined such that

$\eta(m, \delta)dm$ is the mean space density of groups in the mass interval (m,m+dm) in the catalogue $\mathcal{C}(\delta)$. The scaling relation equ. (5.3) for p can now be used to derive a scaling relation for η. From the definitions η must satisfy the following equations

$$\begin{aligned} \eta(m_2, \delta_2) &= \int dm_1\, \eta(m_1, \delta_1) p(m_1, \delta_1 \mid m_2, \delta_2) \\ \rho &= \int dm\, m\, \eta(m, \delta) \end{aligned} \qquad (5.5)$$

Together, these equations require that the scaling relation

$$\eta(m, \delta) = k^2 \, \eta(km, k^{\epsilon} \delta) \qquad (5.6)$$

be satisfied because ρ is independent of δ.

Eliminating k, we thus have the result

$$\eta(m, \delta) = m^{-2} \, g(m \, \delta^{-1/\epsilon}) \qquad (5\cdot7)$$

$$\epsilon = 1-3/D = -\gamma/(3-\gamma) \approx -1\cdot5 \qquad (5.8)$$

where g is an arbitrary dimensionless function.

Let us now consider the evolution of η. We imagine the construction of a family of group catalogues $\mathcal{C}(\delta, t)$ at different proper times t and let $\eta(m, \delta, t)dm$ denote the comoving space density of groups in the catalogue $\mathcal{C}(\delta, t)$ with masses in the interval (m,m+dm). The simplest case is that in which the matter distribution is stable in the sense that groups, once formed, are not altered during the evolution. In this case η must depend on δ and t only through the product $\delta a^{-3}(t)$, where a(t) is the cosmological scale parameter; thus

$$\eta(m, \delta, t) = m^{-2} g(m \delta^{-1/\epsilon} a^{3/\epsilon}) \qquad (5.9)$$

In this case, the distribution is also self-similar in time if ϵ is constant. Of course, this generalised scaling relationship can only be expected to hold at density contrasts high enough ($\delta > \delta_{min}$) to guarantee that groups have reached their equilibrium ('virialised') density. This should depend sensitively on the cosmological density parameter, roughly as $\delta_{min} \gtrsim \Omega^{-3}$ (cf. section 4.4) and may preclude the applicability of equ. (5.9) over much of the range of interest ($1 \lesssim \delta \lesssim 10^3$) if Ω is small. We can now recover the Press-Schechter (1974) multiplicity function as a special case of equ. (5.9) with some additional assumptions. These are: the background cosmology is Einstein-de Sitter ($\Omega = 1$, $a \propto t^{2/3}$), the growth rate is determined by linear theory, and the initial power spectrum (at recombination, say) had power law form ($\langle|\delta\rho/\rho|^2\rangle^{\frac{1}{2}} \propto m^{-\frac{1}{2}-n/6}$). In this case, η must depend on m and t only through the dimensionless combination $m/m_c(t)$ where m_c is the mass-scale which is just beginning non-linear ($\delta \gtrsim 1$) condensation: $m_c(t) \propto t^{4/(3+n)}$. Thus

$$\eta(m, \delta, t) = m^{-2}\, G_n \left[(m/m^*)\ (t/t_0)^{2/\epsilon}\ \delta^{-1/\epsilon} \right] \qquad (5.10)$$

$$\epsilon = -\tfrac{1}{2}(3+n) \qquad (\Omega = 1 \cdot 0) \qquad (5.11)$$

where m^* is the current marginally non-linear mass scale $m_c(t_0)$ and G_n is a function determined only by the initial distribution of perturbations. Assuming that the distribution of group masses is directly related to the initial distribution of densities in randomly sampled volumes, the Gaussian approximation applies and we have

$$G_n(x) \propto x^{\frac{1}{2}+n/6} \exp(-x^{1+n/3}) \qquad (5.12)$$

(Balko, 1971). Equ. (5.12) is equivalent to Peebles' (1974b) scaling relation (equ.4.5) which predicts $n \gtrsim 0$ for $\gamma \approx 1 \cdot 8$ and $\Omega \approx 1 \cdot 0$. Press and Schecter derived equs (5.10)-(5.11) for a fixed density contrast $(\delta \simeq 10)$ and noted that η evolves self-similarly as a consequence of the assumed initial conditions. The stability assumption equ. (5.9) allows us to generalise their formula to other density contrasts provided that relaxation, disruption and virialisation effects are negligible. We note that approximation (5.12) for G_n has never been fully justified in the context of group catalogues but the power law part is almost certainly correct even if the exponential part is not (Schechter, 1976a).

The scaling relation, equ. (5.9) cannot be expected to hold over a large range of density contrasts if Ω is small. This is because there is now a preferred time at which linear perturbations stop growing, corresponding roughly to $z_f \sim 1/\Omega_0 - 1$ (cf. section 4.5). A simple but crude way to modify the scaling relations for $\Omega < 1$ is suggested by the steepening effect of the correlation function (Gott and Rees, 1975, and section 4.4). As in section 4.4 we assume that the $\Omega = 1$ arguments hold approximately up to the time $t_f \simeq \Omega t_0$ with t_f replacing t_0 in equ. (5.10) with the scaling exponent ϵ_f given approximately by equ. (5.11). Furthermore, we assume that linear perturbations ($\delta \lesssim 1$) do not grow at later times and that the stability argument equ.(5.9) holds for all perturbations with $\delta \gtrsim \delta_v$ (say) at time t_f: thus

$$\begin{aligned} \eta(m,1,t) &\approx \eta(m,1,t_f) = m^{-2}\, G_n\left[(m/m*)\right] \\ \eta(m,\Omega^{-3}\delta_v,t) &\approx \eta(m,\delta_v,t_f) \\ &= m^{-2} G_n\left[(m/m*)\,\delta_v^{-1/\epsilon_f}\right] \end{aligned} \qquad (5.13)$$

Extrapolating between these regimes with a power law of exponent ϵ_e now gives

$$\eta(m,\delta,t) \approx m^{-2}\, G_n\left[(m/m*)\,\delta^{-1/\epsilon_e}\right] \qquad (5.14)$$

$$\epsilon_e \approx -\tfrac{1}{2}(3+n)\log(\delta_v/\Omega^3)/\log\delta_v \qquad (5.15)$$

$$(1 \lesssim \delta \lesssim \Omega^{-3})$$

where $\Omega(t)$ is the instantaneous density parameter, δ_v is a parameter (cons $\delta_v \simeq 1 - 2\text{x}10^2$) and G_n is given by equ. (5.12).

The proposed scaling relation (5.14)-(5.15) reduces to the Press-Schechter form (5.10)-(5.11) for $\Omega = 1$ and is equivalent to the correlation function scaling relation of Fall (1979, equ. 65) with δ_v replacing ξ_v. The matter distribution described by equ. (5.14) is, by construction, spatially self-similar over the range of scales to which it applies; but its evolution is not self-similar because the fractal dimension $D \gtrsim 3/(1-\epsilon_e)$ is time dependent. Finally, for a fixed density contrast, the (logarithmic) slope of η at small m (-3/2+n/6) is independent of Ω and therefore, independent of time, This last property is not unique to our model and, in principle, makes the multiplicity function an attractive cosmological probe. The properties listed above are clearly desirable on physical grounds but, of course, the power-law extrapolation must be considered only as an approximation. The main justifications for it are the empirical evidence for a self-similar distribution of galaxies and the approximately power-law form of the correlation functions in the low density N-body models described in the preceeding chapter.

5.3 N-body Experiments.

In order to check this description of clustering, or at least to check for consistency, we have analysed some of the N-body simulations of chapter 4. In addition to the standard experiments, two of the experiments were of the Freeze type (one Poisson and one Cells, $\Omega = 1$) with the same initial particle positions as two standard experiments. (These are the four experiments discussed in Fall, 1978, models 5D, 13E, 22D, 23E here). In the Freeze experiments, the motions of particles within condensed aggregates were artificially stopped in order to assess their influence on the development of clustering. The experiments have been summarised in Table 4.1.

In comparison of theory with experiment it is often convenient to work with the cumulative function

$$\hbar(m,\delta) \quad \frac{\int_0^m d\mu\, \mu\, \eta(\mu,\delta)}{\int_0^\infty d\mu\, \eta(\mu,\delta)} \qquad (5.16)$$

According to the arguments of the previous section, $\hbar$ is given by

$$\begin{aligned} \hbar(m,\delta) &= H\left[(m/m*)^{1+n/3}\, \delta^{-(1+n/3)/\epsilon}\right] \\ H(x) &= \frac{1}{\sqrt{\pi}} \int_0^x dy\, y^{-\frac{1}{2}} \exp(-y) \end{aligned} \qquad (5.17)$$

with ϵ given by equs (5.11) or (5.15) depending on the value of Ω. Because so few rich groups develop in the N-body experiments, we have no hope of testing for the exponential cut off and therefore work with the small mass approximation

$$h(m, \delta) \simeq \frac{2}{\sqrt{\pi}} \quad (m/m^*)^{\frac{1}{2}+n/6} \, \delta^{-(\frac{1}{2}+n/6)/\epsilon} \qquad (5.18)$$

The function has been estimated for each of the N-body experiments using the formula

$$\hat{h}(m, \delta) = \sum_{\mu=1}^{m} \mu \hat{\eta}(\mu, \delta) \Big/ \sum_{\mu=1}^{\infty} \mu \hat{\eta}(\mu, \delta) \qquad (5.19)$$

where $\hat{\eta}(\mu, \delta)$ is the number of groups with μ members at density contrast δ .

From the theory, we expect

$$\begin{array}{ll} \hat{\eta}(m) \propto m^{-1-\alpha} & \\ & \alpha = \begin{cases} \frac{1}{2} \text{ (Poisson)} \\ \frac{1}{3} \text{ (Cells)} \end{cases} \\ \hat{h}(m) \propto m^{1-\alpha} & \end{array} \qquad (5.20)$$

Groups were identified using an algorithm similar to that of Press and Schechter and unless otherwise stated, the density contrast criterion was δ = 10. Some of the results are shown in Figs. 5.2-5.5. Note that in Figs. 5.2 and 5.3, the function $\hat{h}(m)$ rapidly develops a self-similar form.

The cumulative function $\hat{h}$ is generally steeper in the Cells experiments than in the Poisson experiments as would be expected from equ. (5.20). However, there is considerable experiment by experiment variation in

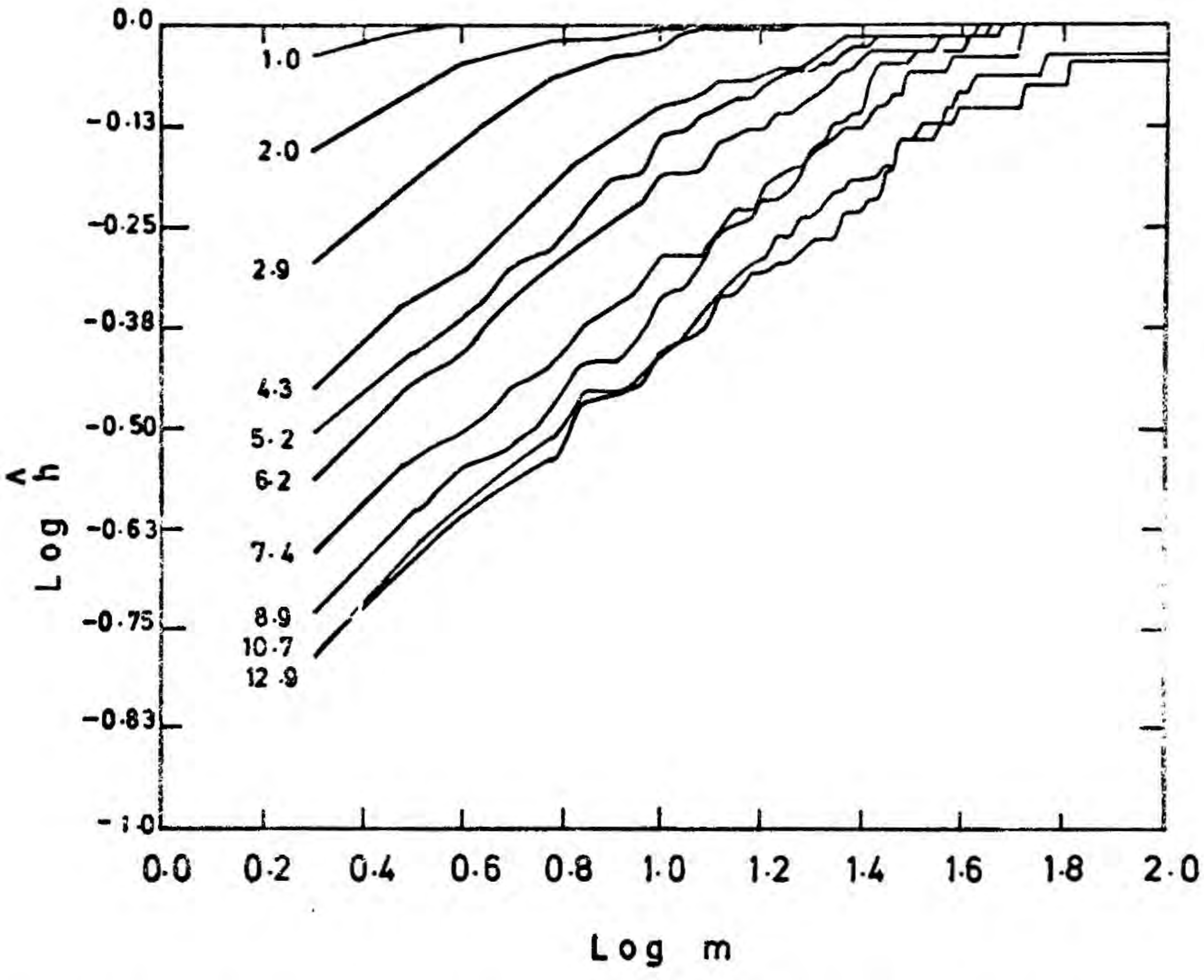

Figure 5.2. Evolution of the multiplicity function at $\mathcal{E} = 10$ for model 5D (Standard, Poisson). Numbers at the left are expansion parameters.

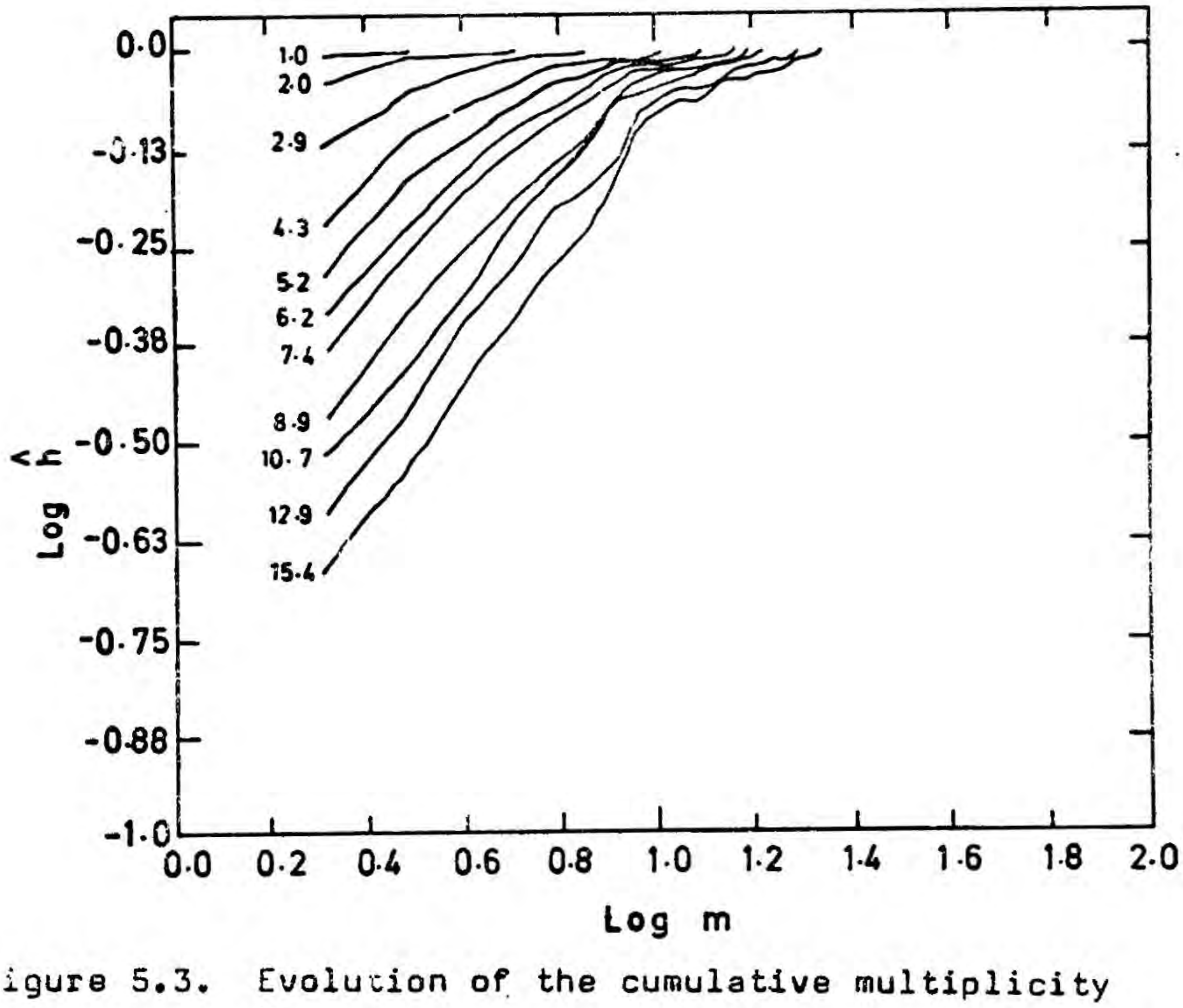

Figure 5.3. Evolution of the cumulative multiplicity function at δ = 10 for model 13E (Standard, Cells). Numbers at the left are expansion parameters.

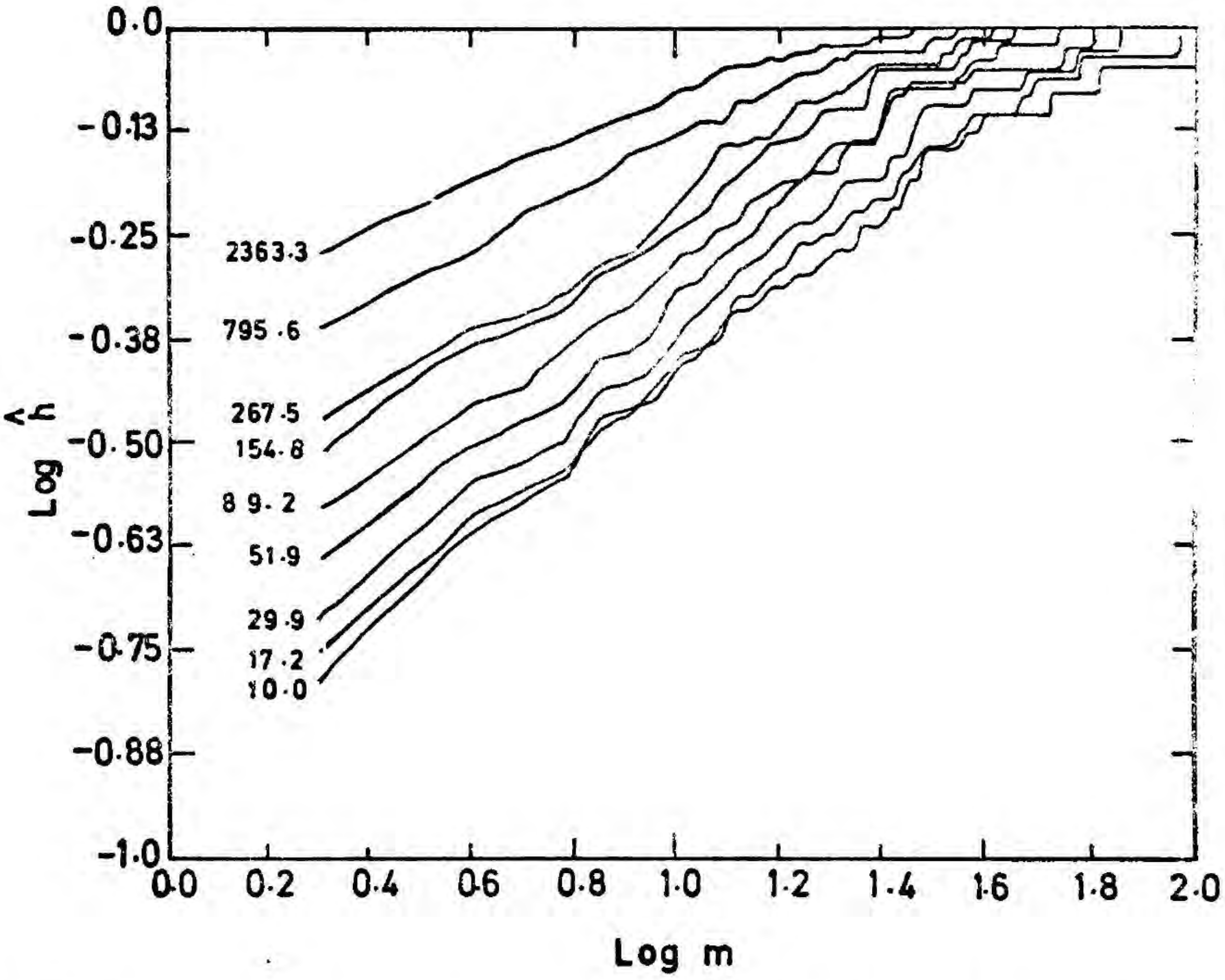

Figure 5.4. Density and time dependence of the cumulative multiplicity function for model 5D. Numbers at the left are density contrasts. Compare with equs. (5.9), (5.22) and Fig. 5.2.

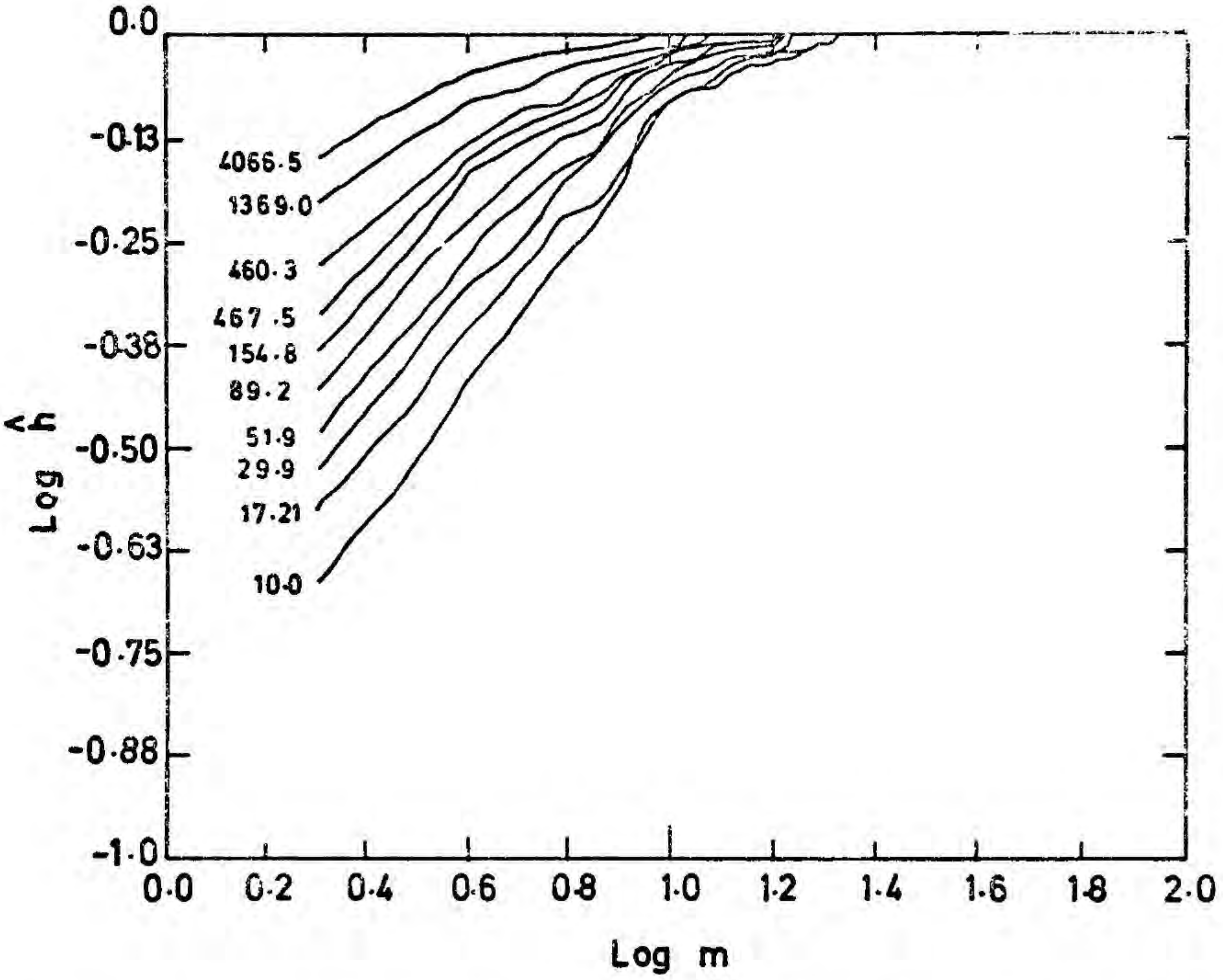

Figure 5.5. Density and time dependence of the cumulative multiplicity function for model 13E. Numbers at the left are density contrasts. Compare with equs. (5.9), (5.22) and Fig. 5.3.

the results even for models with statistically similar initial conditions. Least squares power-law fits to $\hat{h}$ for $4 \leqslant m \leqslant m(75 \text{ percent})$ give the results shown in Table 5.1. They are consistent with theory, with the closed models showing better agreement than the open models. Fitting to a cumulative distribution can be deceptive and we have, therefore, used the method of maximum likelihood to estimate α directly from the differential distribution $\hat{\eta}$. The results are

$$\alpha = 0{\cdot}65 \begin{array}{l} + 0{\cdot}15 \\ - 0{\cdot}17 \end{array} \quad (\text{Poisson}, \Omega_0 = 1{\cdot}0,\ a = 10{\cdot}8)$$

$$\alpha = 0{\cdot}74 \begin{array}{l} + 0{\cdot}25 \\ - 0{\cdot}27 \end{array} \quad (\text{Poisson}, \Omega_0 = 0{\cdot}15,\ a = 19{\cdot}3)$$

$$\alpha = 0{\cdot}29 \begin{array}{l} + 0{\cdot}21 \\ - 0{\cdot}24 \end{array} \quad (\text{ Cells}, \Omega_0 = 1{\cdot}0,\ a = 15{\cdot}8)$$

(5.21)

when all experiments with the same kind of initial conditions and cosmological density parameters are combined. The errors correspond to values of α at which the likelihood function has dropped by a factor of $\exp(-\frac{1}{2})$ from its maximum value. The results are consistent with theory and show a dependence on the initial distribution, but only at about the 2σ level of statistic statistical significance.

Press and Schechter (1974) did two 1000 body experiments, one Poisson and one Cells, with $\Omega = 1$. At early times, the experiments showed good agreement with

Table 5.1. Least squares fits to $\hat{h}$ and $\hat{\xi}$.

Model	a	α(expt)	α(theory)	γ (expt)
1A	10·8	0·60	$\frac{1}{2}$	1·87
2B	10·8	0·47	$\frac{1}{2}$	2·26
3C	10·8	0·43	$\frac{1}{2}$	2·22
4	10·8	0·37	$\frac{1}{2}$	2·24
5D	10·7	0·48	$\frac{1}{2}$	2·13
7A	19·3	0·62	$\frac{1}{2}$	2·34
8B	19·3	0·62	$\frac{1}{2}$	2·61
9C	19·3	0·54	$\frac{1}{2}$	2·65
10	15·8	0·50	$\frac{1}{3}$	2·24
11	15·8	0·33	$\frac{1}{3}$	2·42
13E	15·8	0·21	$\frac{1}{3}$	2·33
22D	10·8	0·65	$\frac{1}{2}$	2·13
23E	15·8	0·26	$\frac{1}{3}$	2·39

Notes:

The expansion parameter at which the estimates were made is denoted a (with $a_s = 1$, initially). The density contrast criterion was $\delta = 10$ in determining the multiplicity function. Also listed is the slope of the two-point correlation function ξ for each model. The fits to $\hat{\xi}$ were made over the range $10^4 \geqslant \hat{\xi} \geqslant 1$, (cf. Figs. 4.5).

the theoretical predictions but, at later times, the behaviour of the Cells experiment approached that of the Poisson experiment. In particular, the 80th percentile mass increased as a^2 in both experiments at late times. By way of comparison, the theory predicts $m_c \propto \Delta_g^{6/(3+n)}$ for the marginally non-linear mass scales ($\delta \sim 1$) where Δ_g is the usual growth factor of linear theory (equ. 4.29). This led Press and Schechter to the 'bootstrap' conjecture where it was supposed that some sort of non-linear effect was to blame. Fig. 5.6 shows the growth of the 80th percentile mass in our experiments. There seems to be a significant dependence on n and Ω , with the Poisson experiments in good agreement with theory. The Cells experiments, however, appear to have a dependence even weaker than $a^{3/2}$. It may well be that both this result and that of Press and Schechter are explained by the variation in similar experiments discussed above. At this stage, we see no need to invoke the bootstrap hypothesis.

Another interesting result is that the multiplicity functions for the Freeze experiments are remarkably similar to those for the corresponding Standard experiments at $\delta = 10$. This shows that the internal evolution of groups is not important in the evolution of the multiplicity function at low density contrasts.

The scaling arguments of Section 5.2 suggest a way to test for stability at higher density contrasts. If the matter distribution is stable, the cumulative multiplicity function should satisfy the relation

$$h(m, \delta_1, t) = h(m, \delta_2, t_2) \text{ for } a(t_1)\,\delta_1^{-\frac{1}{3}} = a(t_2)\,\delta_2^{-\frac{1}{3}} \tag{5.22}$$

This has been checked for the models and the results are shown in Figs. 5.4 and 5.5 for models 5 and 13 with $a(t_2)$ equal to the final expansion parameter. The expansion parameters and density contrasts have been chosen so that Figs 5.4 and 5.5 should be identical with Figs. 5.2 and 5.3 if equ. (5.22) holds. As can be seen, the agreement is not spectacular. As was discussed in chapter 4, the stability assumption is not obeyed in the N-body models for density contrasts $\lesssim 50$ $(\Omega = 1)$ also, self-similarity is not established before expansion by a factor of about three which sets a practical limit of $\delta \lesssim 10^3$ in the tests according to equ. (5.22). Hence, the N-body models are only of very limited use in testing this description of galaxy clustering. The general conclusion to be drawn from the N-body models is that the mass dependence of the multiplicity function is consistent with the Press-Schechter (1974) theory and that we find no evidence for a non-linear bootstrap effect.

Bhavsar (1978) has considered a 'single galaxies' statistic f_s which, for the space distribution, is defined such that $f_s(\delta)$ is the fraction of galaxies in groups of only one member in the catalogue $\mathcal{C}(\delta)$. He has argued that $1-f_s(\delta)$ should be a power-law if the matter distribution is spatially self-similar. (Actually, Bhavsar's arguments are in terms of the

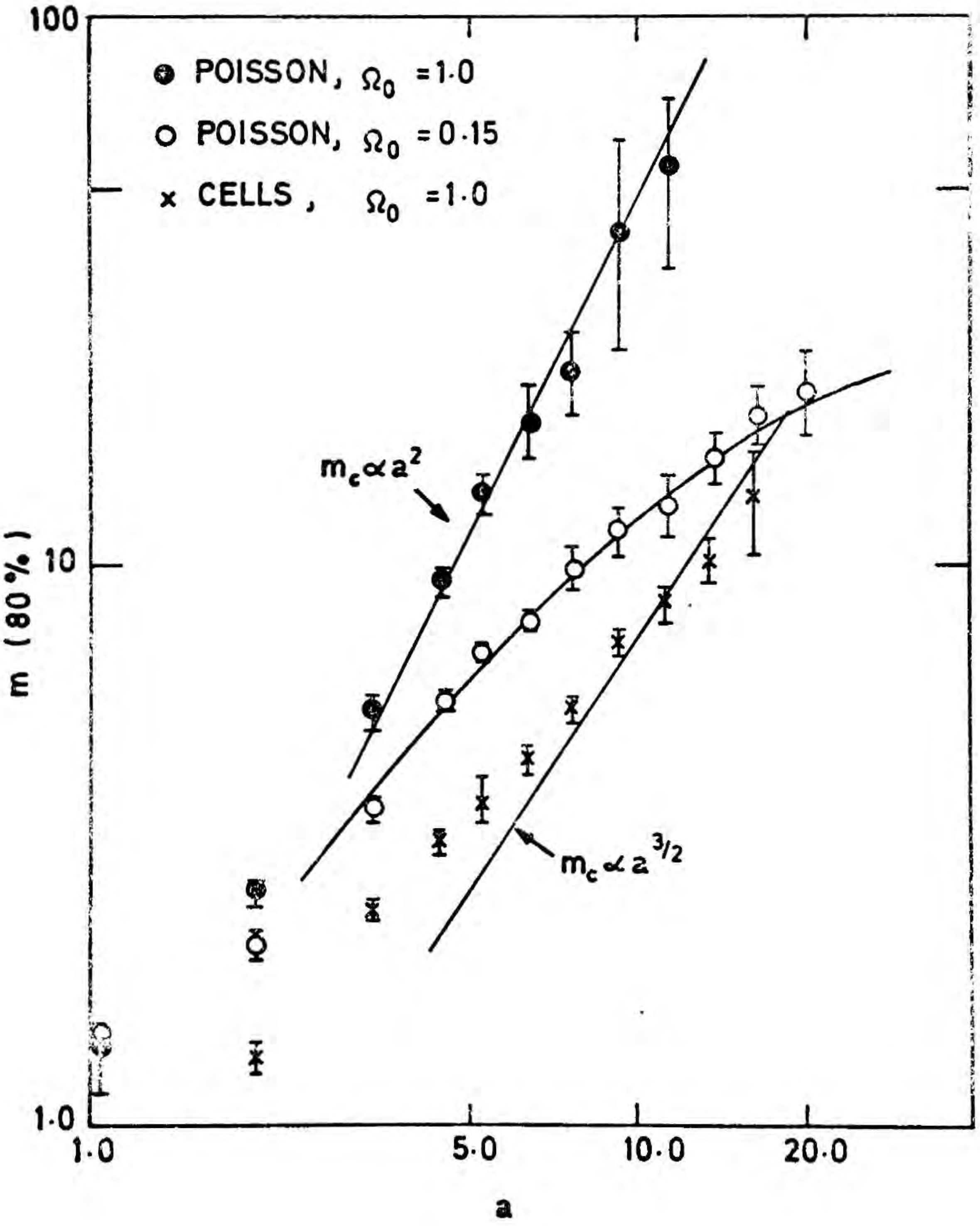

Figure 5.6. Growth of the 80th percentile mass-scale. The averages are for all experiments and the error flags are one standard deviation from the mean. The heavy lines are the predictions of linear theory.

projected distribution of galaxies on the sky, but the difference is not important here; see section 5.5). However, one might reason as follows to conclude that $f_s(\delta)$ itself should be a power-law: $f_s(\delta) \propto h(m_g, \delta) \propto \delta^{-(\frac{1}{2}+n/6)/\epsilon}$ by equ. (5.18), where m_g is the characteristic mass of a single galaxy (unit mass in the N-body experiments). In principle, this statistic offers another cosmological test, but for reasons to be explained in the next section the comparison with observational data is difficult. Figs. 5.7, 5.8 show $f_s(\delta, t)$ for some of our models and it appears that $f_s(\delta)$ does have power law form with index close to that predicted above for $\delta \lesssim 300$.

5.4 Comparison with Observations.

In this section we tackle the problem of applying the results of theory and experiment to the observational data on galaxy clustering. For obvious reasons it will prove convenient to work with luminosities instead of masses. Thus $\eta(L, \delta)dL$ is now taken to represent the space density of groups with (luminosity) density contrast δ and total luminosity in the interval $(L, L+dL)$. If luminosities and masses are proportional, $\eta(L, \delta)$ should have the same dependence on L as $\eta(m, \delta)$ has on m. The estimates of Gott and Turner (1977) are based on a combination of surface density and velocity data for their 14th magnitude sample of galaxies. The surface density criterion is $\beta \gtrsim 8$,

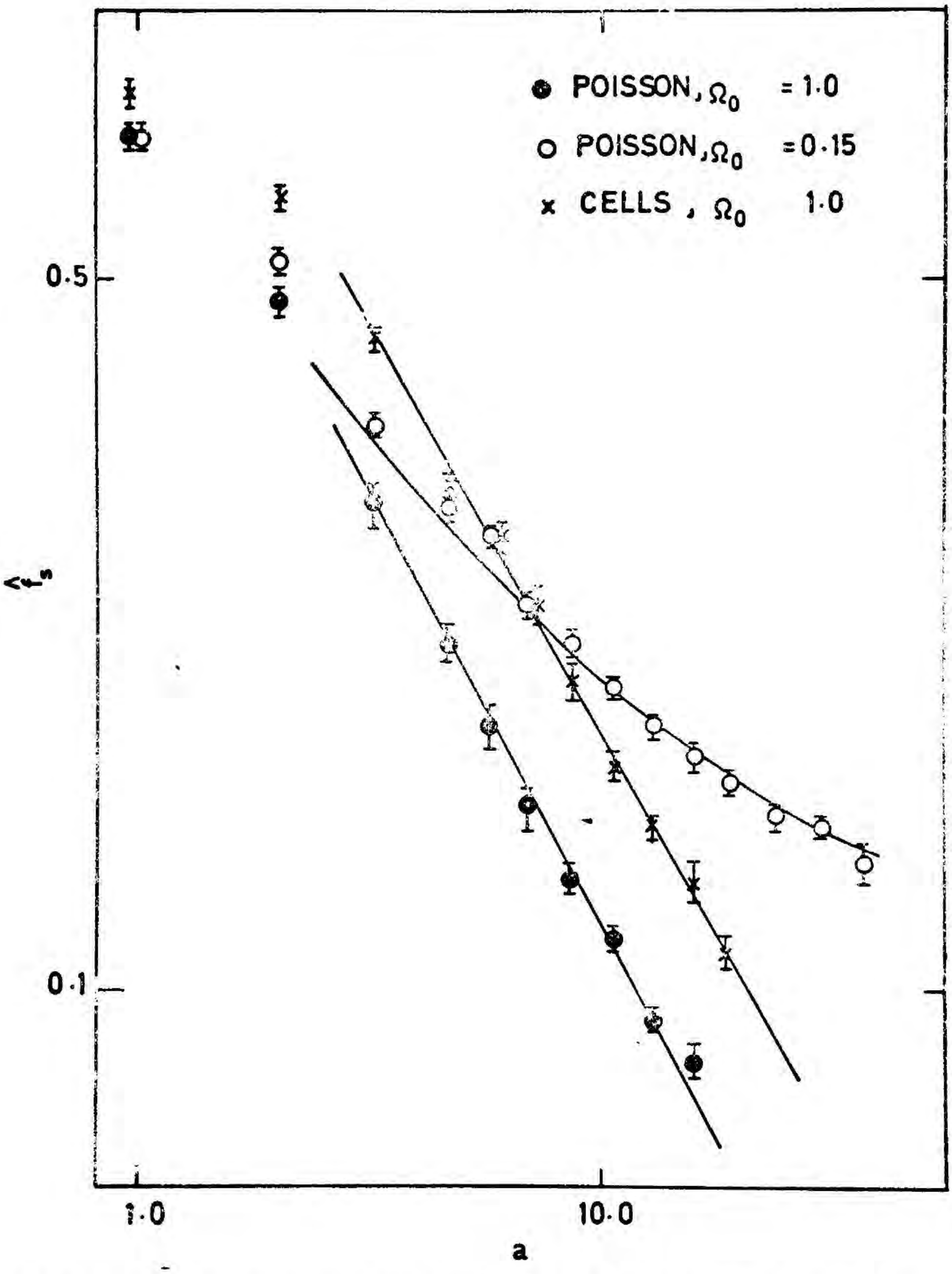

Figure 5.7. Evolution of the single particle statistic determined from all experiments of the same type. The heavy lines are based on the linear growth rate of m_c ($f_s \propto \Delta^{-1}$).

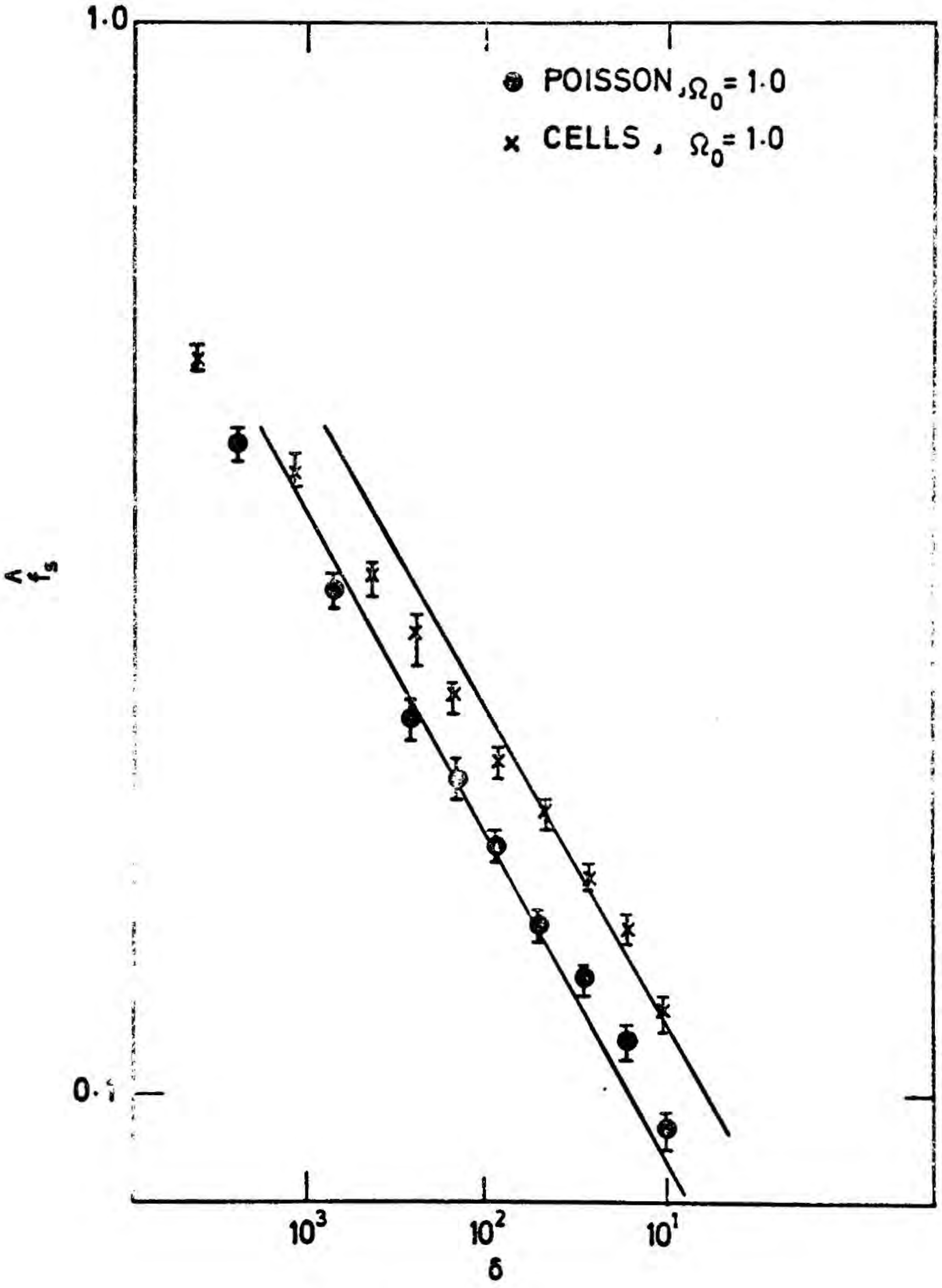

Figure 5.8. Dependence of the single-particle statistic on density contrast. The heavy lines have exponent $\frac{1}{3}$ as expected from the scaling arguments.

corresponding roughly to $\delta \sim 300$-1200, but depending on the distance and richness of groups. After various corrections, the result is

$$\eta(L) \propto L^{-1\cdot 7}$$
$$(8 \times 10^{9}\ h^{-2} L_{\odot} \lesssim L \lesssim 3 \times 10^{12}\ h^{-2} L_{\odot}) \qquad (5.23)$$

which naively suggests $n \simeq -1$ from equs (5.12) and (5.14). However, the theory also predicts a feature in η at the luminosity $\delta^{1/\epsilon} L_{*} \approx (5$-$15) \times 10^{9} L_{\odot}$ where L_{*} is the luminosity corresponding to m* and is given by

$$L_{*} = m^{*}/\langle M/L \rangle \simeq (4\text{-}8) \times 10^{11}\ h^{-2} L_{\odot} \qquad (5.24)$$

(c.f. equations 31 and 49 of Fall, 1979). Thus there is no solid theoretical foundation for inferring n from the power-law form of equ. (5.23) over the observed range of luminosities.

It is also interesting to compare the multiplicity function η_{L} with the galaxy luminosity function ϕ, which is defined such that $\phi(\ell) d\ell$ is the mean density of galaxies with luminosities in the interval $(\ell, \ell + d\ell)$. A group catalogue at a sufficiently high density contrast will include only single galaxies and the two functions must be equal. Thus in any theory of galaxy formation and clustering, we have $\phi(\ell) = \eta(\ell, \delta_{g})$ where δ_{g} is the characteristic density contrast associated with the luminous parts of individual galaxies. If galaxies and groups both formed without dissipation, f should be self-similar all the way up to galactic density, which the scaling relations predict to be $\delta_g \approx (\ell^*/L_*)$ where ℓ^* is the characteristic luminosity of ϕ . Now, Schechter (1976b) has shown that the galaxy luminosity function can be fitted by a function of the form $\phi(\ell) \propto \ell^{-5/4} \exp(-\ell/\ell^*)$ with $\ell^* \approx 8 \times 10^9 h^{-2} L_\odot$. On the dissipationless model, this result and equ. (5.24) imply $\delta_g \sim 10^3$, which is well below the characteristic luminosity contrast $\delta_g \sim 10^7$ associated with the inner 10 h^{-1}kpc of bright galaxies ($\ell \approx \ell^*$). Thus, if galaxies formed from a self-similar hierarchy, their luminous parts must have collapsed by a factor of order 10 from their original equilibrium radii. This conclusion is independent of Ω but may suffer from uncertainties in the shape of the multiplicity function near the bend at L_*. It is compatible with the idea that the luminous parts of galaxies condensed from cool gas in dark halos that clustered without dissipation (White and Rees, 1978, c.f. chapter 2).

Unless redshift information is available, the relation between many clustering statistics, such as η and f_s, and their analogues for the projected distribution on the sky is not simple even if the clustering in space is self-similar. In order to show this, we consider a sample of galaxies, limited at the apparent magnitude m_o, and imagine the construction of a family of group catalogues along the lines of section 5.2 at different surface density contrasts β . The analogue of the multiplicity function on the sky is $N^{-1}f(N,\beta)$ where $f(N,\beta)$ is the fraction of galaxies in groups of N visible members in a catalogue of surface density contrast β. This function is related to Bhavsar's (1978) statistics by the equations

$$f_s(\beta) = f(1,\beta) \qquad f_a(\beta) = \sum_{N=2}^{\infty} f(N,\beta) \tag{5.25}$$

Bhavsar found the empirical result

$$f_a(\beta) \underset{\sim}{\propto} \beta^{-0\cdot 5} \qquad (1 \lesssim \beta \lesssim 10^4) \tag{5.26}$$

and argued that the power-law form of f_a was to be expected for a spatially self-similar matter distribution. In principle, it is possible to relate $\eta(L,\beta)$ and $f(N,\beta)$ as follows.

Consider the function $Q_N(\ell | L,\delta)$ which is defined to be the probability that a group of space density contrast δ and total luminosity L has exactly N galaxies more luminous than ℓ. With some straightforward manipulations we then arrive at the following relations:

$$f(N,\beta) = \frac{N}{\mathcal{N}} \int_0^\infty dr\, r^2 \int_0^\infty dL\, \eta(L,\delta) Q_N(\ell(m_o,r) \,|\, L,\delta) \tag{5.27}$$

$$\mathcal{N} = \int_0^\infty dr\, r^2 \int_{\ell(m_o,r)}^\infty d\ell'\, \phi(\ell') \tag{5.28}$$

$$\ell(m_o, r) \quad r^2 \; d\exp(\,-2m_o/5\,) \tag{5.29}$$

$$\delta = \frac{3}{4}\sqrt{\pi}\;(L/\mathcal{L})(\,\beta\mathcal{N}/N)^{3/2}\; r^{-3} \tag{5.30}$$

Here $\mathcal{N}$ is the mean surface density of sample galaxies, $\mathcal{L}$ is the mean spatial luminosity density, r is a line of sight distance and the numerical factor in equ. (5.30) is for spherical groups. The kernal $Q_N(\ell\,|\,L,\delta)$ in equ. (5.27) accounts for the Scott (1957) effect, the apparent distance-richness correlation, which Bhavsar's arguments neglect.

The problem now is to find a reasonable model for Q_N. Quite generally, we have

$$Q_N(\ell\,|\,L,\delta) = \frac{1}{N!}\,Q_o(\ell\,|\,L,\delta)\int_{\ell}^{L} d\ell_1\; q(\,\ell_1|\,L,\delta\,) \int_{\ell}^{L-\ell_1} d\ell_2\; q(\,\ell_2|L,\delta\,)\;\ldots\ldots\int_{\ell}^{L-\ell_1-\,\ldots\,-\ell_{N-1}} d\ell_N\; q(\,\ell_N|L,\delta\,) \tag{5.31}$$

where q is the group luminosity function; that is, $q(\ell\,|\,L,\delta\,)d\ell$ is the probability that a group of density contrast δ and total luminosity L has a member galaxy with luminosity in the interval $(\,\ell, \ell+d\ell\,)$. The factor 1/N! in equ. (5.31) takes care of over-counting and the upper limits of the integral guarantee that the total luminosity of the N galaxies does not exceed L. For consistency, q must satisfy the following relations

$$q(\ell \mid L, \delta) = 0 \quad \text{for } \ell > L \tag{5.32}$$

$$\int_0^L d\ell \, \ell \, q(\ell \mid L, \delta) = L \tag{5.33}$$

$$\int_0^\infty dL \; q(\ell \mid L, \delta) \, \eta(L, \delta) = \quad (\ell) \tag{5.34}$$

The last equation must hold because all galaxies are members of one group, even if they are the only visible members of their group. In the 'statistical model' (Schechter and Peebles, 1976 and references therein), functions like q are assumed to be independent of δ. In the present context, however, equ. (5.34) shows that this approximation would not be acceptable for small groups because it implies that $q(\ell / L)$ be of the form $(L/\mathcal{L}) \, \phi(\ell)$ which is not consistent with equs. (5.32) and (5.33) for all $\ell < L$.

Clearly, the properties of $f(N, \beta)$ will depend not only on $\eta(L, \delta)$ but also on $q(\ell / L, \delta)$ through $Q_N(\ell / L, \delta)$, including its dependence on all three arguments. Unfortunately $q(\ell / L, \delta)$ cannot have a simple scaling property and still satisfy equs. (5.31)-(5.34). This is because it implicitly recognises a preferred scale: that of individual galaxies (q has two luminosity arguments but only one density argument). In order to make a model for Q_N, one must impose the additional constraint that the galaxy luminosity function join onto the group luminosity function at $\delta \gtrsim \delta_g$. This gives

$$\eta(\ell, \delta_g) = \phi(\ell) \qquad (5.35)$$

$$q(\ell | L, \delta) = p(\ell, \delta_g | L, \delta) \quad (\delta \lesssim \delta_g) \qquad (5.36)$$

$$q(\ell | L, \delta) \simeq (L/\mathcal{L})\, \phi(\ell) \quad (\delta \ll \delta_g,\ \ell \ll L) \qquad (5.37)$$

where p is the nesting kernal introduced in section 5.2 with luminosity instead of mass arguments, but not necessarily satisfying equ. (5.3). This leaves us with a rather formidable set of equations for $f(N, \beta)$ and we have made little progress with it. Thus unlike the relation between the angular and spatial pair-correlation functions (Fall and Tremaine, 1977 and references therein) it appears that the relation between $f(N, \beta)$ and $\eta(L, \delta)$ is not a simple one even when the distribution is spatially self-similar. It may, therefore, be necessary to resort to simulations of the sky that include realistic selection effects (Soneira and Peebles, 1978; Shanks, 1979) or to complete redshift samples (Geller, Huchra and Schechter, in preparation).

5.5 Conclusions and Discussion.

In the previous chapter we discussed the development of the low-order correlation functions under the assumptions of the gravitational instability picture.

In this chapter we have examined some alternative measures of galaxy clustering such as the multiplicity function. The main conclusions may be summarised as follows:

A. Scaling relations can be derived which generalise the Press-Schechter theory to different density contrasts δ and cosmological parameters Ω. They relate the multiplicity function to the hierarchy of correlation functions through the fractal dimension of the matter distribution.

B. The N-body multiplicity function estimates at $\delta \approx 10$ are consistent with the Press-Schechter theory although the statistical significance of the experimental results is fairly low.

C. The growth rates of the marginally non-linear mass scale are in agreement with the predictions of linear theory for the Poisson experiments, but they are somewhat slower than the predicted $a^{3/2}$ behaviour for the Cells experiments. There is no evidence for a non-linear bootstrap effect.

D. Relations between the multiplicity function and other measures of clustering on the sky can be derived but they show a complicated dependence on the luminosity function with no simple scaling property. Therefore, Bhavsar's (1978) empirical results remain unexplained.

E. The scaling relations and estimates of the luminosity function imply that if galaxies formed from a self-similar hierarchy, their luminous parts must have collapsed by a factor of order 10.

It has been suggested (section 5.2) that the multiplicity function is an attractive cosmological probe since it offers a direct measure of the spectral index of primordial inhomogeneities, n, independent of Ω. However, the relationship between the three-dimensional statistic and its analogue in two dimensions is extremely complicated, i.e. there does not exist a simple projection formula. This complicates the comparison with currently available observational data (Gott and Turner, 1977).

Even under the restricted assumption of a self-similar distribution of matter, the theory is far from rigorous. An alternative picture based on the merging of smaller groups to form larger ones, has been proposed by Silk and White (1978). In their model the multiplicity function has the form $\eta(m) \propto m^{-3/2}$ independent of initial conditions, and the evolution is self-similar in time. Thus it is observationally indistinguishable from the Press-Schecter model in the case of white noise $(n = 0)$ initial conditions.

It is important that a new statistic tell us more about the pattern of galaxy clustering than the low-order correlation functions. White (1979) has shown that this is probably not the case for Bhavsar's single galaxy statistic $f_s(\beta)$. In this connection it is important to note the work of Shanks (1979). Shanks considered simple galaxy distributions, the hierarchical model of Soneira and Peebles (1978) and a model in which all galaxies are distributed in identical spherical clusters with a power-law density profile. Shanks then applied a new statistic (Mead's statistic) to static simulations af these models and to galaxy catalogues. He noted that whilst the low-order correlation functions were quite similar in all cases, Mead's statistic suggested that the real data resembled the simple power-law cluster simulations rather than the hierarchy. Some of the N-body models of Table 4.1 have been analysed using Mead's statistic and are found to agree closely with Shank's hierarchical simulations. A complete account of this work may be found in Shanks (1979). Hence, this represents another case in which the N-body simulations disagree with the observed pattern of galaxy clustering apart from those discussed in chapter 4.

It is likely that this will prove to be a difficult result to explain theoretically with any degree of rigour. The important point to note about the low-order correlation functions is that they are directly related to the reduced particle distribution functions, i.e. one can at least write down a set of equations involving directly measurable quantities albeit that they are difficult to solve.

CHAPTER 6

SPECTROSCOPIC OBSERVATIONS OF THREE ELLIPTICAL GALAXIES

6.1 Introduction.

Recently, several studies have been made of the rotational properties of elliptical galaxies, (Bertola and Capaccioli, 1975; Illingworth, 1977; Peterson, 1978; Sargent et al, 1978; Young et al, 1978; Davies, 1978; Schechter and Gunn, 1979). The major result from these studies, discussed in chapter 2, is that most elliptical galaxies rotate more slowly than expected on the basis of the isotropic oblate spheroid model.

Binney (1978) suggested that elliptical galaxies may be triaxial ellipsoids and offered several interpretations consistent with the above result:

A. Elliptical galaxies may be rapidly rotating prolata (cf. Miller, 1978).

B. Whatever the intrinsic shape of elliptical galaxies, their flattening may be due to velocity anisotropy rather than due to rotation.

The careful study by Davies (1978) could not rule out possibility (A) but the recent work of Schechter and Gunn (1979) suggests that (B) is a more likely interpretation.

The motivation for the work described here comes from the photometric studies of Carter (1978), King (1978) and Williams and Schwarzchild (1979). These authors find twists in the isophotes of some elliptical galaxies, which may be interpreted as evidence for triaxiality. An alternative indication of triaxiality would be the detection of rotation along the apparent minor axis of an elliptical galaxy. We have, therefore, observed three elliptical galaxies, (NGC 4472, NGC 5813, IC 4296), with the slit positioned along both the major and minor axes. Similar observations have been carried out by Schechter and Gunn (1979). Another aim of the project was to compare the dynamical properties of our three galaxies with photometric measurements. The latter have yet to be completed, and so in this chapter I present only the results of the spectroscopic study.

In section 6.2 I discuss the observations and preliminary data reduction. In section 6.3 I describe the methods used to obtain the rotational velocities and velocity dispersions. The results are presented in section 6.4. The experimental details and reduction techniques have been discussed by Davies (1978) and the reader is referred to this work for a detailed account.

6.2 Observations and Preliminary Data Reduction.

a) Observations

The galaxies were chosen to be fairly round (E0-E2) in order to (i) offer a favourable configuration for the detection of minor axis rotation, (ii) offer a test of the rapidly rotating prolate hypothesis, since in this case, some round galaxies should be rapidly rotating and (iii) because there has been a noticable bias of previous measurements towards flat (E3-E5) ellipticals. The three galaxies observed were,

NGC 4472: An E2 galaxy, the brightest member of the Virgo cluster. Previous measurements along the major axis have been made by Illingworth (1977), Peterson (1978) and Davies (1978). The most reliable measurements are those of Davies, who finds a low maximum rotational velocity $\lesssim$ 45 km sec^{-1}. He also finds evidence for a rapid fall in the velocity dispersion, from 340 km sec^{-1} in the centre to $\gtrsim$ 240 km sec^{-1} in the outer regions. Interestingly, this galaxy shows a substantial swing in the position angle of its major axis, from 163° at R = 10 arcseconds to 152° at R = 100 arcseconds (King, 1978).

IC 4296 }
NGC 5813 } Neither of these galaxies has been previously studied. IC 4296 is classified as E0 by Sandage and Tamman (1979) but close inspection of Palomar prints and the UK sky survey reveal it to be slightly elongated ($\approx$E1). It is also listed as a radio source PKS 1333-33. NGC 5813 is listed in the Second Reference Catalogue as E2.

The observations described here were made by Drs D. Carter and R.S. Ellis during two nights in March 1979 using the Anglo Australian Telescope. The measurements were taken using the RGO spectrograph together with the Image Photon Counting System (IPCS, Boksenberg, 1972). The observational set up is summarised in Table 6.1. This set up differs from that used by Davies in several respects.

i. The slit was opened up to 3 arcseconds, i.e. twice as large as that used by Davies. The advantages of opening up the slit are obvious, i.e. one lets in more light but only at the expense of degrading the spectral resolution. With our slit width, configuration and taking the optical resolution of the IPCS to be $\gtrsim$ 30 microns our expected resolution is $\gtrsim$ 2·4 Å, i.e. $\gtrsim$ 120 km/sec over our spectral range. Since our galaxies have high velocity dispersions (200-350 km/sec) this was not a problem. In fact the Fourier analysis techniques described below suggested that the spectra were still somewhat over-resolved.

ii. Just before our observing run, the IPCS computer memory was extended to handle $\gtrsim$ 198 000 pixels simultaneously. Prior to this, only $\gtrsim$ 18 000 pixels could be handled. This enabled us to use a data window of 27x2044 pixels. The scans were obtained at spatial increments of $\gtrsim$ 2·5 arcseconds in order to obtain high spatial resolution across the galaxy and to avoid IPCS saturation problems in the central regions of the galaxies. The benefit of high spatial resolution was offset somewhat by the poor seeing $\approx$ 4·5 arcseconds for most of the observing run.

Table 6.1. Observational set up.

Wavelength range:	5000 - 6000 Å
Spectrograph:	25cm camera Grating 1200R in first order; blaze to collimator giving 34 Å mm^{-1}. Slit to detector projection factor ≈ 7 Slit width 450μ = 3 arcseconds.
IPCS:	Spatial increments of 2·5 arcseconds (low gain). Slit length 68 arcseconds. Scan format 34x2048. Data window 27x2044.

1000 second galaxy exposures were interlaced with 200 second exposures on a blank field of sky and a 200 second exposure of a comparison arc. Star spectra, to be used as templates were taken during twighlight. The observations are summarised in Table 6.2.

b) Flat-field correction

In order to correct for non-uniformities in the response of the IPCS, long (9999 secs) flat-field exposures were taken. The flat-field exposures were of very high signal/noise with typically $\gtrsim$ 5000 counts/pixel. Hence the flat-field correction does not add significant noise to the galaxy spectra.

The flat-field correction was obtained to preserve photon counts by fitting a continuum to the flat-field spectrum and then dividing it by this continuum. Prior to the flat-field correction some of the outer spectra of each scan were deleted for computational and instrumental reasons, resulting in 22 spectra/scan.

c) Wavelength calibration

Wavelength calibration is required in order to remove non-linearities in the wavelength scale across a spectrum due to residual S-distortion and also to remove drift in the wavelength scale between each 1000 second galaxy exposure, thereby allowing the addition of several 1000 second exposures. Arc spectra on either side of a 1000 second galaxy exposure were summed, and the positions of typically $\gtrsim$30 arc lines were located. These were then fitted to a fifth order polynomial relating wavelength and channel positions of the arc lines using a standard AAO program.

Table 6.2. Observations.

a) Galaxies.

Object	P.A. of slit	Exposure (secs.)	B_T
IC 4296 MJ	159°	5000	11·58
IC 4296 MN	249°	5000	
NGC 4472 MJ	159°	3000	9·31
NGC 4472 MN	69°	3000	
NGC 5813 MJ	220°	4000	11·65
NGC 5813 MN	130°	4000	

b) Templates.

Object	Exposure (secs.)	Type	M_V
SAO 136727	1000	K2 III	5·24
SAO 136622	2000	G6 III	5·45
SAO 183686	585	K0	5·6
SAO 136832	1000	K5 III	5·6
SAO 155588	1000	M2 III	4·9
NGC 6441	800	Metal rich globular cluster	9·0

This procedure is known as 'scrunching'. In order to check the scrunching, the night sky emission line at 5577 Å was used to monitor residual wavelength shifts. These were found to be less than 0·15 Å over the two nights that the observations were made.

d) Sky subtraction

Mean skies were formed by summing the 22 sky spectra within a scan. The galaxy spectra were then sky subtracted assuming a linear response for the detector. The accuracy of the sky subtraction was checked by comparing the residual flux of the sky line at 5577 Å in the sky subtracted spectrum to the total flux of the line (cf. Davies, 1978). This test indicated that the sky subtraction was good to $\lesssim$ 8%.

e) Conversion to ln λ scale

In order to apply the Fourier techniques described in the next section, the star and galaxy spectra were rebinned on a logarithmic wavelength scale by linear interolation between the original channels. The transformed spectra consist of 2048 channels, each channel corresponding to a velocity shift of 25·47 km sec^{-1}.

Figs. 6.1 (a,b,c) show the central spectrum of each galaxy at this stage in the data analysis. Fig. 6.2 shows the spectrum of SAO 136622, together with line identifications taken from Davies (1978). Most of the features shown in Fig. 6.2 may also be found in the galaxy spectra.

Fig. 6.1(a).

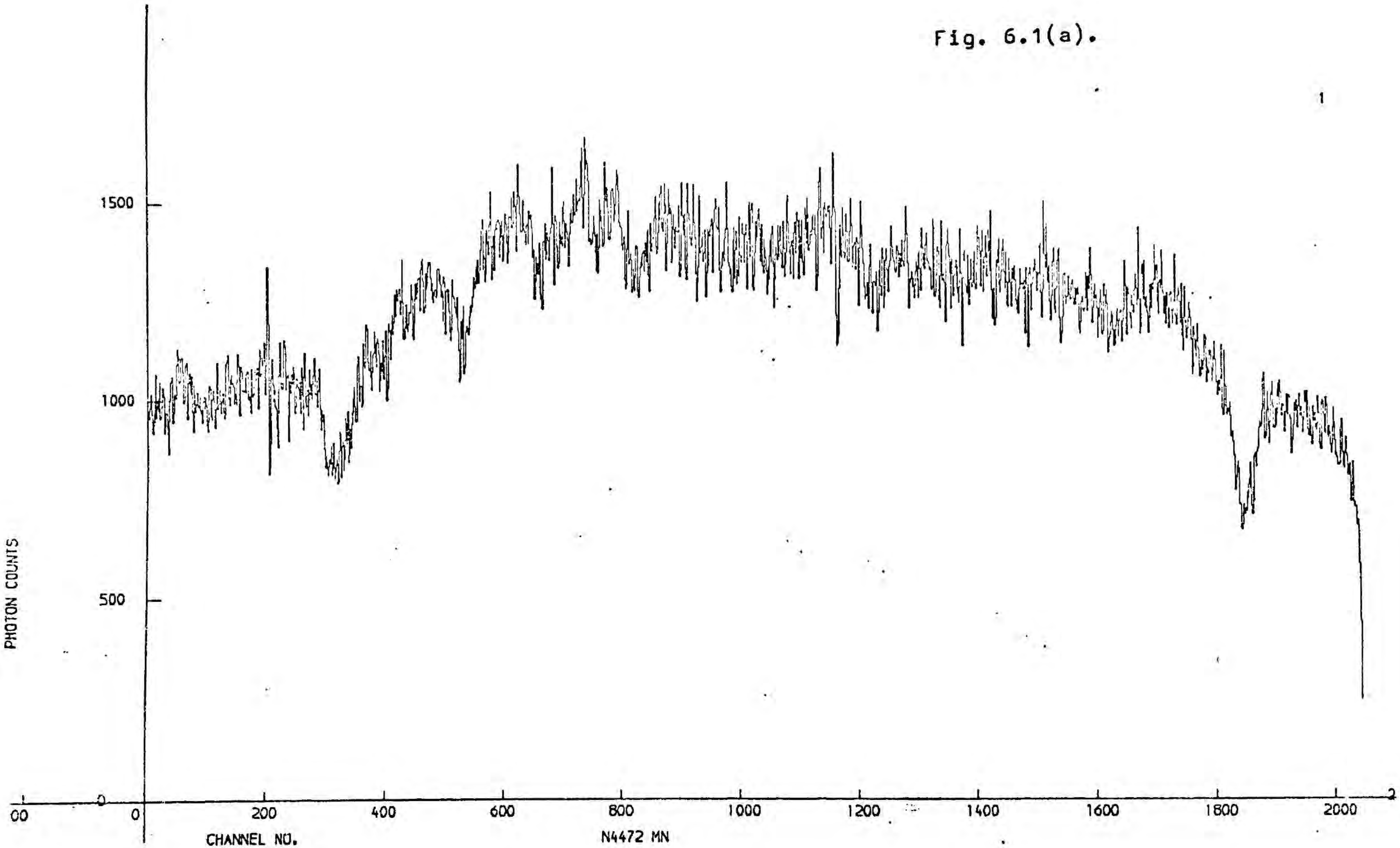
1500
1000
500
PHOTON COUNTS
0
200
400
600
800
1000
1200
1400
1600
1800
2000
CHANNEL NO.
N4472 MN

Fig. 6.1(b)

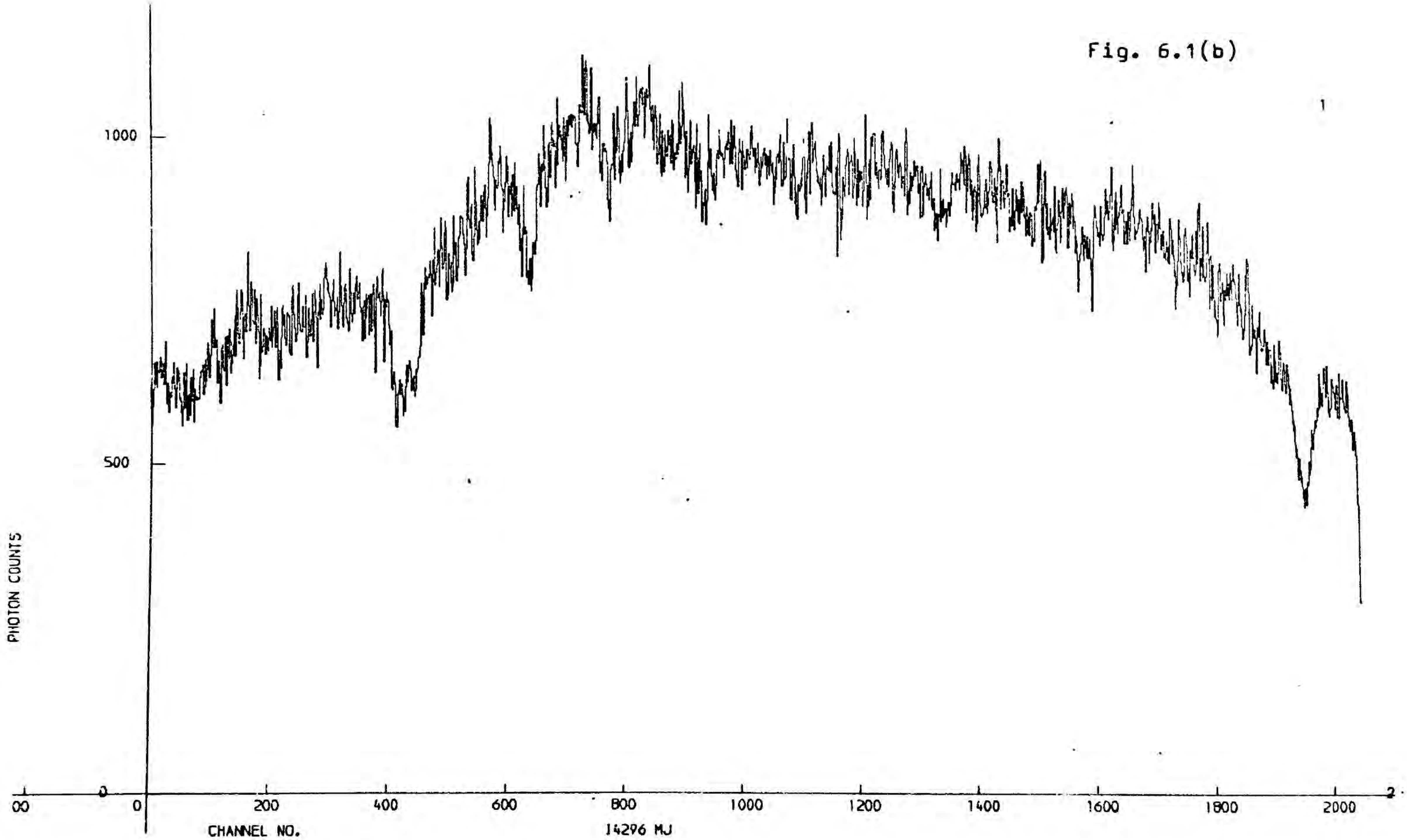
1
1000
500
0
PHOTON COUNTS
00
0
200
400
600
800
1000
1200
1400
1600
1800
2000
2
CHANNEL NO.
14296 MJ

Fig. 6.1(c).

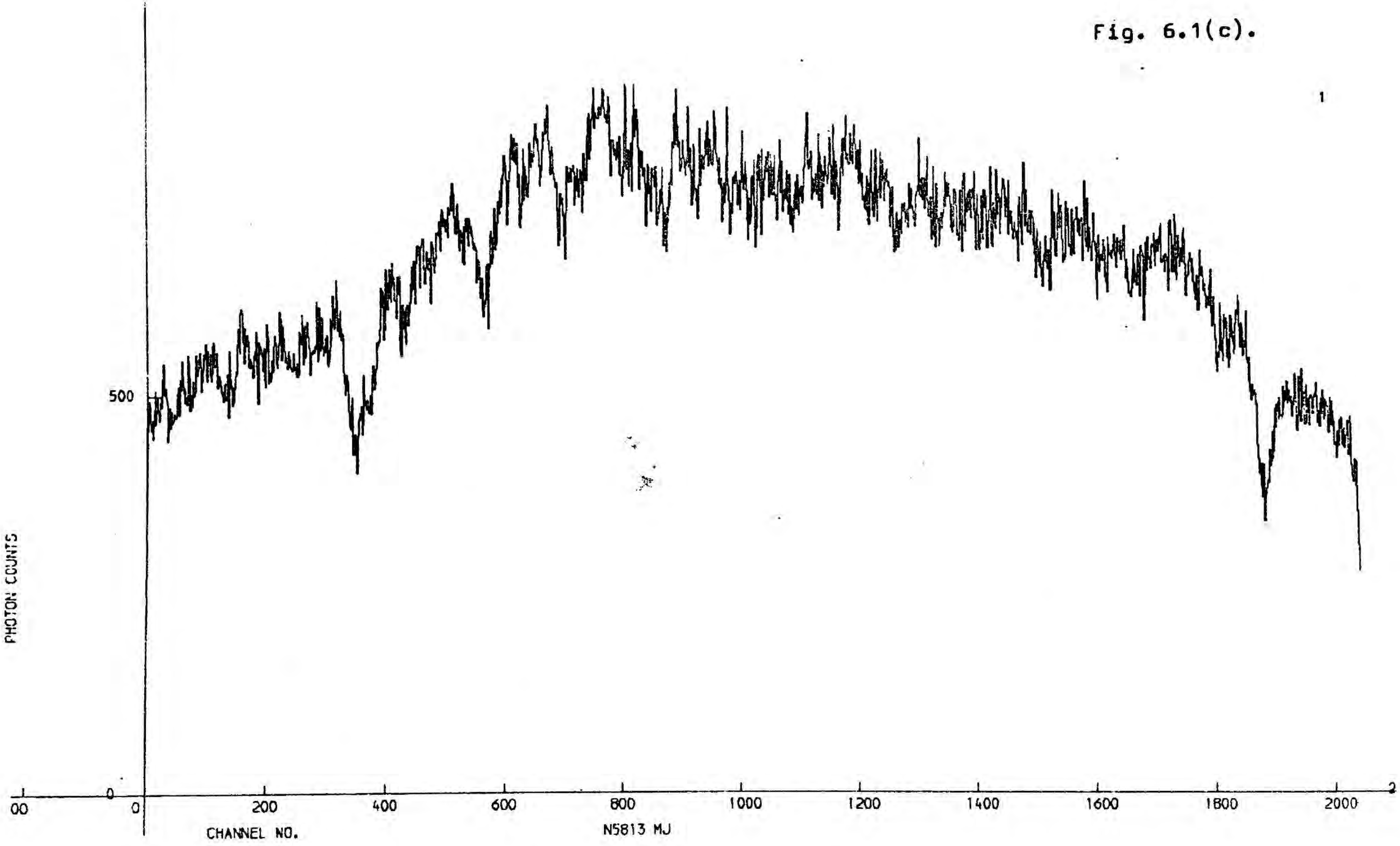
1
500
0
PHOTON COUNTS
00
0
200
400
600
800
1000
1200
1400
1600
1800
2000
2
CHANNEL NO.
N5813 MJ

Fig. 6.2.

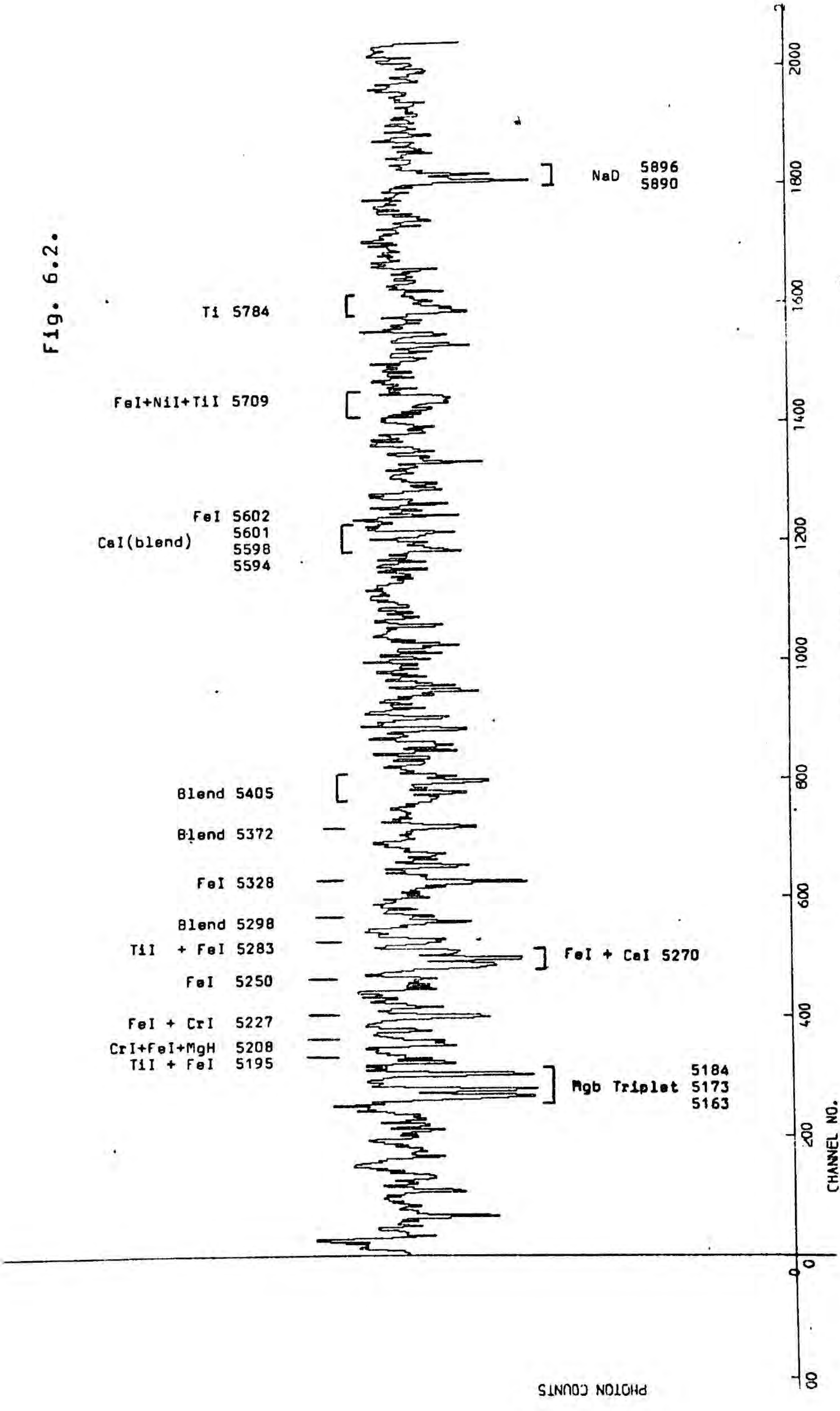

SAO 136622

6.3 Fourier Methods.

Recently, Fourier techniques have been applied in the analysis of galaxy spectra in order to obtain rotational velocities and velocity dispersions (Sargent et. al., 1977, hereafter SSBS). We have applied two methods in the analysis of our data, the Fourier quotient method of SSBS and the cross correlation method of Tonry and Davis (1979). Each method is briefly discussed below.

Before Fourier methods may be applied, the spectra must be continuum divided (or subtracted) in order to reduce the power at low frequencies due to continuum trends. This was accomplished by choosing several points (10-20) of the spectrum free from strong features and interpolating between these points using cubic splines. This was done interactively for each spectrum. When the fit was judged to be satisfactory, the spectrum was divided by the fitted continuum. Prior to Fourier transforming, the continuum divided spectrum was normalised to have zero mean and the outer 5 percent of the data was tapered by application of a cosine bell to reduce the effects of leakage.

In order to obtain a high signal/noise template spectrum for the application of Fourier analysis methods, all the templates of Table 6.2 (except SAO 183686) were added together. The redshift of each template was determined relative to SAO 136622 using the cross correlation method described below and each spectrum was shifted, using linear interpolation between channels, prior to addition. No detectable broadening or velocity shift in the final spectrum was introduced by this procedure.

a) Fourier quotient method

Let $\tilde{G}(k)$ be the Fourier transform of the continuum divided, mean subtracted, end-masked galaxy spectrum and let $\tilde{S}(k)$ be the Fourier transform of a similarly manicured star spectrum. The quotient $\tilde{G}(k)/\tilde{S}(k)$ is then fitted to a broadening function $\tilde{B}(k)$ which assumes a Gaussian velocity distribution,

$$\tilde{Q}(k) = \frac{\tilde{G}(k)}{\tilde{S}(k)} \approx \tilde{B}(k) = \gamma \exp\left[-\tfrac{1}{2}\left(\frac{2\pi k\sigma}{N}\right)^2 + \left(\frac{2\pi ikv}{N}\right)\right] \quad (6\cdot1)$$

where γ is the "line strength", σ is the velocity dispersion and v is the redshift, here N is the total number of channels (N=2048).

The values for the parameters γ, σ, and v judged to give the best fit to (6.1) are chosen by minimising the χ^2 statistic

$$\chi^2 = \sum_{k_L}^{k_H} \left| \frac{\tilde{Q}(k) - \tilde{B}(k)}{\Delta \tilde{Q}(k)} \right|^2 \quad (6\cdot2)$$

where $\Delta\tilde{Q}(k)$ represents the error on the quotient. SSBS take

$$\frac{\Delta \tilde{Q}(k)}{\tilde{Q}(k)} = \left[\left| \frac{\Delta \tilde{G}(k)}{\tilde{G}(k)} \right|^2 + \left| \frac{\Delta \tilde{S}(k)}{\tilde{S}(k)} \right|^2 \right]^{\frac{1}{2}} \quad (6.3)$$

on the assumption that the error distribution of $\tilde{Q}(k)$ is described by a normal distribution. As pointed out by Davies (1978), when one function with a normal error distribution is divided by another, the errors are Cauchy distributed, hence, equ. (6.3) does not apply. Davies proposed an intricate way of treating this problem whilst still retaining the main feature of the method, the comparsion of the quotient $\breve{Q}(k)$ with $\tilde{B}(k)$.

During a timely visit to Durham, Dr. Marc Davis suggested that we try using the cross-correlation method of Tonry and Davis (1979) which avoids forming the quotient and also allows an elegent determination of measurement errors.

b) Cross correlation method.

The cross correlation method is conceptually very simple. Consider the cross correlation function

$$C(n) = \sum_{m} G(m)S(m-n) \tag{6.4}$$

where G(j) and S(j) are the galaxy and star spectra respectively, j refers to the bin number on a $\ln\lambda$ scale and the summation extends over all bins. If it is assumed that G may be expressed as the convolution of S with some symmetric broadening function B, the quantity

$$\chi^2 = \sum_{k} \left| \tilde{G}(k) - \tilde{S}(k)\tilde{B}(k) \right|^2 \tag{6.5}$$

is minimised by finding the highest peak of the cross-correlation function. The displacement of the peak from the origin yields the redshift v, the width of the peak gives the dispersion and the height gives the line strength. Tonry and Davis prove this, under some reasonable assumptions, in some mathematical detail but this can easily be seen as follows. Suppose that

$\tilde{S}(k)$ can be approximated as a Gaussian of width τ with unconstrained phases and let $\tilde{B}(k)$ be modelled by equ. (6.1). When (6.5) has been minimised, $\tilde{G}(k) \approx \tilde{S}(k)\tilde{B}(k)$, hence from (6.4) the cross correlation peak will have the form

$$C(v) \approx \frac{\sigma_s \gamma \tau \sqrt{2}}{\sigma_g \mu^2} \exp\left[- \frac{(v-v_o)^2}{2\mu^2} \right] \tag{6.6}$$

where $\mu^2 = \sigma^2 + 2\tau^2$ and $\sigma_g^2 = \frac{1}{N}\sum_m G(m)$. In practice, the cross correlation peak will be distorted due to noise in the spectra and template mismatch. To reduce the noise, the spectra are filtered before calculating the cross correlation function. In our case, we multiplied $\tilde{G}(k)$ and $\tilde{S}(k)$ by a linear filter which had the form

$$f(k) = \begin{cases} 0 & k \leq k_1 \\ \dfrac{k_2-k}{k_2-k_1} & k_1 \leq k \leq k_2 \\ 1 & k_2 \leq k \leq k_3 \\ \dfrac{k_4-k}{k_4-k_3} & k_3 \leq k \leq k_4 \\ 0 & k \geq k_4 \end{cases} \tag{6.7}$$

Unless otherwise stated, we took $k_1 = k_2 = 10$, and $k_3 = 100$, $k_4 = 200$.

Hence, the filtered cross correlation peak will, in general, have negative lobes on either side of the central peak. This is illustrated in Fig. 6.3(a) which shows the auto-correlation of the central major axis spectrum of NGC 4472. Note that the function is perfectly symmetric about the centre of the cross-correlation peak. Fig. 6.3(b) shows the same spectrum cross-correlated with the composite template. In this case C(n) has a significant antisymmetric component due to mismatch between the spectra and noise. Tonry and Davis use σ_a, the mean square of the antisymmetric component of C(n) about v_0 to estimate errors.

A noise peak that overlaps with the cross-correlation peak will cause distrtions in the shape of the peak. Let the ratio of the height of the true peak in C(n) to the average height of a noise peak be $r = h/\sqrt{2}\,\sigma_a$, and let the typical distance between a noise peak and the true peak be $\Delta\epsilon$, then the errors on the height (h), width (w) and position of the maximum (v_0) will be approximately,

$$\Delta w \simeq \Delta v_0 \approx \frac{\Delta\epsilon}{(1 + r)} \tag{6.8a}$$

$$\frac{\Delta h}{h} \approx \frac{1}{r} - \frac{4(\Delta\epsilon)^2}{w^2(1 + r)} \tag{6.8b}$$

and $\Delta\epsilon \approx N/8B$, where B is the half-maximum point of the Fourier transform of C(n). After inspecting plots of $\tilde{C}(k)$ for our galaxies, we chose B=30, hence $\Delta\epsilon \approx 8{\cdot}5$ and this value was used in subsequent error estimation. Fig. 6.3(c) shows C(n) for one of our worst spectra. Even in this case, there is no danger of selecting a noise peak rather than the true cross correlation peak.

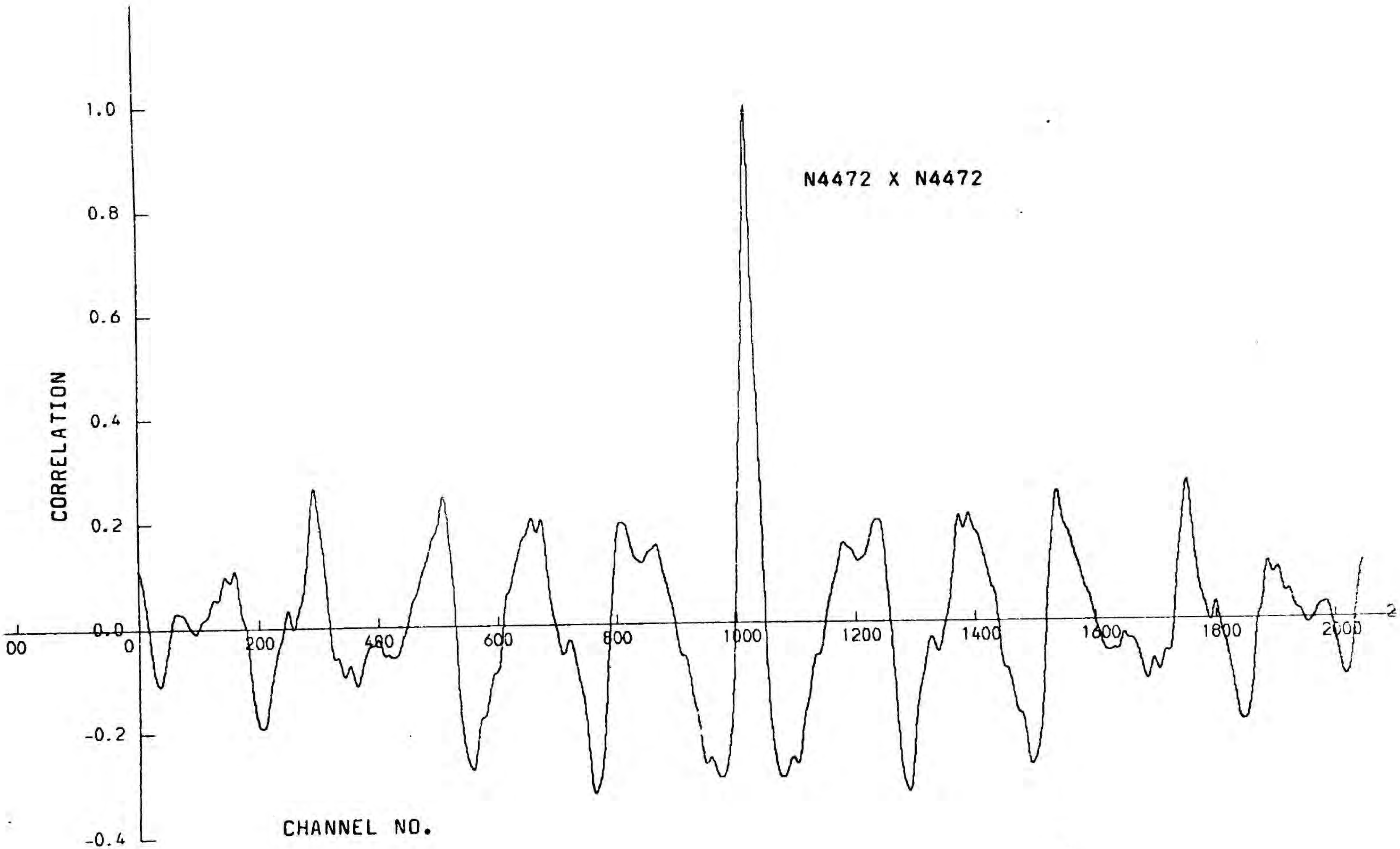
N4472 X N4472
CORRELATION
1.0
0.8
0.6
0.4
0.2
0.0
-0.2
-0.4
CHANNEL NO.
00
0
200
400
600
800
1000
1200
1400
1600
1800
2000

Fig. 6.3(a).

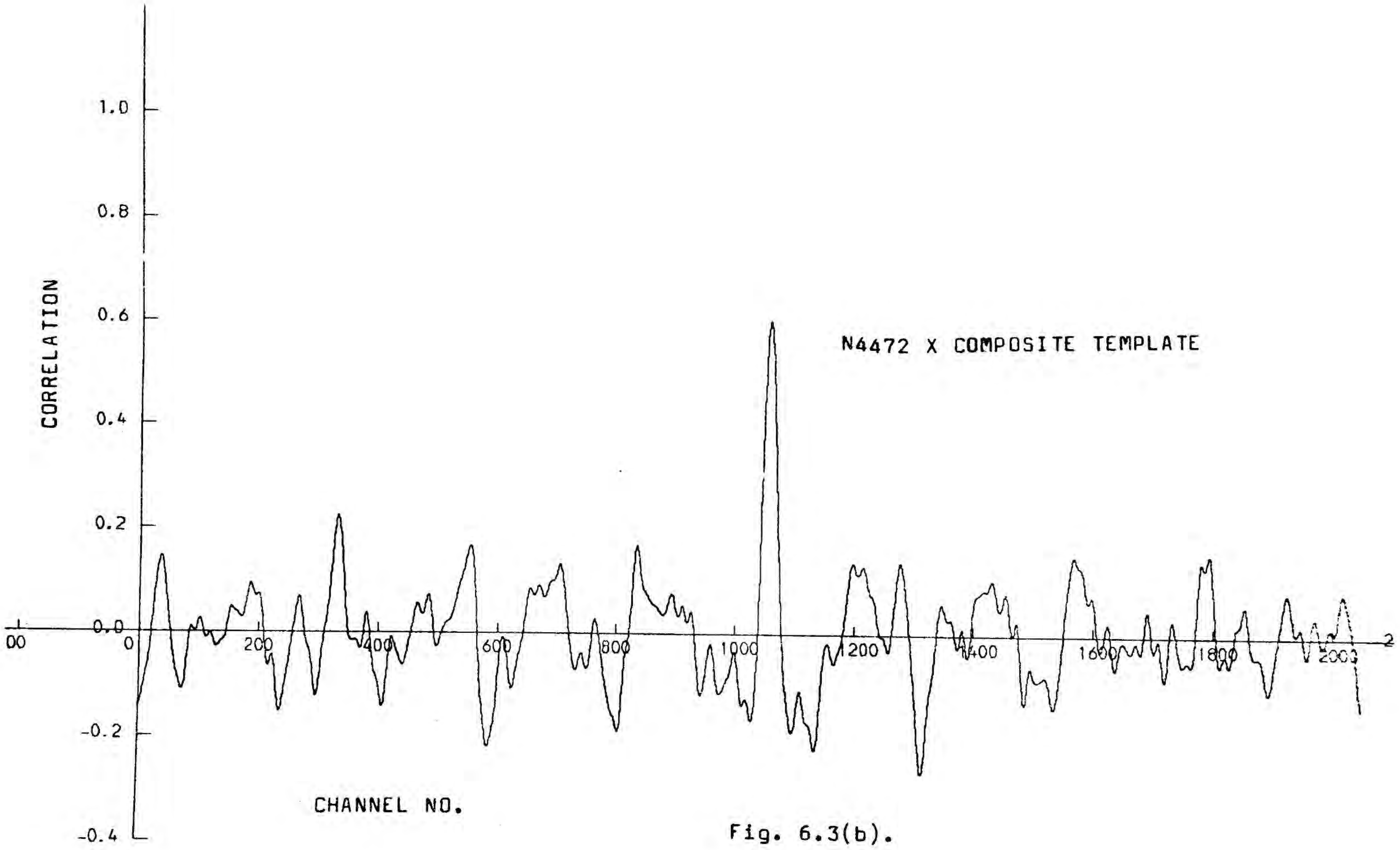
N4472 X COMPOSITE TEMPLATE
CORRELATION
1.0
0.8
0.6
0.4
0.2
0.0
-0.2
-0.4
CHANNEL NO.
00
0
200
400
600
800
1000
1200
1400
1600
1800
2000
2

Fig. 6.3(b).

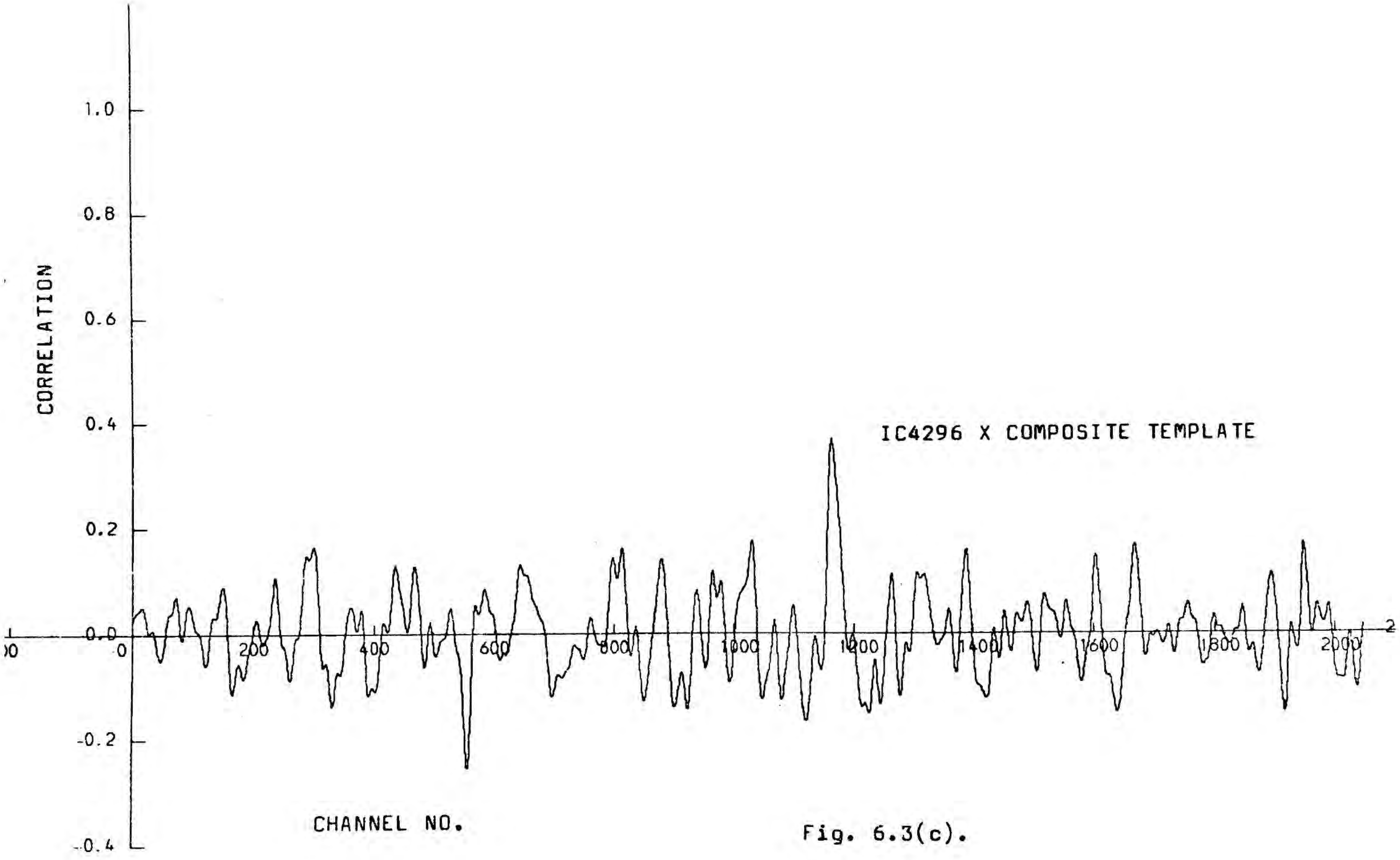
IC4296 X COMPOSITE TEMPLATE
CORRELATION
1.0
0.8
0.6
0.4
0.2
0.0
-0.2
-0.4
)0
0
200
400
600
800
1000
1200
1400
1600
1800
2000
2
CHANNEL NO.

Fig. 6.3(c).

c) Comparison of the methods.

Fig. 6.4 shows a test of the methods. SAO 136622 was used as the template and the other stars of Table 6.2 were broadened by known amounts. The total number of photons in the star spectra span a wide range, hence the test also serves as an indicator of the effects of varying signal/noise.

In applying the SSBS method, we chose $k_L = 10$ and $k_H = 100$ (equ. 6.2) unless otherwise stated. In the cross-correlation method, 18 points on either side of the maximum of the cross-correlation peak were fitted to a parabola. In addition, the cross-correlation peak of equ. (6.6) has effectively been filtered by the application of (6.7). The width (w) of the fitted parabola must be related to the width of a Gaussian (σ), after the application of a filter. In Fig. 6.4 it can be seen that the dispersion in $\sigma_{out} / \sigma_{in}$ using the cross-correlation method is greatest when $\sigma_{in} \lesssim 200$ km sec^{-1} due to our choice of filter and the number of points used to fit the parabola. We found it difficult to choose a combination to give better results over a wider range of σ_{in}. For this reason, the estimates of σ derived from the cross-correlation method are probably less reliable than those derived from the SSBS method.

The methods are in excellent agreement (usually to within a few km/sec) in estimating redshift, (see section 6.4 below). In applying the SSBS method, a first order redshift correction is necessary in order to avoid secondary minima in (6.2). Although not essential, we also applied a first order correction in the application of the cross-correlation method. Finally, we have not included calculation of the line strength parameter in our present cross-correlation

Caption for Figure 6.4:

Test of the Fourier methods. Each of the templates listed in the figure was broadened by a known amount σ_{in}. The cross-correlation and SSBS methods were used to determine σ_{out} using SAO 136622 as template in each case. The numbers in brackets refer to the total number of photons in each spectrum ($\times 10^6$). The spectrum of SAO 136622 contains $2{\cdot}1 \times 10^6$ photons.

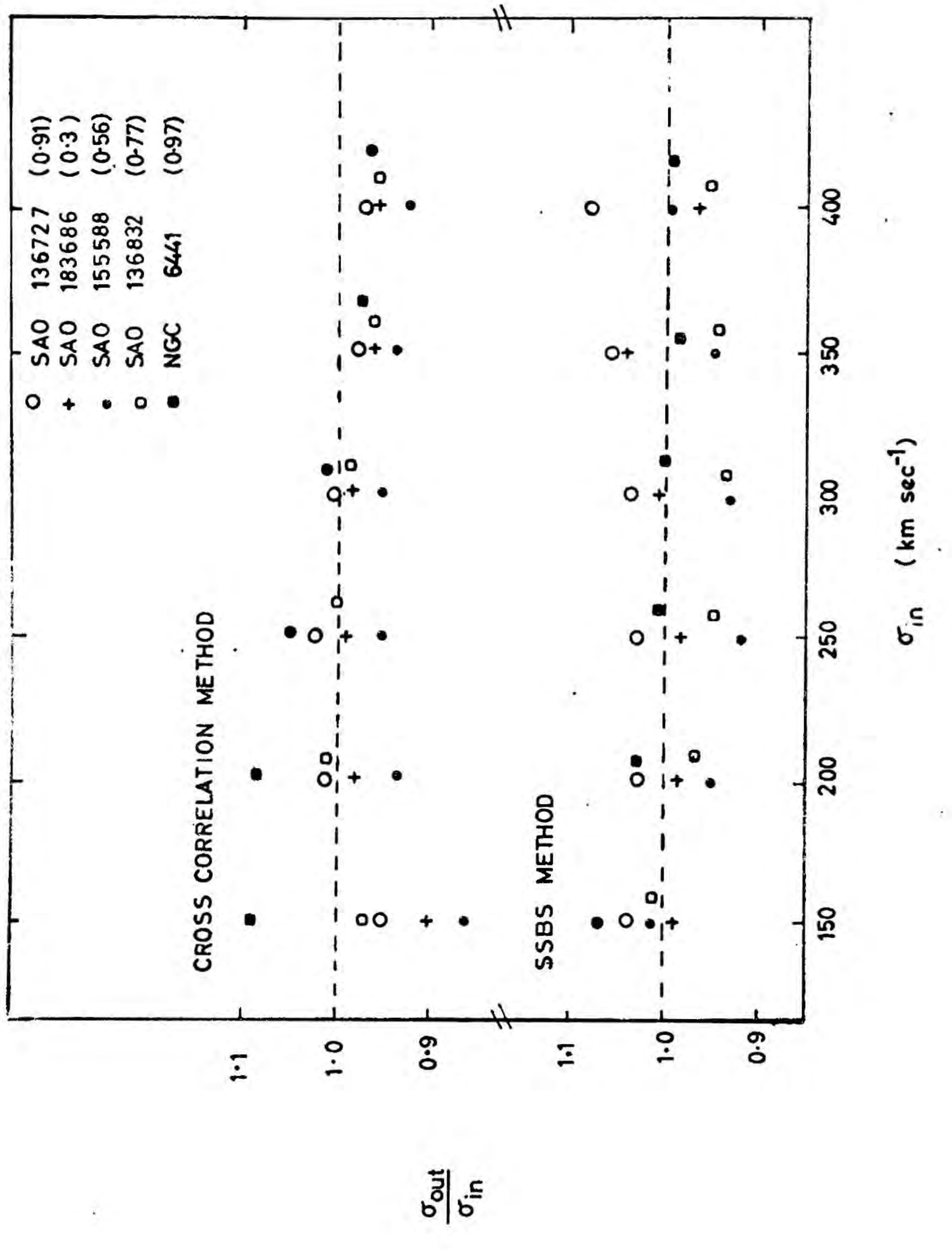
○ SAO 136727 (0·91)
+ SAO 183686 (0·3)
• SAO 155588 (0·56)
▫ SAO 136832 (0·77)
■ NGC 6441 (0·97)
CROSS CORRELATION METHOD
SSBS METHOD
1·1
1·0
0·9
1·1
1·0
0·9
150
200
250
300
350
400
σ_in (km sec⁻¹)
σ_out / σ_in

Figure 6.4.

analysis program.

6.4 Results.

In order to obtain accurate results using Fourier analysis methods, high signal/noise spectra are required. Hence, some of the outer spectra of each scan were added together to produce spectra containing $\gtrsim 3 \times 10^5$ photons.

The results for each galaxy and each position angle are shown in Figs. 6.5-6.7. The error flags on v and σ were determined from the cross-correlation method as described above, and the error-flags on γ represent the formal errors determined from the SSBS method. The values of v, σ and γ for each galaxy are listed in Tables 6.3-6.7.

As an illustration of the sensitivity of the Fourier methods to the range of wavenumbers used, Table 6.4 lists the results obtained taking $k_H = 50$ (equ. 6.2) when applying the SSBS method and $k_3 = 70$, $k_4 = 120$ (equ. 6.7) when applying the cross-correlation method. The results are not particularly sensitive to the choice of these parameters.

The two methods are in fairly good agreement. The differences between the two methods are, in general, smaller than our 1 σ error flags but they do give a reasonable indication of the differences encountered when using other stars as templates and when changing the range of wavenumbers used.

The results have not yet been interpreted in detail, hence a brief discussion, summarising general impressions obtained fron Figs. 6.5-6.7, is given below.

Tables 6.3-6.6. Notes:

CR refers to results obtained using the cross correlation method of Tonry and Davis (1979) described in section 6.4. SSBS refers to results obtained using the Fourier quotient method of Sargent et. al. (1977). As indicators of the quality of the spectra, the total number of photons and the r parameter (equs. 6.9) are listed.

Figs. 6.5-6.6 Captions:

Results for each galaxy along major and minor axes. The crosses represent the results obtained form the cross correlation method and the dots show the results obtained using the SSBS method. Also shown on Fig. 6.5(a) are the results obtained by Davies (1978). The dashed lines represent eye estimates of the mean redshift for each galaxy.

Table 6.5(a). Results for NGC 4472 Major axis, P.A. = 159^{o}

Spectrum No.	No. of Photons ($\times 10^6$)	v (km/sec) CR	±	v (km/sec) SSBS	σ (km/sec) CR	±	σ (km/sec) SSBS	γ SSBS	±	r
1-2	0·45	964	21	958	268	23	239	0·79	0·09	8·51
3-4	0·57	954	21	945	308	19	286	0·86	0·09	8·48
5	0·42	1000	32	989	261	34	262	0·82	0·10	5·46
6	0·47	972	23	981	290	22	316	0·94	0·11	7·85
7	0·56	945	20	931	325	18	350	1·11	0·11	8·98
8	0·78	945	16	944	345	14	342	1·09	0·09	11·60
9	1·1	936	18	931	307	16	323	1·04	0·08	10·30
10	1·6	906	14	903	316	13	325	1·00	0·06	13·64
11	2·1	921	12	933	324	11	326	1·14	0·06	16·37
12	2·2	926	14	923	305	13	298	1·01	0·05	13·25
13	1·7	922	15	920	313	14	307	0·95	0·05	12·51
14	1·3	915	16	916	336	14	337	1·05	0·07	11·40
15	0·88	921	17	912	340	14	344	1·04	0·09	11·18
16	0·65	917	18	915	345	16	332	1·03	0·10	10·25
17	0·52	891	18	889	310	16	299	0·99	0·10	10·15
18	0·44	920	20	929	309	17	297	0·98	0·11	9·42
19-20	0·67	855	22	862	319	19	324	0·98	0·09	8·45
21-22	0·52	844	17	840	266	18	284	0·92	0·09	11·21

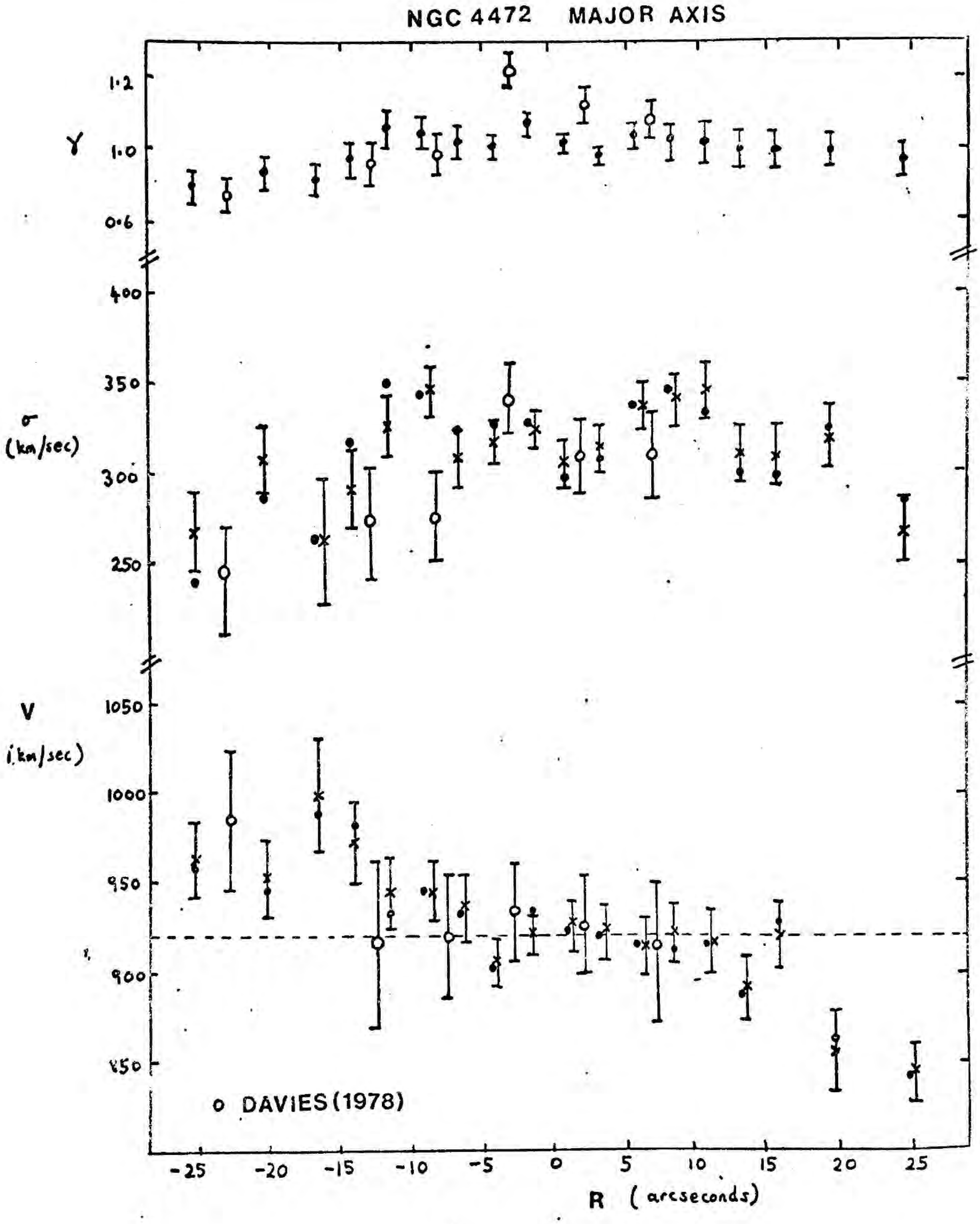
NGC 4472 MAJOR AXIS
Y
1·2
1·0
0·6
σ
(km/sec)
400
350
300
250
V
(km/sec)
1050
1000
950
900
850
o DAVIES (1978)
-25
-20
-15
-10
-5
0
5
10
15
20
25
R (arcseconds)

Figure 4.5(a).

Table 6.3(b). Results for NGC 4472 Minor axis, P.A. = 69°

Spectrum No.	No. of Photons ($\times 10^6$)	v(km/sec) CR	±	v(km/sec) SSBS	σ(km/sec) CR	±	σ(km/sec) SSBS	γ SSBS	±	r
1-2	0·36	903	27	912	287	26	273	0·67	·11	6·54
3-4	0·47	900	25	910	315	22	308	0·92	·10	7·14
5	0·34	891	25	893	259	28	258	0·94	·11	7·19
6	0·41	962	22	966	272	23	308	1·01	·11	8·38
7	0·47	909	21	904	263	23	276	0·92	·10	8·58
8	0·69	921	15	924	310	14	308	1·11	·09	12·24
9	1·0	901	21	925	354	18	386	1·17	·09	8·70
10	1·5	903	12	903	285	12	287	0·96	·06	16·19
11	2·2	904	14	909	347	12	352	1·14	·07	14·08
12	2·5	930	15	926	325	13	334	1·13	·06	12·28
13	1·9	892	13	893	316	12	322	1·06	·06	14·27
14	1·3	913	18	908	273	19	278	0·91	·06	10·16
15	0·85	899	19	914	284	19	308	0·95	·08	9·57
16	0·60	906	21	906	310	18	302	1·12	·09	8·86
17	0·47	904	22	902	336	19	359	1·05	·12	8·31
18	0·38	940	24	921	320	20	351	0·99	·13	7·57
19-20	0·56	889	18	902	253	21	246	0·76	·13	10·39
21-22	0·43	942	23	949	258	25	253	0·79	·14	8·03

NGC 4472   MINOR AXIS

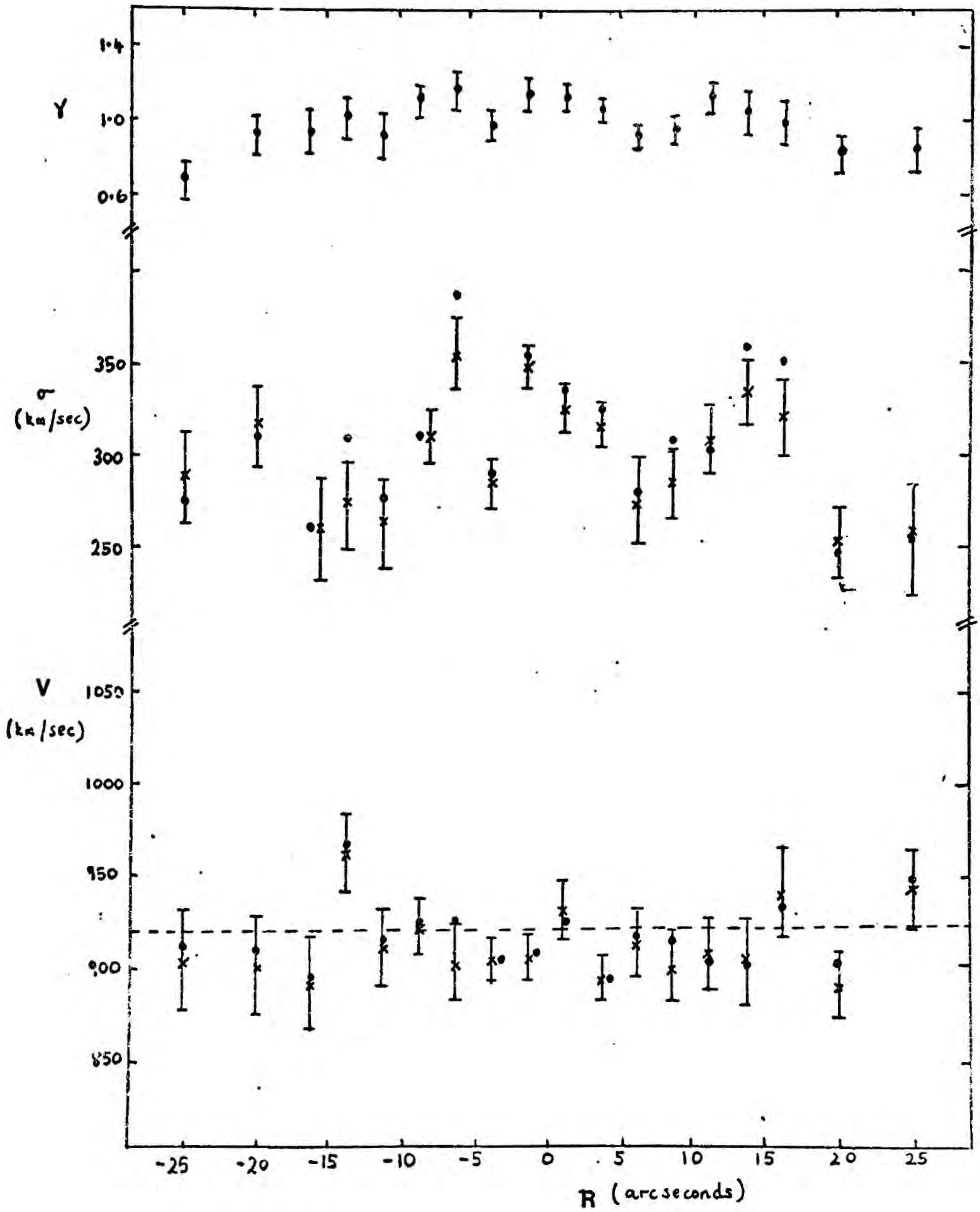

Figure 4.5(b).

Table 6.4. Results for NGC 4472 Major axis using a smaller interval in wavenumber than in Table 6.3(a).

Spectrum No.	No. of Photons (x 10^6)	v(km/sec)			σ(km/sec)			γ		r
		CR		SSBS	CR		SSBS	SSBS		
			±			±			±	
1-2	0·45	962	20	960	263	22	224	0·77	·09	9·61
3-4	0·57	956	20	937	285	20	290	0·87	·09	9·26
5	0·42	995	31	986	268	33	271	0·83	·10	5·61
6	0·47	969	22	985	299	21	323	0·95	·11	8·37
7	0·56	946	19	928	324	18	349	1·10	·11	9·68
8	0·78	944	15	945	349	14	338	1·08	·09	12·31
9	1·1	935	17	926	313	16	330	1·06	·08	10·78
10	1·6	905	13	902	318	13	321	1·00	·06	14·46
11	2·1	923	10	937	326	10	328	1·14	·06	18·64
12	2·2	928	13	920	308	13	300	1·02	·05	14·50
13	1·7	920	14	917	314	14	317	0·[illegible]7	·05	13·42
14	1·3	914	15	916	339	14	335	1·05	·07	12·21
15	0·88	921	15	913	335	14	348	1·05	·09	12·60
16	0·65	918	16	914	341	15	329	1·03	·09	11·73
17	0·52	893	17	891	310	16	288	0·97	·10	11·24
18	0·44	917	18	932	306	17	288	0·96	·10	10·43
19-20	0·67	857	21	864	323	19	324	0·97	·09	8·90
21-22	0·52	839	16	841	267	18	311	0·97	·10	11·61

Table 6.5(c). Results for IC 4296 Major axis, P.A. = 159°

Spectrum No.	No. of Photons (x 10^6)	v(km/sec)			σ(km/sec)					r
		CR		SSBS	CR		SSBS	SSBS		
			±			±			±	
1-4	0·32	3635	39	3671	257	43	319	0·94	·14	4·26
5-6	0·31	3741	30	3742	285	29	315	0·94	·14	5·69
7-8	0·52	3702	27	3727	260	30	296	0·77	·10	6·52
9	0·53	3671	24	3669	270	25	265	0·81	·10	7·48
10	0·98	3651	20	3645	268	21	271	0·82	·07	9·34
11	1·7	3678	18	3663	285	17	315	0·88	·06	10·55
12	1·8	3656	19	3637	302	17	310	0·86	·06	9·99
13	0·98	3629	22	3634	263	24	302	0·77	·08	8·10
14	0·55	3601	28	3610	286	27	307	0·88	·10	6·34
15-16	0·55	3632	27	3614	272	28	280	0·81	·10	6·43
17-18	0·31	3566	32	3583	266	34	320	0·79	·14	5·28
19-22	0·38	3553	41	3557	196	64	191	0·48	·09	3·93

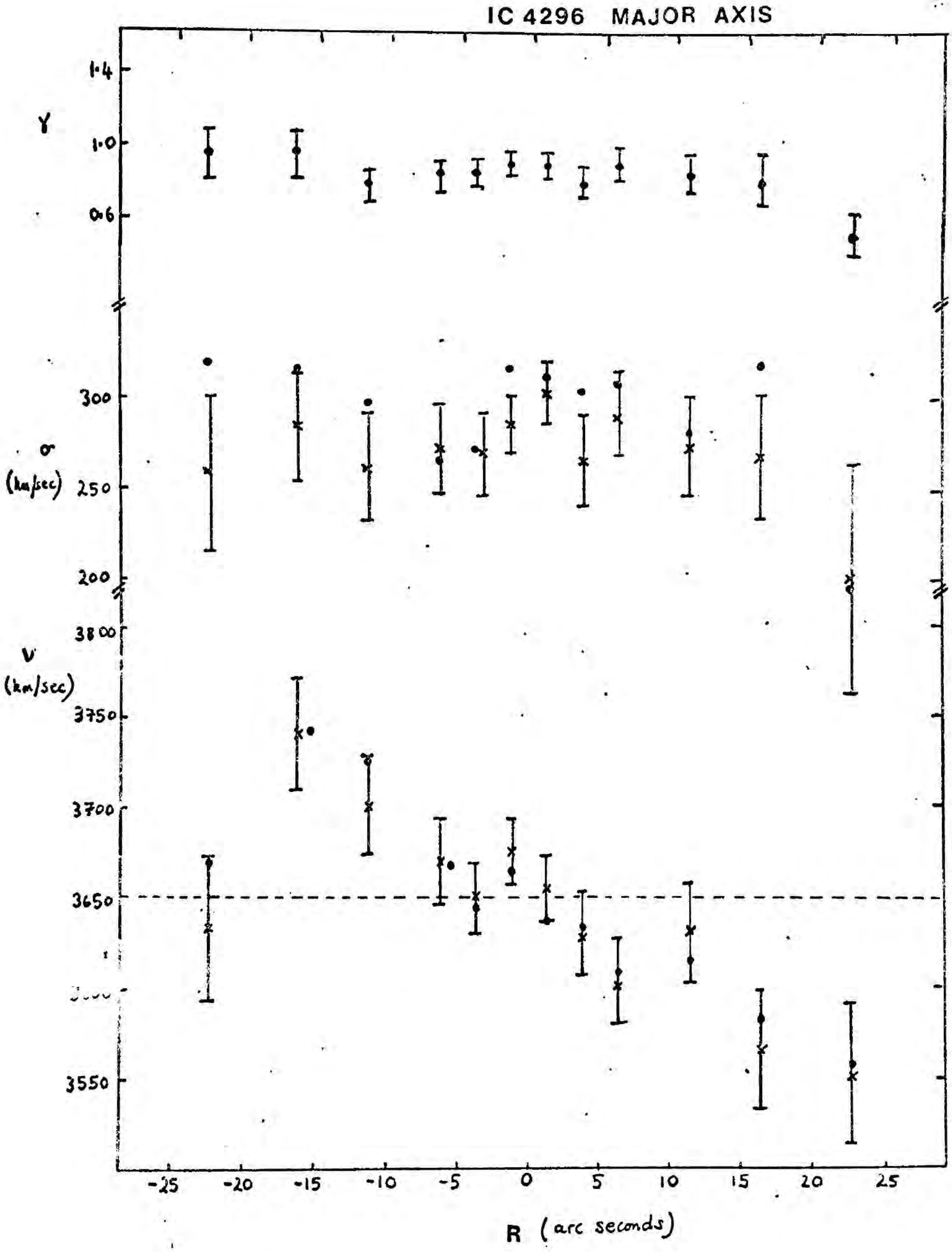
IC 4296 MAJOR AXIS
Y
1·4
1·0
0·6
σ (km/sec)
300
250
200
V (km/sec)
3800
3750
3700
3650
3550
-25
-20
-15
-10
-5
0
5
10
15
20
25
R (arc seconds)

Figure 4.6(a)

Table 6.5([illegible]). Results for IC 4296 Minor axis, P.A. = 69°

Spectrum No.	No. of Photons ($\times 10^6$)	v(km/sec) CR	±	v(km/sec) SSBS	σ(km/sec) CR	±	σ(km/sec) SSBS	γ SSBS	±	r
1-4	0·26	3733	41	3727	296	37	351	0·90	·16	4·01
5-6	0·25	3684	38	3647	382	36	365	1·10	·17	4·32
7-8	0·42	3613	30	3603	284	30	279	0·75	·11	5·69
9	0·40	3598	29	3610	264	32	321	0·87	·12	5·96
10	0·77	3662	17	3647	320	15	315	0·98	·09	10·77
11	1·40	3659	19	3651	296	18	310	0·95	·07	9·66
12	1·70	3660	18	3640	320	15	324	0·99	·07	10·58
13	1·10	3638	21	3633	281	21	293	0·92	·07	8·76
14	0·60	3689	24	3681	304	21	309	0·92	·10	7·64
15-16	0·57	3642	22	3630	273	23	265	0·74	·09	8·06
17-18	0·29	3647	32	3631	227	42	251	0·79	·12	5·35
19-22	0·34	3672	39	3662	308	34	275	0·69	·12	4·27

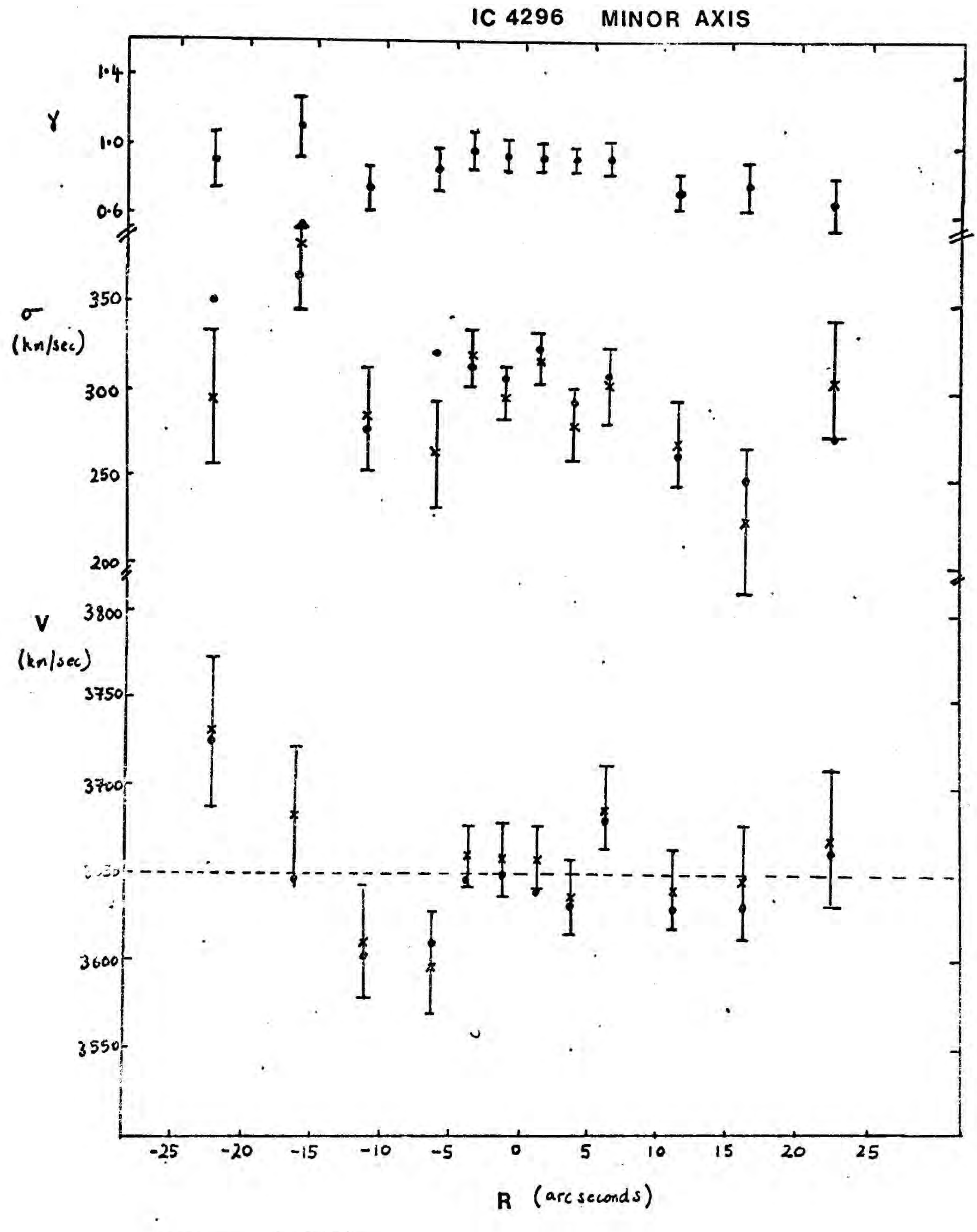
IC 4296 MINOR AXIS
γ
1·4
1·0
0·6
σ (km/sec)
350
300
250
200
V (km/sec)
3800
3750
3700
3650
3600
3550
-25
-20
-15
-10
-5
0
5
10
15
20
25
R (arc seconds)

Figure 4.6(b).

Table 6.[illegible](a). Results for NGC 5813 Major axis, P.A. = 220°

Spectrum No.	No. of Photons	v(km/sec)			σ(km/sec)			γ		r
	$(\times 10^6)$	CR		SSBS	CR		SSBS	SSBS		
			±			±			±	
1-5	0·39	1924	36	1924	265	38	231	0·67	·09	4·66
6-8	0·51	1882	19	1881	252	23	247	0·88	·09	9·53
9	0·36	1913	21	1919	196	33	194	0·78	·09	8·70
10	0·65	1914	16	1915	259	18	251	1·00	·08	11·83
11	1·20	1893	13	1894	236	17	236	0·99	·06	15·11
12	1·40	1845	12	1844	247	15	245	0·98	·06	15·44
13	0·83	1801	16	1804	229	22	226	0·88	·07	11·70
14	0·45	1833	19	1827	210	28	210	0·81	·08	9·77
15-17	0·59	1861	23	1871	265	25	264	0·84	·08	7·77
18-22	0·45	1889	24	1888	248	29	256	0·72	·09	7·39

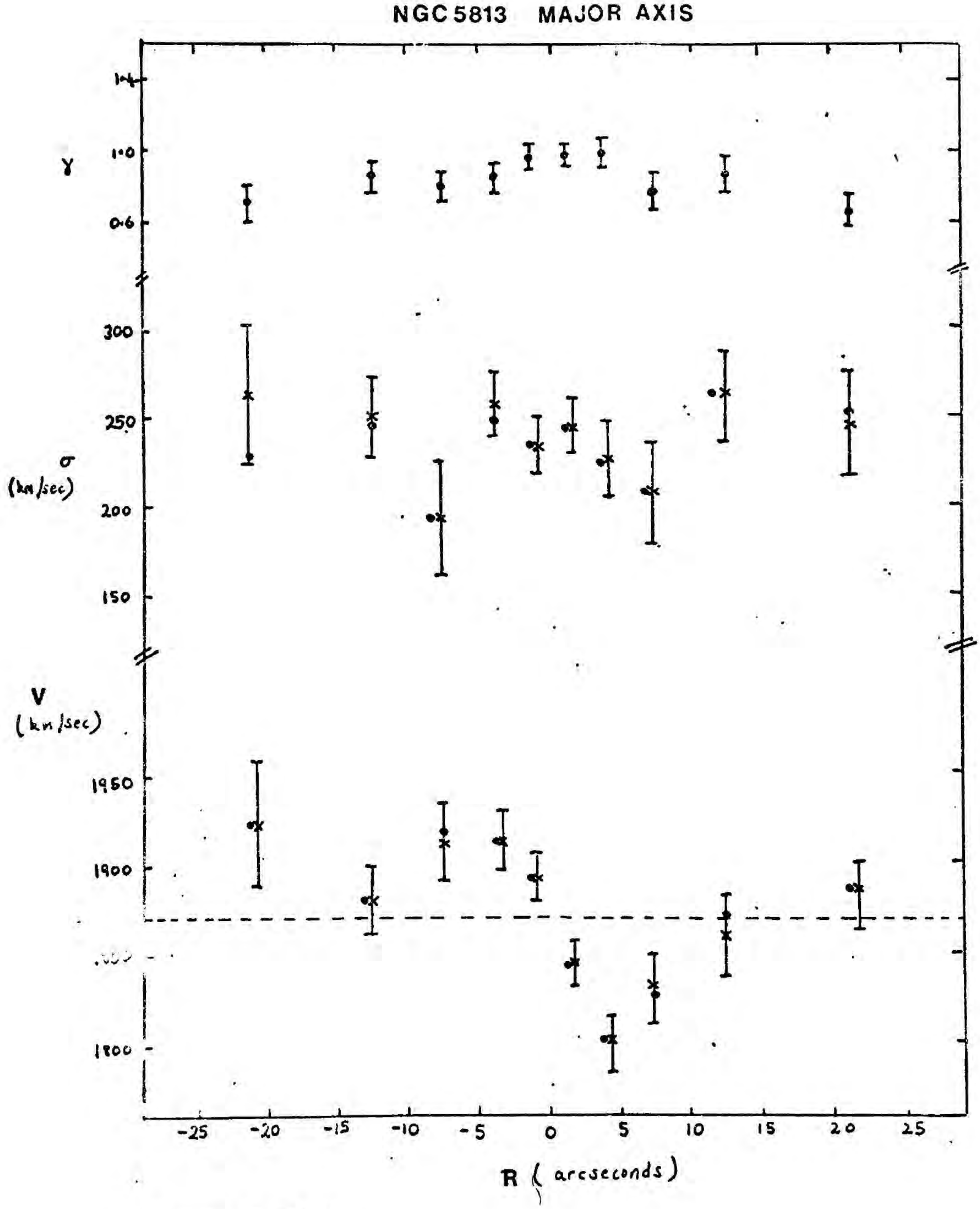
NGC 5813 MAJOR AXIS
γ
1.4
1.0
0.6
σ (km/sec)
300
250
200
150
V (km/sec)
1950
1900
1800
-25
-20
-15
-10
-5
0
5
10
15
20
25
R (arcseconds)

Figure 4.7(a).

Table 6.6(b). Results for NGC 5813 Minor axis, P.A. = 130°

Spectrum No.	No. of Photons ($\times 10^6$)	v(km/sec)			σ(km/sec)			γ		r
		CR		SSBS	CR		SSBS	SSBS		
			±			±			±	
1-5	0·30	1846	28	1853	251	32	228	0·78	·11	6·33
6-8	0·43	1847	22	1846	209	32	221	0·77	·09	8·40
9	0·31	1893	23	1899	257	25	285	0·99	·12	8·05
10	0·56	1905	17	1903	243	21	252	0·92	·08	10·81
11	1·0	1882	13	1887	239	17	239	0·96	·06	14·75
12	1·4	1878	12	1877	245	16	245	1·02	·06	15·40
13	0·92	1845	16	1851	248	19	242	0·90	·07	11·72
14	0·48	1867	18	1868	212	26	204	0·84	·08	10·27
15-17	0·56	1860	20	1869	240	25	238	0·93	·08	9·10
18-22	0·38	1855	33	1864	200	50	208	0·62	·09	5·28

NGC 5813 MINOR AXIS

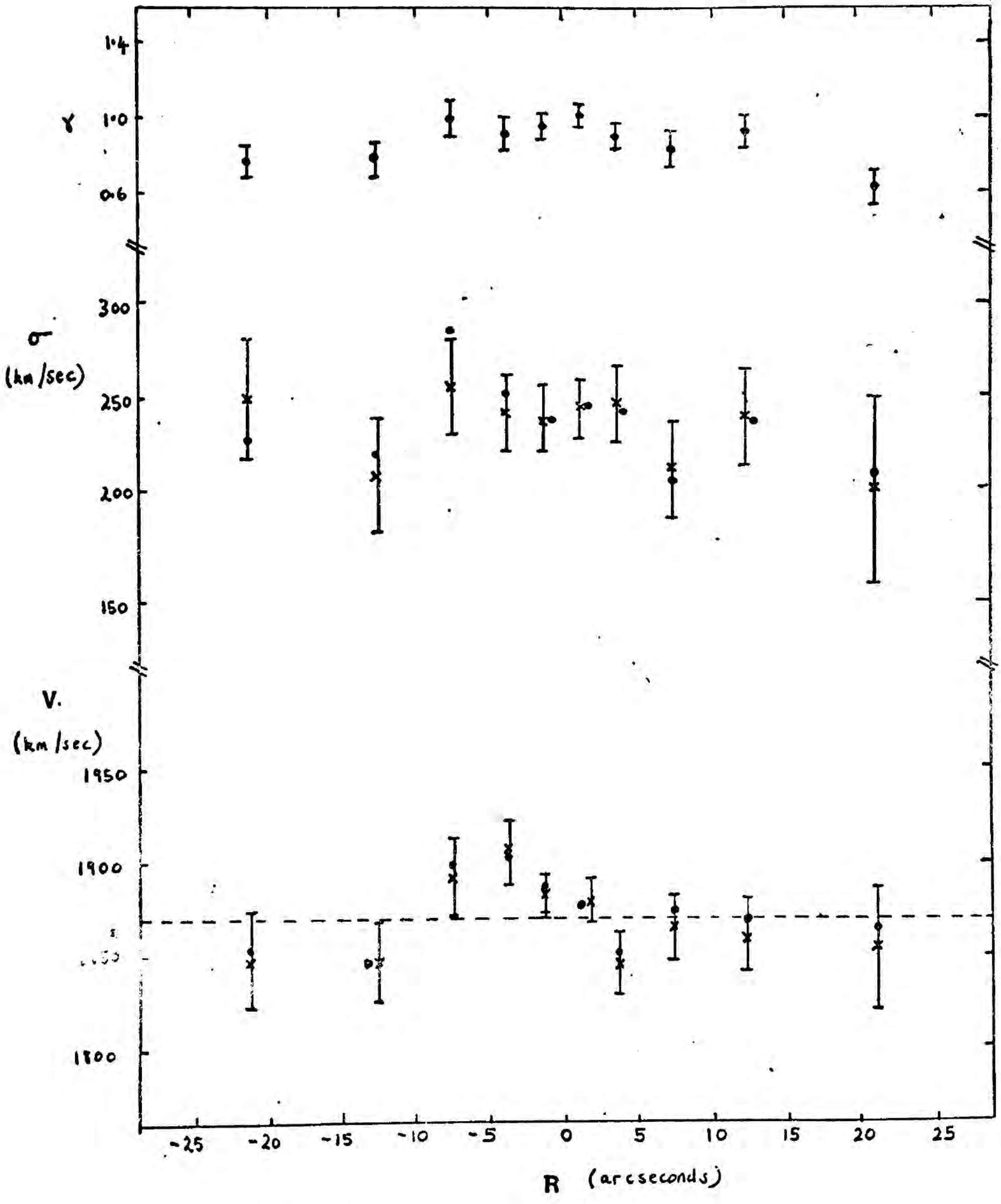

Figure 4.7(b).

a) NGC 4472.

NGC 4472 has been studied along the major axis by Illingworth (1977), Peterson (1978) and Davies (1978). The most reliable results are those of Davies. His results are plotted on Fig. 6.5(a). 40 km/sec has been subtracted from his redshift measurements in order to bring the central velocities into agreement. This correction is totally arbitrary and has been applied because we have not taken into account the relative velocity of our composite template.

The values for the central velocity dispersion are in excellent agreement, however, there is some disagreement for $R > 5$ arcseconds in that Davies finds a rapid decline in the velocity dispersion between 5 and 25 arcseconds. We also find evidence for a decline in σ , although less steep than found by Davies. However, in both cases, there is a strong correlation between the line strength parameter and the velocity dispersion across the galaxy. This correlation, also noted by Schechter and Gunn (1979), shows that the Fourier methods cannot unambiguously distinguish between variations in σ and variations in γ , hence, it is difficult to assess the significance of this result. The velocity dispersion determinations along the minor axis appear to be much more noisy than those along the major axis although the same general trend of a decline of σ with R is present.

An eye-estimate of the maximum rotational velocity along the major axis suggests $v_{max} \approx 50$ km/sec in good agreement with the results obtained by Davies. Davies has observed the rotation curve out to $\gtrsim 60$ arcseconds and finds no evidence for an increase in the rotational velocity at large radii, although large errors ($\gtrsim$ 50 km/sec) are associated with points at $R > 30$ arcseconds. The minor axis scan shows little evidence for any minor axis rotation $v \lesssim 20$ km/sec.

b) IC 4296

The velocity dispersions for both major and minor axis scans are in good agreement and are consistent with a constant velocity dispersion of $\gtrsim$ 300 km/sec for $R \lesssim 25$ arcseconds.

Although IC 4296 is the roundest of the three galaxies observed, it is also the most rapidly rotating! The major axis scan reveals a high central angular velocity of $\gtrsim 4{\cdot}5 \pm 1{\cdot}5$ km/sec/arcsecond for $R \lesssim 20$ arcseconds. We find little evidence for a turn-over in the rotation curve of IC 4296 within 25 arcseconds. In the absence of detailed photometry it is difficult to asses the significance of this result. IC 4296 is probably rounder than E1. A rotationally supported oblate galaxy with apparent ellipticity E1 would be expected to have $v/\sigma \simeq 0{\cdot}33$ (Binney, 1978). Our present data suggest $v/\sigma \simeq 0{\cdot}3 \pm 0{\cdot}1$ and are not inconsistent with this.

The minor axis scan shows little evidence for minor axis rotation. The errors here are somewhat larger than in the case of NGC 4472 but the data suggest $v \lesssim 30$ km/sec.

c) NGC 5813

The velocity dispersions for both major and minor axis scans are in excellent agreement, being consistent with a constant velocity dispersion of $\gtrsim$ 250 km/sec for $R \lesssim 25$ arcseconds.

The rotation curve along the major axis shows a quite peculiar behaviour with a high central angular velocity of

13 km/sec/arcsecond for R $\lesssim$ 5 arcseconds. The rotation curve appears to peak at $\gtrsim$ 5 arcseconds and then fall rapidly to zero. It would be extremely interesting to obtain detailed photometry of this galaxy. Judging from the work of Binney(1979), this behaviour may be related to the form of the ellipticity profile. There appears to be weak evidence for a small amount of minor axis rotation v $\gtrsim$ 20 km/sec.

6.5 Conclusions.

Most of the work that has been done on this project so far has been concerned with the technicalities of the data reduction. Hence, the discussion of the results given above has been, of necessity, rather sketchy. A more detailed analysis is currently in progress. The main conclusions may be summarised as follows:

A. Good agreement was found in determinations of rotational velocities and velocity dispersions using two methods which utilise Fourier transform techniques.

B. The velocity dispersion profiles for all three galaxies are consistent with constant σ for R $\lesssim$ 25 arcseconds, the only possible exception being NGC 4472.

C. Two galaxies (NGC 4472 and NGC 5813) have been found to be slowly rotating and inconsistent with the oblate isotropic models. IC 4296, however, was found to rotate quite rapidly, consistent with the isotropic oblate models.

D. No convincing evidence for minor axis rotation was found in the present study. The data suggests upper limits of $\lesssim$ 10 percent of the velocity dispersion for each galaxy.

CHAPTER 7

GENERAL COMMENTS
AND
PROSPECTS FOR THE FUTURE

The most detailed study in this thesis is the work on galaxy clustering of chapters 4 and 5. Yet, it is the most unconvincing. That this should be so lies in our ignorance of the real Universe. Some relevant questions are as follows: Do bright galaxies act as point particles? Are the number weighted correlation functions good indicators of the mass distribution? How good is the evidence for a clustering hierarchy? Does the correlation function really have a break at $9h^{-1}$ Mpc?

An interesting comparison may be made of the present study of galaxy clustering and the study of elliptical galaxies five years ago. Prior to 1975, the only detailed information available to theorists were photometric studies and meagre observations of the centres of elliptical galaxies. Although elegant and detailed work was done by many authors, most theorists were under the impression that elliptical galaxies were rotationally supported. This impression has now been convincingly shattered by the recent deluge of spectroscopic studies.

At present, most theorists are content in the belief (or hope) that galaxies are hierarchically clustered. What is urgently needed to either encourage or shatter this viewpoint are large numbers of galaxy redshifts, i.e. we require velocity information and not simply the "density run" of the projected galaxy distribution. Such information should help to answer the questions which I raised above.

Fortunately, such redshift projects are under way, by Marc Davis and collaborators at Harvard, by the Durham group and others. For such studies, the 20000 body models of chapter 4 have an important use. These calculations contain a sufficient number of particles, with the necessary dynamics, to simulate magnitude limited redshift samples and thereby offer a means of checking analysis techniques. In fact, during the time it has taken to write this thesis, two more calculations have been run using a harder potential than used in chapter 4. These new calculations largely remove any discrepancies between the 1000 body ensembles and the 20000 body ensembles noted in section 4.5 (e).

On the theoretical side, both the direct N-body and the kinetic theory approaches will be very difficult to extend and make more exact. A rather clever N-body approach has been taken by Fry and Peebles, but unfortunately their results are not yet available for comparison with the work presented in this thesis.

At the very least, I would hope that the work of chapter 4 has shown that the direct N-body approach is not free from ambiguity. At best, it has shown that pre-virialization does not occur in the self-similar solution. If true, this result implies that either the hierarchical clustering model is not correct or that the result of Groth and Peebles (1977) indicating $\xi_{break} \sim 0{\cdot}3$ is incorrect. It is interesting that the first application of a complete redshift sample to the large scale pattern of galaxy clustering by Kirshner, Oemler and Schechter (1979) indicates the latter.

The work on the tidal torque theory is encouraging. The recent results of the rotation of elliptical galaxies indicate that there is less angular momentum in these systems than was originally thought. The results of chapter 2 show that this is consistent with the predictions of the tidal torque theory. An important conclusion from this work is that if the angular momentum of the discs of spiral galaxies is due to tidal torques, the gas destined to form the luminous disc must have collapsed onto a massive halo. There is considerable evidence that spiral galaxies possess dark massive haloes, but the tidal torque theory, if correct, suggests that the formation of the haloes preceeded that of the discs. This raises many interesting questions, e.g. are the discs of spiral galaxies self-gravitating? What fraction of the mass of the Universe lies in the unseen component, and what is its nature?

The origin of the Hubble sequence poses another interesting problem. On the basis of the hierarchical clustering picture, I have outlined the arguments (in chapter 2) for suggesting that dissipation is not the key physical process in differentiating between whether a gas cloud will become a spiral disc or an elliptical-like assembly of stars. The hypothesis that ellipticals formed by the merging of spiral discs has been discussed in some detail by Aarseth and Fall (1979). Considerable further work needs to be done on this problem. For example, are elliptical galaxies more nearly oblate or prolate? What physical process is the cause of the frozen-in velocity anisotropies of elliptical galaxies? Further studies of the dynamical properties of elliptical galaxies should help to solve these problems.

A major aim of the work described in chapter 6 was to obtain dynamical evidence indicating triaxiality in elliptical galaxies. The results have only recently been obtained and, therefore, I have probably given an over-cautious interpretation of the data. Only one galaxy (NGC 5813) shows any evidence for minor axis rotation and this is of comparable size to our probable measurement errors. Another aim of this project is to couple the spectroscopic measurements with detailed photometry.

This investigation is continuing in collaboration with Drs. D. Carter and R.S. Ellis. Binney (1979) has shown that photometry may be coupled with simple models for the velocity structure in elliptical galaxies in order to predict their rotation curves. An empirical test of these models should be possible in the near future.

APPENDIX A

Davis and Peebles (1977) have derived a closed set of equations describing an N-body system, from the BBGKY hierarchy of kinetic equations. The closure scheme has been summarised in chapter 4. Here I write down the equivalent of Davis and Peebles' equations (89) in terms of the variables x,t and I include the terms due to discreteness. The equations may, perhaps be useful in treating cases when clustering is not self-similar (such as $\Omega \neq 1$, or particle discreteness important). As in chapter 4, I conform to the notation and definitions of Davis and Peebles.

$$\left(\frac{d}{dt} + 2\frac{\dot{a}}{a}\right)\frac{\langle p_1^2\rangle}{2m^2a^2} = \left(\frac{d}{dt} + \frac{\dot{a}}{a}\right)\frac{G\rho a^2}{2}\int\frac{\xi\, d^3\underline{x}}{x} \tag{A.1}$$

$$\frac{\partial\xi}{\partial t} + \frac{1}{x^2a^2}\frac{\partial}{\partial x}\left(\frac{x^3\, A(x,t)}{m}\right) = 0 \tag{A.2}$$

$$\frac{\partial^2\xi}{\partial t^2} + 2\frac{\dot{a}}{a}\frac{\partial\xi}{\partial t} - 8\pi G\rho\xi =$$

$$\frac{1}{m^2a^4x^2}\frac{\partial}{\partial x}\left\{\frac{\partial}{\partial x}\left[x^2\,\Pi(x,t)\right] - 2x\Sigma(x,t)\right\}$$

$$+ \boxed{\frac{8\pi Gm}{a^3}\delta(\underline{x})\left[1 + \xi(0)\right]} + \boxed{\frac{2Gm}{a^3x^2}\frac{\partial\xi}{\partial x}} \tag{A.3}$$

$$\frac{\partial}{\partial t}\;\frac{1}{x^2}\left[\frac{\partial}{\partial x}\,(x^2\,\Pi\,) - 2x\Sigma'\right] + \frac{3}{ax^2}\;\frac{\partial^2}{\partial x^2}\left[x^2 v\,\Pi\right]$$

$$- \frac{6}{ax^3}\;\frac{\partial}{\partial x}\left[x^2 v\Sigma'\right] + \frac{2m^2 a}{x^3}\langle v_1^2\rangle\,\frac{\partial}{\partial x}\left[x^4\,\frac{\partial}{\partial x}\,(V/x)\right]$$

$$- \frac{2m}{x^2}\;\frac{\partial^2}{\partial x^2}\left[x^3 V^2 A\right] + 8\pi G\rho\,ma^2 xA(x,t)$$

$$+ \boxed{\frac{4Gm^2}{a}\left[\frac{1}{x^2}\,\frac{\partial(xA)}{\partial x}\right]} + 8\pi\,G\rho\,Qma^2\,\frac{1}{x^2}\;\frac{\partial}{\partial x}\left[x^3\,\mathcal{J}_2\right]$$

$$+ 8\pi\,G\rho\,Qma^2\;\frac{x^\alpha}{x}\,\frac{\partial}{\partial x^\beta}\,\mathcal{J}_3^{\alpha\beta} = 0 \qquad \text{(A.4)}$$

$$\frac{\partial\Sigma}{\partial t} + \frac{1}{ax^4}\;\frac{\partial}{\partial x}\left\{x^4 v\left[\Sigma + \frac{2}{3}\,(ma)^2\,\langle v_1^2\rangle\right]\right\}$$

$$- \frac{8\pi}{3}\,G\rho\,ma^2\left[\frac{1}{x^2}\int_0^x dz\; z^4\,A(z) + \int_x^\infty dz\; z\;A(z)\right]$$

$$+ 8\pi\,G\rho\,ma^2\,\mathcal{J}_3^{\alpha\beta}\,\Delta^{\alpha\beta} = 0 \qquad \text{(A.5)}$$

and

$$\mathcal{J}_1(x,t) = \frac{G}{4\pi}\;\frac{\partial}{\partial x^\alpha}\int d^3z\;\;\frac{z^\alpha}{z^3}\,\xi(|\underline{x} - \underline{z}|)\left[\xi(x) + \xi(z)\right]$$

$$\frac{x^\beta}{x}\,\mathcal{J}_2(x,t) = \frac{G}{2\pi}\int d^3z\;\frac{z^\beta}{z^3}\left[A(x)\,\xi(|\underline{x} - \underline{z}|) + A(|\underline{x} - \underline{z}|)\;\xi(z)\right]$$

$$\mathcal{J}_3^{\alpha\beta}(x) = \frac{Q}{2\pi}\int d^3z \; \frac{z^\alpha z^\beta}{z^3}\left[A(z)\,\xi(|\underline{z} - \underline{x}|) - A(|\underline{z} - \underline{x}|)\,\xi(z)\right]$$

The terms enclosed by boxes in equs. (A.3) and (A.4) are the discretness terms which vanish in the continuum limit. The major problem in the present work has been the relative importance of the discreteness terms compared to the collective terms.

In the limit $\xi \gg 1$ with discreteness terms dominant one obtains equs. (4.10) under the additional assumption of stability.

From these equations one may also derive the integral constraint (section 4.5). Integrating equ. (A.3) over $n d^3\underline{x}$ one obtains

$$\frac{\partial^2 \Delta^2}{\partial t^2} + 2\frac{\dot{a}}{a}\frac{\partial \Delta^2}{\partial t} - 8\pi G\rho\,\Delta^2 = \frac{4\pi n}{m^2 a^4}\mathcal{S}'(x_o, t)$$

$$+ n\int_o^{x_o} 8\pi G\rho\,\mathcal{J}_1(x,t)\,d^3\underline{x} + \frac{8\pi G m n}{a^3}\,\xi(x_o)$$

$$+ 8\pi G\rho \qquad \text{(A.6)}$$

where, $\Delta^2 = n\int_o^{x_o} \xi\, d^3\underline{x}$ and $\mathcal{S}'(x,t) = \frac{\partial}{\partial x}\left[x^2\Pi\right] - x\Sigma$

If x_o is chosen such that $\xi(x_o) \ll 1$, then the integral involving the three-point function may be neglected as may the second term on the right hand side of equ. (A.6).

In this case

$$\frac{\partial^2 \Delta^2}{\partial t^2} + 2\frac{\dot{a}}{a}\frac{\partial \Delta^2}{\partial t} - 8\pi G\rho\Delta^2$$

$$= \frac{4\pi n}{m^2 a^4}\mathcal{S}(x_0,t) + 8\pi G\rho \qquad (A.7)$$

In the linear case, (A.4) becomes,

$$\frac{\partial \mathcal{S}}{\partial t}(x_0,t) = -8\pi G\rho m a^2 x_0 A(x_0,t)$$

$$-\frac{4Gm^2}{a}\left[\frac{1}{x^2}\frac{\partial(xA)}{\partial x}\right]_{x_0} \qquad (A.8)$$

hence, together with equ.(A.2), neglecting discreteness terms, $\mathcal{S}(x_0,t)$ may be elliminated from (A.7) to give

$$\frac{d\Delta^2}{\partial t^2} + 2\frac{\dot{a}}{a}\frac{d\Delta^2}{\partial t} - \frac{1}{2\Delta^2}\left[\frac{\partial\Delta^2}{dt}\right]^2 - 8\pi G\rho\Delta^2 = 0 \qquad (A.9)$$

which is equivalent to

$$\frac{d\Delta}{\partial t} + 2\frac{\dot{a}}{a}\frac{d\Delta}{\partial t} - 4\pi G\rho\Delta = 0 \qquad (A.10)$$

Hence, $\Delta(x_0)$ obeys the linear growth equation as long as $\xi(x_0) \ll 1$ whatever the non-linear behaviour of ξ.
If discreteness terms are included, then notice that the second term on the right hand side of equ. (A.7) acts to generate correlations. In this case, if $4/3\,\pi n x_0^3 \gg 1$, equ. (A.9) is obtained with Δ^2 replaced with $1+\Delta^2$.

References

Aarseth, S.J., 1972, in "The Gravitational N-Body Problem". Edited by M. Lecar. (Reidel, Dordrecht). p373.

Aarseth, S.J., Gott, J.R. and Turner, E.L., 1978, in "The Large Scale Structure of the Universe" (IAU Symposium No. 79) edited by M. Longair and J. Einasto. (Reidel, Dordrecht) pp. 21, 63, 189.

Aarseth, S.J., Gott, J.R. and Turner, E.L., 1979, Astrophys. J., 228, 664.

Aarseth, S.J., and Fall, S.M., 1979, submitted to the Astrophys. J., 228

Ahmad, A. and Cohen, L., 1973, J. Comp. Phys., 12, 389.

Balko, A.V., 1971, Soviet Phys. JETP, 33, 237.

Barrow, J.D., 1977, Mon. Not. R. astr. Soc., 178, 625.

Bertola, F., and Capaccioli, M., 1975, Astrophys. J. 200, 439.

Bhavsar, S.P., 1978, Astrophys. J., 222, 412.

Binney, J.J., 1974, Mon. Not. R. astr. Soc., 168, 73.

Binney, J.J., 1976, D. Phil. Thesis, Oxford University.

Binney, J.J., 1977, Mon. Not. R. astr. Soc., 181, 735.

Binney, J.J., 1978, Mon. Not. R. astr. Soc., 183, 501.

Binney, J.J., 1979, Mon. Not. R. astr. Soc., in the press.

Binney, J.J., and Silk, J., 1978, Comm. Astrophys. Sp. Sci. 7, 139.

Binney, J.J., and Silk, J., 1979, Mon. Not. R. astr. Soc., in the press.

Boksenberg, A., 1972, in "Auxiliary Instrumentation for Large Telescopes". Proc. of the ESO-CERN Conference, ed. S. Lausten and A. Reiz. p295.

Boynton, P.E., 1977, in "The Large Scale Structure of the Universe" (IAU Symposium No. 79) edited by M. Longair and J. Einasto. (Reidel, Dordrecht) p313.

Carr, B., 1975, Astrophys. J., 201, 1.

Carter, D., 1978, Mon. Not. R. astr. Soc., 182, 797.

Davies, R.L., 1978, Ph. D. Thesis, Cambridge University.

Davis, M., and Peebles, P.J.E., 1977, Astrophys. J. Suppl. Ser., 34, 425.

Davis, M., Groth, E.J., and Peebles, P.J.E., 1977, Astrophys. J. Lett., 212, L107.

Davis, M., Geller, M.J., and Huchra, J., 1978, Astrophys. J., 221, 1.

Doroshkevich, A.G., Shandarin, S.F., and Saar, E., 1978, Mon. Not. R. astr. Soc., 184, 643.

Dzyuba, B.M., and Yakubov, V.B., 1970, Soviet Astronomy-AJ, 14, 1.

Eastwood, J.W., 1976, in "Computational Methods in Classical and Quantum Physics". edited by M. Hooper. (Advance Publications). p206.

Eastwood, J.W., and Hockney, R.W., 1974, J. Comp. Phys. 16, 342.

Eastwood, J.W., Hockney, R.W., and Lawrence, D.N., 1979, submitted to Computer Phys. Commun.

Efstathiou, G., and Jones, B.J.T., 1979, submitted to Comm. Astrophys. Sp. Sci.

Eggen, O.J., Lynden-Bell, D., and Sandage, A.R., 1962, Astrophys. J., 136, 748.

Ellis, G.F.R., 1971, in "General Relativity and Cosmology", edited by R.K. Sachs. (Academic Press, New York).

Fall, S.M., 1975, Mon. Not. R. astr. Soc., 172, 23p.

Fall, S.M., 1976, D. Phil. Thesis. Oxford University.

Fall, S.M., 1978, Mon. Not. R. astr. Soc., 185, 165.

Fall, S.M., 1979, Rev. Mod. Phys., 51, 21.

Fall, S.M., and Saslaw, W.C., 1976, Astrophys. J., 204, 631.

Fall, S.M., and Severne, G., 1976, Mon. Not. R. astr. Soc., 174, 241.

Fall, S.M., and Tremaine, S., 1977, Astrophys. J., 216, 682.

Field, G.B., 1974, in "Stars and Stellar Systems" vol 9. (Chicago Press).

Fish, R.A., 1964, Astrophys. J., 139, 284.

Freeman, K.C., 1973, IAU Symposium No. 58.

Fry, J.N., and Peebles, P.J.E., 1978, Astrophys. J., 221, 19.

Geller, M.J., and Davis, M., 1978, Astrophys. J., 208, 304.

Gott, J.R., Gunn, J.E., Schramm, D.N., and Tinsley, B.M., Astrophys. J., 194, 543.

Gott, J.R., and Rees, M.J., 1975, Astr. Astrophys., 45, 365.

Gott, J.R., and Thuan, T.X., 1976, Astrophys. J., 204, 649.

Gott, J.R., and Turner, E.L., 1977, Astrophys. J., 216, 357.

Gott, J.R., Turner, E.L., and Aarseth, S.J., 1979, submitted to the Astrophys. J.

Gregory, S.A., and Thompson, L.A., 1978, Astrophys. J., 222, 784.

Groth, E.J., and Peebles, P.J.E., 1976, Astron. Astrophys., 53, 131.

Groth, E.J., and Peebles, P.J.E., 1977, Astrophys. J., 217, 385.

Harrison, E.R., 1968, Mon. Not. R. astr. Soc., 141, 397.

Harrison, E.R., 1971, Mon. Not. R. astr. Soc., 154, 167.

Hauser, M.G., and Peebles, P.J.E., 1973, Astrophys. J., 185, 757.

Hockney, R.W., Goel, S.P., and Eastwood, J.W., 1974, J. Comp. Phys., 6, 247.

Hoyle, F., 1949, in "Problems of Cosmological Aerodynamics", (International Union of Theoretical and Applied Mechanics and International Astronomical Union).

Illingworth, G., 1977, Astrophys. J. Lett., 218, L43.

Inagaki, S., 1976, Publ. Astron. Soc. Jpn., 28, 77.

Innanen, K., 1966, Astrophys. J., 143, 150.

Irvine, W.M., 1961, Ph.D. Thesis. Harvard University.

Jones, B.J.T., 1976, Rev. Mod. Phys., 48, 107.

Jones, B.J.T., 1977, Mon. Not. R. astr. Soc., 180, 151.

Kiang, T., 1967, Mon. Not. R. astr. Soc., 135, 1.

King, I.R., 1978, Astrophys. J., 222, 1.

Kirshner, R.P., Oemler, A., and Schechter, P.L., 1979 submitted to the Astron. J.

Krumm, N. and Salpeter, E.E., 1977, Astron. Astrophys., 56, 465.

Kurskov, A.A., and Ozernoi, L.M., 1974, Sov. Astron., 18, 157.

Layzer, D., 1963, Astrophys. J., 138, 174.

Limber, D.N., 1953, Astrophys. J., 117, 134.

Limber, D.N., 1954, Astrophys. J., 119, 655.

Mandelbrot, B.B., 1977, "Fractals". (Freeman, San Fransisco).

Mestel, L., 1963, Mon. Not. R. astr. Soc., 125, 127.

Mezaros, P., 1974, Astron. Astrophys., 37, 225.

Miller, R.H., 1978, Astrophys. J., 224, 32.

Miyoshi, K., and Kihara, T., 1975, Publ. Astron. Soc. Jpn., 27, 333.

Neyman, J., Scott, E.L., and Shane, C.D., 1953, Astrophys. J., 117, 92.

Nilson, P., 1973, Uppsala Astro. Obs. Ann., 6, (Uppsala General Catalogue of Galaxies).

Norman, C.A., and Silk, J., 1978, Astrophys. J., 224, 293.

Novikov, I.D., 1965, Soviet Astronomy- AJ, 8, 857.

Oort, J., 1970, Astr. Astrophys., 7, 381.

Ostriker, J.P., and Tremaine, S.D., 1975, Astrophys. J. Lett., 202, L113.

Ozernoi, L.M. and Chernin, A.D., 1968, Soviet Astronomy-AJ, 11, 907.

Peebles, P.J.E., 1965, Astrophys. J., 142, 1317.

Peebles, P.J.E., 1966, Astrophys. J., 146, 542.

Peebles, P.J.E., 1969, Astrophys. J., 155, 393.

Peebles, P.J.E., 1971a, Astrophys. and Sp. Sci., 11, 443.

Peebles, P.J.E., 1971b, Astr. Astrophys., 11, 377.

Peebles, P.J.E., 1973a, Publ. Astron. Soc. Jpn., 25, 291.

Peebles, P.J.E., 1973b, Astrophys. J., 185, 413.

Peebles, P.J.E., 1974a, Astron. Astrophys., 32, 391.

Peebles, P.J.E., 1974b, Astrophys. J., 189, L51.

Peebles, P.J.E., 1974c, Astrophys. and Sp. Sci., 31, 403.

Peebles, P.J.E., 1976a, Astrophys. and Sp. Sci., 45, 3.

Peebles, P.J.E., 1976b, Astrophys. J. Lett., 205, L109.

Peebles, P.J.E., 1977, in "The Large Scale Structure of the Universe".(IAU Symposiun No. 79) edited by M. Longair and J. Einasto, (Reidel, Dordrecht) p194.

Peebles, P.J.E., 1978, Astron. Astrophys., 68, 345.

Peebles, P.J.E., 1979, Mon. Not. R. astr. Soc., in the press.

Peebles, P.J.E., and Dicke , R.H., 1969, Astrophys. J., 154, 891.

Peebles, P.J.E., and Yu, J.T., 1970, Astrophys. J., 162, 815.

Peebles, P.J.E., and Hauser, M.G., 1974, Astrophys. J. Suppl. Ser., 28, 19.

Peebles, P.J.E., and Groth, E.J., 1975, Astrophys. J., 196, 1.

Peterson, C.J., 1978, Astrophys. J., 222, 84.

Penzias, A.A., and Wilson, R.W., 1965, Astrophys. J., 187, 425.

Press, W.H., and Schechter, P., 1974, Astrophys. J., 187, 425.

Press, W.H., and Lightman, A.P., 1978, Astrophys. J., 219, L73.

Rees, M.J., 1978, Nature, 275, 35.

Rees, M.J., and Ostriker, J.P., 1977, Mon. Not. R. astr. Soc., 179, 541.

Rubin, V.C., 1954, Proc. Natl. Acad. Sci. USA., 40, 541.

Sandage, A., and Tammann, G.A., 1979, Revised Shapley-Ames Catalogue of Galaxies. Carnegie Institute of Washington, Washington, in the press.

Sargent, W.L.W., Schechter, P.L., Boksenberg, A., and Shortridge, K., 1977, Astrophys. J., 212, 236.

Sargent, W.L.W., Young, P.J., Boksenberg, A., Shortridge, K., Lynds, C.R., and Hartwick, F.D.A., 1978, Astrophys. J., 221, 731.

Schechter, P., 1976a, Ph.D. Thesis, California Institute of Technology.

Schechter, P., 1976b, Astrophys. J., 203, 297.

Schechter, P., and Peebles, P.J.E., 1976, Astrophys. J., 209, 670.

Schechter, P.L., and Gunn, J.E., 1979, preprint.

Scott, E.L., 1957, Astron. J., 62, 248.

Seldner, M., and Peebles, P.J.E., 1977, Astrophys. J., 215, 703.

Shanks, T., 1979, Mon. Not. R. astr. Soc., 186, 583.

Sharp, N.A., Lin, D.N.C. and White, S.D.M., 1979, Mon. Not. R. astr. Soc., in the press.

Silk, J., 1968, Astrophys. J., 151, 459.

Silk, J., 1977, Astrophys. J., 211, 638.

Silk, J., and White , S.D.M., 1978, Astrophys. J., 223, L59.

Soneira, R.M., and Peebles, P.J.E., 1978, Astron. J., 83, 845.

Stecker, F.W., and Puget, J.L., 1972, Astrophys. J., 178, 57.

Sunyaev, R.A., and Zeldovich, Ya.B., 1972, Astron and Astrophys., 20, 189.

Thuan, T.X., and Gott, J.R., 1975, Nature, 257, 774.

Thuan, T.X., and Gott, J.R., 1977, Astrophys. J., 216, 194.

Tinsley, B.M, 1977, Astrophys. J., 211, 621.

Tomita, K., 1973, Publ. Astron. Soc. Jpns., 25, 287.

Tonry, J., and Davis, M., 1979, submitted to the Astrophys. J.,

Toomre, A., 1977, in "The Evolution of Galaxies and Stellar Populations". Edited by B.M. Tinsley and R.B. Larson. (Yale University Observatory, New Haven, Conn.) p401.

Totsuji, H., and Kihara, T., 1969, Publ. Astron. Soc. Jpn., 21, 221.

Tulley, R.B., 1977, in "The Large Scale Structure of the Universe" (IAU Symposium No. 79) edited by M. Longair and J. Einasto. (Reidel, Dordrecht) p214.

Turner, E.L., and Gott, J.R., 1976, Astrophys. J. Suppl. Ser., 32, 409.

van den Bergh, S., 1977, in "The Evolution of Galaxies and Stellar Populations". Edited by B.M. Tinsley and R.B. Larson. (Yale University Observatory, New Haven, Conn.).

de Vaucouleurs, G., de Vaucouleurs, A., and Corwin, H.G, 1976, Second Reference Catalogue of Brights Galaxies, University of Texas Press, Austin.

Wagoner, R.V., Fowler, W.A., and Hoyle, F., 1967, Astrophys. J., 148, 3.

Wasserman, I., 1978, Astrophys. J., 224, 337.

Weinberg, S., 1972, Gravitation and Cosmology, Wiley, New York.

Weinberg, S., 1979, Phys. Rev. Lett., 42, 850.

White, S.D.M., 1976, Mon. Not. R. astr. Soc., 177, 717.

White, S.D.M., 1979, Mon. Not. R. astr. Soc., 186, 145.

White, S.D.M., and Rees, M.J., 1978, Mon. Not. R. astr. Soc., 183, 341.

Williams, T.B., and Schwarzschild, M., 1979, Astrophys. J., 227, 156.

Young, P.J., Sargent, W.L.W., Boksenberg, A., Lynds, C.R., and Hartwick, F.D.A., 1978, Astrophys. J., 222, 450.

Zeldovich, Ya., B., 1970, Astron. and Astrophys., 5, 84.

Zeldovich, Ya., B., 1974, in "Confrontation of Cosmological Theories with Observational Data" (IAU Symposium No. 63), edited by M. Longair, (Reidel, Dordrecht).

Acknowledgments

I would like to thank my collaborators and friends, Dave Carter, Richard Ellis, Mike Fall, Craig Hogan and Bernard Jones for their help and guidance during various stages of this work. Special thanks are due Bernard Jones for setting me off in research, and to Mike Fall for many stimulating discussions.

I thank Drs. S.J. Aarseth, J. Eastwood and R. James for the loan of their computer programs and for advice on computational aspects of this work.

I would like to thank my colleagues at Durham, John Bean, Iain Inglis, Steve Phillips and Tom Shanks for many discussions over the last three years. Also Professor A.W. Wolfendale and my supervisor Dr. R. Fong, for their interest in this work and for their help in providing travel grants. I am indebted to Richard Ellis for his helpful comments on various parts of this thesis.

I acknowledge the receipt of an SRC studentship and would like to thank the SRC for provision of computing facilities.

Finally, were it not for the patience and understanding of my wife Janet, this thesis would never have been completed.